

2009

Segmented field electron conformal therapy with an electron multi-leaf collimator

John Gordon Eley

Louisiana State University and Agricultural and Mechanical College

Follow this and additional works at: https://digitalcommons.lsu.edu/gradschool_theses



Part of the [Physical Sciences and Mathematics Commons](#)

Recommended Citation

Eley, John Gordon, "Segmented field electron conformal therapy with an electron multi-leaf collimator" (2009). *LSU Master's Theses*. 1746.

https://digitalcommons.lsu.edu/gradschool_theses/1746

This Thesis is brought to you for free and open access by the Graduate School at LSU Digital Commons. It has been accepted for inclusion in LSU Master's Theses by an authorized graduate school editor of LSU Digital Commons. For more information, please contact gradetd@lsu.edu.

SEGMENTED FIELD ELECTRON CONFORMAL THERAPY WITH AN ELECTRON MULTI-LEAF COLLIMATOR

A Thesis

Submitted to the Graduate Faculty of the
Louisiana State University and
Agricultural and Mechanical College
in partial fulfillment of the
requirements for the degree of
Master of Science

in

The Department of Physics and Astronomy

by
John Gordon Eley
B.S., College of Charleston, 2005
December 2009

Acknowledgements

I thank my advisor Dr. Kenneth Hogstrom for being an inspiring teacher and mentor and for guiding my entrance into the field of medical physics. I thank Dr. Kenneth Matthews for his outstanding commitment to education. I thank Dr. Erno Sajo for his enthusiasm for teaching and radiation transport physics. I thank Dr. John Gibbons and the medical physicists at Mary Bird Perkins Cancer Center for my clinical education. I thank the members of my supervisory committee and all of the medical physics and health physics faculty who have given me a wonderful education. I thank Yvonne Thomas for her assistance and friendship throughout my graduate work.

I thank my classmate and friend Olivier Blasi for hundreds of hours of conversation and debate that has enriched my understanding of physics and nature. I thank my parents, James and Leigh Eley, for placing high values on family, education, and art.

I appreciate the time I have spent at Louisiana State University and Mary Bird Perkins Cancer Center and am grateful for the physical and financial resources provided by each institution.

Table of Contents

Acknowledgements	ii
List of Tables	v
List of Figures	vii
Abstract	xii
Chapter 1. Introduction	1
1.1 Background and Significance	1
1.1.1 Fundamental Advantages of Electron Therapy	1
1.1.2 Developments in Electron Conformal Therapy	2
1.1.3 Potential for Electron Multi-leaf Collimators	4
1.1.4 Purpose of Current Study	8
1.2 Hypothesis	8
1.3 Specific Aims	8
1.3.1 Aim 1: Define eMLC Leaf Positions for General Electron Fields	8
1.3.2 Aim 2: Commission the eMLC for Dose Computation	8
1.3.3 Aim 3: Feather Field Edges to Improve Dose Homogeneity	8
Chapter 2. Methods and Materials	10
2.1 Aim 1: Define eMLC Leaf Positions for General Electron Fields	10
2.1.1 Establish Geometry of Leaf Positioning	10
2.1.2 Software Developed to Position Leaves for General Fields	14
2.1.3 Calibrate Leaf Positions at the Plane of Leaves	16
2.1.4 Measure eMLC Fields with Radiographic Films	18
2.1.5 Analyze Film Measurements	22
2.2 Aim 2: Commission the eMLC for Dose Computation	24
2.2.1 Measure Electron Dose Distributions with a Water Scanning System	25
2.2.2 Measure Dose Output in a Water Phantom	32
2.2.3 Measure Photon Transmission through eMLC Leaves	33
2.2.4 Input Required PBA Data into Pinnacle Beam Models	34
2.2.5 Validate Relative Dose Computations with Isodose Measurements	36
2.2.6 Validate Implementation of Output Factors by Pinnacle	40
2.3 Aim 3: Feather Field Edges to Improve Dose Homogeneity	40
2.3.1 Determine Analytical Solution to Edge Feathering Based on PBA	40
2.3.2 Computer Algorithm Developed to Implement Discrete Gaussian Edge Feathering	44
2.3.3 Compute Effect of Discrete Gaussian Edge Feathering on Dose Distributions	50
2.3.4 Measure Dose Distributions for Segmented Field ECT plans with and without Edge Feathering	54

Chapter 3. Results and Discussion	56
3.1 Aim 1: Define eMLC Leaf Positions for General Electron Fields	56
3.1.1 Calibration of Field Width at the Plane of Leaves	56
3.1.2 Radiation Field Widths for Rectangular Fields	57
3.1.3 Delivery of Irregular Fields with the eMLC	59
3.1.4 Delivery of Segmented Fields with the eMLC	63
3.2 Aim 2: Commission the eMLC for Dose Computation	74
3.2.1 Measured Electron Beam Data for Pencil Beam Algorithm	74
3.2.2 Validate Dose Computations with Measured Isodose Curves	88
3.3 Aim 3: Investigate eMLC Segmented-field Plans and Edge Feathering	105
3.3.1 Impact of Number of Discrete Steps on Feathering Solution	105
3.3.2 Two-step PTV	105
3.3.3 Wedge PTV	113
3.3.4 Inverted Well PTV	116
3.3.5 Concentric Cylinders PTV	121
3.3.6 Summary of PTV Dose Statistics	142
Chapter 4. Conclusions	144
4.1 Summary of Results	144
4.2 Conclusions	145
4.3 Recommendations for Future Study	146
References	148
Appendix A: Film Dose Measurements	150
Appendix B: Pinnacle Photon Model	156
Vita	165

List of Tables

2.1	Electron beam model parameters for Pinnacle.	36
3.1	Isocentric field width measurements parallel to leaf motion (y-axis).	58
3.2	Isocentric field widths defined by the number of leaves open.	59
3.3	Isocentric field width measurements perpendicular to leaf motion (x-axis).	60
3.4	6 MeV comparison of measured output data with Pinnacle computed output data.	80
3.5	9 MeV comparison of measured output data with Pinnacle computed output data.	80
3.6	12 MeV comparison of measured output data with Pinnacle computed output data.	86
3.7	16 MeV comparison of measured output data with Pinnacle computed output data.	86
3.8	20 MeV comparison of measured output data with Pinnacle computed output data.	87
3.9	eMLC photon transmission factors.	87
3.10	6 MeV comparison of measured and computed dose distributions.	100
3.11	9 MeV comparison of measured and computed dose distributions.	101
3.12	12 MeV comparison of measured and computed dose distributions.	102
3.13	16 MeV comparison of measured and computed dose distributions.	103
3.14	20 MeV comparison of measured and computed dose distributions.	104
3.15	Computed dose statistics for two-step PTV treatment plans with no feathering and 5 step Gaussian edge feathering.	108
3.16	Computed dose statistics for wedge PTV treatment plans with no feathering and 5 step Gaussian edge feathering.	116
3.17	Computed dose statistics for inverted well PTV treatment plans with no feathering and 5 step Gaussian edge feathering.	126
3.18	Computed dose statistics for concentric cylinders PTV treatment plans with no feathering, 1D 5-step Gaussian edge feathering, and 2D 5-step Gaussian edge feathering.	142

3.19 Computed dose statistics for test PTV treatment plans with no feathering and 5-step discrete Gaussian edge feathering.	143
A.1 Film calibration curve data used in the Matlab program.	155

List of Figures

1.1	Central axis depth-dose data comparing electron and x-ray beams with similar peak kinetic energies.	2
1.2	Transverse section of bolus ECT plan compared with segmented field ECT plan.	3
1.3	Segmented field ECT plan for a patient with recurrent squamous cell carcinoma of the left ear.	5
1.4	Prototype eMLC used in the current study	7
2.1	eMLC leaf dimensions.	11
2.2	Radiation field projected through rounded leaf ends	12
2.3	Discrepancy between focal point of leaves and virtual electron source	13
2.4	eMLC leaf calibration photograph	17
2.5	eMLC film measurements	19
2.6	Water phantom and eMLC Setup	29
2.7	Discretizing the Gaussian edge spread function.	46
2.8	1D (vertical) dilation and erosion of an irregular segment aperture.	48
2.9	2D dilation and erosion of an irregular segment aperture.	49
2.10	Two-step PTV dimensions.	51
2.11	Wedge PTV dimensions.	51
2.12	Inverted well PTV dimensions.	52
2.13	Concentric cylinders PTV dimensions.	53
3.1	Pentagon, irregular field with eMLC leaves overlaying general field shape.	60
3.2	Crescent, irregular field with eMLC leaves overlaying general field shape.	61
3.3	Pentagon, irregular field isodose curves overlaying the eMLC aperture at the isocentric plane.	62
3.4	Crescent, irregular field isodose curves overlaying the eMLC aperture at the isocentric plane.	62
3.5	Pentagon, irregular field isodose curves overlaying the desired general field at the isocentric plane.	64

3.6	Crescent, irregular field isodose curves overlaying the desired general field at the isocentric plane.	64
3.7	Two 20 MeV fields ($15 \times 5 \text{ cm}^2$) abutting on central axis delivered with the eMLC.	65
3.8	Two 12 MeV fields ($15 \times 5 \text{ cm}^2$) abutting on central axis delivered with the eMLC.	66
3.9	20 MeV field abutting a 12 MeV field (each $15 \times 5 \text{ cm}^2$) on central axis delivered with the eMLC.	67
3.10	Two 20 MeV fields (15×5 and $15 \times 15 \text{ cm}^2$) abutting 5 cm off central axis delivered with the eMLC.	68
3.11	Two 12 MeV fields (15×5 and $15 \times 15 \text{ cm}^2$) abutting 5 cm off central axis delivered with the eMLC.	69
3.12	12 MeV field ($15 \times 5 \text{ cm}^2$) abutting a 20 MeV field ($15 \times 15 \text{ cm}^2$) 5 cm off central axis delivered with the eMLC.	70
3.13	Two 20 MeV fields abutting diagonally delivered with the eMLC.	71
3.14	Two 12 MeV fields abutting diagonally delivered with the eMLC.	72
3.15	20 MeV field abutting a 12 MeV field diagonally delivered with the eMLC.	73
3.16	6 MeV central axis depth dose curves.	75
3.17	6 MeV, $3 \times 3 \text{ cm}^2$ PDD, computed with the square root method, compared with a measured $3 \times 3 \text{ cm}^2$ PDD.	75
3.18	9 MeV central axis depth dose curves.	76
3.19	9 MeV, $3 \times 3 \text{ cm}^2$ PDD, computed with the square root method, compared with a measured $3 \times 3 \text{ cm}^2$ PDD.	76
3.20	12 MeV central axis depth dose curves.	77
3.21	12 MeV, $3 \times 3 \text{ cm}^2$ PDD, computed with the square root method, compared with a measured $3 \times 3 \text{ cm}^2$ PDD.	77
3.22	16 MeV central axis depth dose curves.	78
3.23	16 MeV, $3 \times 3 \text{ cm}^2$ PDD, computed with the square root method, compared with a measured $3 \times 3 \text{ cm}^2$ PDD.	78
3.24	20 MeV central axis depth dose curves.	79
3.25	20 MeV, $3 \times 3 \text{ cm}^2$ PDD, computed with the square root method, compared with a measured $3 \times 3 \text{ cm}^2$ PDD.	79

3.26	6 MeV output factors vs. field size at 3.26(a) 100 cm SSD, 3.26(b) 105 cm SSD, and 3.26(c) 110 cm SSD.	81
3.27	9 MeV output factors vs. field size at 3.27(a) 100 cm SSD, 3.27(b) 105 cm SSD, and 3.27(c) 110 cm SSD.	82
3.28	12 MeV output factors vs. field size at 3.28(a) 100 cm SSD, 3.28(b) 105 cm SSD, and 3.28(c) 110 cm SSD.	83
3.29	16 MeV output factors vs. field size at 3.29(a) 100 cm SSD, 3.29(b) 105 cm SSD, and 3.29(c) 110 cm SSD.	84
3.30	20 MeV output factors vs. field size at 3.30(a) 100 cm SSD, 3.30(b) 105 cm SSD, and 3.30(c) 110 cm SSD.	85
3.31	Measured (black) vs. Pinnacle computed (red) isodose curves for 6 MeV. . .	90
3.32	Measured (black) vs. Pinnacle computed isodose curves for 9 MeV.	91
3.33	Measured (black) vs. Pinnacle computed (red) isodose curves for 12 MeV at 100 cm SSD.	92
3.34	Measured (black) vs. Pinnacle computed (red) isodose curves for 12 MeV at 110 cm SSD.	93
3.35	Measured (black) vs. Pinnacle computed (red) isodose curves for 16 MeV at 100 cm SSD.	94
3.36	Measured (black) vs. Pinnacle computed (red) isodose curves for 16 MeV at 110 cm SSD.	95
3.37	Measured (black) vs. Pinnacle computed (red) isodose curves for 20 MeV, 7×7 cm ² field at 100 cm SSD.	96
3.38	Measured (black) vs. Pinnacle computed (red) isodose curves for 20 MeV, 15×15 cm ² field at 100 cm SSD.	97
3.39	Measured (black) vs. Pinnacle computed (red) isodose curves for 20 MeV, 7×7 cm ² field at 110 cm SSD.	98
3.40	Measured (black) vs. Pinnacle computed (red) isodose curves for 20 MeV, 15×15 cm ² field at 110 cm SSD.	99
3.41	Investigation of the optimal number of discrete feathering steps.	106
3.42	Beam's eye view of the two-step PTV segmented field ECT plan.	107
3.43	Beam's eye view of the two-step PTV segmented field ECT plan with discrete Gaussian edge feathering.	107
3.44	Computed isodose contours in YZ plane for two-step PTV for 1-step and 5-step feathering.	109

3.45	Computed isodose contours in YX plane for two-step PTV for 1-step and 5-step feathering.	110
3.46	Computed vs. measured off-axis dose profiles for two-step PTV with 1-step and 5-step feathering.	111
3.47	Measured isodose contours in YX plane for two-step PTV for 1-step and 5-step) feathering.	112
3.48	Beam's eye view of the wedge PTV segmented field ECT plan.	114
3.49	Beam's eye view of the wedge PTV segmented field ECT plan with discrete Gaussian edge feathering.	115
3.50	Computed isodose contours in YZ plane for wedge PTV for 1-step and 5-step feathering.	117
3.51	Computed isodose contours in YX plane for wedge PTV for 1-step and 5-step feathering.	118
3.52	Computed vs. measured off-axis dose profiles for wedge PTV with 1-step and 5-step feathering.	119
3.53	Measured isodose contours in YX plane for wedge PTV for 1-step and 5-step feathering.	120
3.54	Beam's eye view of the inverted well PTV segmented field ECT plan.	122
3.55	Beam's eye view of the inverted well PTV segmented field ECT plan with discrete Gaussian edge feathering.	123
3.56	Computed isodose contours in YZ plane for inverted well PTV for 1-step and 5-step feathering.	124
3.57	Computed isodose contours in YX plane for inverted well PTV for 1-step and 5-step feathering.	125
3.58	Computed vs. measured off-axis dose profiles for inverted well PTV with 1-step and 5-step feathering.	126
3.59	Measured isodose contours in YX plane for inverted well PTV for 1-step and 5-step feathering.	127
3.60	Beam's eye view of the concentric cylinders PTV segmented field ECT plan.	129
3.61	Beam's eye view of the concentric cylinders PTV segmented field ECT plan with 1D discrete Gaussian edge feathering.	130
3.62	Beam's eye view of the concentric cylinders PTV segmented field ECT plan with 2D discrete Gaussian edge feathering.	131

3.63	Beam's eye view of the concentric cylinders PTV segmented field ECT plan with 2D discrete Gaussian edge feathering and infinitesimal eMLC leaf width.	132
3.64	Computed isodose contours in YZ plane for concentric cylinders PTV for 1-step and 1D 5-step feathering.	134
3.65	Computed isodose contours in YZ plane for two-step PTV for 2D 5-step and 2D continuous aperture 5-step feathering.	135
3.66	Computed isodose contours in YX plane for concentric cylinders PTV for 1-step and 1D 5-step feathering.	136
3.67	Computed isodose contours in YX plane for two-step PTV for 2D 5-step and 2D continuous aperture 5-step feathering.	137
3.68	Computed vs. measured off-axis dose profiles for concentric cylinders PTV with 1-step and 1D 5-step feathering.	138
3.69	Computed vs. measured off-axis dose profiles for concentric cylinders PTV with 2D 5-step and 2D continuous aperture 5-step feathering.	139
3.70	Measured isodose contours in YX plane for concentric cylinders PTV (red) for 1-step and 1D 5-step feathering.	140
3.71	Measured isodose contours in YX plane for two-step PTV for 2D 5-step feathering.	141
A.1	Beam's eye view of a calibration film.	152
A.2	Film calibration setup geometry for one of 4 fields used to irradiate film.	153
A.3	Film dose calibration curve	154
B.1	Photon model off-axis dose profiles for 20 MeV, 20×20 cm ² field data.	157
B.2	Photon model off-axis dose profiles for 20 MeV, 7×7 cm ² field data.	157
B.3	Modified photon model off-axis dose profiles for 20 MeV, 20×20 cm ² field data.	159
B.4	Modified photon model off-axis dose profiles for 20 MeV, 7×7 cm ² field data.	159
B.5	Computed vs. measured isodose contours for 20 MeV, 7×7 cm ² field size.	160
B.6	Computed vs. measured isodose contours for 20 MeV, 15×15 cm ² field size.	161
B.7	Computed vs. measured isodose contours for 20 MeV, 7×7 cm ² field size.	162
B.8	Computed vs. measured isodose contours for 20 MeV, 15×15 cm ² field size.	163

Abstract

Purpose: The purpose of this work was to investigate the potential of a prototype electron multi-leaf collimator (eMLC) to deliver segmented-field electron conformal therapy (ECT) and to improve dose homogeneity to the planning target volume (PTV) by feathering the abutting edge of the higher energy electron fields. *Methods:* Software was developed to define the eMLC leaf positions that most closely fit a general field shape. Electron beams (6-20 MeV) using a prototype eMLC were commissioned for the pencil beam dose algorithm in the Pinnacle treatment planning system. A discrete (5-step) Gaussian edge spread function was used to match electron dose penumbras of differing energies at a specified depth in a water phantom. The effect of 1D edge feathering on dose homogeneity was computed and measured for segmented-field ECT treatment plans for three 2D PTVs in a water phantom (depths varied along axis parallel to leaf motion) and one 3D PTV (depth varied along both axes normal to beam). Additionally, the effect of 2D edge feathering was computed for the 3D PTV. *Results:* 1D discrete Gaussian edge feathering reduced the standard deviation of dose in the 2D PTVs by 34, 34, and 39%. In the 3D PTV, 1D discrete Gaussian edge feathering reduced the standard deviation of dose by 19%. The physical constraints (1-cm leaf width) of the eMLC hindered the 2D application of the feathering solution to the 3D PTV, and the standard deviation of dose increased by 10%. However, 2D discrete Gaussian edge feathering with a smooth-aperture (infinitesimal leaf width) reduced the standard deviation of dose in the 3D PTV by 33%. *Conclusions:* A 5-step discrete Gaussian edge spread function applied in 2D improves the abutment dosimetry but requires an eMLC leaf resolution better than 1 cm.

Chapter 1. Introduction

1.1 Background and Significance

1.1.1 Fundamental Advantages of Electron Therapy

The dose distributions of electron radiotherapy are well suited for treating disease sites within 6 cm of the external patient surface. Charged particles deposit energy continuously through inelastic scattering that ionizes and excites the target matter. The relatively low mass of the electron compared to the target nuclei also gives rise to bremsstrahlung energy losses and multiple Coulomb scattering. As a result of these interactions, the electron depth-dose distribution has an approximately uniform dose throughout the therapeutic range, a rapid distal falloff beyond the therapeutic range, and little exit-dose that often proves superior to the photon therapy dose distribution when critical structures are present deep to the planning target volume (PTV). Figure 1.1 compares depth-dose distributions for electron and x-ray beams with similar peak kinetic energies. Typical shallow sites treated with electron therapy include: skin, lips, ear, eyelid, nose, salivary glands, chest wall, upper respiratory, and digestive malignancies (Tapley 1976; Hogstrom 2003; Hogstrom and Almond 2006; Million et al. 1991). Common critical structures deep to the PTV include the spinal cord, brain, salivary glands, and lungs (Hogstrom et al. 2003; Million et al. 1991).

Electron treatment planning typically involves choosing a single electron beam with an energy high enough that the therapeutic range, R_{90} , provides adequate dose coverage for the deepest portion of the PTV, yet low enough to keep dose to normal tissue dose deep to the tumor minimal. Lateral field shaping is achieved by the custom fabrication of cerrobend collimator inserts and sometimes with the addition of lead, skin collimation. Typically, PTV depth varies with off-axis position. In these cases, using a single-energy electron field treats shallow regions of the PTV and deep regions of the PTV the same by using the greatest depth to choose the electron energy that will cover the target volume with adequate dose.

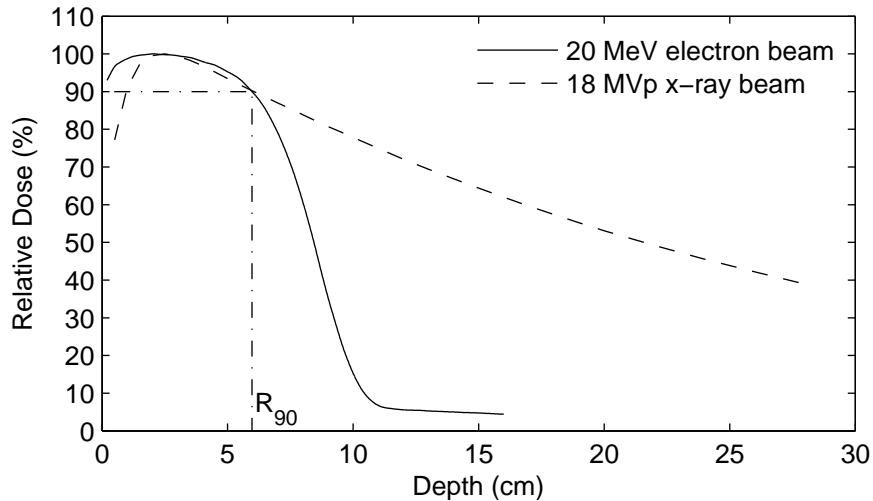


Figure 1.1: Central axis depth-dose data comparing electron and x-ray beams with similar peak kinetic energies. The therapeutic range, R_{90} , occurs as the dose falls distally to 90% of the maximum dose and is selected to contain the deep PTV surface. Data extracted from the MBPCC treatment planning system for a Varian Clinac 21EX linear accelerator with 20×20 cm² field size, 100 cm SSD, water phantom.

Without electron conformal therapy techniques (Hogstrom et al. 2003), the patient receives unnecessary dose to healthy tissue deep to the shallow regions of the PTV.

1.1.2 Developments in Electron Conformal Therapy

The desire to reduce dose to healthy tissue deep to the tumor has led to research developments in electron conformal therapy (ECT). Electron conformal therapy involves modulating the depth of the 90% isodose curve to most closely fit the deep surface of the PTV, achieving a homogeneous dose to the PTV, and minimizing the dose to underlying critical structures and normal tissue (Hogstrom et al. 2003). Two well known methods for delivering electron conformal therapy are either using customized bolus or segmenting the treatment field into regions of different electron energy (Hogstrom et al. 2003; Zackrisson and Karlsson 1996). Figure 1.2 shows modulation of 90% isodose curves possible with bolus and segmented-field ECT.

Electron bolus is a nearly tissue equivalent material (e.g., wax) that is placed on the patient surface to increase surface dose or to decrease the therapeutic range of the electrons and improve normal tissue sparing deep to the PTV (Hogstrom et al. 2003). Low et al. (1992)

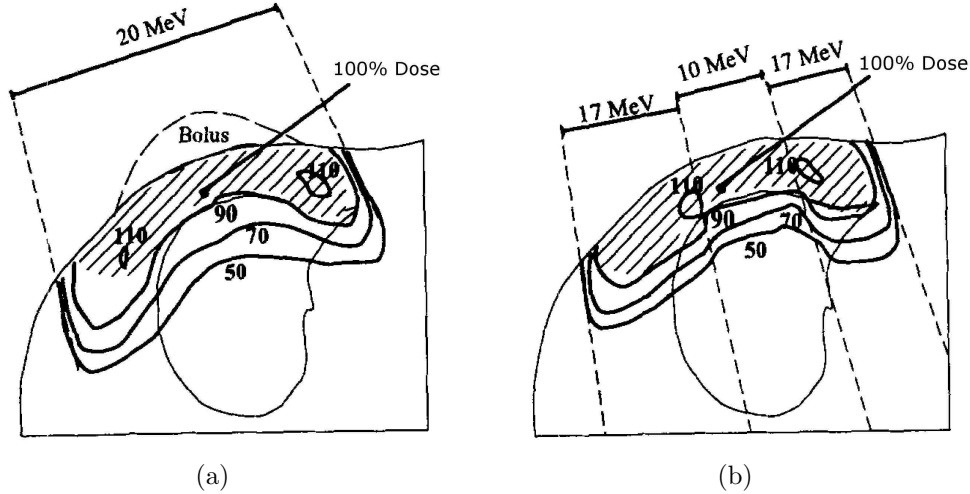


Figure 1.2: Transverse section of bolus ECT plan compared with segmented field ECT plan (modified from Zackrisson and Karlsson (1996)). PTV indicated by the hatched lines. Both methods modulate the distal 90% isodose contour to match the deep PTV surface and spare healthy lung tissue, and both methods introduce dose heterogeneity into the PTV as seen in the 110% isodose hot spots.

developed a bolus ECT design algorithm that projected fan lines from the virtual electron source to the distal surface of the PTV, varied the bolus thickness to match R_{90} to the distal PTV surface for each fan line, computed the dose distribution, and iteratively smoothed the proximal bolus surface to minimize dose heterogeneity resulting from multiple Coulomb scattering over the irregular bolus surface (Hogstrom et al. 2003). The patient receiving therapy with bolus is typically re-imaged with a computed tomography (CT) scanner with the bolus in place. The dose may then be computed again with the updated CT data set. Bolus ECT has the advantage of continuous energy modulation which provides highly conformal dose distributions while requiring only a single electron beam delivered with an unmodified linear accelerator. The disadvantages of bolus ECT arise from the hot and cold dose regions resulting from the irregular proximal surface and the higher range straggling of the high energy beam incident over shallow regions of the PTV where the dose distribution does not exhibit the sharper distal falloff found when lower energy beams are delivered to shallow PTV regions as with segmented-field ECT. Customized bolus may also need to be refabricated over the course of treatment for a patient with large changes in skin contour

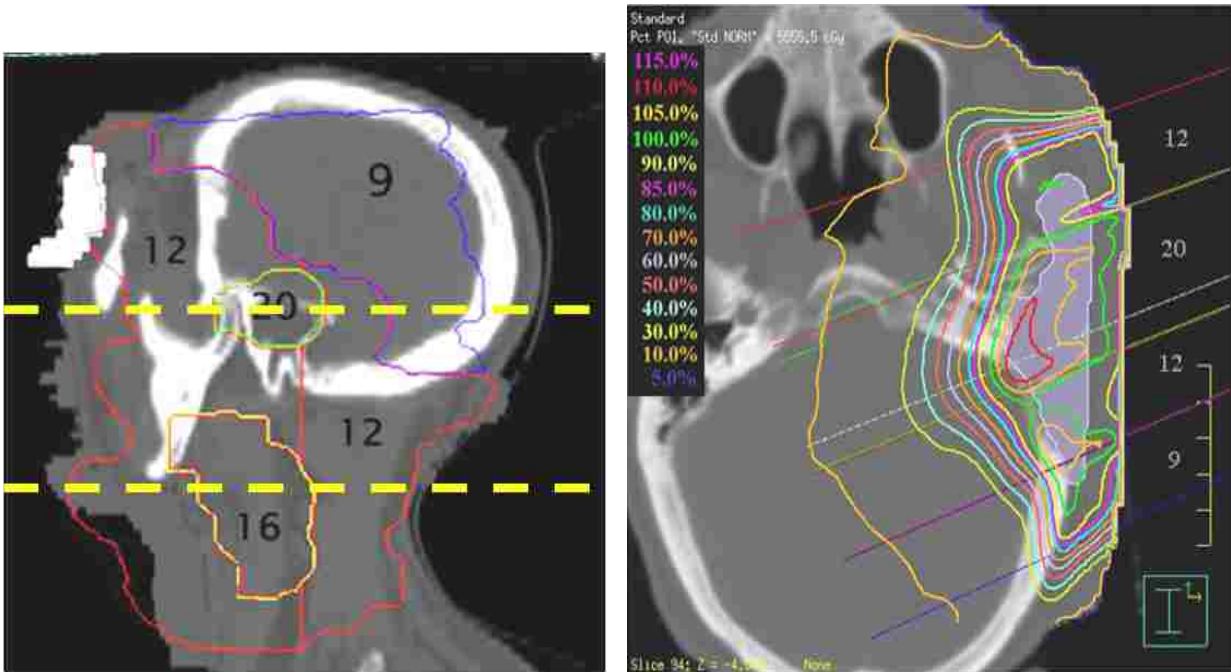
due to successful shrinking of the tumor volume. Segmented-field ECT may achieve effects similar to bolus ECT, although typically less conformity than bolus ECT due to large energy intervals in radiotherapy linear accelerators. Delivering the treatment field, that is segmented into multiple energy regions, is the focus of the current study.

Segmented-field ECT has been defined by Hogstrom et al. (2003) as “the utilization of multiple abutted electron fields, each having a common virtual source position but each having its own energy and weight, so as to conform the therapeutic dose surface (e.g., 90% of given dose) to the PTV.” Treatment planning may be achieved through forward planning with a 3-D treatment planning system, or, preferably, with a computer based segmented-field ECT planning algorithm such as designed by Perrin (2008). Figure 1.1.2 shows a segmented field treatment plan created with forward planning (Richert 2006). When segmenting electron fields, practical, but effective, methods for delivering the segments and achieving good abutment dosimetry must be utilized.

Regarding abutment dosimetry, it is well known that abutting fields of different energy results in hot and cold dose spots due to their having different penumbral widths (Million et al. 1991). Richert et al. (2007) have shown the utility of a variable source-to-collimator distance (SCD) to match the penumbras for abutted electron field segments of differing energy and achieved a mean reduction in the standard deviation of dose in hypothetical PTVs of 29%. Current methods for delivering the segments use patched cerrobend cut-outs, which are inefficient due to the need to enter the treatment room to change the inserts between segments.

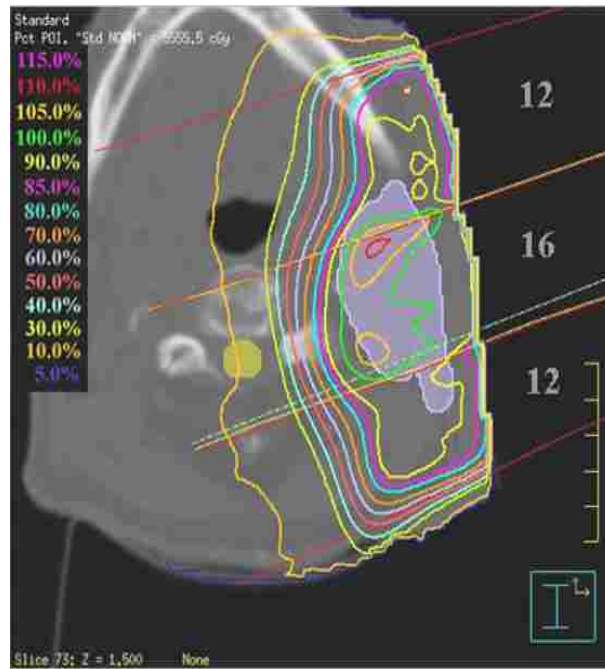
1.1.3 Potential for Electron Multi-leaf Collimators

The use of an electron multi-leaf collimator (eMLC) offers an attractive alternative for segmented-field ECT (Hogstrom et al. 2004). The development of eMLCs stands to accomplish similar advancements achieved through the development of x-ray multi-leaf collimators (xMLC). An eMLC will eliminate the need to construct custom cerrobend inserts and will open the potential to deliver segmented field ECT and intensity modulated electron therapy without the need to enter the treatment room during delivery. Commercial development



(a)

(b)



(c)

Figure 1.3: Segmented field ECT plan for a patient with recurrent squamous cell carcinoma of the left ear (adapted from Richert (2006)). A beams eye view (a) of the segmented field shows the geometric field edges and energies of the segments overlaying the patient CT data. The dashed, yellow lines in (a) indicate the location of axial slices (b and c) in the treatment plan. The axial slices (b and c) show the PTV (lavender) with depth varying off-axis, the forward planned beam placement, and the corresponding, computed isodose contours. Dose hot spots and heterogeneities are seen in the segment abutment regions.

of the eMLC has lagged behind the xMLC, largely believed due to the smaller number of patients suitable for electron therapy.

One type of eMLC design places the multi-leaf system in the insert tray of a standard electron applicator. Ma et al. (2000) utilized this type of design for the 25×25 cm² electron applicator of the Varian Clinac accelerator. Ravindran et al. (2002) also designed this type of system for the 15×15 cm² electron applicator of the Siemens Mevatron accelerator. The advantages of these eMLC systems are low mass and compact design. Flaws of these systems include leaf geometries that are not divergent from the virtual electron source (perpendicular to leaf motion) and the lack of rounded leaf-ends needed so that the electron beam tangentially intersects the leaf-end as the leaf travels across the electron field. Neglecting these two design specifications leads to off-axis dependency of the penumbra shape. Also, neither were motorized.

The eMLC used in the current study has been developed and evaluated by Hogstrom et al. (2004) and has the potential to deliver segmented, irregular field ECT. The prototype eMLC is shown in Figure 1.4. The leaves are divergent perpendicular to leaf motion and have rounded leaf ends to ensure minimal off-axis dependence of penumbra shape and, therefore, proper abutment of segments off central-axis. The variable SCD method of Richert (2006) to improve abutment dosimetry, mentioned above, was not considered here because the eMLC does not easily change SCD and differences in SCD would create additional issues due to differing leaf widths projecting to isocenter.

In consideration of the benefits of the variable SCD for dose homogeneity, an alternate method for improving abutment dosimetry of the segments of different energy was investigated. An edge-feathering algorithm was developed that modulated the eMLC leaf positions to match the penumbras of abutting segments and improve dose homogeneity. The impact of such penumbra modulation has not been previously studied. This principle was investigated in the current work, and software was developed to facilitate its future research and clinical implementation.

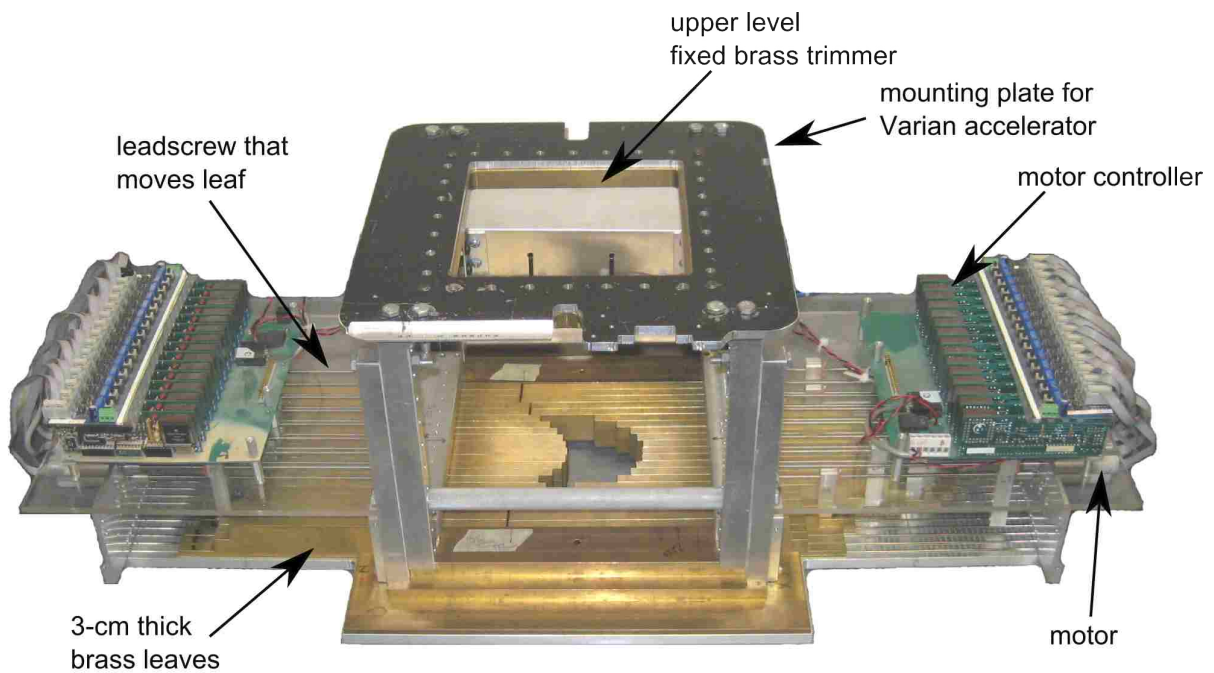


Figure 1.4: Prototype eMLC used in the current study. The eMLC (Hogstrom et al. 2004) has 21 brass leaves on each side that project to approximately 1 cm width at isocenter; 15 leaves on each side are motorized to currently deliver a maximum $15 \times 20 \text{ cm}^2$ field size. The device docks to the accelerator via a custom fabricated plate identical to the top plate of a standard electron applicator for a Varian Clinac 21EX accelerator and has a fixed air gap of 10 cm.

1.1.4 Purpose of Current Study

The purpose of this work was to investigate the potential of a prototype electron multi-leaf collimator to deliver segmented-field electron conformal therapy and to improve dose homogeneity to the planning target volume by feathering the abutting edge of the higher energy electron fields.

1.2 Hypothesis

By feathering the abutting edges of the higher energy electron fields in segmented-field ECT, the standard deviation of the PTV dose distribution will be reduced by 30% relative to segmented-field ECT delivered by an eMLC without edge feathering.

1.3 Specific Aims

1.3.1 Aim 1: Define eMLC Leaf Positions for General Electron Fields

The geometric relationships of the eMLC and the linear accelerator will be evaluated. Software will be developed to define the eMLC leaf positions that closely fit a general segmented-field shape. Calibration checks will be performed by delivering electron fields to films positioned at the accelerator isocenter, measuring the exposed regions of the film, and confirming that the leaf positioning software creates radiation fields with a leaf position uncertainty of ± 1 mm.

1.3.2 Aim 2: Commission the eMLC for Dose Computation

Electron beam data required to commission the eMLC for the electron pencil beam dose algorithm of the Pinnacle treatment planning system will be measured. The measured data and the physical specifications of the eMLC will be added to the treatment planning system and commissioned for treatment planning. The eMLC will be installed on a linear accelerator, and commissioning of the PBA will be validated through measurement. Isodose curves will be generated to compare dose computation with measurements.

1.3.3 Aim 3: Feather Field Edges to Improve Dose Homogeneity

One-dimensional and two-dimensional edge feathering for abutting segments of different electron energies in a water phantom will be investigated. Analytical feathering solutions will

be converted into clinically practical feathering solutions. The impact of the feathering solutions on dose homogeneity will be computed using an electron pencil beam dose algorithm. Hypothetical 2D PTVs in a water phantom will be used to compare dose homogeneity in the PTV for one-dimensional edge feathering and no feathering. An additional 3D PTV will be used to evaluate 1D, 2D, and no feathering for a SFECT plan with segment abutment regions both perpendicular to leaf motion and parallel to leaf motion. The computed improvements to dose homogeneity through edge feathering will be validated with film measurements in a plastic water phantom.

Chapter 2. Methods and Materials

2.1 Aim 1: Define eMLC Leaf Positions for General Electron Fields

Accurate leaf positioning was necessary to ensure accurate delivery of the radiation field, evaluated by comparisons of measurements with computed dose distributions. Particularly important was the exact alignment of abutting electron fields to avoid hot and cold dose spots in segmented-field ECT plan delivery. An investigation of the effects of leaf width for both rectangular and irregular fields was important to understand the possible limitations of the eMLC for segmented-field ECT.

In this aim the geometric relationships of the eMLC, the linear accelerator, and the radiation field were evaluated. Software was developed to calculate and set eMLC leaf positions for an arbitrary electron field shape. Calibration procedures were developed to ensure accuracy of leaf positions. Radiographic film measurements were used to assess the accuracy of calculated leaf positions for rectangular, irregular, and segmented fields.

2.1.1 Establish Geometry of Leaf Positioning

Relationship of the eMLC to the Linear Accelerator and Electron Field

The geometric relationships of the linear accelerator, the eMLC, and the radiation field were evaluated. Electrons were considered to diverge from a virtual point source, as described by Schroder-Babo (1983) and to project through the eMLC-defined aperture to create a field defined in a plane at the accelerator isocenter normal to the beam axis. The accelerator used in the present work was a Varian Clinac 21EX (serial no. 1412).

Based on the findings of Jamshidi, Kuchnir, and Reft (1986) and Shiu et al. (1994) the virtual point source was approximately 90 cm from isocenter (location of primary scattering foil). The eMLC collimator-to-axis distance (CAD) was 11.5 cm from the midline of the 3.0-cm thick leaves to isocenter. The eMLC consists of 21 pairs of brass leaves with the central 15 pairs motorized. The physical leaf width was 0.9 cm at the bottom of the leaves. The leaf

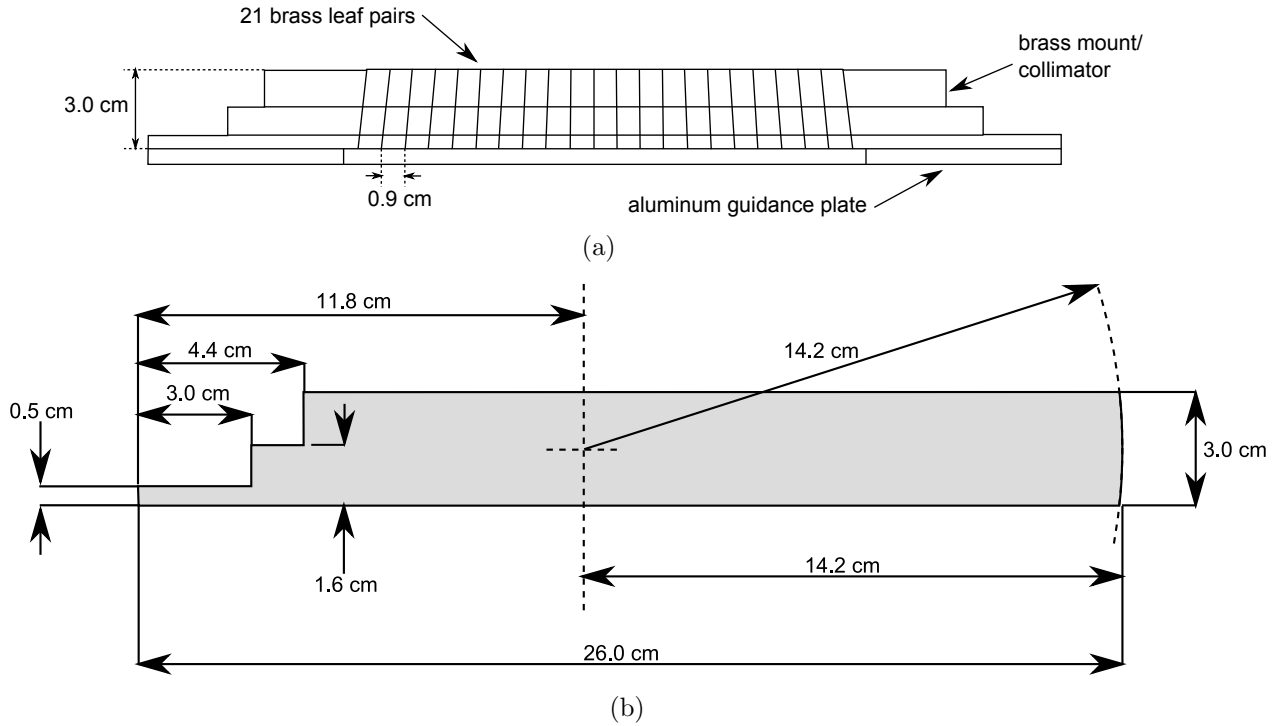


Figure 2.1: eMLC leaf dimensions. End view (a) of 21 divergent eMLC leaves. Side view (b) of an eMLC leaf. Redrawn from (Hogstrom et al. 2004).

edges were divergent, perpendicular to leaf motion, and focused to a point 85 cm above the bottom of the leaves (cf. Figure 2.1) to minimize dependence of penumbra shape on off-axis position of the leaves defining the electron field. Each leaf was designed to fully extend or retract (± 10 cm with respect to central axis) across the 20 cm isocentric field length parallel to the leaves. To minimize the dependence of penumbra shape on off-axis leaf position, the leaf ends were rounded such that as the leaves traveled across the field, the mean direction of the primary electrons was tangential to the leaf ends. A side view of the leaves and additional dimensions are presented in Figure 2.1. For rectangular field sizes for which side-scatter equilibrium exists on central axis, the geometric projection from the virtual electron source through the eMLC aperture was expected to coincide with 50% of the central-axis dose for lateral dose profiles (\perp to field edge) in a homogeneous phantom. It was assumed that one side of the geometric field edge was fully irradiated with an infinitely-broad, uniform, electron field and the other side was fully blocked. The relation of 50% central axis dose to the geometric field edge was not expected for small fields or near the practical range of the

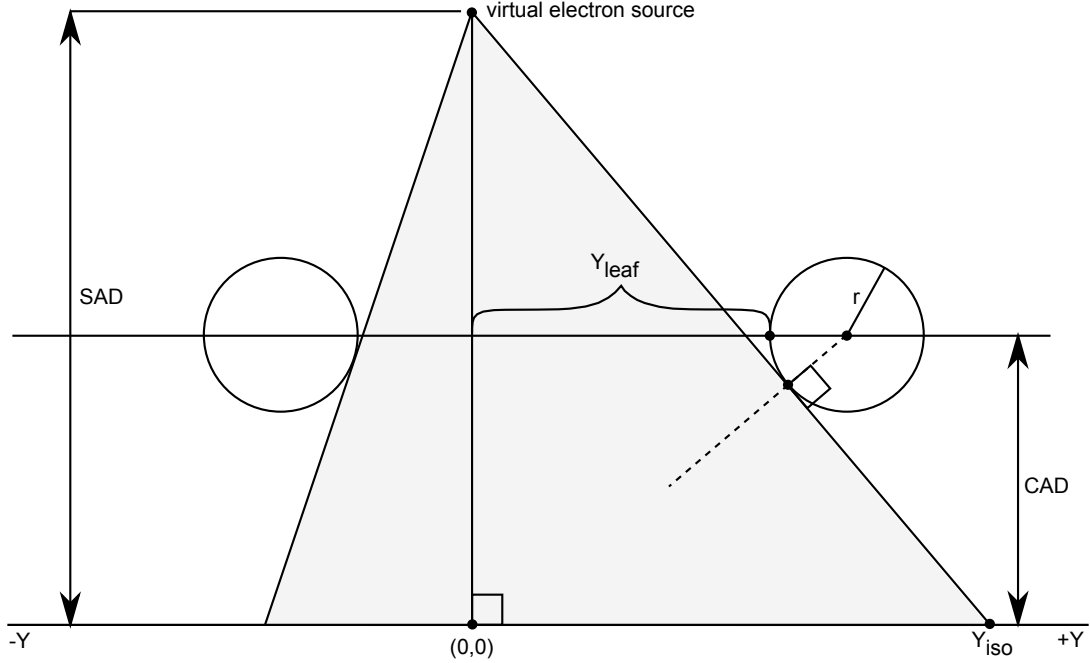


Figure 2.2: Radiation field projected through rounded leaf ends.

electrons due to lack of side-scatter equilibrium and non-uniform photon contamination.

Geometry of Electron Collimation Across Rounded Leaf Ends

In order to determine the leaf positions at the plane of the eMLC leaves, the projection of the edge of the electron field defined by the the rounded leaf-ends to the isocentric plane was derived. This was done by projecting the geometric field edge, a tangent line anchored at the virtual electron source and extending to the isocentric plane, where the circle was constrained to slide on a line parallel to the leaf central axis as shown in Figure 2.2. The solution of this equation for the coordinate of the leaf tip, y_{leaf} at the plane of the leaf midline, as a function of the desired geometric field edge at y_{iso} , was found to be

$$y_{leaf} = y_{iso} \left(1 - \frac{CAD}{SAD}\right) + r \left(\sqrt{1 + \left(\frac{y_{iso}}{SAD}\right)^2} - 1\right) \quad (2.1)$$

for leaves anchored on the positive side of the coordinate system, and

$$y_{leaf} = y_{iso} \left(1 - \frac{CAD}{SAD}\right) - r \left(\sqrt{1 + \left(\frac{y_{iso}}{SAD}\right)^2} - 1\right) \quad (2.2)$$

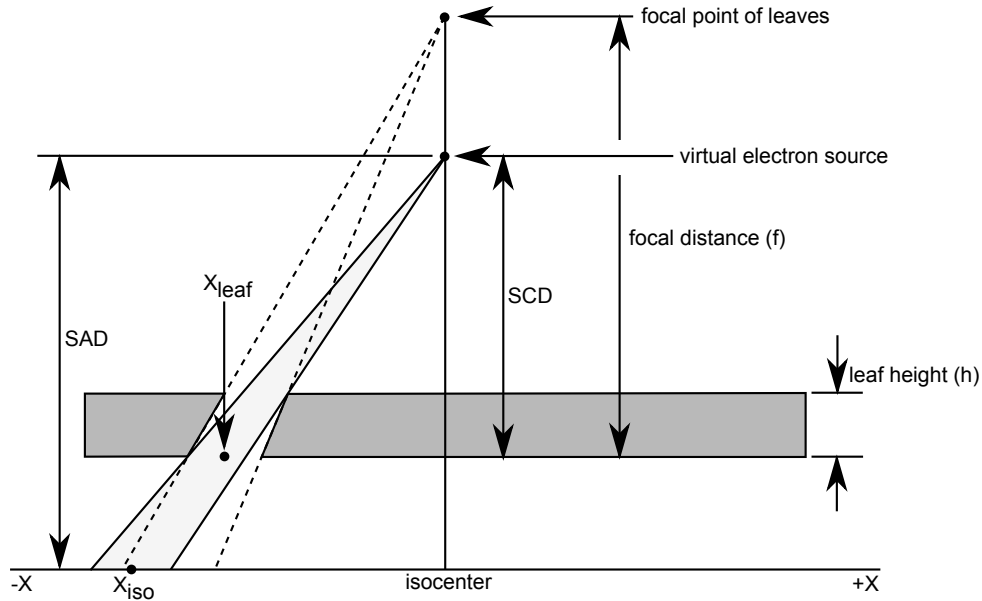


Figure 2.3: Discrepancy between focal point of leaves and virtual electron source.

for leaves anchored on the negative side of the coordinate system. The CAD was 11.5 cm from isocenter to the leaf midline, the virtual SAD for the Clinac was assumed 90 cm, and the radius of the rounded leaf end (r) was 14.2 cm as previously described in Section 2.1.1.

Geometry of Electron Collimation Across Divergent Leaf Edges

Perpendicular to leaf motion, the leaves were divergent and focused to a point 85 cm above the bottom of the leaves. This design specification was created for a Siemens accelerator that was not used in the current work. The difference between the position of the electron virtual point source for the presently used Varian accelerator and the focal point of the eMLC leaves was approximately 5 cm, and as a result, the original design intent of 1 cm leaf-width projections at the isocentric plane was not exact. Figure 2.3 illustrates this issue and shows that the radiation field was collimated by the top of a leaf that is between the field and the central axis and collimated by the bottom of a leaf that was exterior to the field and central axis. For a symmetric field on central axis, the field was collimated by the bottom of the leaf plane on both sides. As the physical leaf width, w_{leaf} , was 0.9 cm, the isocentric field

width, W_{iso} , for a symmetric field with the number of open leaves, n_{leaves} , was found

$$W_{iso} = \frac{w_{leaf} n_{leaves} SAD}{SCD}. \quad (2.3)$$

The electron field passing through a single, open leaf-pair at a central displacement $+x_{leaf}$ from the central axis projected to a field at isocenter centered at x_{iso} and was given by

$$x_{iso} = \frac{(x_{leaf} + \frac{w_{leaf}}{2}) \frac{SAD}{SCD} + (x_{leaf} + \frac{w_{leaf}}{2}) \frac{f-h}{f} \frac{SAD}{SCD-h}}{2} \quad (2.4)$$

where focal distance, f , was 85 cm, leaf height, h , was 3 cm, and leaf width, w_{leaf} , was 0.9 cm. A leaf pair centered at displacement $-x_{leaf}$ projected to a field at isocenter centered at x_{iso} and,

$$x_{iso} = \frac{(x_{leaf} - \frac{w_{leaf}}{2}) \frac{SAD}{SCD} + (x_{leaf} + \frac{w_{leaf}}{2}) \frac{f-h}{f} \frac{SAD}{SCD-h}}{2}. \quad (2.5)$$

Equations relating the leaf projection at isocenter to the leaf positions at the plane of the collimator were utilized in software that positioned the eMLC leaves for general field shapes.

2.1.2 Software Developed to Position Leaves for General Fields

Purpose of Software and Description of Input and Output

Software was developed using Interactive Data Language (IDL) version 6.2 whose purpose was to compute the eMLC leaf positions that most closely modeled a general, irregularly-shaped electron field. As input, the software accepted the plan.Trial file created by the Pinnacle treatment planning system. During execution, the software extracted the block points that defined the general field, converted the field to the eMLC aperture, and exported: 1) leaf position files in a format compatible with the existing eMLC QBasic control software, 2) graphical output showing the eMLC aperture overlaying the desired general field shape, and 3) a modified plan.Trial file with the collimator block points modified to match the newly generated eMLC aperture.

Organization of Program Operations

The developed software, `emleafpositions2.pro`, contained geometric information about the eMLC and the relations discussed in Section 2.1.1. The conversion of a general, collimator block shape to an eMLC aperture was achieved by intersecting the leaf mid-lines, described by Equations 2.4 and 2.5, with the edges of the block shape at the isocentric plane. The isocentric intersection points were backprojected with Equations 2.1 and 2.2 to determine the y_{leaf} coordinates at the plane of the leaves.

The software provided the user with a graphical output of the eMLC aperture overlaying the original requested field shape. Control files for the eMLC containing the leaf position commands and inverse leaf position commands, necessary to return the eMLC to the parked position, were produced in addition to a modified `plan.Trial` file for the Pinnacle treatment planning system that contained modified block points to permit dose computation with the eMLC aperture.

Transfer of Data between the IDL Software and Treatment Planning System

The software required that the user create a treatment plan in Pinnacle version 7.4f and draw the Pinnacle collimator block aperture by hand. After an initial plan was developed, the user exited Pinnacle. A File Transfer Protocol (FTP) connection was used to move files between the remote Pinnacle server and a personal computer. The `plan.Trial` file was located in the directory for the appropriate institution, patient, and plan in the Pinnacle directory structure. The `plan.Trial` file contained planning specifications for a treatment plan including the beam list, beam geometry, energy, collimator block points, and prescription dose. The file was used as input for the IDL software. Once the program completed execution, the generated files were available for input to the eMLC QBasic control software and the modified Pinnacle `plan.Trial` file was moved via FTP back into the correct directory on the remote Pinnacle server. Dose calculation in Pinnacle was repeated with the modified file in place.

2.1.3 Calibrate Leaf Positions at the Plane of Leaves

Communication with the eMLC Electronics

Communication with the eMLC electronics was achieved through in-house QBasic software that controlled leaf positions at the plane of the leaves. Communication passed from a Dell Inspiron 4000 personal computer (PC) through an interface board labeled “Central Junction”, mounted aside the eMLC, to the on-board electronics and individual motor-control circuits. Signals were transmitted using the RS-232 standard through the COM1 port on the PC at 19200 baud, no parity, eight data bits, 2 stop bits, and no flow control. A universal serial bus (USB) to serial converter was used with EasySYNC software drivers to allow communication through the PC USB port. Thirty, leaf encoder-motors (MicroMo Electronics 1624E0125123 HEM1624E16 16/5 22:1) were controlled with the QBasic software by transmitting the desired encoder count to the on-board leaf motor memory. Knowledge of the correct relation of encoder counts (directly proportional to motor rotations) to lateral movement of the eMLC leaves via drive screws was necessary. An in-house document created by David Robinson reviewed the QBasic software and communication protocol (Robinson 2006).

Loading an eMLC Field with the Control Software

The QBasic control software was used to load leaf positions for eMLC fields. The software was renamed ELEY-MLC.BAS and ELEY-MLC.EXE since parameters were modified for the current study from the original software MLC.BAS developed by David Robinson. Upon launching the software, the user typed “oi” to receive a prompt for an input leaf-position file name. The command “a” was entered to automatically load the file and send the requested leaf positions to the on-board electronics. The command “mov” was entered to command the eMLC leaves to move to the positions in the file. Power supply to the eMLC was controlled with a surge-protector switch. Power was cycled after the leaves reached their requested destination after every movement. The effect of this was to reset the encoder counts to the on-board electronics after every move and to eliminate the need to constantly track the encoder counts.

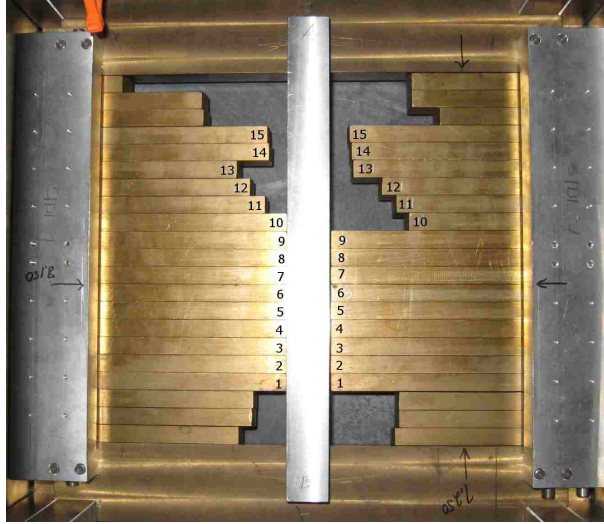


Figure 2.4: eMLC leaf calibration photograph. Motorized leaf pairs numbered 1 through 15.

Leaf Calibration with the Control Software

Calibration procedures were designed to ensure agreement between computer requested leaf position and actual leaf position at the plane of the leaves. The QBasic control software was used for leaf calibration by entering the “cal” command at the initial software start-up screen. In calibration mode, individual leaves were moved incrementally by specifying the leaf number and side number (e.g., “13,2”) and using the keyboard arrow keys to shift the leaves towards or away from the center of the field. The default increment to move was 0.5 mm and could be changed by typing “m” in calibration mode. Leaf calibration before each eMLC measurement-set utilized a machined aluminum bar, 2 cm thick, that mounted in holes on top of the eMLC collimator plane. As shown in Figure 2.4, leaves were individually moved from outer field positions towards the calibration bar. When the leaves were within approximately 2 mm of the bar, the movement increment was set to 0.5 mm. The leaves were moved to touch the calibration bar until the motors could not push the leaf further, resulting in an audible buzzing sound. Upon hearing the buzzing sound, the leaf was retracted 0.5 mm from the calibration bar. The method was repeated for all leaves, alternating from side 1 to side 2 while increasing from leaf pair 1 to leaf pair 15. All 21 leaf pairs were not utilized in the current work because only the central 15 pairs were equipped with motors. These

15 motor pairs were adapted from in-house electronic supplies and were deemed suitable for the present research though the full set of 21 leaf pairs could be motorized if desired. The calibration leaf numbers and side numbers were marked with a graphite pencil at the top of the collimator plane for the duration of the study. The calibration bar was marked with a graphite pencil to ensure that it was installed in the same orientation throughout the course of the current work.

Measurement of Leaf Travel Versus Encoder Count

The QBasic software used a coordinate system at the plane of the leaf midline. The leaves were moved by transmitting a desired encoder count to the eMLC on-board electronics. The QBasic control software contained a constant, “CntMM”, that defined the relation of encoder counts per millimeter of leaf travel. Iterative measurements were made with a ruler of the leaf opening width at the top of the eMLC leaves and compared with the expected opening. The CntMM constant was determined to accurately translate the leaves between the parked position (15×20 cm² field size at isocenter) and a 9×9 cm² square field.

The file calOut.txt was loaded to move the leaves from the calibration bar to the eMLC parked position. Due to the staggered heights of the leaf drive screws, different torques were applied to the odd and even leaf pairs during the calibration procedure leading to a slight staggering of the calibrated leaves upon retraction to the parked position. To counter this effect, the file calOut.txt contained the desired parked leaf positions with staggered positions for the even and odd leaf pairs. The odd and even positions were determined to accurately park the eMLC leaves and to produce precise leaf alignment for the 9×9 cm² field.

2.1.4 Measure eMLC Fields with Radiographic Films

Purpose of Film Measurement

The accuracy and precision of the radiation field size delivered by the eMLC using the leaf positioning methods described in Sections 2.1.1 and 2.1.2 was evaluated by measuring the electron planar dose distribution at the linear accelerator isocenter. Electron fields were delivered to radiographic films placed normal to the electron beam at isocenter. Films were processed and scanned, and the radiation field size (defined by the 50% off-axis dose) was

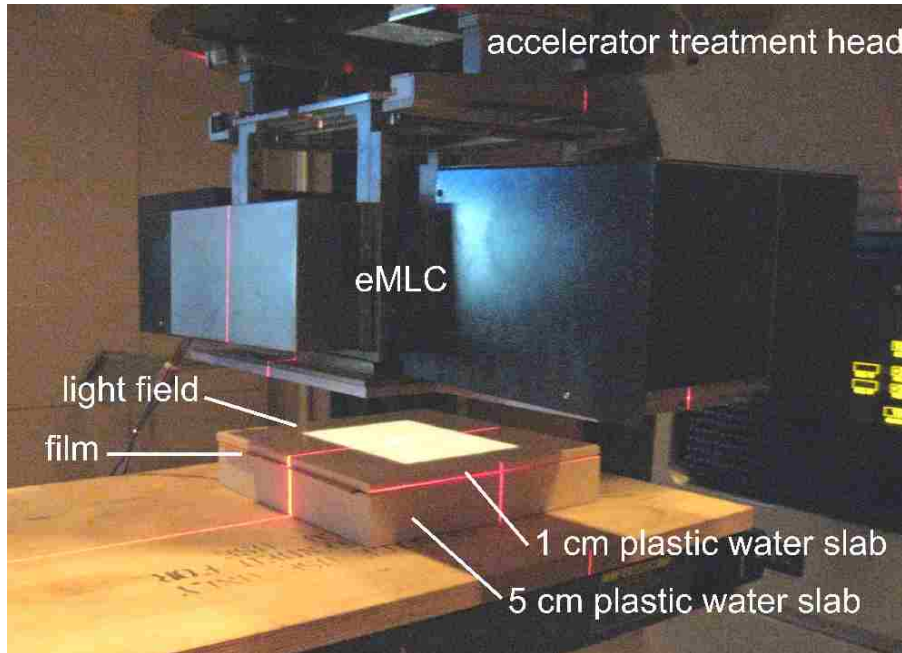


Figure 2.5: eMLC film measurements.

compared with the expected geometric field size (Khan et al. 1991) to estimate the accuracy of the eMLC field sizes.

Measurement Setup

The Varian Clinac 21EX linear accelerator with serial number 1412 was set with a mechanical level to gantry angle 180° and collimator angle 180° (digital readouts were gantry 180.1° and collimator 180.8°) The x-ray jaws were positioned to $28 \times 28 \text{ cm}^2$. The dose rate was set to 400 monitor units per minute. Isocentric film measurements were made with Kodak X-Omat V (XV) film as shown in Figure 2.5. A 16 MeV electron beam delivered 50 monitor units ($\approx 0.5 \text{ Gy}$) to the film placed beneath a 1-cm slab of Plastic Water (PW) and above a 5-cm slab of PW. The film was positioned at the linear accelerator isocenter to measure the expected field sizes. The optical distance indicator (ODI) was used to set the film SAD to $(100 \pm 0.2) \text{ cm}$. The distal plane of the eMLC leaves was measured to be $(10.20 \pm 0.03) \text{ cm}$ above the film surface (isocenter). The PW slabs were visually centered with the light field of the eMLC. Films were taped in place with masking tape on the bottom 5 cm slab. Pin pricks were made in the upper right corner of the film to record orientation of

the measurement. When viewed from above (BEV) the three pin pricks make an “L” shape where the vertical tip of the “L” points towards the accelerator gantry and the horizontal tip of the “L” points towards the right side of the treatment vault as viewed facing the accelerator from the foot of the patient table in standard position.

Film Calibration

A film calibration procedure was performed prior to eMLC film measurements to enable absolute dosimetry with the film. The calibration procedure has been explained in further detail in Appendix A. Briefly, calibration fields used the 10×10 cm² electron applicator with the 10×10 cm² standard insert. A 9 MeV beam was delivered to XV films at d_{max} beneath a 2 cm slab of PW and above a 5 cm slab of PW, to ensure charged particle equilibrium, at 100 cm SSD. Four films were used for each calibration set to calibrate doses of (0, 1.11, 7.2, 13.2, 19.3, 25.6, 31.6, 37.7, 43.7, 50, 56, 62, and 68) cGy. Three calibration sets were acquired to evaluate the uncertainty in film dose measurement introduced by intra-batch variation in silver bromide distribution and variations in processing and scanning conditions.

eMLC Installation

The eMLC was inserted into the electron cone receiver of the accelerator. Because the motorized eMLC mass was approximately 50 kg, the following document procedure was used. The wooden, service couch-top was used to prevent damage to the standard carbon-fiber top. The eMLC was lifted onto 10 cm of plastic water covered with a bed linen at the head of the couch. Once on the couch, the eMLC was docked into the electron cone receiver via the motorized lift-control on the patient couch. Lateral and longitudinal couch motions were performed manually with the couch motors unlocked. With the potential imbalance to the gantry, the gantry was never moved from the upright 180° position with the eMLC installed.

In order to operate the Varian accelerator with the eMLC in place, the accelerator console was used in service mode. The x-ray jaws were set to 28×28 cm² with the handheld control pendant. As the eMLC did not have an electronic interlock circuit that identifies the dimensions of the electron applicator (prevents treatment of patients with the wrong appli-

cator), the accessory (ACC) and collimator (COLL) interlocks were manually overridden at the accelerator console to allow beam delivery with the eMLC.

Description of Measurements

Film measurements included square fields with side length (3.0, 5.1, 9.1, 15.2) cm and rectangles with dimension (2.0×15.2, 4.0×15.2, 6.0×15.2, 8.0×15.2, 10.0×15.2, 12.0×15.2, 15.0×15.2, and 20.0×15.2) cm². Rectangular fields were delivered with all 15 leaf pairs open to create the rectangles and, as discussed in Section 2.1.1, projected to a field width at isocenter of 15.2 cm. Two irregular fields were delivered to films to assess the impact of finite leaf width on general field shapes. The first irregular field was a pentagon shape, and the second was a crescent shape. Nine segmented fields were delivered to films to evaluate the ability of the eMLC to properly abut electron fields. Each of 3 segmented-field geometries was tested with 1) both segments delivered with 20 MeV beams, 2) both segments delivered with 12 MeV beams, and 3) one segment delivered with a 20 MeV beam and the other segment delivered with a 12 MeV beam. The purpose of these energy selections was to evaluate the precision of abutment at a mid-range energy (12 MeV) and at the higher energy (20 MeV) where the lateral dose falloff was sharper and abutment precision was most important. The three plan geometries, each receiving the three energy combinations, were 1) abutment of two (5.0×15.2 cm²) segments on central axis with the abutment perpendicular to leaf motion, 2) abutment of two segments (one 5.0×15.2 cm² and one 15.0×15.2 cm²) 5 cm off central-axis with abutment perpendicular to leaf motion, and 3) abutment of two segments with the abutment diagonal to leaf motion (composite field was 20.0×15.2 cm²).

Film Processing

Films were processed in the Kodak X-Omat 270 RA Processor with processing chemicals, Kodak RP X-Omat Developer Replenisher Part A,B,C and Kodak RP X-Omat LO Fixer Replenisher Part A,B. Prior to use, three scrap films were processed to warm up and stabilize the processor temperature and chemical distribution. The temperature throughout the duration of processing was $(37.3 \pm 0.1)^\circ\text{C}$ as displayed on the processor thermometer

readout. The order of processing from first to last was: calibration set A, eMLC parked, squares, rectangles, calibration set B, segmented fields, irregular fields, calibration set C.

Film Readout

Films were scanned with the Vidar Dosimetry Pro Advantage (serial no. 320419). All films were manually loaded into the scanner with the long axis of the film parallel to the scanner feed direction. The film was oriented so that the film edge irradiated closest to the accelerator gantry was fed in first and the film face closest to the electron source was facing the scanner. The RIT 113 version 5.0 software was used to communicate with the scanner and acquire scanner A/D data. Prior to scanning films, a pixel calibration was forced at a resolution setting of 178 μm . Films were scanned in the same order that they were processed. All eMLC film data were saved without dose calibration to a Matlab format and exported for analysis with Matlab software developed in the current work. The RIT calibration tool was used to extract the mean and standard deviation of 16 bit pixel A/D values within a 1 cm calibration square visually placed in the center of the digitized images of the calibration fields. Means and standard deviations of A/D values throughout the three calibration sets were computed for each of the 13 dose calibration points. Values were used to construct a calibration curve, shown in Appendix A, for use in the Matlab film analysis software described in the following section.

2.1.5 Analyze Film Measurements

Develop Software to Convert Raw Scanner Values to Planar Dose

Software was developed in Matlab version 7.2 to convert the digitized film image to a planar dose distribution. The software generated dose profiles and plots. In addition, the software enabled uncertainty propagation for the film dose measurements as described in Appendix A. As input, the software accepted the RIT exported film image in a .mat format. The program output a series of plots including a greyscale dose plane, x and y dose cross-profiles with uncertainties, a greyscale dose plane showing the location of the cross profiles, 3-D rendered surface plots, and a calculated field width measurement at 50% of the central axis dose with uncertainty and standard deviation of the width across the open

eMLC leaves. The software linearly interpolated the calibration curve data. More robust interpolation methods, e.g., piecewise polynomial interpolation, found in RIT had negligible effect on the calculated field width (i.e., < 0.1 mm), and would have required more time to propagate uncertainties.

Calculate Radiation Field Widths for Square and Rectangular Fields

Radiation field widths computed with the software were compared with the expected geometric field widths for square and rectangular fields. The field width was determined by, first, finding the central axis (CAX) dose value of a manually placed cross profile, second, searching the profile dose values to find the dose values bounding 50% of the central axis value on each side of the field, third, linearly interpolating the bounding dose values to find the lateral positions of the 50% dose values, and, fourth, calculating the distance between the two values to get the field width. The $y_{50\%}$ coordinate of each point at 50% of CAX dose was found by interpolating between the dose point above 50% of CAX dose (d_h at y_h) and the dose point below 50% of CAX dose (d_l at y_l)

$$y_{50\%} = \left(\frac{y_h - y_l}{d_h - d_l}\right)\left(\frac{d_{CAX}}{2}\right) + y_l - \left(\frac{y_h - y_l}{d_h - d_l}\right)d_l, \quad (2.6)$$

and the field width, W , was found as the distance between $y_{50\%,1}$ and $y_{50\%,2}$

$$W = |y_{50\%,1} - y_{50\%,2}| \quad (2.7)$$

Uncertainty in the calculated field width was determined by propagating the individual dose uncertainties and including a term for the uncertainty in SAD when positioning the films with the optical distance indicator (ODI) (± 2 mm).

$$\sigma_W^2 = \left(\frac{\partial W}{\partial d_{l,1}}\right)^2 \sigma_{d_{l,1}}^2 + \left(\frac{\partial W}{\partial d_{h,1}}\right)^2 \sigma_{d_{h,1}}^2 + \left(\frac{\partial W}{\partial d_{l,2}}\right)^2 \sigma_{d_{l,2}}^2 + \left(\frac{\partial W}{\partial d_{h,2}}\right)^2 \sigma_{d_{h,2}}^2 + \left(\frac{\partial W}{\partial d_{CAX}}\right)^2 \sigma_{d_{CAX}}^2 + \left(\frac{\partial W}{\partial SAD}\right)^2 \sigma_{SAD}^2 \quad (2.8)$$

For field width measurements parallel to leaf motion, the field width was calculated for each open leaf pair except the outermost pairs (e.g., for a 5×5 cm² field, the field width was measured for the central 3 leaf pairs). The mean field width across multiple leaf pairs was reported along with the standard deviation of field width across the leaf pairs to estimate the variation of field width across the leaf pairs.

Compare Irregular Field Measurements with eMLC Aperture

For irregular fields, the 10, 50, and 90% dose contours (normalized to 100% on central axis) were extracted from the measured dose planes and plotted overlaying the geometric eMLC aperture at isocenter.

To evaluate the difference between a general field shape and the dose distribution delivered with the eMLC, the (10%, 50%, and 90%) CAX dose contours were also plotted overlaying the original field shape, as drawn before conversion to an eMLC aperture.

Evaluate Abutment of Segmented Fields

Measured segmented fields were plotted as 3-D surfaces to demonstrate the effect of leaf-position uncertainty on the abutment region dose distribution. Fields delivered with different energy segments were evaluated to show the effects of unmatched penumbra on the dose distribution. A 10×10 pixel equal-weight smoothing window (physical dimension 1.78×1.78 mm²) was applied to the planar dose distribution from the measured film data to reduce high frequency noise and improve visualization of the individual leaf abutment dosimetry.

2.2 Aim 2: Commission the eMLC for Dose Computation

The eMLC and Varian Clinac 21EX were commissioned for the 3D version of the Hogstrom electron pencil beam dose algorithm (Hogstrom, Mills, and Almond 1981; Starkschall et al. 1991) in Pinnacle version 7.4f treatment planning system. Required commissioning data were measured with a water scanning system. Additional beam model parameters, based on previously determined clinical values for the accelerator, were modified to appropriate values

for the eMLC installation. Commissioning of the dose algorithm was validated by comparing isodose curves computed with the treatment planning system with measured isodose curves.

2.2.1 Measure Electron Dose Distributions with a Water Scanning System

The required measurements for the electron pencil beam algorithm (PBA) in the Pinnacle version 7.4f treatment planning system were described in the Pinnacle Electron Physics and Data Requirements section of the user manual (ADAC 2001). This included central-axis depth-dose profiles, cross-axis dose profiles, absolute output, output factors, and photon transmission through the eMLC leaves.

Central-axis Depth-dose Measurements

Central-axis depth-dose data was necessary for two purposes. First, depth-dose data from the large, side-scatter equilibrium field sizes were used to establish the reference depths needed for off-axis profiles. Second, for each energy the treatment planning system required depth-dose data at 100 cm SSD for multiple field sizes spanning the range of desired computation to be used directly for dose calculation.

To obtain the depth-dose data for equilibrium fields, the eMLC was placed in the parked-position, 15×20 cm² field size. Central-axis depth-dose profile were measured with a diode detector, which scanned from 20-cm to 0.2-cm depth for all beam energies (6, 9, 12, 16, and 20 MeV). The practical range, R_p , and therapeutic range, R_{90} , were determined for each energy from the measured data.

For dose calculation, square field data with side of square of 1, 2, 3, 5, 7, 9, 11, 15, and 20 cm were desired for all energies. Depth-dose data were measured at all energies for field sizes of 3×3 , 5×5 , 7×7 , 9×9 , 11×11 , 15×15 , 1×5 , 2×5 , 3×5 , and 15×20 cm² at 100 cm SSD. Depth-dose profiles for the 1×1 , 2×2 , and 20×20 cm² fields were determined using the square root method (explained in Section 2.2.1) using measured data for the 1×5 , 2×5 , and 15×20 cm² fields. A 3×3 cm² field was computed in a similar manner from the 3×5 and 5×5 cm² measured fields to validate the method.

Off-axis Dose Profiles

X and Y cross profiles at depths of $R_{90}/2$ and $R_p + 2$ cm (for the equilibrium field size) were required by the treatment planning system. The profiles at depths of $R_{90}/2$ were acquired to evaluate flatness of the electron beam and to determine the off-axis scaling of the incident electron fluence. However, for the present work, all off-axis ratios were assumed to be unity, so measured profiles at $R_{90}/2$ depth were not used in dose computation.

X cross profiles at depths of $R_p + 2$ cm were used by the treatment planning system to model the off-axis distribution of bremsstrahlung (photon) dose. Data was required for each energy at all field sizes at 100 cm SSD. The cross profile measurement range was ± 20 cm. Cross profile commissioning data were acquired at each energy (6, 9, 12, 16, and 20 MeV) for field sizes of 3×3 , 5×5 , 7×7 , 9×9 , 11×11 , 15×15 , 1×5 , 2×5 , and 20×15 cm² at 100 cm SSD. Commissioning data used by the Pinnacle beam model was only accepted for square fields, and the beam model only used a single profile to model the photon contribution (off-axis photon dose assumed identical for X and Y axes). Therefore, the appropriate off-axis photon contamination profiles from the 1×5 , 2×5 , and 20×15 cm² fields were copied into files formatted for input to the Pinnacle beam model for the 1×1 , 2×2 , and 20×20 cm² fields. Any effect of the different field dimension perpendicular to the profile direction was considered negligible.

Square Root Method to Obtain Small-field Data

Since the eMLC had an odd number of leaves on each side, square fields with even side lengths could not be created on central axis. Additionally, the 1×1 cm² and 2×2 cm² field PDDs were difficult to measure because of small size and lack of side scatter equilibrium. In order to reduce the measurement alignment difficulties to a single dimension, rather than two dimensions, the square-root method of Hogstrom, Mills, and Almond (1981), applied for small fields (Meyer, Palta, and Hogstrom 1984) and reviewed by Khan et al. (1991), was utilized to compute the square field depth dose for the (1, 2, and 20) cm fields from measured rectangular field data of dimension (1×5 , 2×5 , and 15×20) cm². The percent depth dose,

PDD, was calculated by

$$\text{PDD}_{l \times l} = \left[\frac{\text{PDD}_{l \times w}^2}{\text{PDD}_{w \times w}} \right]_{\text{normalize max}} = 100\%. \quad (2.9)$$

In order to validate the method, the depth dose from a measured 3×3 cm² field was compared with a computed 3×3 cm² depth dose from measured (3×5 and 5×5) cm² field depth doses. Likewise, the same procedure and relation was applied for the measurement of output factors, OF, at these geometries.

$$\text{OF}_{l \times l} = \frac{\text{OF}_{l \times w}^2}{\text{OF}_{w \times w}}, \quad (2.10)$$

which has been validated by Shiu et al. (1994) for the Varian Clinac.

Physical Setup of Water Phantom and Linear Accelerator

Percent depth-dose curves and cross profiles were measured in the 3D Wellhofer Dosimetric Waterphantom Typ 1010 (serial number 592). The Wellhofer Dosimetrie CU 500 E dual processor control unit (serial number 5300) was used to control the detector position and acquire detector signals. The Scanditronix Wellhofer electron diode EFD-3G (serial number DEB022-3341) was used to measure the relative dose distribution, and the Scanditronix Wellhofer RFD-3G (serial number DEB022-3341) was used as a reference diode to correct the signal for variations in linear accelerator output. A Dell laptop with Omni-Pro Accept version 6.2 software was used to record data and communicate with the scanning system. Two triaxial extension cables with threaded TNC endpieces were used with 2 triaxial-threaded to triaxial-bayonet adapters and 2 triaxial-bayonet to coaxial-bayonet adapters to connect the diode detectors to the electrometer control unit.

The water phantom was filled with tap water to 6 cm below the top of the tank walls to allow a clearance of 2.5 cm for the eMLC for 100 cm SSD. The Varian Clinac 21EX (serial number 1412) gantry angle and collimator angle were set using a mechanical level to 180° (digital gantry readout = 180.1°; digital collimator readout = 180.7°). The water phantom was positioned beneath the linear accelerator head, and the accelerator light field was used to visually align the rotation of the water phantom to match the angle of the light

field edge. The mechanical front pointer for the accelerator (95-101 cm range) was used to position the water surface at machine isocenter (100 cm SSD). The tank was raised until the water surface was approximately at the tip of the front pointer, and the water tank was leveled using a linear level on the tank walls and a circular bubble level on the bottom surface of the tank. Once the water tank was level, the water surface was raised to the front pointer so that a piece of wax paper (patient exam table paper) floating on the water surface was slightly touching the tip of the front pointer and resisted lateral sliding, yet was not deformed by the pressure of the front pointer. Once the water phantom was positioned to 100 cm SSD, masking tape was attached and marked with a pen to show the intersection of the coronal patient lasers with both sides of the water tank. The water tank was lowered to permit installation of the eMLC, as described in Section 2.1.4, and, then, raised to align the masking tape marks with the coronal lasers. This installation method was used to position the water surface at (100.0 ± 0.2) cm SSD. A photograph in Figure 2.6 shows the eMLC and water phantom setup. Also, the alignment mark indicated the water level, which could be checked periodically to ensure water evaporation would create no errors in detector depth.

Use of the accelerator with the eMLC required that two machine interlocks be overridden in service mode. The COLL and ACC interlocks were overridden because the accelerator did not recognize the identifying key found on the standard electron applicators, and the eMLC did not have the on-board circuitry found on the standard electron applicators.

Installation of Diode Detectors

A diode detector was selected for electron beam scanning of relative dose distributions based on the small detector size (active volume diameter = 2 mm and thickness = 0.06 mm specified by manufacturer), corresponding to reduced volume-averaging effects, high sensitivity compared to ionization chambers, and the ability to measure relative dose distributions directly, i.e., without the need for stopping-power ratio corrections (required for ion chamber measurements), as recommended by the American Association of Physicists in Medicine Task Group Report 25 (Khan et al. 1991). The EFD-3G electron diode was attached to the motorized drive of the scanning system with the aid of an in-house acrylic bracket with



Figure 2.6: Water phantom and eMLC Setup.

plastic screws. The bracket allowed the horizontal detector mount of the scanning system to be converted to a vertical detector mount suitable for the electron diode. A scrap piece of radiographic film was used to shim the mounting adapter to level. The acrylic bracket holding the detector was checked to be level with a mechanical level, and the detector axis was visually evaluated to be plumb with an uncertainty of $\pm 2^\circ$. The scanning limits were set with the water phantom hand-controller to prevent collision of the detector with the tank walls. The diode was initially centered with the accelerator crosshairs ($x=y=0$). The surface of the diode was positioned to align with the water surface. A series of visual observations from different angles was used to position the detector surface at the water surface, and the effects of surface tension were taken into consideration. Through visual positioning, the detector surface was placed to agree with the water surface with an uncertainty of ± 0.3 mm. The water surface and isocenter drive-motor positions were stored to controller memory with the hand controller. The detector was moved laterally approximately ± 20 cm along both axes parallel to the water surface to verify that the motor drives were level and the change in detector depth during this test was less than 0.4 mm for all directions. The RFD-3G reference diode was positioned 1 cm above the eMLC leaves, in the light field of the linear accelerator (x-ray jaws were 28×28 cm²), and 1 cm outside the open (20×15 cm²) eMLC electron field.

Software Settings for Water Scanning System

The Omni-Pro Accept control software was configured to the water scanning system, and scanning was set for the continuous mode. A comparison of data measured in step-by-step mode and continuous mode indicated that continuous mode provided scans with less structural noise. The continuous mode data often had high frequency statistical noise that was easily removed with a low-pass filter, whereas the step-by-step mode data often appeared with unexpected structural noise; waves were observed in the water tank via the video monitor during step-by-step scanning. The effective point of measurement of the EFD-3G electron diode was 0.4 mm below the surface of the detector as specified by the manufacturer. The software control panel was used to raise the detector 0.4 mm to position

the effective point of measurement at the water surface. The hand controller on the water phantom was then used to re-set the water surface and isocenter so that the effective point of measurement was at zero depth. The EFD-3G detector gain was set to 7 and the RFD-3G detector gain was set to 6. The voltage was set to zero for all diode measurements. A 20 MeV electron beam was delivered while the software CAX tool was used to automatically position the detector in the center of the radiation field while the eMLC formed the parked 15×20 cm² field; the origin coordinates normal to the beam were reset via software after completing the CAX process. The detector was positioned at the approximate R_{100} for the electron beam (using an Omni-Pro software tool which automatically searched for R_{100} while the beam was on) and the detector signal was normalized to 100% in the software control panel. Depth-doses were scanned at low speed (4) and cross profiles were scanned at medium speed (7). Higher scan speeds resulted in noisier profiles and loss of sharp inflections in the dose distribution, and lower scan speeds were unacceptable due to time required to complete measurement sets. Depth-dose curves were scanned from 20-cm to 0.2-cm depth (deep to shallow).

Quality Assurance of Water Scanning Measurements

To ensure that the detector depth and central axis alignment were correct, quality assurance scans were acquired throughout the course of extended measurements. The eMLC parked position 15×20 cm² field size was used as a quality assurance and reference field size. The accelerator was set to deliver a 9 MeV beam, and the scanning system acquired one depth dose curve, one X cross profile, and one Y cross profile at cross-profile depths of $R_{90}/2 = 1.41$ cm. Quality assurance (QA) scans were acquired before and after measurement sets. Agreement between QA scans of R_{50} and OAR_{50} within ± 0.5 mm before and after a measurement set was considered to indicate that the measurement set was valid and did not suffer loss of detector position.

One observation, revealed through the QA scans, was that water evaporation from the tank was a relevant issue for extended multi-hour measurement blocks. For the commissioning data sets, which were acquired prior to establishment of the QA scan procedure, PDD

depth coordinates were corrected for water evaporation from the water phantom at a rate of 0.1 mm/hr. Depth corrections based on the evaporation rate were possible because of timestamps on the data files and a post-measurement study of water evaporation. For the isodose scanning measurements, QA scanning indicated agreement with the evaporation rate of 0.1 mm/hr from the water phantom, and the problem was eliminated by intermittently adding water to the tank. The volume of water needed to raise the linear water level was computed based on the dimensions of the tank, and a graduated cylinder was used to measure the water to add.

2.2.2 Measure Dose Output in a Water Phantom

Dose Output Measurement

Dose output measurements were necessary for the treatment planning system to relate the number of accelerator monitor units to an absolute dose for a reference field. For each energy, the dose output (dose per monitor unit) was determined for the 11×11 cm² and 20×15 cm² field size at R_{100} at 100 cm SSD in the 3D Wellhofer Dosimetric Waterphantom.

As outlined in AAPM TG-51, ionization was measured at d_{ref} in the water phantom with a plane-parallel ionization chamber, ionization was converted to dose, and measured percent depth-dose was used to scale the dose at d_{ref} to the dose at R_{100} .

The PTW TN34001 plane-parallel ionization chamber (serial number 1001) active volume had a diameter of 1.5 cm. The IC charge was collected with a Keithley MK 614 Electrometer (serial number 312275). 50 monitor units were delivered for each measurement, and all dose measurements were repeated 3 times and averaged.

Output Factor Measurements

Output factors were measured for a range of field sizes and SSDs to allow accurate normalization of dose for small field sizes and surface geometries with varying SSD. Output factor measurements were taken as the ratio of output for the specified conditions to that for the 11×11 cm² field at 100 cm SSD. The diode detector was chosen for relative output measurements to reduce the impact of volume averaging for the small fields. Output factor was taken as the ratio of diode charge per monitor unit collected for the specified geometry at

R_{100} to that for the 11×11 cm² field size at 100 cm SSD at R_{100} . The Scanditronix Wellhofer electron diode EFD-3G (serial number DEB022-3341) active volume had a diameter of 2 mm, as specified by the manufacturers.

Relative output factors were measured for all energies at (100, 105, and 110) cm SSD. Square fields were measured with side length 3, 5, 7, 9, 11, and 15 cm. Also, relative output for rectangular fields (1×5 , 2×5 , and 15×20 cm²) were measured to calculate the output factors for square fields (with side lengths 1, 2, and 20 cm) using Equation 2.10.

50 monitor units were delivered for each measurement. All diode measurements were performed at energy and field-size specific R_{100} depths in the water phantom determined from the depth doses acquired previously. The electrometer voltage supply was turned off to zero volts.

Electrometer Setup for Output Measurements

Output (dose/MU) measurements were performed in the water phantom described in Section 2.2.1. Rather than acquiring measurements directly with the Wellhofer Dosimetric CU 500 E, detector charge signals were collected with the Keithley MK 614, and the Wellhofer was used to control the depth of the detector. Prior to commencing measurements, the Wellhofer controller was used with the Omni-pro software to automatically scan the electron field and find the central axis of the beam. Once the detector was correctly positioned in the center of the field and the depth of the detector's effective point of measurement was zeroed at the water surface, the Wellhofer high voltage supply to the ionization chamber was switched off, the detector cable was disconnected from the Wellhofer, and the detector was connected to the Keithley electrometer for the duration of measurement.

2.2.3 Measure Photon Transmission through eMLC Leaves

The treatment planning system modeled the photon contamination present in the electron beam from the measured cross profiles at depths of 2 cm beyond the practical range of the electrons. These data were acquired for a set of open electron fields (3×3 , 5×5 , 7×7 , 9×9 , 11×11 , 15×15 , 1×5 , 2×5 , and 20×15 cm²) for all energies. To further improve the modeling of photon contribution to the dose distribution for irregular fields, the PBA considered the

attenuation of photons passing through closed eMLC leaves. The treatment planning system required measurement of the photon transmission factor. The factor was the ratio of photon dose beneath a fully blocked field compared with the photon dose for a fully open field.

For all energies, output was measured at a depth of $R_p + 2$ cm for an 11×11 cm² field size at 100 cm SSD. Then, all leaves were closed and positioned 5 cm off-axis. For otherwise identical measurements, the output was measured again with the leaves closed. The ratio of these two measurements gave the photon transmission factor.

Measurements were made in Plastic Water slabs including a slab customized to house a PTW TN30013 ionization chamber centered in the $2 \times 30 \times 30$ cm³ slab. The PTW TN30013 (serial number 03435) was used with the Keithley MK 614 Electrometer (serial number 312275) to measure charge collected during the delivery of 500 monitor units with the Varian Clinac 21EX linear accelerator. The electrometer voltage was set to the nominal -300 V. The temperature was (22 ± 1) °C throughout the entire measurement process, and the pressure was (760 ± 1) mmHg throughout the entire measurement process; therefore, no corrections were required for temperature or pressure as only relative dose was needed. Likewise, no corrections were made for ion recombination, polarity effects, dose calibration, or beam quality effects, and the ratios were determined directly from the collected charge readings.

The accelerator gantry and collimator were set to 180° with a mechanical level, and the x-ray jaws were set to 28×28 cm² (required eMLC setting). A 5 cm thick slab of Plastic Water was placed below the chamber slab to provide backscatter dose. The top surface of the plastic water slabs was set to (100.0 ± 0.2) cm SSD with the accelerator optical distance indicator.

2.2.4 Input Required PBA Data into Pinnacle Beam Models

Processing of Dose Distribution Data

Prior to loading data into the Pinnacle treatment planning system, the diode scanning data, acquired in continuous scan mode, was filtered to remove statistical detector noise. An envelope filter with a 5 mm window and 1 mm linearly interpolated resampling was used.

The filter was chosen by plotting filtered data over the raw data and choosing a window size that removed the greatest amount of high frequency noise while preserving the inflection regions of the central axis depth dose and cross profiles. The inflection regions of greatest concern were the region near R_p for the 6 MeV beam and the shallowest cross profiles of the 20 MeV beam in the penumbra region. Cross profiles were, then, centered and made symmetric using the mean value of opposing points equally spaced from the central axis.

Importing Dose Profiles into Pinnacle

Commissioning profile data stored in the Omni-Pro Accept software format was prepared for importation to the Pinnacle treatment planning system. The RTPS Query Bar in Omni-Pro Accept was used to convert the data into a format acceptable for Pinnacle. The data was transferred to the Pinnacle server via FTP. Data was imported to Pinnacle version 7.4f using physics mode. Using the import profiles tool, options were set as follows: fault tolerant import = 'no', Wellhofer crossplane in x = 'yes', and multi data profiles in grid format = 'no'.

Pinnacle Beam Model Parameters

Parameters necessary for the Pinnacle electron beam models were determined. The most probable electron energy at the water phantom surface, $E_{p,o}$, was computed internally by Pinnacle based on the practical range of the electron energy determined from the equilibrium field size. The photon contamination depth was required to be 2 cm beyond the practical range of the electrons. The calibration setup SSD was input as 100 cm in agreement with the nominal accelerator value. The calibration virtual SSD was input as 90 cm, as described in Section 2.1.1; however, the previous work of Richert (2006) indicated the virtual SSD parameter was not used by the dose algorithm, and only the 100 cm value was used in dose computation. The root mean square (RMS) of the angular distribution of an electron pencil beam at the plane of the collimating eMLC leaves (after scattering through the accelerator foils and air) was denoted σ'_{Θ_x} and was determined from MBPCC clinical values of σ_{Θ_x} .

Table 2.1: Electron beam model parameters for Pinnacle.

Electron Model	6 MeV	9 MeV	12 MeV	16 MeV	20 MeV
$E_{o,p}$ (MeV)	6.33	8.92	12.68	16.69	20.60
Photon Contam. Depth (cm)	4.92	6.27	8.23	10.32	12.36
Cal. Setup SSD (cm)	100	100	100	100	100
Cal. Virtual SSD (cm)	90	90	90	90	90
Drift Distance (cm)	11.5	11.5	11.5	11.5	11.5
σ_{Θ_x} (radians)	0.0635	0.0471	0.0344	0.0281	0.0247
FMCS	1.2	1.2	1.2	1.2	1.2
Cutout Transmission Factor	0.44	0.49	0.51	0.52	0.52

(previously measured according to Hogstrom, Mills, and Almond (1981)) corrected for the source to collimator distance of the eMLC device, SCD' , by the equation

$$\sigma'_{\Theta_x} = \sigma_{\Theta_x} \sqrt{\frac{SCD'}{SCD}} \quad (2.11)$$

as described by Richert et al. (2007), where the standard $SCD = 85$ cm from the virtual electron source to the bottom of the standard collimator plane and the eMLC $SCD' = 80$ cm. The FMCS correction factor was used to increase the RMS of the lateral distribution of the pencil beam dose in the water phantom to correct for the underestimation of large angle elastic scattering inherent in the Fermi-Eyges theory of multiple elastic scattering (Eyges 1948; Hogstrom et al. 1984). The previously determined MBPCC clinical value of $FMCS = 1.2$ was input into the beam models. The cutout transmission factor was determined as described in Section 2.2.3 and input into the beam model. A list of the beam model parameters for all electron energies is given in Table 2.1. Off-axis ratios were not determined for the scaling of off-axis electron fluence in the present study; the electron beams were considered to be flat and all off-axis scaling factors were unity.

2.2.5 Validate Relative Dose Computations with Isodose Measurements

Comparisons of planar dose distributions were performed using central axis yz dose planes parallel to the beam axis (z axis) and parallel to eMLC leaf motion (y axis). Software

developed in Matlab analyzed the dose distributions and determined distance to agreement and percent dose difference between the computed and measured isodose planes.

Required Data for Isodose Measurement

Rectangular field isodose data was measured in a water phantom for comparison with computed isodose contours. Isodose planes including the beam axis were created by measuring, first, a central axis depth-dose curve, and second, Y cross profiles at various depths. With consideration of multiple Coulomb scattering and the change in the σ of the pencil beam with depth in the water phantom, cross profiles were measured at 10 depths: shallowest depth possible (2 mm), 3 evenly-spaced depths between 2 mm and distal R_{90} , distal R_{90} , halfway between R_{90} and R_{20} , R_{20} , $R_p + (1, 2, \text{ and } 5)$ cm. Cross-profile depths from equilibrium field size PDDs were used for all field sizes.

Isodose data were acquired for all energies, for field sizes (3×3 , 5×5 , 7×7 , 9×9 , 11×11 , 15×15 , 1×5 , 2×5 , and 15×20) cm^2 at 100 cm SSD. Extended SSD isodose measurements were made for (7×7 and 15×15) cm^2 fields for all energies at 110 cm SSD.

The water scanning system was set up as described in Section 2.2.1, and the electron diode detectors were installed as described in Section 2.2.1. The Varian Clinac 21EX was set to gantry and collimator angle of 180° with a mechanical level; the x-ray jaws were set to 28×28 cm^2 , and the eMLC was inserted. The Omni-pro Accept software was used to control the scanning system. The field detector gain was 7, and the reference detector gain was 6; both were set to zero volts. Depth doses were scanned in continuous mode on low speed; the numerical scan speed control was set to speed 3 as the detector scanned from $R_p + 5$ cm to the approximate $R_p + 1$ cm and set to speed 2 as the detector scanned from $R_p + 1$ cm to the shallowest 2 mm depth. Cross profiles were scanned in continuous mode on medium speed (numerical speed 7), extended laterally to ± 15 cm for the Y cross profiles (axes parallel to leaf motion).

After acquiring data, the depth-dose curves were normalized to 100% at R_{100} . An envelope filter with a 5 mm window and 1 mm linear interpolation was used to filter statistical

noise for the depth dose curves and cross profiles. The cross profiles were, additionally, filtered, centered, and made symmetric prior to analysis.

Dose Computation with the Treatment Planning System

Dose computations were performed with the treatment planning system to generate data for isodose plotting to evaluate agreement with the measured isodose data described previously. Electron beams were incident on a water phantom model available in the Pinnacle software. Beams were placed to gantry angle 180° and collimator angle 90° . 90° was selected for the collimator angle because the resolution of the collimator block was not identical for X and Y directions (Richert 2006); to achieve the highest resolution in geometric beam edge placement, the collimator was set to 90° , and the axial patient planes were examined for the geometric field edge (the accelerator physical collimator angle was 180° with the eMLC installed) Initially, the collimator block was hand drawn to the approximate field size with the block editor tool; however, the precise block points were manually entered by accessing the plan.Trial file from the Pinnacle server with FTP and explicitly defining the block points to create field sizes identical to those delivered in the isodose measurements.

Dose computation were performed for $(7\times 7$ and $15\times 15)$ cm^2 field sizes for all energies at (100 and 110) cm SSD. The 7×7 cm^2 fields were defined by block points at ± 3.60 cm, and the 15×15 cm^2 fields were defined by block points at ± 7.70 cm. The dose grid resolution in Pinnacle was set to 0.1 cm lateral, 0.2 cm anterior/posterior (AP), and 0.4 cm superior/inferior (SI). The dose grid dimensions were 359 pixels lateral, 95 pixels AP, and 63 pixels SI. The dose grid origin was -17.661 cm lateral, 6.729 cm AP, and -12.438 cm SI. For the 100 cm SSD computations the beam isocenter was positioned at the water surface at 0.00 cm lateral, 25.09 cm AP, and 0.00 cm SI. For the 110 cm SSD computations the beam isocenter AP coordinate was changed to 35.09 cm, and the lateral and SI coordinates remained 0.00 cm.

To enable analysis of the computed dose distributions outside of the Pinnacle system, the treatment plan was exported to RTOG file format. Following export, over 200 RTOG files were found in the specified export directory. The largest of these files contained the

dose data and was utilized for plotting the computed dose outside of the treatment planning system.

For all computations, the linear computed tomography (CT) number to density table was used. Using this table, the Pinnacle water phantom was assigned a density of 1.00 g/cm³. The stopping power ratio (material stopping power/water stopping power) and scattering power ratio (material scattering power/water scattering power) for a density of 1.00 g/cm³ were 1.00 for the water phantom.

Develop Software to Process Measured Data and Plot Overlaying Isodoses

Software was developed in Matlab version 7.2 to plot measured isodoses overlaying computed isodoses. As input, the software required the measured data be exported from the Omni-Pro Accept system in an ASCII format and required the computed data be exported from the Pinnacle system in the RTOG format. As output, the software provided graphical output of the overlaying isodose contours and exported the output in the Portable Document Format (PDF). The software required the coordinates and dimensions of the Pinnacle dose grid and beam isocenter to establish the correct coordinates of the dose values in the RTOG file and correctly read the dose values into a three-dimensional array. Additionally, a Linux command

```
tr -cd '11\12\40-\176' <fileNameIn> fileNameOut
```

was needed to delete characters from the RTOG files other than the standard ASCII characters prior to use with the software. The software imported the depth dose and cross profiles from the Omni-Pro Accept ASCII file. The depth dose was normalized to 100% at R_{100} and the cross profiles were converted to off-axis ratios (normalized to 1 on central axis). The off-axis ratios were multiplied by the normalized depth dose corresponding to the off-axis profile depth creating a two-dimensional array. Divergent fanline interpolation from the electron virtual point source (90 cm SSD) was used to interpolate the off-axis ratios to 1 mm depth spacings and provide a higher resolution for isodose contour plotting. The isodose curves were generated with the Matlab “contour” function.

2.2.6 Validate Implementation of Output Factors by Pinnacle

Dose calculations were performed in Pinnacle for electron beams with different energies and field sizes and a constant prescription to deliver 100 monitor units. The computed maximum dose was recorded for each beam and used to find the computed absolute output (dose per monitor unit) for square field sizes with side length 1, 2, 3, 5, 7, 9, 11, 15, and 20 cm and with energies 6, 9, 12, 16, and 20 MeV at 100 cm SSD. The computed absolute output was compared with the measured absolute output used in commissioning the dose algorithm to validate the correct implementation of the data for dose calculation.

2.3 Aim 3: Feather Field Edges to Improve Dose Homogeneity

One-dimensional and two-dimensional edge feathering for abutting segments of different electron energies in a water phantom was investigated. An analytical feathering solution was converted into a clinically practical feathering solution. The impact of the feathering solution on dose homogeneity was computed using an electron pencil beam dose algorithm. Hypothetical 2D PTVs in a water phantom were used to compare dose homogeneity in the PTV for one-dimensional edge feathering and no feathering. An additional 3D PTV was used to evaluate 1D, 2D, and no feathering for a SFECT plan with segment abutment regions both perpendicular to leaf motion and parallel to leaf motion. The computed improvements to dose homogeneity through edge feathering were validated with film measurements in a plastic water phantom.

2.3.1 Determine Analytical Solution to Edge Feathering Based on PBA

Edge Spread Function

The edge spread function $h(x, z, E_l, E_h)$ was determined to match the penumbras of the high and low energy electron fields, E_h and E_l , at a specified depth in a water phantom so that the convolution

$$h(x, z, E_l, E_h) \otimes p(x, z, E_h) = p(x, z, E_l) \quad (2.12)$$

where $p(x, z, E)$ is the penumbra dose distribution, x is the lateral position perpendicular to the electron beam, z is the depth in a water phantom, and E is the kinetic energy of

the incident electron beam (utilizing the most probable electron energy, $E_{p,o}$, of the beam incident on the phantom). The solution, $h(x, z, E_l, E_h)$, was found by considering the source of the electron penumbra dose distribution. The penumbra may be computed by integrating pencil-beam dose distributions from the edge of the electron collimator towards the center of the field. If one places the collimator at $x = 0$ and assumes the field extends infinitely away from the collimator, the penumbra may be expressed by

$$p(x, z, E) = \int_0^\infty f(x - x', z, E) dx', \quad (2.13)$$

where $f(x, z, E)$ is the lateral dose distribution from a single pencil beam passing through a slab phantom calculated with the Fermi-Eyges theory of multiple elastic scattering (Eyges 1948) as applied to electron radiotherapy by Hogstrom, Mills, and Almond (1981) given by

$$f(x, z, E) = \frac{1}{2\pi\sigma_{z,E}^2} e^{\frac{-x^2}{2\sigma_{z,E}^2}}, \quad (2.14)$$

and the RMS of the lateral distribution, $\sigma_{z,E}$, depends on depth in the water phantom and the incident electron energy. The solution was simplified by considering the individual pencil beam distributions rather than the penumbra functions. It can be shown from Equations 2.12 and 2.13 that the same solution, $h(x, z, E_l, E_h)$, holds for the matching of two pencil beams

$$h(x, z, E_l, E_h) \otimes f(x, z, E_h) = f(x, z, E_l). \quad (2.15)$$

Solving

$$h(x, z, E_l, E_h) = \mathcal{F}^{-1} \left\{ \frac{\mathcal{F}\{f(x, z, E_l)\}}{\mathcal{F}\{f(x, z, E_h)\}} \right\} = a e^{\frac{-x^2}{2(\sigma_{z,E_l}^2 - \sigma_{z,E_h}^2)}}, \quad (2.16)$$

where

$$a = \frac{\sigma_{z,E_h}}{\sigma_{z,E_l} \sqrt{2\pi(\sigma_{z,E_l}^2 - \sigma_{z,E_h}^2)}}. \quad (2.17)$$

Practically, the analytical solution was implemented by feathering the collimator leaf positions for the higher energy field at discrete steps with equal area Gaussian spacing as described in Section 2.3.2. The constant, a , in Equation 2.17 was determined so that the sum of dose for all feathering steps equaled the prescribed dose for the segment.

Lateral Dose Distribution from an Electron Pencil Beam

The RMS of the lateral distribution of electrons from a single pencil beam at depth z in a water phantom was denoted $\sigma_{z,E}$. As discussed by Hogstrom, Mills, and Almond (1981),

$$\sigma_{z,E}^2 = \sigma_{ph}^2 + (z + L_o)^2 \sigma_{\Theta_x}^2, \quad (2.18)$$

where L_o was defined as the collimator-to-surface distance of 11.5 cm for the eMLC. The RMS of the lateral distribution of an electron pencil beam resulting from multiple elastic scattering of electrons in the phantom materials (i.e. air and water) downstream from the eMLC collimating plane was denoted σ_{ph} and was calculated by

$$\sigma_{ph}^2 = \frac{1}{2} \int_{-L_o}^z (z - z')^2 T_{z'} dz', \quad (2.19)$$

where $T_{z'}$ is the linear angular scattering power for the phantom material and most probable energy at z' , calculated according to the recommendations of ICRU (1984) with the suggested correction to include Møller scattering

$$T_{z'} = \rho\pi\left(\frac{2r_e}{(\tau + 1)\beta^2}\right)^2(Z(Z + 1))\frac{N_A}{M_A} \left\{ \ln\left(1 + \left(\frac{\Theta_m}{\Theta_\mu}\right)^2\right) - 1 + \left(1 + \left(\frac{\Theta_m}{\Theta_\mu}\right)^2\right)^{-1} \right\}. \quad (2.20)$$

Here ρ is the density of the material, r_e is the classical electron radius, Z is the atomic number, N_A is the Avogadro constant, and M_A is molar mass.

$$\tau = \frac{E}{m_o c^2} \quad (2.21)$$

where T is the kinetic energy of the electrons at depth z' in the phantom, m_o is the rest mass of an electron, and c is the speed of light. Additionally,

$$\beta = \frac{v}{c} = \sqrt{1 - \left(\frac{m_o c^2}{E + m_o c^2}\right)^2}. \quad (2.22)$$

The maximum angle of elastic scattering, Θ_m , is limited by the finite size of the nucleus

$$\Theta_m = \frac{2A^{-1/3}}{\alpha\beta(\tau + 1)}, \quad (2.23)$$

where A is the number of nucleons, α is the fine structure constant $= 7.2974 \times 10^{-3}$. The minimum angle of elastic scattering, Θ_μ , occurs due to a charge screening effect of the orbital electrons

$$\Theta_\mu = 1.130 \frac{\alpha Z^{1/3}}{\beta(\tau + 1)}. \quad (2.24)$$

The most probable energy, E_p , of the electrons at depth, z' , in the water phantom was determined using Harder's linear relationship (Zuppinger and Poretta 1965)

$$E_p(z') = E_{p,o}(1 - z'/R_p), \quad (2.25)$$

where $E_{p,o}$ is the most probable energy incident on the water phantom surface and R_p is the practical range of the electron field. To compute the kinetic energy of electrons in the air between the collimator and the phantom surface, Equation 2.25 was used with the further approximation that the total mass stopping power was identical for air and water for electrons in the range of 6 to 20 MeV, and only a density correction was applied.

The linear angular scattering power for a mixture of elements was determined by calculating the linear angular scattering powers for each element, weighting the values to represent the fractional density of the elements in the mixture, and summing the weighted scattering powers to determine the linear angular scattering power for the mixture. The compositions of the air and water mixtures were obtained from NIST (2009). A water composition was

used with 0.111894 fractional mass of hydrogen and 0.888106 fractional mass of oxygen. A water density of 1 g/cm^3 was used. An air composition was used with 0.755267 fractional mass of nitrogen, 0.231781 fractional mass of oxygen, 0.012827 fractional mass of argon, and 0.000124 fractional mass of carbon. An air density for dry air near sea level of $1.20479 \times 10^{-3} \text{ g/cm}^3$ was used.

The accuracy of calculation of linear angular scattering powers by Equation 2.20 was verified by testing the IDL software and comparison with the tabular values reported by ICRU (1984). Agreement with the tabular values, when omitting the term for Møller scattering, confirmed that the equation and constants were accurately entered in the software, though the term for Møller scattering was later added and used in the present work.

The RMS of the angular distribution of an electron pencil beam at the plane of collimating leaves, σ_{θ_x} , resulted from scatter introduced by the components of the accelerator head (e.g. scattering foils, air, monitor chambers) upstream of the eMLC collimating plane and was determined by modifying a clinical, previously-determined value as described in Section 2.2.4.

2.3.2 Computer Algorithm Developed to Implement Discrete Gaussian Edge Feathering

A computer algorithm was designed to implement discrete Gaussian edge feathering for segmented field ECT treatment plans. Software was developed in IDL to implement the feathering algorithm and read and write files compatible with the Pinnacle treatment planning system. As input, the program accepted the plan.Trial file created with Pinnacle, a user specified depth at which to match the penumbras of the different energy segments, and the discrete number of feathering steps to generate.

Prepare Segmented Field ECT Plan in Pinnacle

Segmented field ECT treatment plans were created in a forward planning manner in Pinnacle. Beam block apertures were hand drawn with the block editor tool. Precise assignment of block point coordinates was achieved by exporting the plan.Trial file via FTP to a local PC and manually entering the coordinates of the desired block points with a text editor. The file was then assigned a unique name to indicate the date of modification and a reference to

the exact plan in Pinnacle. The file path and file name specified in the IDL edge feathering program was modified to retrieve data from the desired plan.Trial file.

Read Beam Data from Pinnacle Plan File

The IDL program read the beam data from the plan.Trial file. The beam names and energies were extracted for use in the edge feathering algorithm. The lowest energy in the plan was used as a reference, and all higher energy segments were feathered to match the penumbra distribution of the lowest energy segment. The block points defining the original segment apertures were extracted to compute the feathered apertures.

Compute $\sigma_{z,E}$ at Depth to Match Penumbras

Equations described in Section 2.3.1 were implemented numerically to determine $\sigma_{z,E}$ at the desired matching depth for each of the original segments in the plan. As previously described, the energy-dependent, constant values of σ_{Θ_x} were incorporated with Equation 2.18, and σ_{MCS} was calculated with the integral and required linear angular scattering powers of Equation 2.19 and implemented through numerical integration using a rectangular approximation

$$\sigma_{ph}^2(z) = \frac{1}{2} \sum_{i=0}^N (z - z_i)^2 T_{z'}(z_i) \Delta z \quad (2.26)$$

where $N = (z + L_o)/\Delta z$, $\Delta z =$ depth step-size of 10 μm , and $z_i = i\Delta z$.

Discretize Gaussian Edge Spread Function

To apply the continuous edge spread function determined in Section 2.3.1 with an eMLC would have required precise control of leaf motor speed and continuous monitoring of the linear accelerator flux. Hence, a discrete number of segment apertures was determined to best represent the continuous Gaussian solution. With the discrete technique, the existing accelerator beam monitors were suitable for delivering the desired fluence (i.e., monitor units) for each discrete segment aperture.

As shown in Equation 2.16, the edge spread function was determined to be Gaussian. The Gaussian function was discretized by dividing the function into regions of equal area.

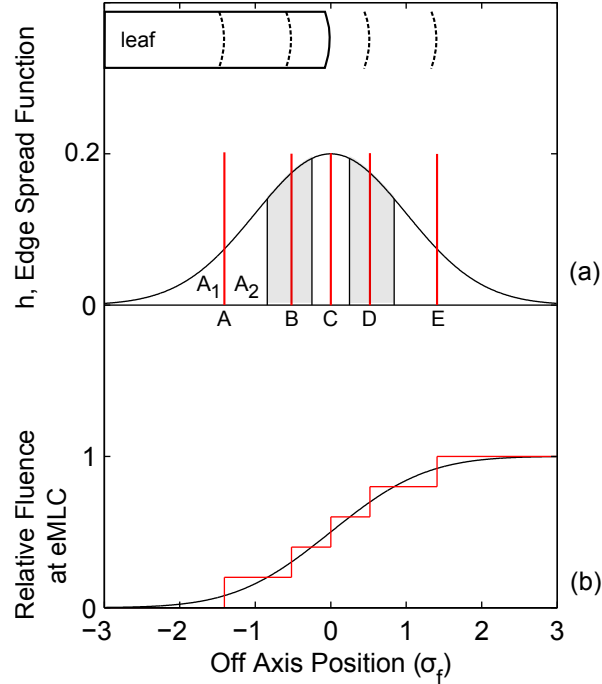


Figure 2.7: Discretizing the Gaussian edge spread function. The Gaussian function (a) is divided into 5 equal areas (A, B, C, D, and E) shown by the white and grey regions divided by black lines. The geometric beam edges indicated by red lines are positioned so that the region is subdivided into two equal area sections as demonstrated here for area A ($A_1 + A_2$) where the subdivided area $A_1 = A_2$. The corresponding eMLC leaf positions are shown at the top. The resulting lateral fluence distributions (at the plane of collimation) from the continuous Gaussian edge spread function (black) and the discrete Gaussian edge spread function (red) are shown (b).

Geometric field edges were shifted to positions centered in each region of the Gaussian. Figure 2.7 exemplifies this concept for five discrete steps. Dividing the Gaussian into regions of equal area and locating the feathering positions was implemented via a lookup table created from values of the error function evaluated at lateral positions ranging from $-5\sigma_f$ to $5\sigma_f$ with a resolution of $\sigma_f/100$, where $\sigma_f^2 = \sigma_{z,E_l}^2 - \sigma_{z,E_h}^2$ for the Gaussian edge spread function. The locations of the feathering positions were then obtained using the closest matching value of the desired area.

The impact of the number of discrete steps was evaluated computationally. For a worst case scenario of abutting a 20 MeV and a 6 MeV beam, the resulting lateral dose distribution was computed at 1 cm depth in a water phantom using the relations of Section 2.3.1. Based

on the results of this evaluation, a method using five discrete steps was determined to be both clinically practical and dosimetrically acceptable and was used for the current work (see results).

In order to further improve the abutment dosimetry, the outermost feathering positions (positions A and E in Figure 2.7) were shifted manually to search for minima in the abutment dose deviation for the PBA theoretical abutment of the 20 MeV and 6 MeV beams at 1 cm depth in water. The five discrete feathering positions used in the present work were $(-1.41, -0.52, 0.0, 0.52, \text{ and } 1.41)\sigma_f$ where σ_f depends on the energies of the abutting segments and the depth to match the penumbras. The outermost feathering shift value $1.41\sigma_f$ was found by manually searching for minima compared with the equal area predicted value of $1.28\sigma_f$.

Create New Segment Apertures using the Discrete Feathering Shifts

The discrete Gaussian edge feathering solution was applied to the segment apertures of the treatment plans. Using the block points extracted from the Pinnacle plan, electron segment apertures were expanded and contracted to the positions determined from the discretization of the Gaussian edge spread function. Both 1D and 2D applications of the discrete edge feathering were developed for the segment apertures.

The IDL function library contained dilate and erode functions which assisted in the application of the discrete feathering solution to a 2D aperture (IDL 2005). The dilate function accepted as input the original segment aperture and a dilation structure. The original segment aperture was converted to a binary array where elements within the aperture were assigned values of 1 and elements outside the aperture were assigned values of 0.

For 1D feathering, the dilation structure was defined in the current work as a linear array with N elements (containing only values of 1) where N was twice the desired feathering-shift distance. For 2D feathering, the dilation structure was defined as a circle in a 2D NxN array where elements within the circle radius were given a value of 1 and elements outside the circle radius (radius = N/2) were assigned a value of 0. The dilate function translated the dilation structure over the original segment aperture in two dimensions. When the center of the dilation structure overlapped the original aperture, the aperture was grown by the

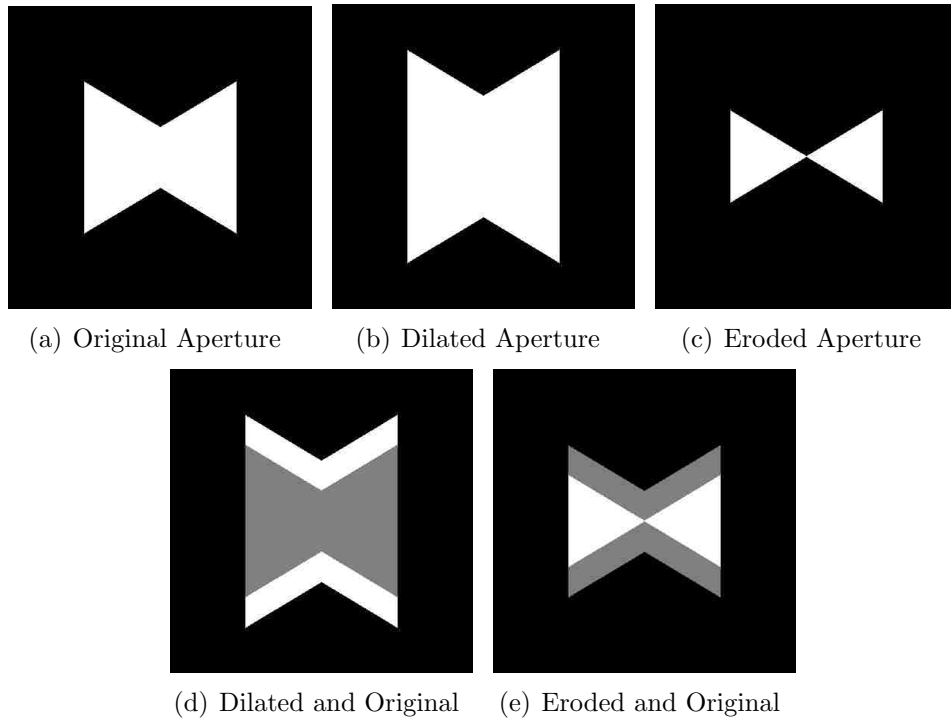


Figure 2.8: 1D (vertical) dilation and erosion of an irregular segment aperture.

immediate position and size of the dilation structure. The result was a larger aperture based on the desired feathering shift. The IDL erode function operated as the inverse of the dilate function to contract the size of the segment aperture for the negative feathering shift positions. Figure 2.8 illustrates the dilation and erosion of an irregular segment aperture by the 1D structure. The direction of the 1D dilation and erosion was parallel to eMLC leaf motion. Figure 2.9 demonstrates the dilation and erosion of the irregular segment by the 2D circular structure.

Generate New Beams in Pinnacle Plan with Feathered Apertures

The feathered segment apertures were used to create new beams in the Pinnacle treatment plan. The original beam data were copied into new beams and input into the plan. Trial file automatically. The block points were modified to reflect the feathered apertures, and the monitor units were equally divided among the number of new beams for each segment.

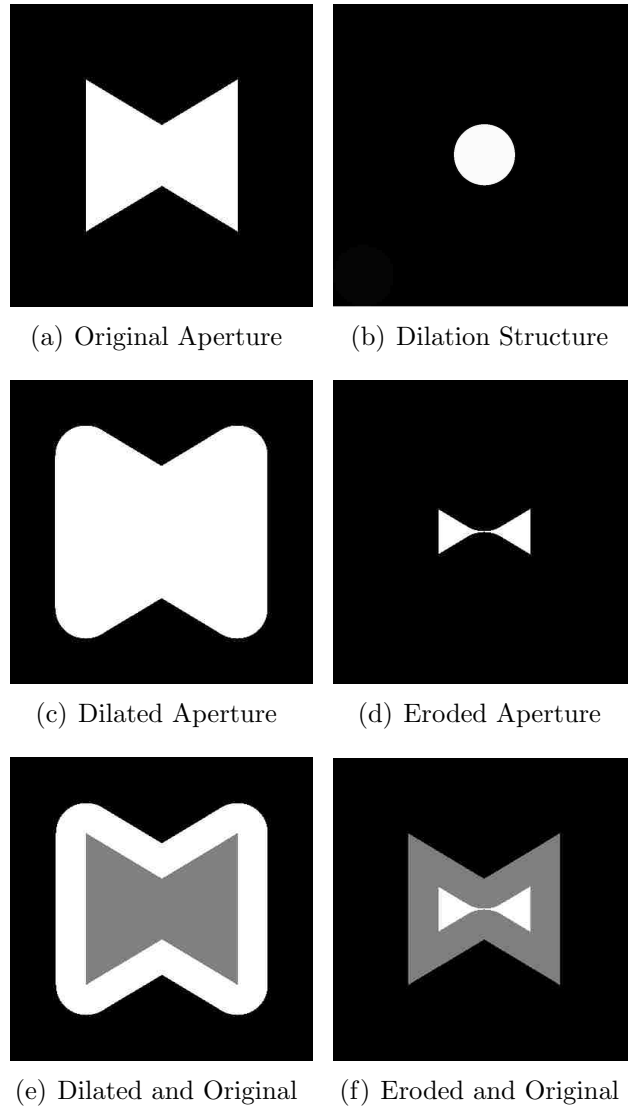


Figure 2.9: 2D dilation and erosion of an irregular segment aperture.

Determine eMLC Leaf Positions for Feathered Plans and Compute Dose in Pinnacle

Software discussed in Section 2.1.2 was used to convert the segment apertures with discrete Gaussian edge feathering to eMLC apertures. Leaf position files were exported for communication with the eMLC. The plan.Trial file was returned to Pinnacle via FTP, and the dose distribution was computed for the plan.

2.3.3 Compute Effect of Discrete Gaussian Edge Feathering on Dose Distributions

Segmented field ECT plan dose distributions were computed for four test PTVs both with and without discrete Gaussian edge feathering. Test PTV geometries were created, and forward planning methods were used to create beam apertures and energies for the treatment plans in Pinnacle. Three PTV geometries were identical to those used by Richert et al. (2007) so that the present method could be compared with Richert's method. The Richert PTVs varied in depth along one axis parallel to eMLC leaf motion and had uniform cross sections perpendicular to leaf motion. A fourth PTV was designed for the current study with an irregular shape and variation in depth along both axes perpendicular to the beam direction. The edge feathering algorithm described in Section 2.3.2 was utilized to improve abutment dosimetry for the plans. Dose computations were performed in Pinnacle for the plans with and without discrete Gaussian edge feathering with the eMLC and accelerator data commissioned for the 3D version of the Hogstrom electron pencil beam algorithm (Starkschall et al. 1991) as described in Section 2.2. Computed dose distributions were exported from Pinnacle in RTOG format. Matlab software was developed to generate isodose plots and off-axis profiles from the computed dose data.

Two-step PTV

A two-step PTV was used to illustrate a segmented field plan with two abutting electron beams. The PTV varied in depth along the axis parallel to eMLC leaf motion and had uniform cross section perpendicular to leaf motion. The PTV cross section and dimensions are shown in Figure 2.10. The 1D application of the discrete Gaussian edge feathering algorithm was tested for the two-step PTV.

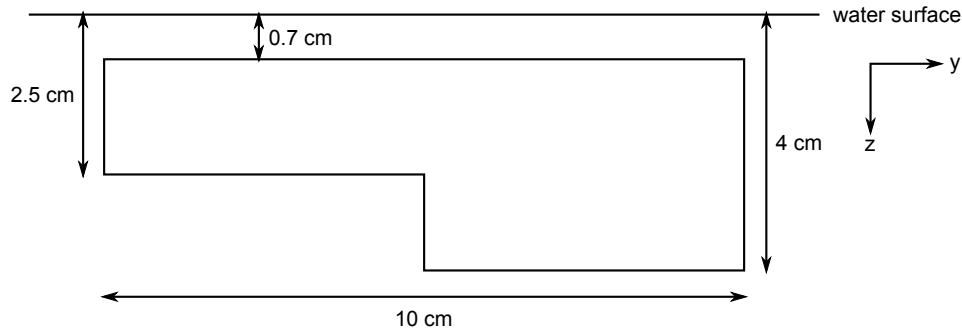


Figure 2.10: Two-step PTV dimensions. The z axis corresponds to depth in water, and the y axis is parallel to eMLC leaf motion.

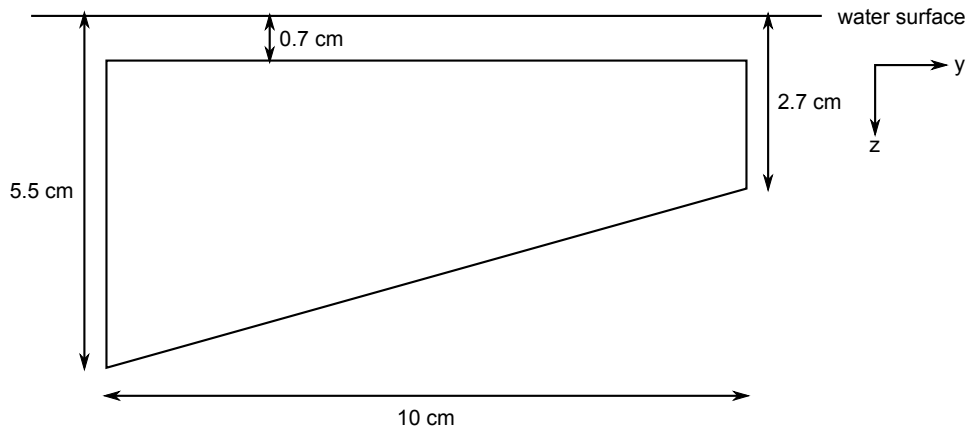


Figure 2.11: Wedge PTV dimensions. The z axis corresponds to depth in water, and the y axis is parallel to eMLC leaf motion.

Wedge PTV

A wedge PTV was used to represent a target with continuously increasing depth. Three electron beams were used in the segmented field ECT plan for the wedge target. The PTV cross section and dimensions are shown in Figure 2.11. The 1D application of the discrete Gaussian edge feathering algorithm was tested for the wedge PTV.

Inverted Well PTV

An inverted well target was used to simulate a target with the shallowest depth on central axis and increasing depth away from central axis. The segmented field ECT plan for the

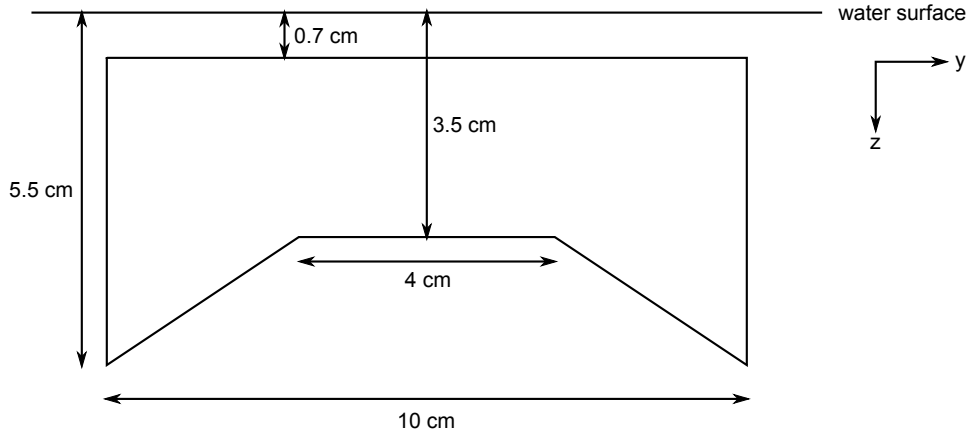


Figure 2.12: Inverted well PTV dimensions. The z axis corresponds to depth in water, and the y axis is parallel to eMLC leaf motion.

inverted well target was composed of three abutting electron beams. The PTV cross section and dimensions are shown in Figure 2.12. The 1D application of the discrete Gaussian edge feathering algorithm was tested for the inverted well PTV.

Concentric Cylinders PTV

A 3D concentric cylinders PTV was designed to test the limitations of the eMLC for use in segmented field ECT. The 3D PTV was created to present two challenges for the eMLC. First, the PTV was irregular in shape, consisting of two concentric cylinders that appeared circular from a beam's eye view (BEV). The irregular shape was chosen to evaluate the impact of the finite eMLC leaf width on the dose distribution. Second, the PTV varied in depth along axes both parallel to eMLC leaf motion and perpendicular to leaf motion. Hence, the segmented-field plan created to treat the PTV consisted of electron segments of with abutment regions both perpendicular and parallel to leaf motion. The PTV cross section and dimensions are shown in Figure 2.13. The 1D and 2D applications of the discrete Gaussian edge feathering algorithm were tested for the 3D concentric cylinders PTV. The 2D feathering algorithm was tested to address the abutment dosimetry in regions parallel to leaf motion.

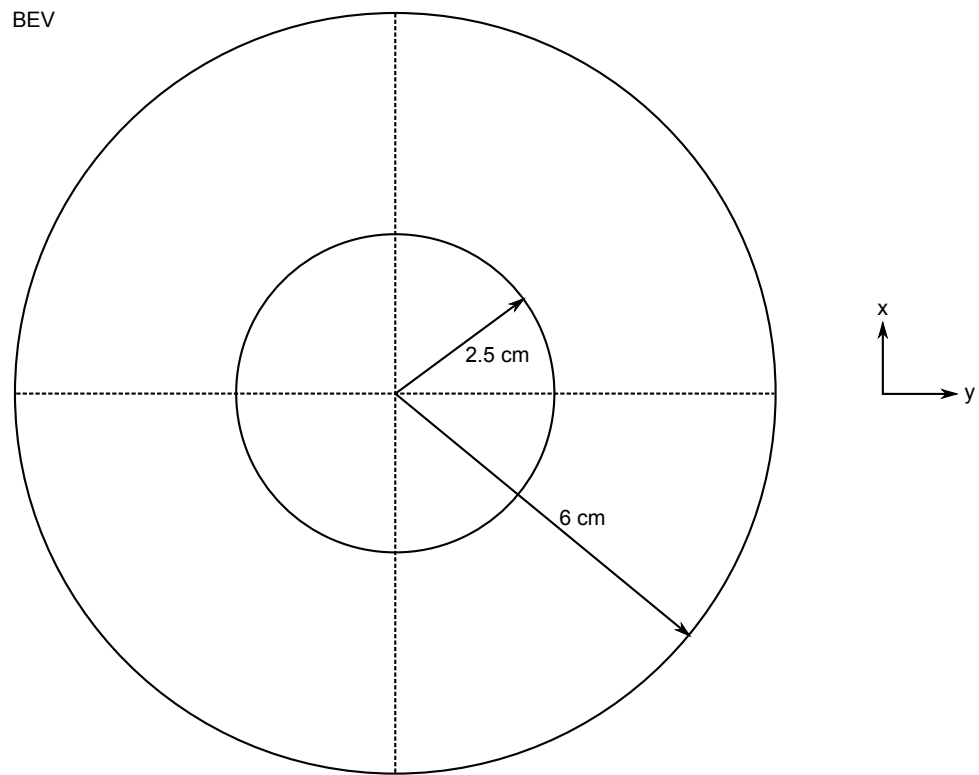
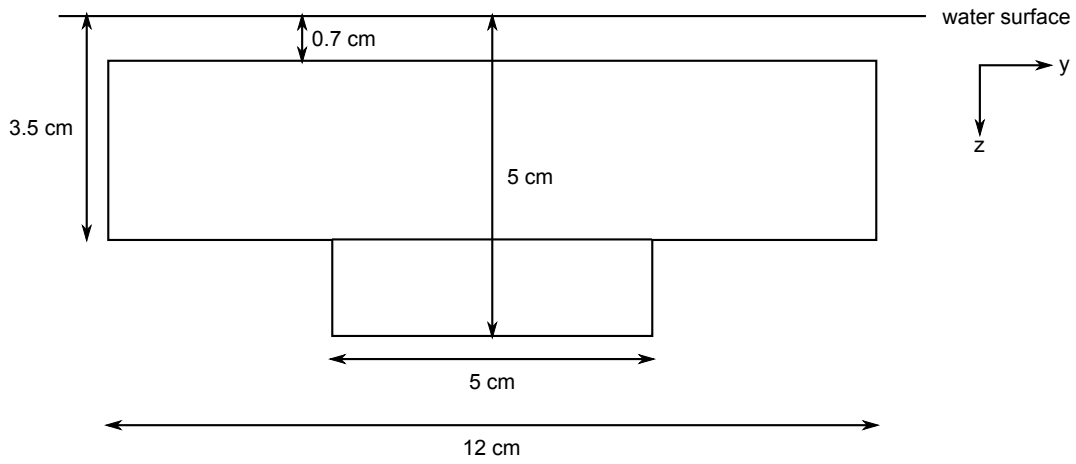


Figure 2.13: Concentric cylinders PTV dimensions. The z axis corresponds to depth in water, the y axis is parallel to eMLC leaf motion. A beam's eye view (BEV) of the PTV is shown below.

2.3.4 Measure Dose Distributions for Segmented Field ECT plans with and without Edge Feathering

Radiographic Film Measurements

Dose distributions were measured for segmented field ECT plans delivered with the eMLC with and without discrete Gaussian edge feathering. The eMLC was installed on the linear accelerator as described in Section 2.1.4. Electron fields were delivered to radiographic films placed normal to the beam in a plastic water phantom.

The accelerator collimator and gantry angle were set to 180° with a mechanical level. Calibration films were irradiated with 9 MeV electrons as described in Appendix A prior to installation of the eMLC. The eMLC was installed, and the x-ray jaws were set to 28×28 cm² at isocenter. For the segmented field ECT treatment plan deliveries, the Kodak XV film (in jacket) was placed beneath 2 cm of plastic water (at the depth of penumbra matching for the feathered plans) and above 5 cm of plastic water. Pin holes were made in the film jacket to denote film orientation and to release air trapped in the jacket. The phantom surface was positioned at 100 cm SSD using the optical distance indicator. As each segmented field plan delivery required multiple eMLC segments, the eMLC leaf position calibration routine was performed prior to each plan. The treatment plan monitor units were scaled to deliver 50 cGy to the prescription point of the plans.

Treatment plans were delivered to the films for the two-step PTV, wedge PTV, and inverted well PTV with no feathering and with 1D discrete Gaussian edge feathering. For the 3D concentric cylinders PTV, plans were delivered with no feathering, 1D feathering, and 2D feathering.

Film Processing

The XV films were processed in the AFP Imaging Corp. Mini Medical 90 film processor with serial number 21426. The manufacturer specified processing temperature was 95° F. Three unirradiated warm-up films were processed to stabilize the processing temperature and clean debris from the processor film feed rollers. The film calibration set was processed prior to processing the measurement set.

Film Scanning

Films were scanned with the Vidar Dosimetry Pro Advantage Red scanner with serial number 351709. RIT 113 version 5.2 software was used to acquire data from the scanner and convert the data files to a Matlab format. The scanning resolution was set to 178 μm , and a scanner calibration (via a RIT software option) was performed prior to use. Calibration film A/D values were recorded manually and used in the Matlab software described in Section 2.1.5 to obtain isodose plots and off-axis dose profiles from the film measurement data.

Chapter 3. Results and Discussion

3.1 Aim 1: Define eMLC Leaf Positions for General Electron Fields

3.1.1 Calibration of Field Width at the Plane of Leaves

The parameter controlling motor encoder counts per millimeter of leaf travel at the plane of the center of the leaves, determined to be 177.32 counts per millimeter, was inputted in the QBasic eMLC control software. To move the leaves to the parked position from the calibration bar, a leaf position file was created named calOut.txt.

The desired positions of the leaf ends to form a parked field length of 20 cm (field edges at ± 10 cm on y-axis) were ± 8.81 cm off-axis at the plane of leaf midline using the relations derived in Section 2.1.1. Regardless of the actual leaf position, the leaf position value transmitted to the the motor electronics upon cycling power was always the parked position (± 88.1 mm), so, in order to move the leaves from the calibration bar to the parked position (after cycling power at the position touching the calibration bar), the leaves were requested to move to the new positions at 88.1 mm (position value in motor memory electronics) + 88.1 mm (desired parked position) - 10 mm (off-axis position when touching calibration bar) = 166.2 mm (± 166.2 mm).

Due to the staggered heights of the leaf drive screws in relation to the leaf midlines, different torques were applied to each of the leaf connecting-rods during the calibration procedure (corresponding to different strains and deformations of the connecting rods) leading to a slight staggering of the calibrated leaves upon retraction from the calibration bar when the torques were removed. To counter this effect the file calOut.txt contained the desired parked leaf positions but with staggered positions for the even and odd leaves. Odd leaf positions were ± 166.51 mm and even leaf positions were ± 166.14 mm. No further corrections for even and odd leaves were made to individual leaf position files. It was assumed that the

differing torques only presented problems when the leaves were forcefully pressing against the calibration bar, and, that, when properly moved to the parked position, multiple fields could be generated without unwanted staggering effects.

The width of the open field was measured with a ruler (uncertainty ± 0.03 cm) for each leaf pair at the top of the leaves. The measured field width at the top of the leaves was corrected by subtracting 0.16 cm (rounded leaf ends) to determine the field width at the midline of the leaves.

For a parked, 15×20 cm², isocentric field size, the mean leaf opening for the 15 leaf pairs at the midline of the leaves was 17.62 cm with a standard deviation of 0.04 cm. The expected opening (corresponding to 20 cm at isocenter) was 17.62 cm. For a 9×9 cm², isocentric field size, the mean leaf opening for the 9 leaf pairs at the midline of the leaves was 7.88 cm with a standard deviation of 0.03 cm. The expected opening was 7.86 cm. For a 5×5 cm², isocentric field size, the mean leaf opening for the 5 leaf pairs at the midline of the leaves was 4.35 cm with a standard deviation of 0.04 cm. The expected opening was 4.36 cm. For the (9×9 and 5×5) cm² fields, the mean field width agreed with the expected field width within one standard deviation. The greatest standard deviation in field width at the plane of the leaf midlines was 0.04 cm. The mean field width for the 15×20 cm² (parked position) was slightly outside one standard deviation of the expected field width.

The leaf control parameter (encoder counts per millimeter = 177.32) was optimized for the 9×9 cm² field which was chosen to represent a mid-sized field. The differences in leaf calibration and encoder counts per millimeter of leaf travel for the different field sizes may warrant further investigation of leaf sagging (as the leaves moved across the field the protruding leaf edges were pulled downward) and frictional forces that varied in magnitude as the leaves moved across the field.

3.1.2 Radiation Field Widths for Rectangular Fields

Isocentric film measurements of dose planes normal to the beam showed the accuracy of field size calculations and indicated whether the electron virtual point source was an

Table 3.1: Isocentric field width measurements parallel to leaf motion (y -axis). Standard deviation (SD) calculated to show variation in field width across the open leaf pairs. The asterisk (*) indicates the length was set to match the field width perpendicular to leaf motion (cf. Table 3.2).

Field Description	Expected (cm)	Measured (cm)	SD (cm)	Difference (cm)
<i>Parked</i>	20.00	19.99	0.04	-0.01
<i>Squares</i>				
3×3 cm ²	3.04*	3.08	0.01	0.04
5×5 cm ²	5.06*	5.10	0.01	0.04
9×9 cm ²	9.11*	9.17	0.03	0.06
15×15 cm ²	15.19*	15.27	0.03	0.08
<i>Rectangles</i>				
2×15 cm ²	2.00	2.08	0.03	0.08
4×15 cm ²	4.00	4.05	0.03	0.05
6×15 cm ²	6.00	6.05	0.03	0.05
8×15 cm ²	8.00	8.05	0.03	0.05
10×15 cm ²	10.00	10.05	0.03	0.05
12×15 cm ²	12.00	12.06	0.03	0.06
15×15 cm ²	15.00	15.08	0.03	0.08
20×15 cm ²	20.00	20.03	0.04	0.03

acceptable model for field size calculations. Additionally, analysis of the radiographic film measurements at the isocentric plane revealed the precision of leaf positioning influenced by the motorized leaf-drive circuits and physical construction of the eMLC.

As discussed in Section 2.1.1, the field width parallel to leaf motion was defined by the intersection of a tangent line anchored at the virtual electron source, passing tangentially past the rounded leaf ends, and passing through the isocentric plane where the desired field width was defined. The available field widths parallel to leaf motion were continuous and possible from 0 to 20 cm. Table 3.1 gives the results for measured field widths parallel to leaf motion. All measured field sizes agreed with the calculated field size within 0.08 cm. The standard deviation in field width across the leaf pairs was 0.04 cm or less for all measurements and indicates the precision of leaf positioning.

The field widths available perpendicular to leaf motion were discrete and were limited by the finite width of the leaves. The field was collimated at the bottom of the leaf planes for

Table 3.2: Isocentric field widths defined by the number of leaves open.

n_{leaves}	Isocentric Width (cm)
3	3.04
5	5.06
7	7.09
9	9.11
11	11.14
15	15.19

symmetric fields. Table 3.2 gives isocentric field widths calculated with Equation 2.3 as a function of the number of leaves open, n_{leaves} . Table 3.3 gives the results for measured field widths perpendicular to leaf motion. All measured field sizes agreed with the calculated field size within 0.08 cm. The major component of the measured width uncertainty was the film setup SAD with the accelerator ODI (± 2 mm), and the uncertainty was dependent on field size.

3.1.3 Delivery of Irregular Fields with the eMLC

The eMLC aperture was plotted overlaying the desired general field. The center of each eMLC leaf intersected the general field aperture. Figure 3.1 shows the eMLC aperture overlaying a pentagon shaped irregular field. Figure 3.2 shows the eMLC aperture overlaying a crescent shaped irregular field. Irregular-field edges delivered with the eMLC agreed best with desired field edges in regions where the leaf axes were most perpendicular to the general field shape boundary. In regions where the leaf axes were most parallel to the general field shape boundary, the field could suffer cropping or overextension up to 0.5 cm perpendicular to leaf motion. In regions where the leaf axes were nearly diagonal to the general field shape boundary, the eMLC introduced a stair-step pattern to the field edge.

The ability of the eMLC to accurately deliver irregular fields was evaluated. The isocentric planar dose distribution measured at 100 cm SAD and 1 cm depth in plastic water was plotted overlaying the geometric eMLC aperture. Agreement of the measured 50% isodose curve with the geometric eMLC aperture (at center of leaves) indicated accurate leaf position-

Table 3.3: Isocentric field width measurements perpendicular to leaf motion (x-axis). Expected field widths calculated with Equation 2.3.

Field	Expected (cm)	Measured (cm)	Uncertainty (cm)	Difference (cm)
<i>Parked</i>	15.19	15.11	0.03	-0.08
<i>Squares</i>				
3×3 cm ²	3.04	3.03	0.01	-0.01
5×5 cm ²	5.06	5.05	0.01	-0.01
9×9 cm ²	9.11	9.06	0.02	-0.05
15×15 cm ²	15.19	15.13	0.03	-0.06
<i>Rectangles</i>				
2×15 cm ²	15.19	15.14	0.03	-0.05
4×15 cm ²	15.19	15.14	0.03	-0.05
6×15 cm ²	15.19	15.13	0.03	-0.06
8×15 cm ²	15.19	15.13	0.03	-0.06
10×15 cm ²	15.19	15.13	0.03	-0.06
12×15 cm ²	15.19	15.13	0.03	-0.06
15×15 cm ²	15.19	15.11	0.03	-0.08
20×15 cm ²	15.19	15.13	0.03	-0.06

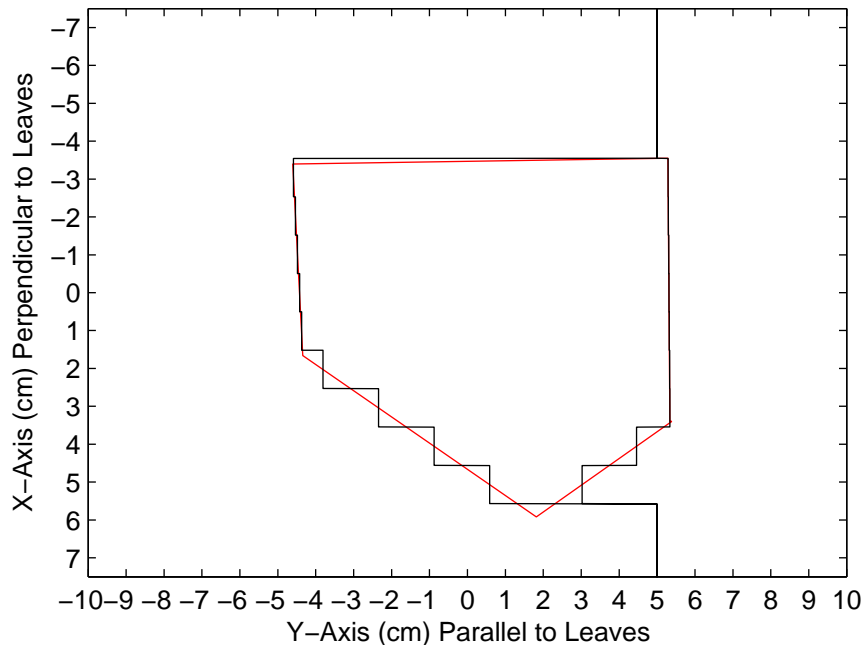


Figure 3.1: Pentagon, irregular field with eMLC leaves overlaying general field shape.

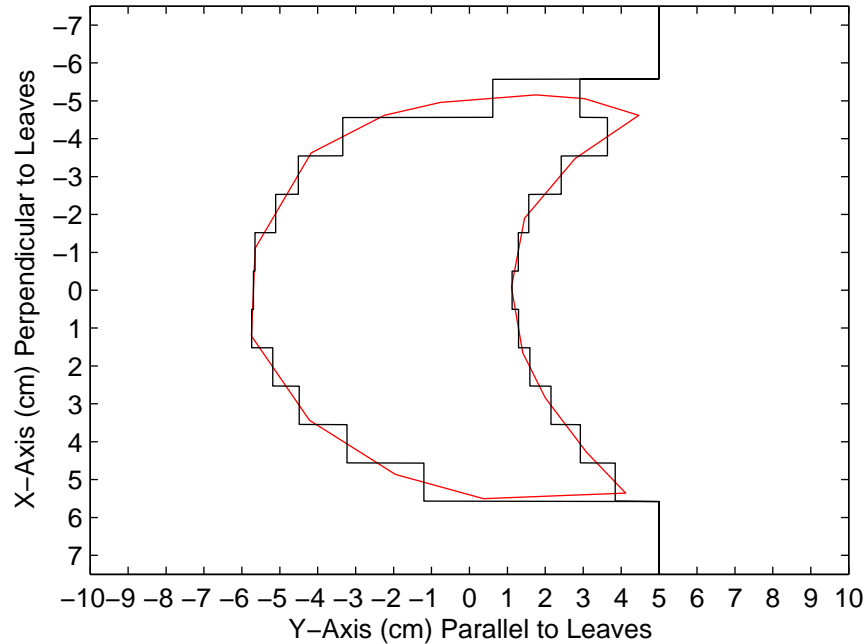


Figure 3.2: Crescent, irregular field with eMLC leaves overlaying general field shape.

ing for both the pentagon-shaped irregular field shown in Figure 3.3 and the crescent-shaped field shown in Figure 3.4. At the sharp corners of the geometric eMLC aperture, a dose value of 25% is expected. The 90% isodose was plotted to demonstrate the effect of the leaf widths on the therapeutic dose contour. The 10% isodose curves indicated the lateral dose falloff around the aperture and leakage through opposing leaf pairs that were not completely closed due to leaf position uncertainty.

The effect of finite leaf width on the delivered dose distribution for the two irregular fields was studied. The measured 50% isodose contours from the calibrated radiographic film measurements were plotted overlaying the initial irregular field shape in Figures 3.5 and 3.6. As described previously, the best agreement between field edge and 50% dose contour was found in regions where the direction of leaf motion was perpendicular to the field edge. Regions where the field edge was parallel to the direction of leaf motion suffered cropping or overextension of up to 0.5 cm due to the 1-cm eMLC leaf widths. In regions where the field edge was diagonal to leaf motion, a stair step pattern was introduced to the delivered field, though the pattern was blurred compared with the geometric eMLC aperture

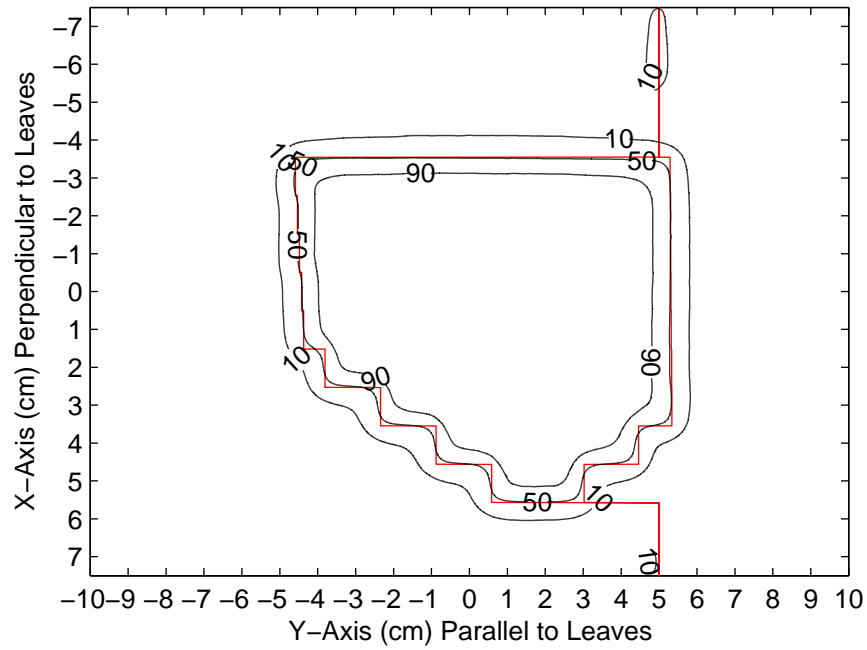


Figure 3.3: Pentagon, irregular field isodose curves overlaying the eMLC aperture at the isocentric plane. Film measurement at 1 cm depth in plastic water phantom, 100 cm SAD.

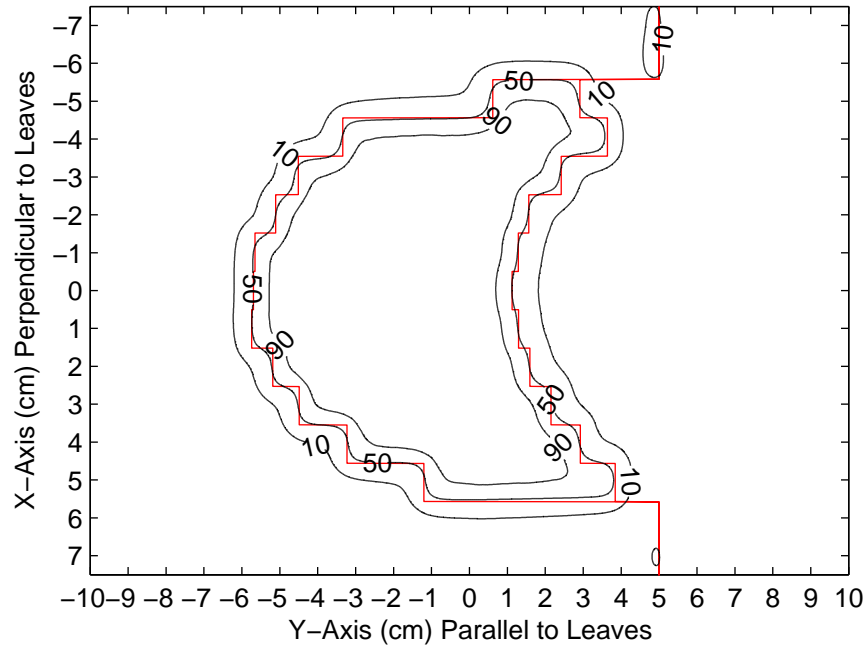


Figure 3.4: Crescent, irregular field isodose curves overlaying the eMLC aperture at the isocentric plane. Film measurement at 1 cm depth in plastic water phantom, 100 cm SAD.

due to multiple Coulomb scattering (MCS) of the electrons. At depths greater than the measured 1 cm depth plane, the stair step effect was expected to become less prominent due to increased MCS; however, the cropped and overextended regions of the field parallel to leaf motion were not expected to improve with depth.

3.1.4 Delivery of Segmented Fields with the eMLC

The radiographic film measurements of segmented fields delivered with the eMLC were converted to planar dose distributions using the calibration data and plotted as isodose contours along with profiles parallel to eMLC leaf motion and profiles along the abutment regions. Figures 3.7, 3.10, and 3.13 show two abutting 20 MeV segments. Compared with Figures 3.8, 3.11, and 3.14, which show abutting 12 MeV segments, the 20 MeV leaf positional uncertainties result in sharper and greater variations in the dose distribution due to imperfect abutment. The broader penumbra of the 12 MeV segments reduces the effect of leaf position uncertainty on the variation of dose in the abutment region and reduces the slope of the lateral dose falloff at the edges of the composite field.

To demonstrate the dose heterogeneity resulting from the abutment of segments of different energies, segmented fields with a 20 MeV segment abutting a 12 MeV segment were delivered to radiographic films. Figures 3.9, 3.12, and 3.15 show a 20 MeV field abutting a 12 MeV field. In all cases, the dose distribution exhibits a peak on the 20 MeV side of the abutment and a trough on the 12 MeV side of the abutment. This was expected and attributed to the sharper lateral dose falloff of the higher energy beam that does not match the more gradual lateral dose falloff of the lower energy beam. The difference in penumbral widths for the different energies is seen at the outer edges of the composite field for the different segments. Additionally, the uncertainty in leaf position gave rise to variations in the dose distribution that appeared to increase with distance from central axis. Figure 3.15 shows the greatest dose hot spot ($x \approx -7.5$ cm, $y \approx -10$ cm) where the abutment is defined by a fully retracted leaf and a fully extended leaf.

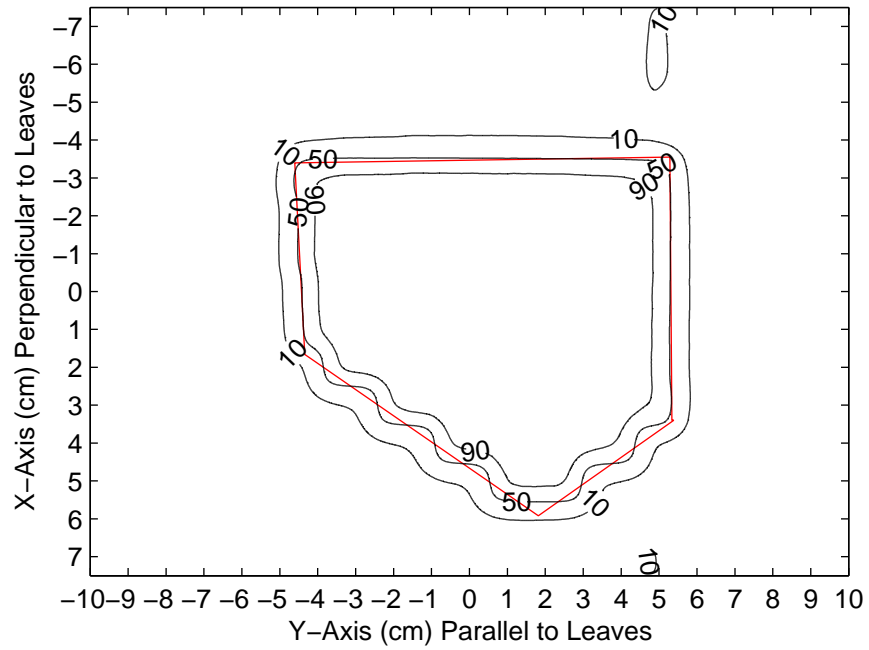


Figure 3.5: Pentagon, irregular field isodose curves overlaying the desired general field at the isocentric plane. Film measurement at 1 cm depth in plastic water phantom, 100 cm SAD.

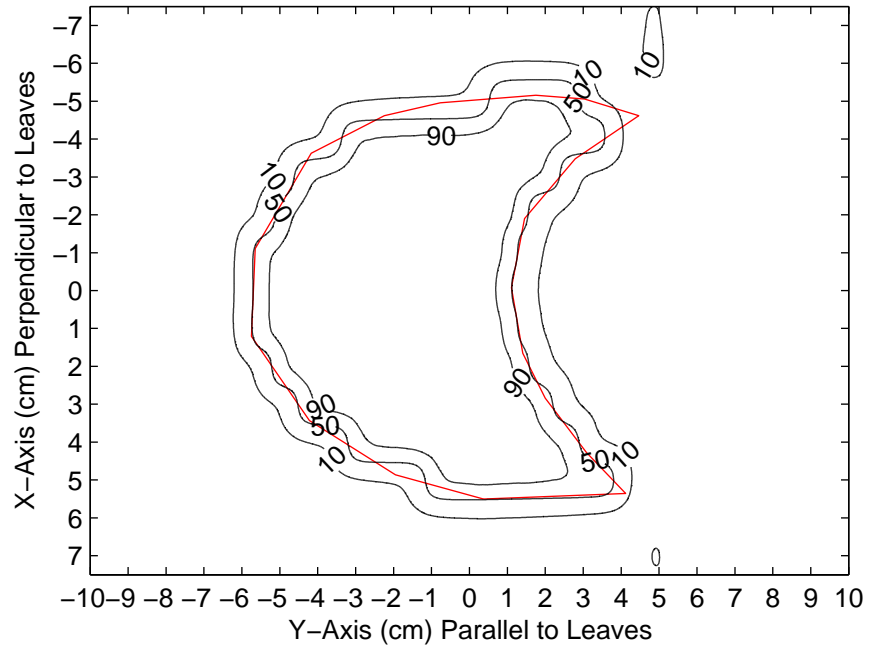
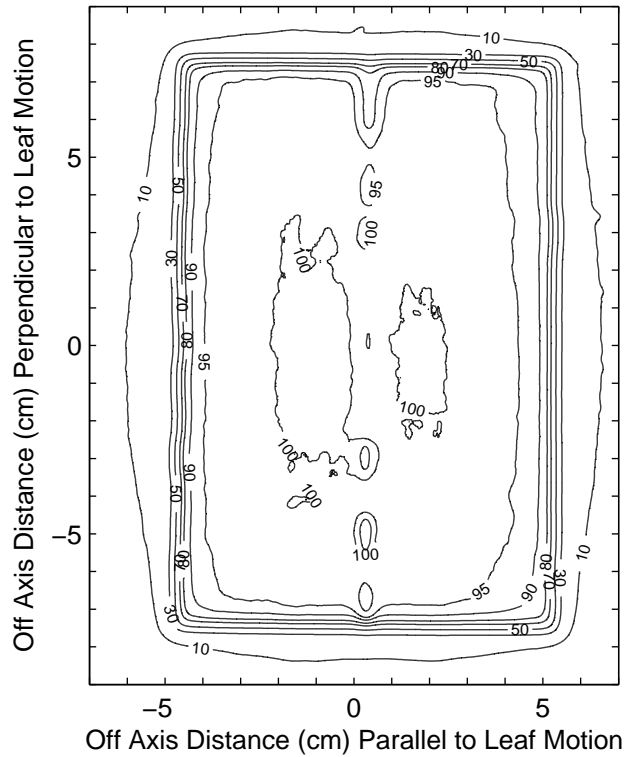
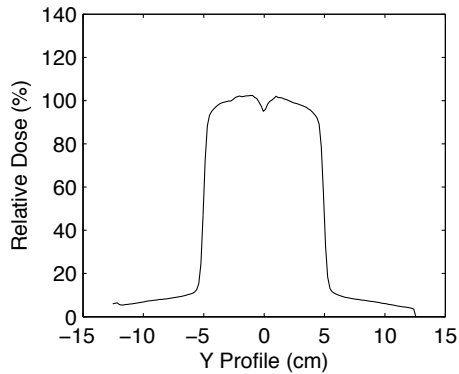


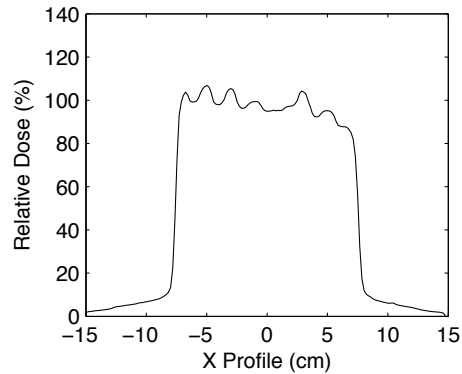
Figure 3.6: Crescent, irregular field isodose curves overlaying the desired general field at the isocentric plane. Film measurement at 1 cm depth in plastic water phantom, 100 cm SAD.



(a)

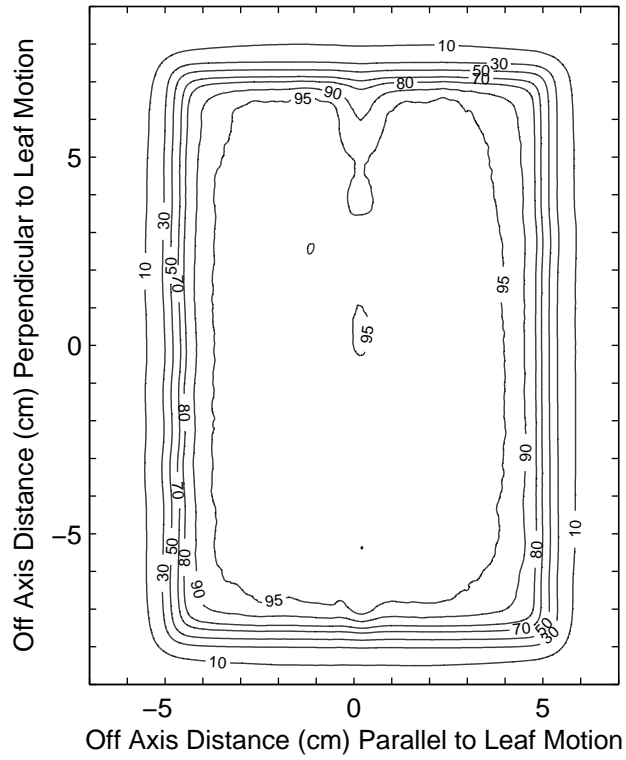


(b)

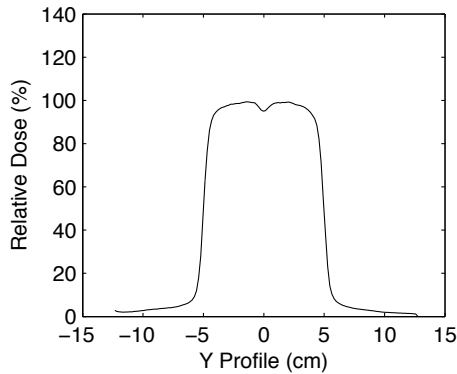


(c)

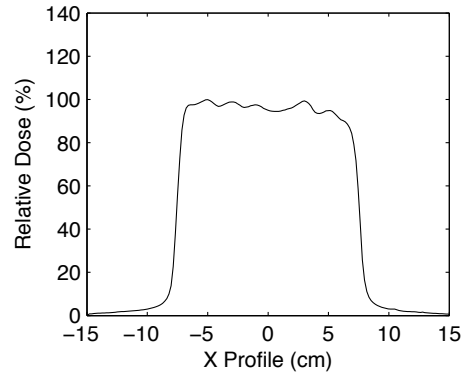
Figure 3.7: Two 20 MeV fields ($15 \times 5 \text{ cm}^2$) abutting on central axis delivered with the eMLC (normalized to 100% at 50 cGy). Film measurement at 1-cm depth in plastic water phantom, 100 cm SAD. Figure 3.7(a) shows the planar dose measured with the film. Figure 3.7(b) shows a y-axis cross profile on central axis. Figure 3.7(c) shows an x-axis cross profile on central axis along the abutment line and reveals the effect of leaf position uncertainty on the abutment region.



(a)

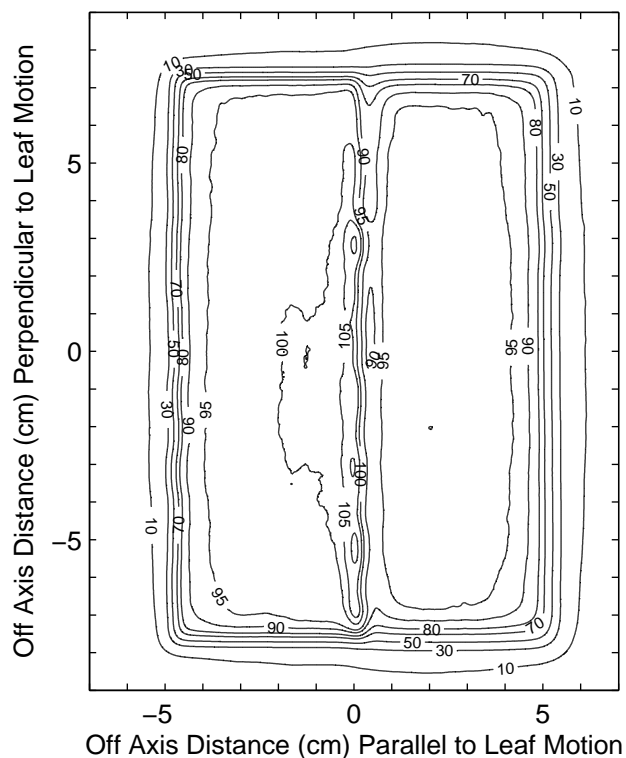


(b)

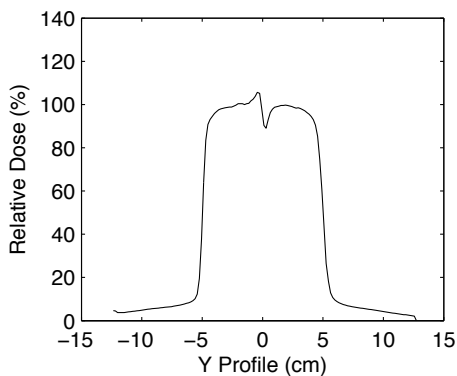


(c)

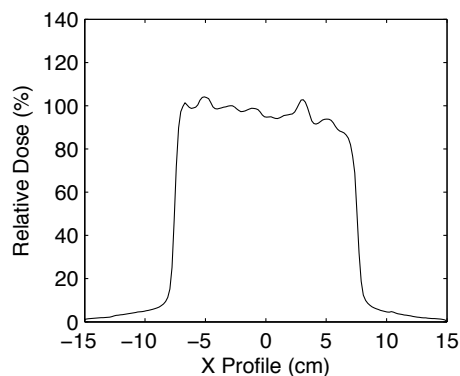
Figure 3.8: Two 12 MeV fields ($15 \times 5 \text{ cm}^2$) abutting on central axis delivered with the eMLC (normalized to 100% at 50 cGy). Film measurement at 1-cm depth in plastic water phantom, 100 cm SAD. Figure 3.8(a) shows the planar dose measured with the film. Figure 3.8(b) shows a y-axis cross profile on central axis. Figure 3.8(c) shows an x-axis cross profile on central axis along the abutment line and reveals the effect of leaf position uncertainty on the abutment region.



(a)

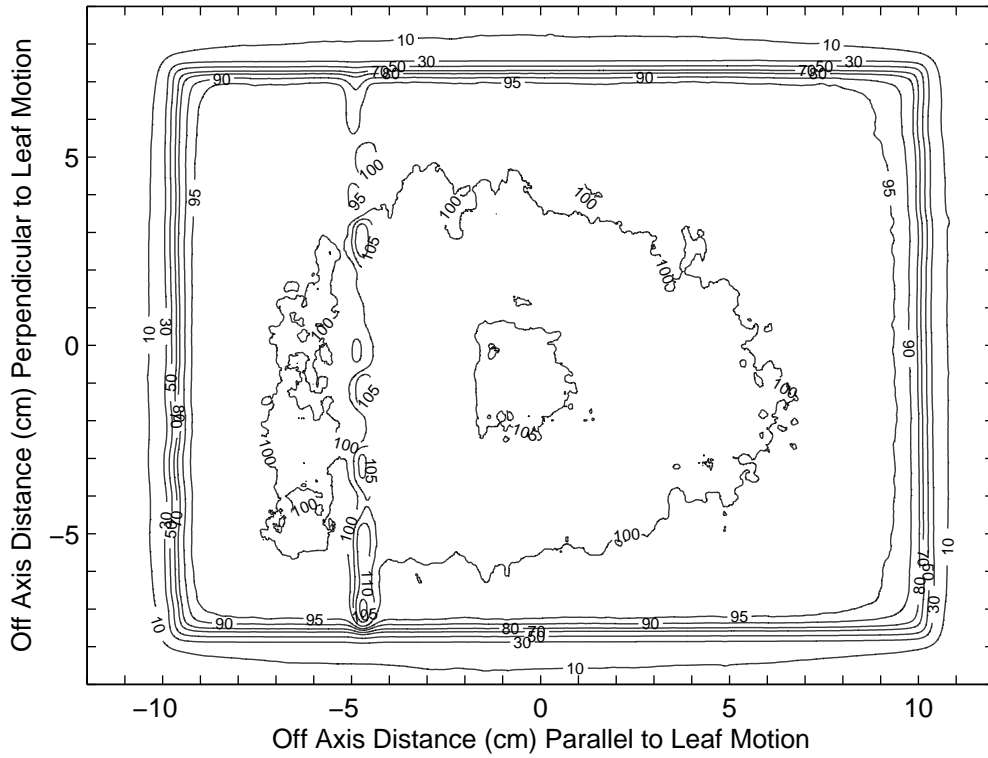


(b)

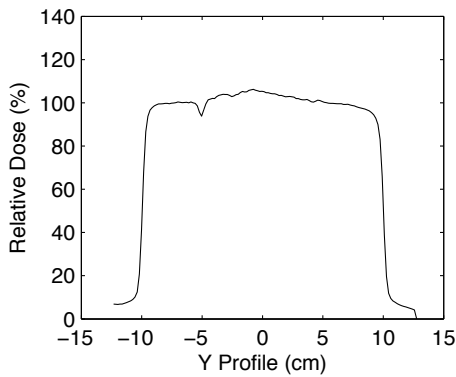


(c)

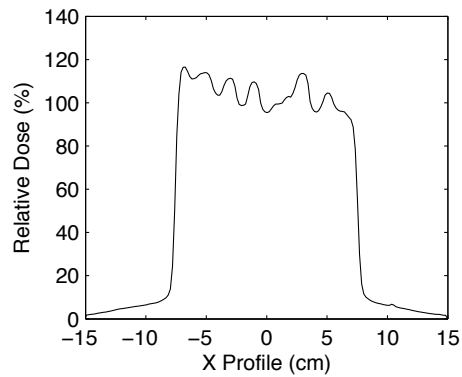
Figure 3.9: 20 MeV field abutting a 12 MeV field (each $15 \times 5 \text{ cm}^2$) on central axis delivered with the eMLC (normalized to 100% at 50 cGy). Film measurement at 1-cm depth in plastic water phantom, 100 cm SAD. Figure 3.9(a) shows the planar dose measured with the film. Figure 3.9(b) shows a y-axis cross profile on central axis and indicates the effect of abutting beams of differing energy. Figure 3.9(c) shows an x-axis cross profile on central axis along the abutment line and reveals the effect of leaf position uncertainty on the abutment region.



(a)

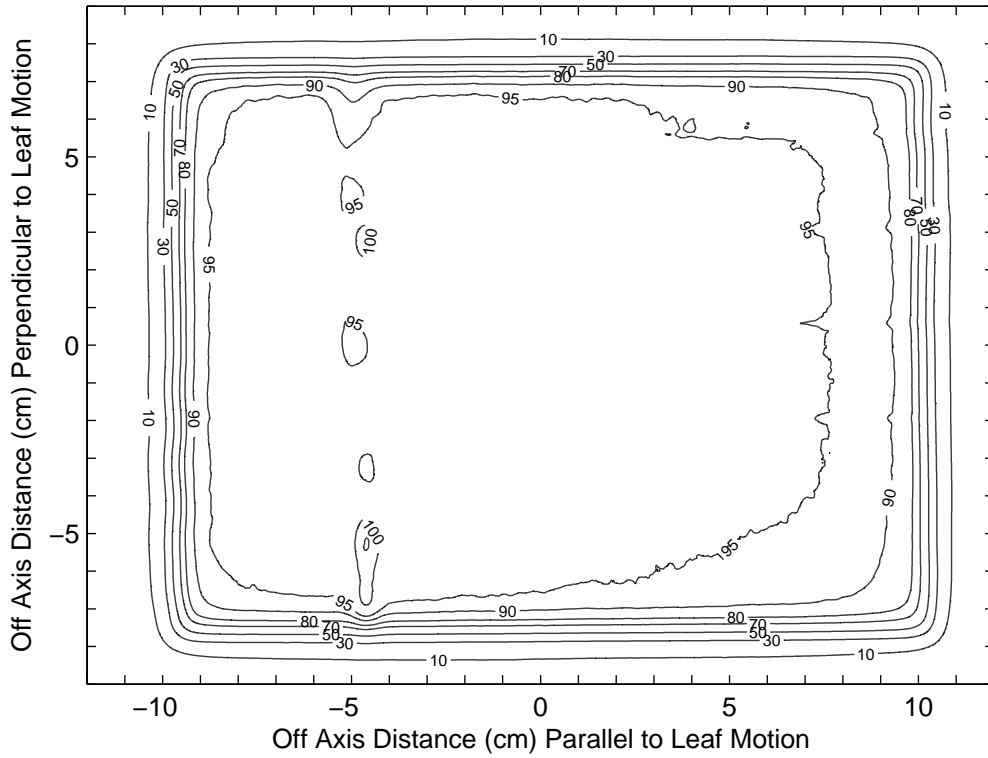


(b)

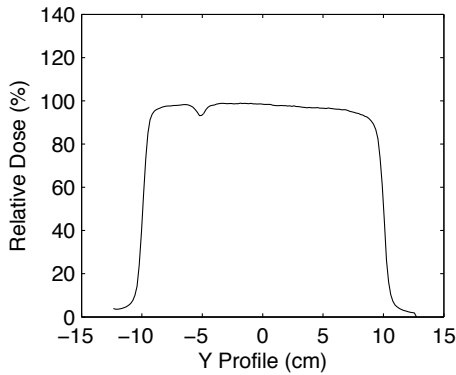


(c)

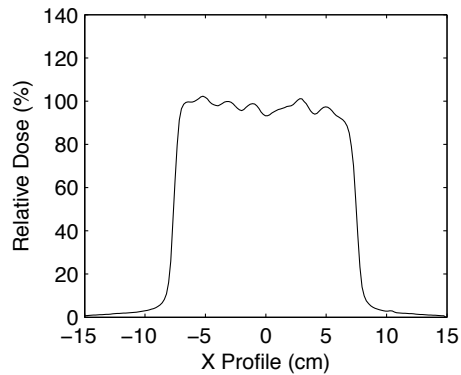
Figure 3.10: Two 20 MeV fields (15×5 and 15×15 cm²) abutting 5 cm off central axis delivered with the eMLC (normalized to 100% at 50 cGy). Film measurement at 1-cm depth in plastic water phantom, 100 cm SAD. Figure 3.10(a) shows the planar dose measured with the film. Figure 3.10(b) shows a y-axis cross profile on central axis. Figure 3.10(c) shows an x-axis cross profile -5 cm off central axis along the abutment line and reveals the effect of leaf position uncertainty on the abutment region.



(a)

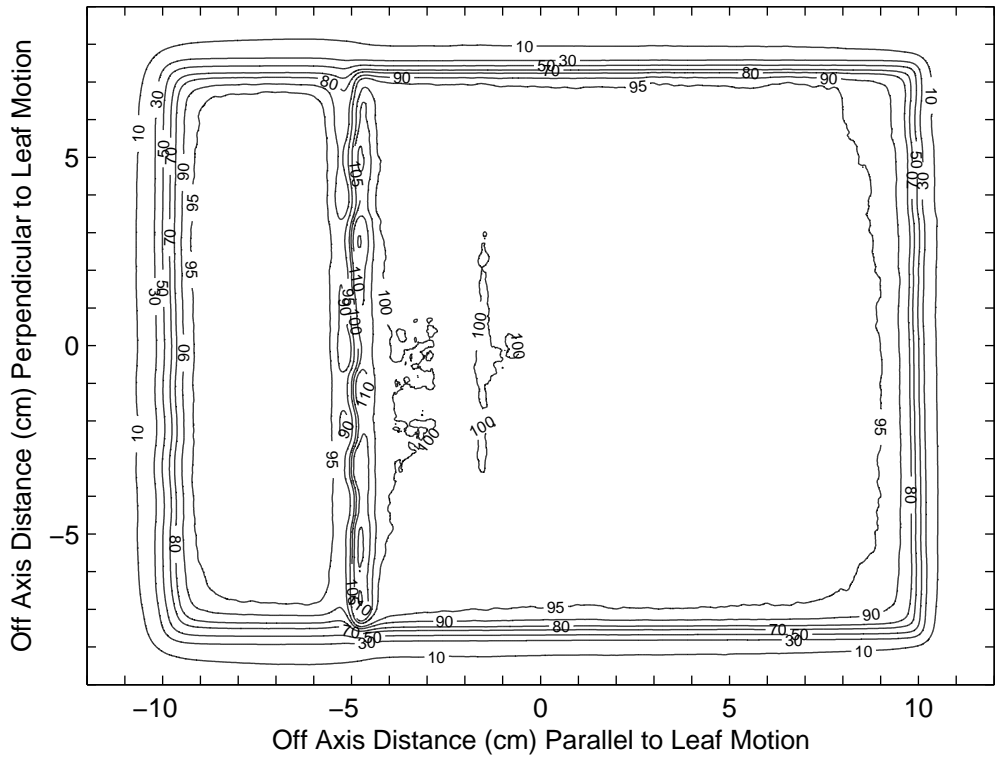


(b)

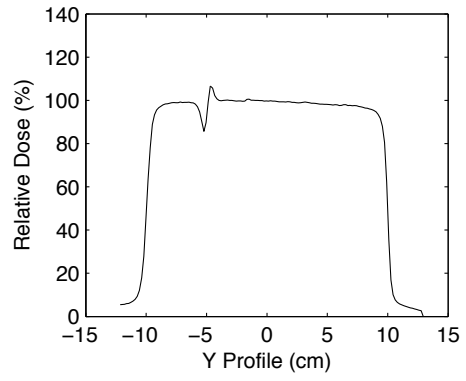


(c)

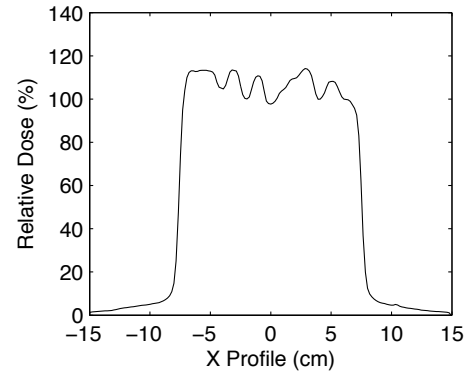
Figure 3.11: Two 12 MeV fields (15×5 and 15×15 cm²) abutting 5 cm off central axis delivered with the eMLC (normalized to 100% at 50 cGy). Film measurement at 1-cm depth in plastic water phantom, 100 cm SAD. Figure 3.11(a) shows the planar dose measured with the film. Figure 3.11(b) shows a y-axis cross profile on central axis. Figure 3.11(c) shows an x-axis cross profile -5 cm off central axis along the abutment line and reveals the effect of leaf position uncertainty on the abutment region.



(a)

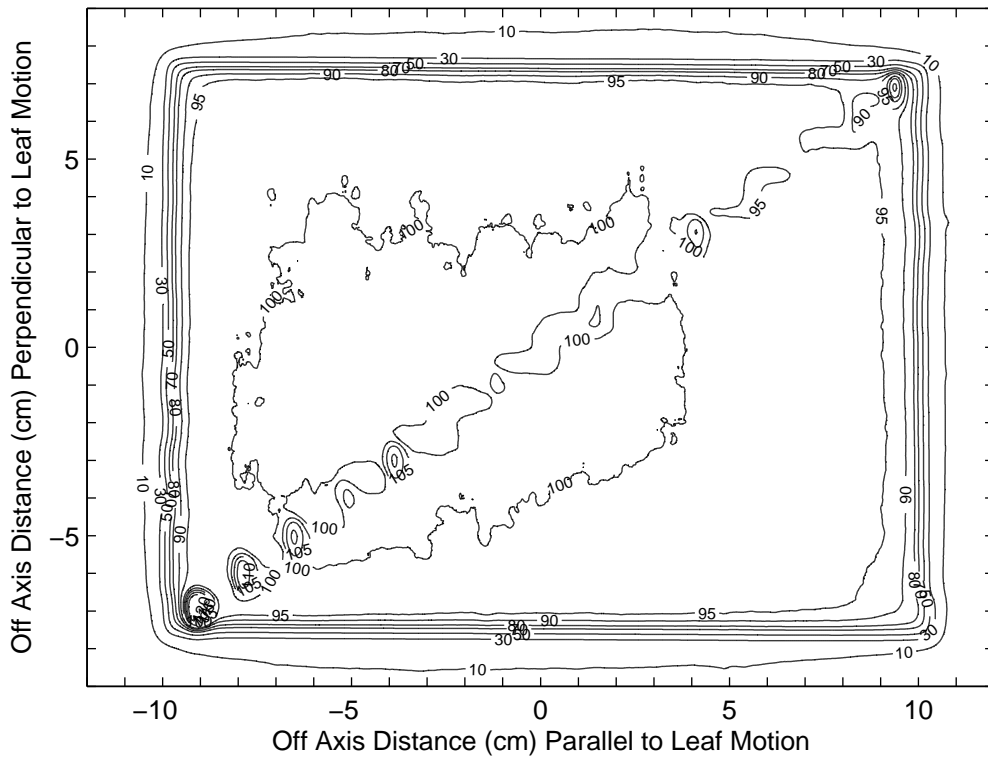


(b)

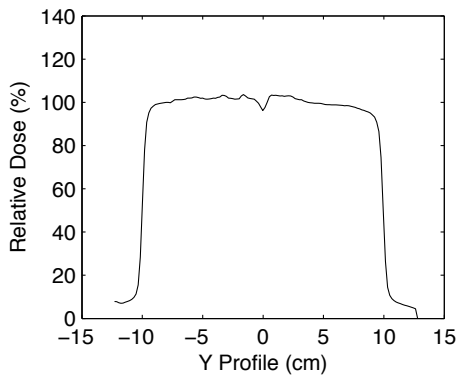


(c)

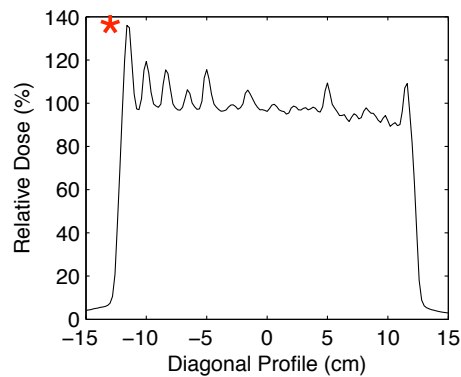
Figure 3.12: 12 MeV field ($15 \times 5 \text{ cm}^2$) abutting a 20 MeV field ($15 \times 15 \text{ cm}^2$) 5 cm off central axis delivered with the eMLC (normalized to 100% at 50 cGy). Film measurement at 1-cm depth in plastic water phantom, 100 cm SAD. Figure 3.12(a) shows the planar dose measured with the film. Figure 3.12(b) shows a y-axis cross profile on central axis and indicates the effect of abutting beams of differing energy. Figure 3.12(c) shows an x-axis cross profile -5 cm off central axis along the abutment line and reveals the effect of leaf position uncertainty on the abutment region.



(a)

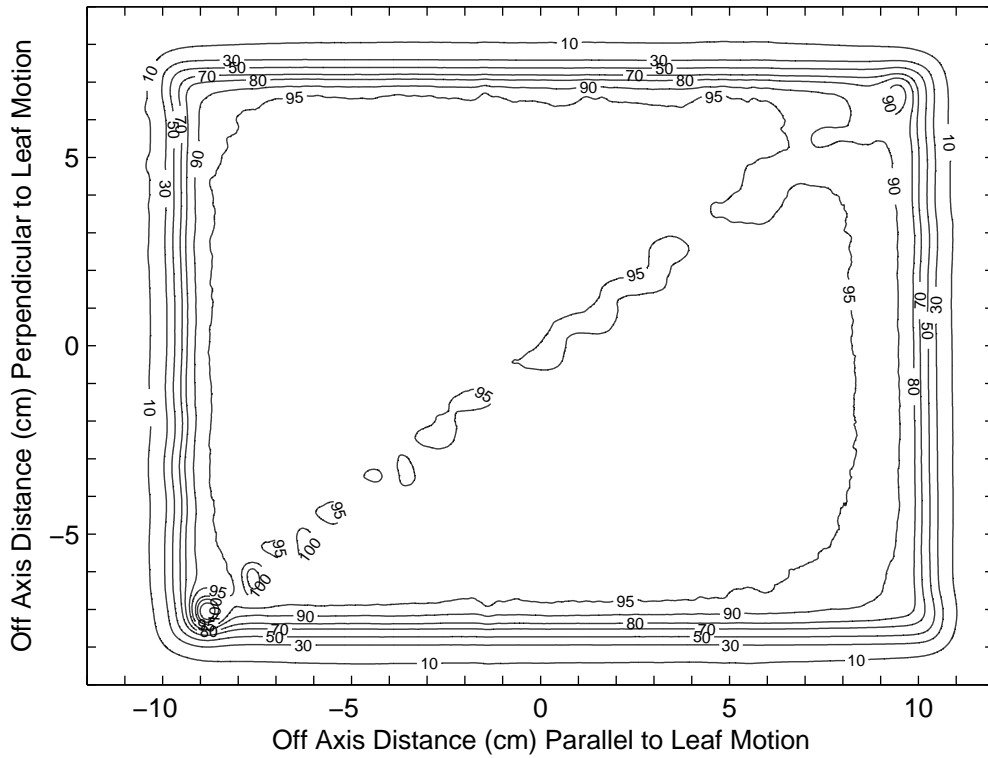


(b)

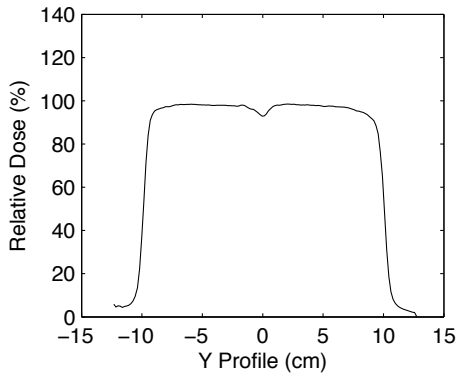


(c)

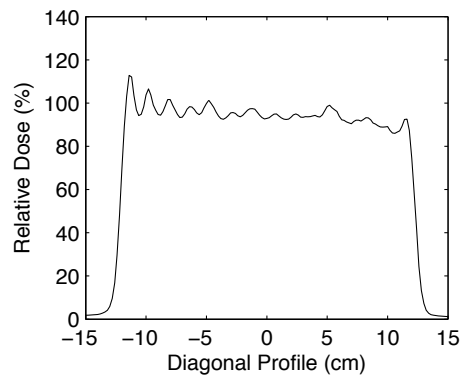
Figure 3.13: Two 20 MeV fields abutting diagonally delivered with the eMLC (normalized to 100% at 50 cGy). Film measurement at 1-cm depth in plastic water phantom, 100 cm SAD. Composite field size $15 \times 20 \text{ cm}^2$. Figure 3.13(a) shows the planar dose measured with the film. Figure 3.13(b) shows a y-axis cross profile on central axis. Figure 3.13(c) shows a diagonal cross profile along the abutment line and reveals the effects of leaf position uncertainty and leaf width on the abutment region. The red asterisk in Figure 3.13(c) indicates that the maximum film calibration dose was 68 cGy, measured doses above 68 cGy were clipped, and the dose value at the peak near the asterisk was likely higher than 68 cGy (136%) but was unknown.



(a)

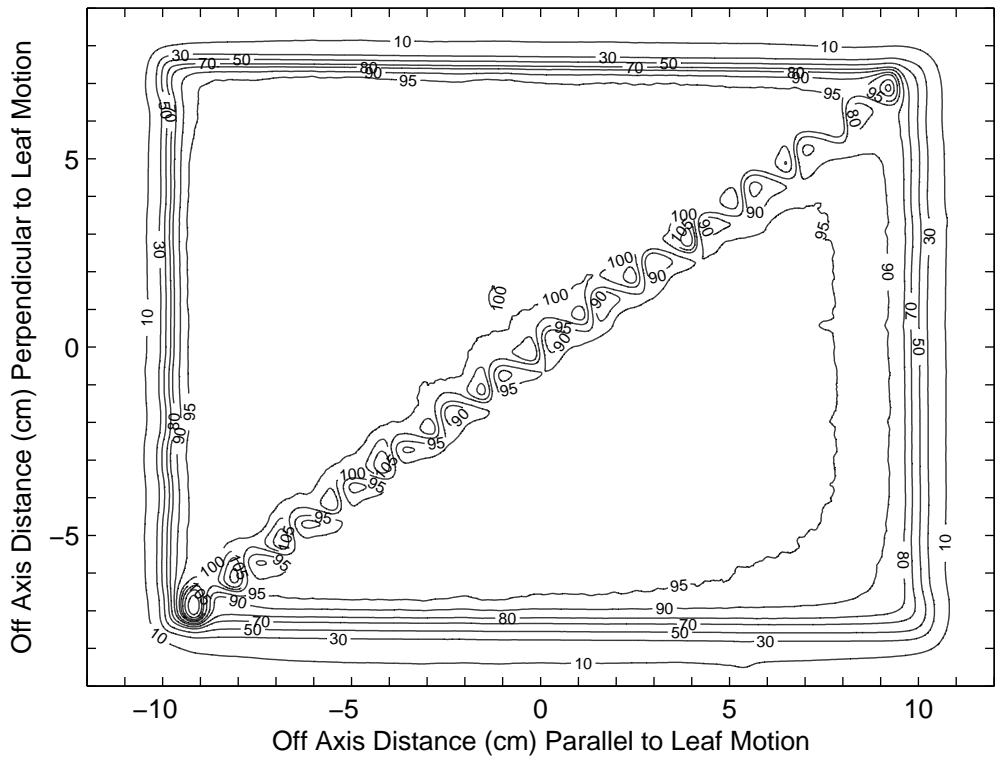


(b)

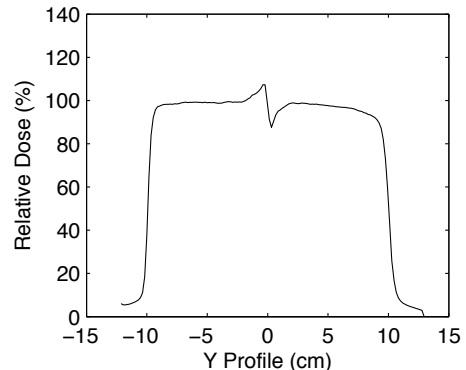


(c)

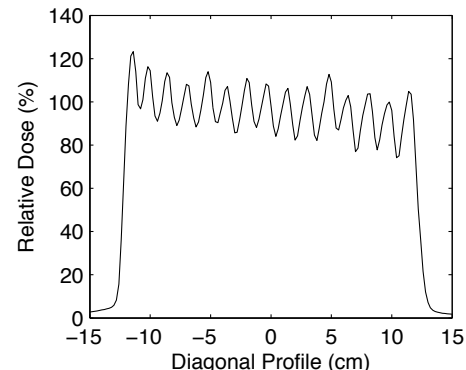
Figure 3.14: Two 12 MeV fields abutting diagonally delivered with the eMLC (normalized to 100% at 50 cGy). Film measurement at 1-cm depth in plastic water phantom, 100 cm SAD. Composite field size 15×20 cm². Figure 3.14(a) shows the planar dose measured with the film. Figure 3.14(b) shows a y-axis cross profile on central axis. Figure 3.14(c) shows a diagonal cross profile along the abutment line and reveals the effects of leaf position uncertainty and leaf width on the abutment region.



(a)



(b)



(c)

Figure 3.15: 20 MeV field abutting a 12 MeV field diagonally delivered with the eMLC (normalized to 100% at 50 cGy). Film measurement at 1-cm depth in plastic water phantom, 100 cm SAD. Composite field size $15 \times 20 \text{ cm}^2$. Figure 3.15(a) shows the planar dose measured with the film. Figure 3.15(b) shows a y-axis cross profile on central axis and indicates the effect of abutting beams of differing energy. Figure 3.15(c) shows a diagonal cross profile along the abutment line and reveals the effects of leaf position uncertainty and leaf width on the abutment region.

3.2 Aim 2: Commission the eMLC for Dose Computation

3.2.1 Measured Electron Beam Data for Pencil Beam Algorithm

Central Axis Depth Dose Data

Figures 3.16, 3.18, 3.20, 3.22, and 3.24 show field-size dependence of the depth-dose commissioning data input into the Pinnacle treatment planning system electron beam models for the 6, 9, 12, 16, and 20 MeV beams, respectively. The measured data show the therapeutic range of the electron beam increases with field size as the field approaches side scatter equilibrium. The $(1\times 1, 2\times 2, \text{ and } 20\times 20)\text{cm}^2$ field data have been theoretically determined with the square root method described in Section 2.2.1. Agreement of the $3\times 3\text{ cm}^2$ computed depth doses with the $3\times 3\text{ cm}^2$ measured depth dose shown in Figures 3.17, 3.19, 3.21, 3.23, and 3.25 for the 6, 9, 12, 16, and 20 MeV beam, respectively, validates the accuracy ($\pm 1\%$) of this method.

Absolute Output Measurements

Tables 3.2.1, 3.2.1, 3.2.1, 3.2.1, and 3.2.1 contain the output measurements input into the Pinnacle treatment planning system electron beam models for the $11\times 11\text{ cm}^2$ reference fields. The output was measured at R_{100} in the water phantom at 100 cm SSD. Output is tuned to 1 cGy/MU for the reference field ($10\times 10\text{ cm}^2$ open applicator at 100 cm SSD at R_{100} in the water phantom). The absolute output values differ slightly from 1 cGy/MU and were input to match the eMLC $11\times 11\text{ cm}^2$ reference fields.

Output Factor Measurements

Figures 3.26, 3.27, 3.28, 3.29, and 3.30 show the energy, field-size, and SSD dependent output factor commissioning data input into the Pinnacle treatment planning system beam models. The field-size dependent data show the relative output increasing with field size as the field approaches side scatter equilibrium. Output factor data for square fields with side lengths (1, 2, and 20) cm were theoretically determined with the square root method described in Section 2.2.1.

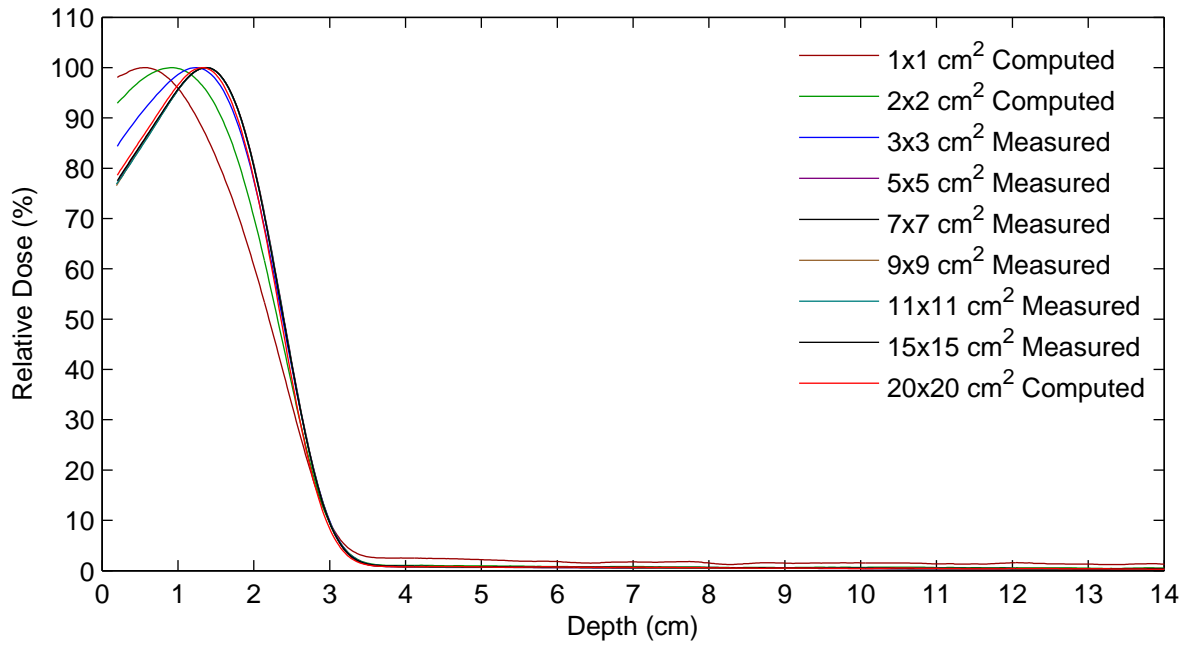


Figure 3.16: 6 MeV central axis depth dose curves. Commissioning data input into Pinnacle treatment planning system.

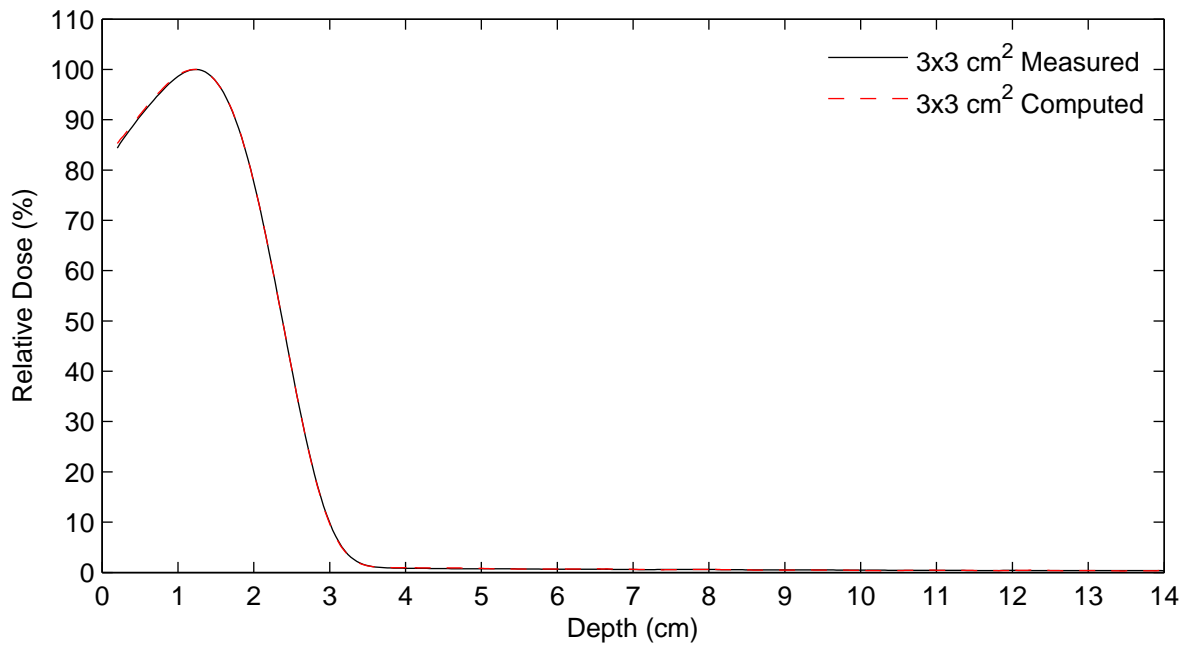


Figure 3.17: 6 MeV, $3 \times 3 \text{ cm}^2$ PDD, computed with the square root method, compared with a measured $3 \times 3 \text{ cm}^2$ PDD.

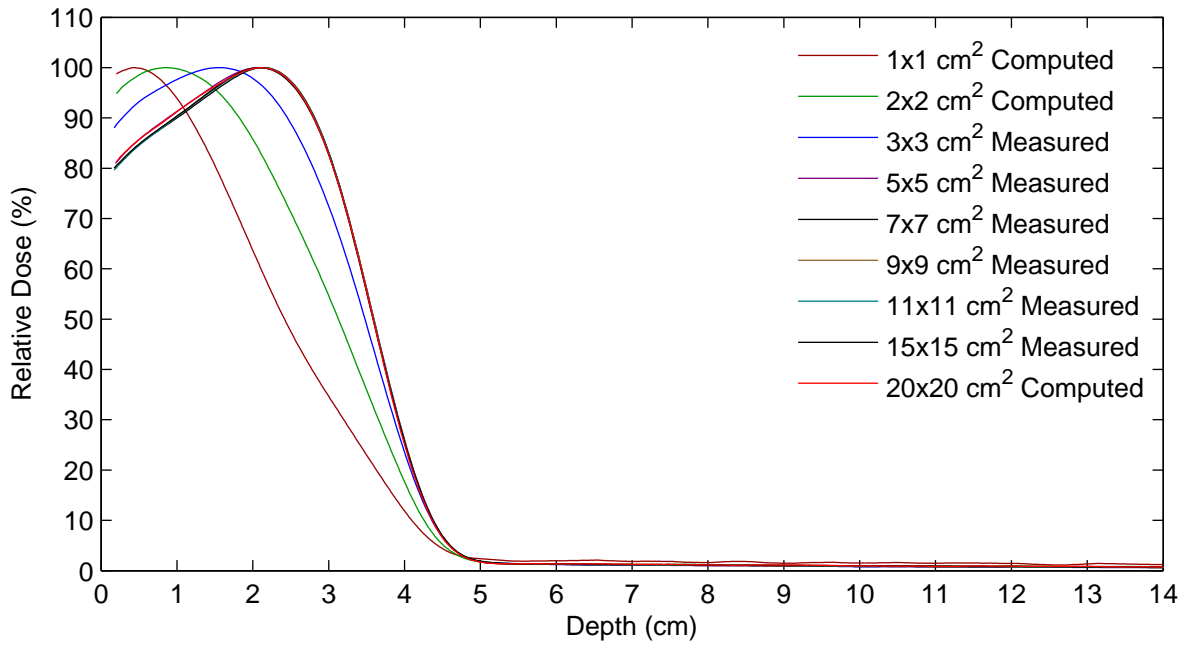


Figure 3.18: 9 MeV central axis depth dose curves. Commissioning data input into Pinnacle treatment planning system.

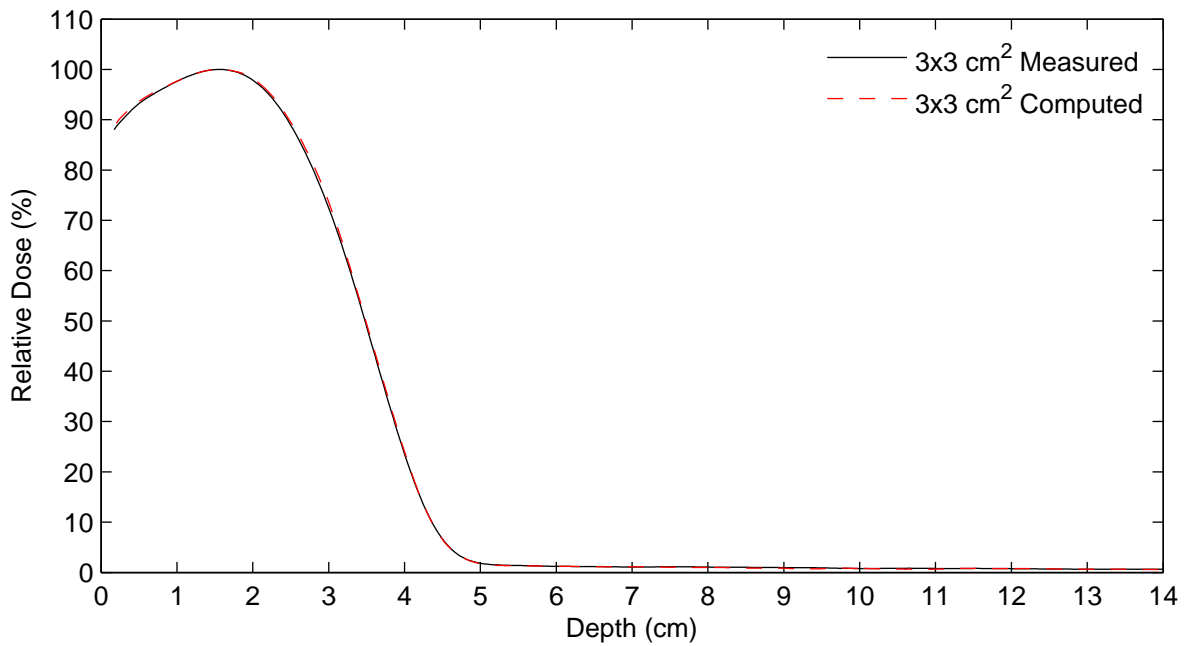


Figure 3.19: 9 MeV, 3×3 cm² PDD, computed with the square root method, compared with a measured 3×3 cm² PDD.

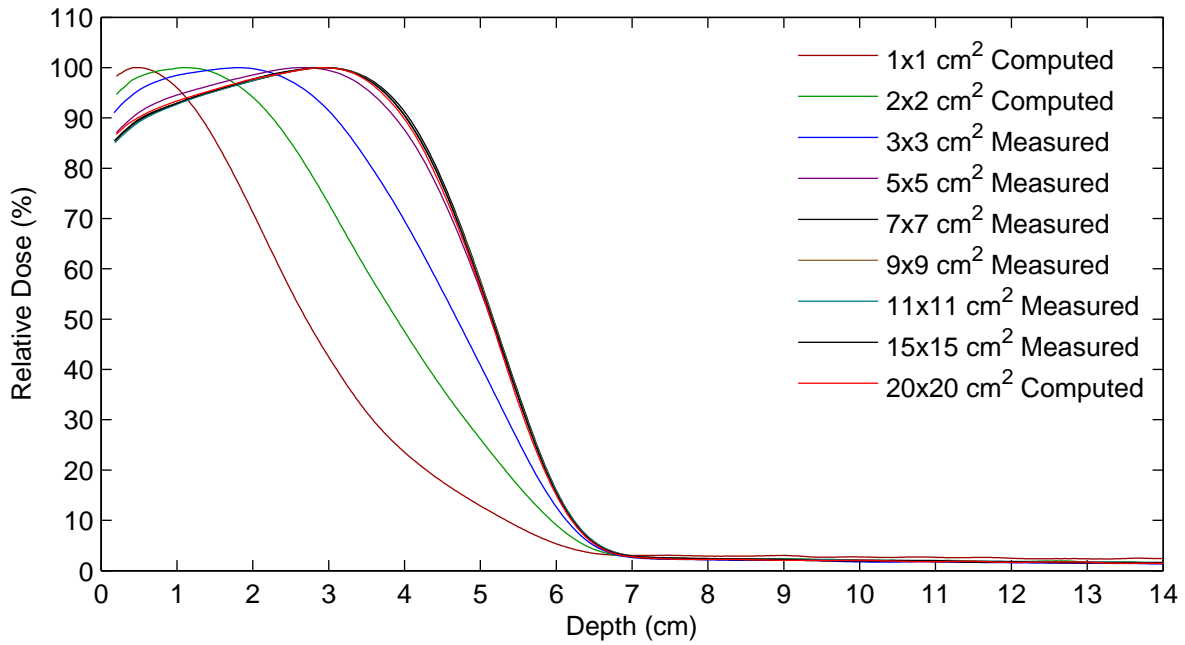


Figure 3.20: 12 MeV central axis depth dose curves. Commissioning data input into Pinnacle treatment planning system.

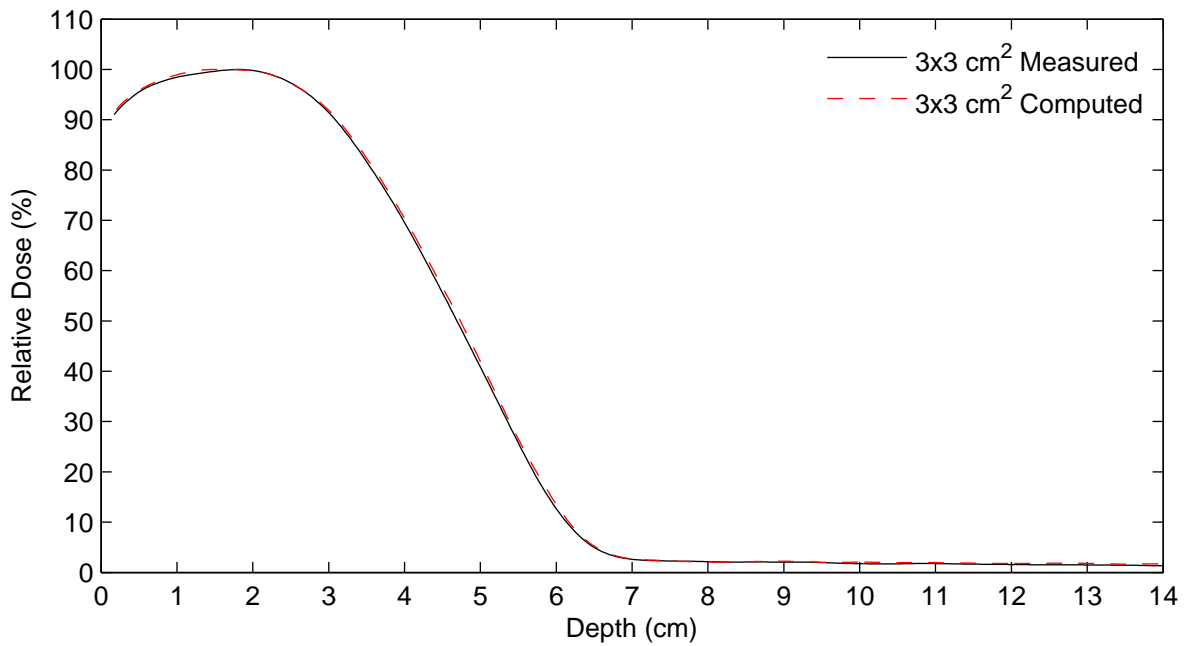


Figure 3.21: 12 MeV, 3×3 cm² PDD, computed with the square root method, compared with a measured 3×3 cm² PDD.

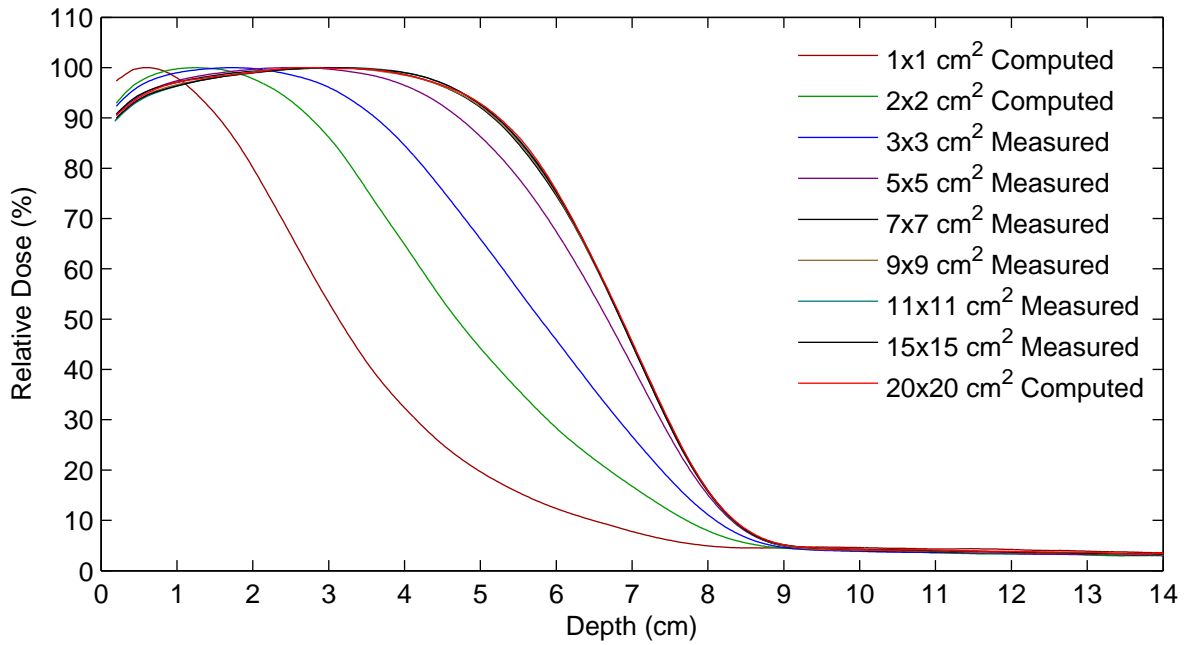


Figure 3.22: 16 MeV central axis depth dose curves. Commissioning data input into Pinnacle treatment planning system.

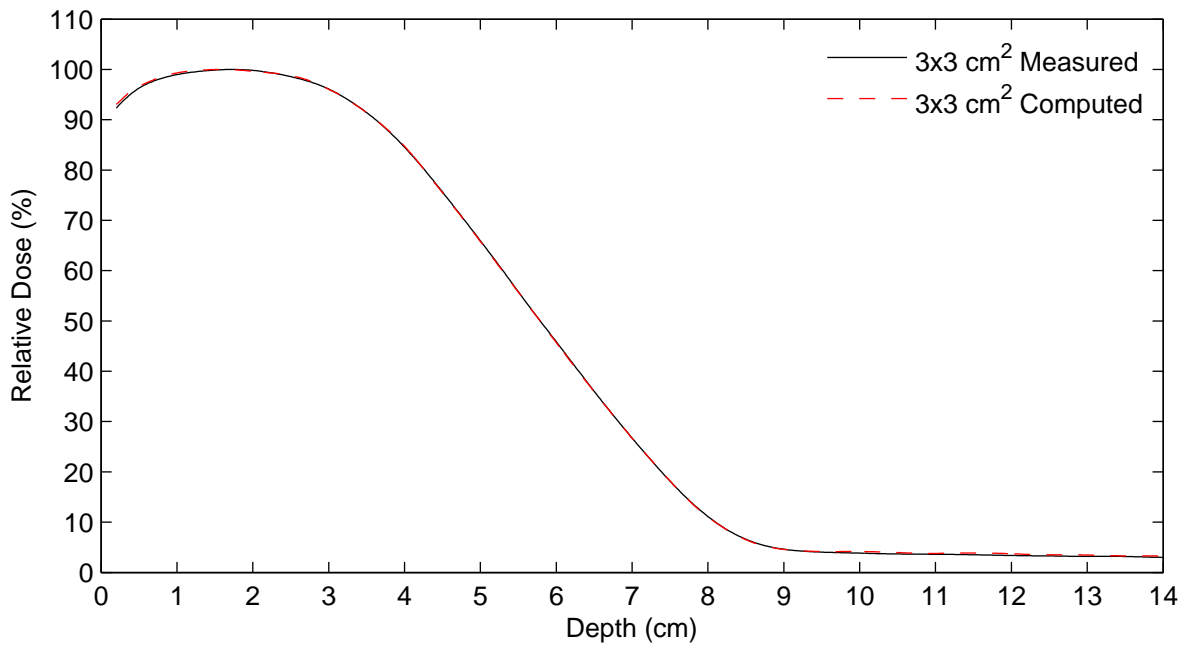


Figure 3.23: 16 MeV, 3×3 cm² PDD, computed with the square root method, compared with a measured 3×3 cm² PDD.

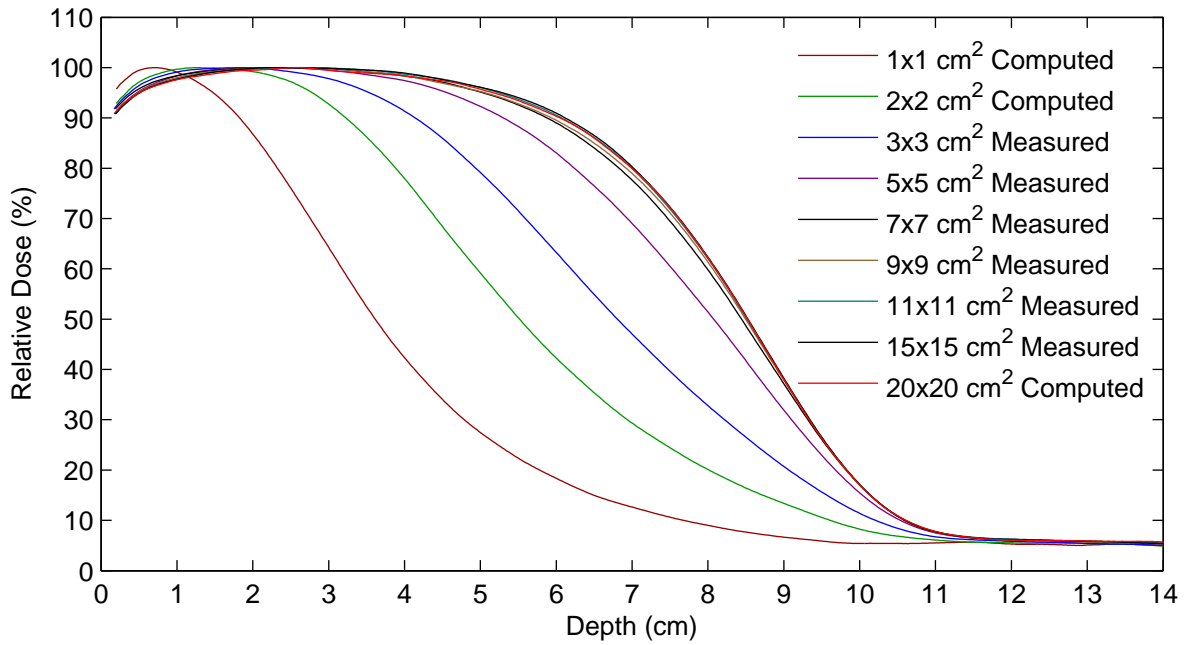


Figure 3.24: 20 MeV central axis depth dose curves. Commissioning data input into Pinnacle treatment planning system.

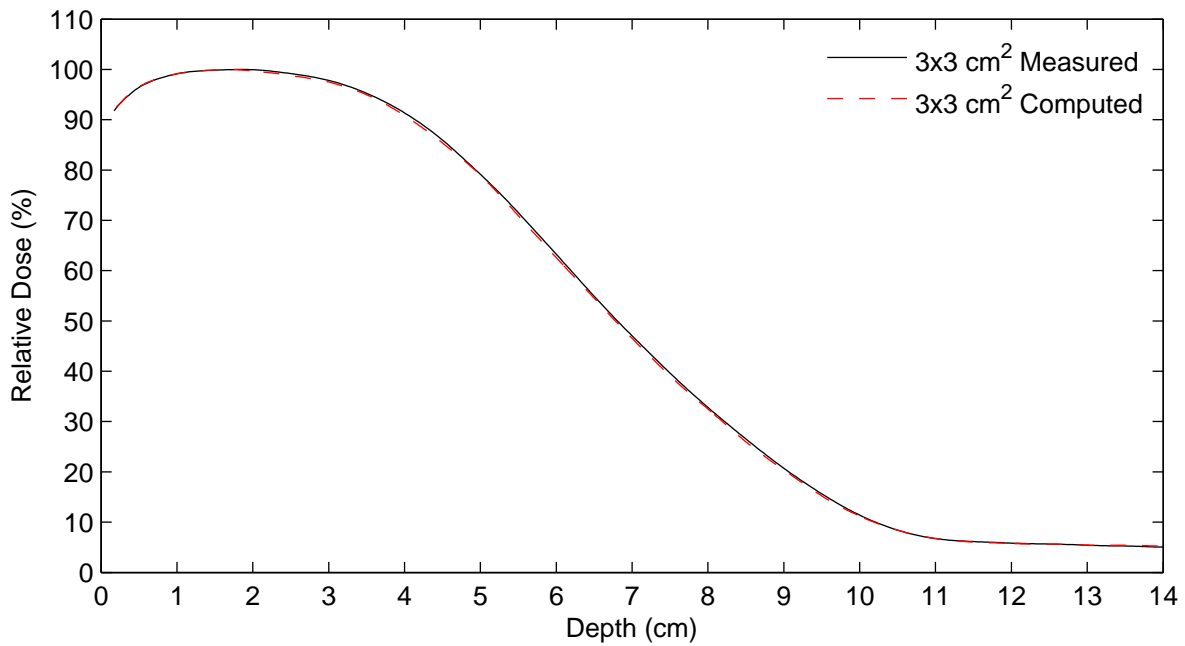


Figure 3.25: 20 MeV, 3×3 cm² PDD, computed with the square root method, compared with a measured 3×3 cm² PDD.

Table 3.4: 6 MeV comparison of measured output data with Pinnacle computed output data. Percent difference = $100\% \times (\text{computed} - \text{measured}) / \text{measured}$.

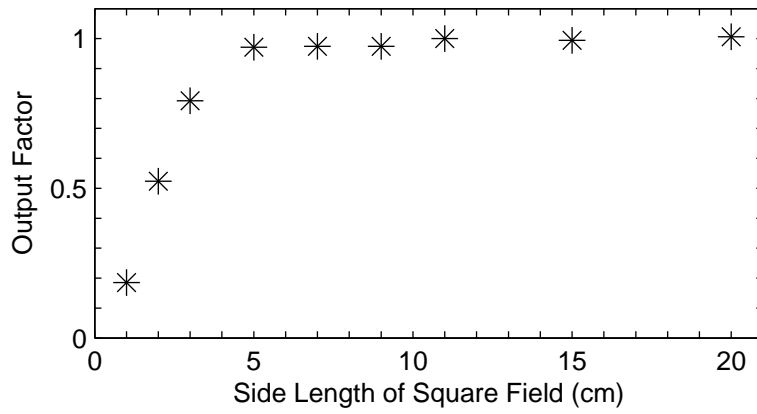
Field Size (cm ²)	Meas. Output (cGy/MU)	Comp. Output (cGy/MU)	% Difference (%)
1×1	0.194	0.218	12.5
2×2	0.549	0.542	-1.2
3×3	0.829	0.817	-1.5
5×5	1.017	1.014	-0.3
7×7	1.020	1.018	-0.2
9×9	1.020	1.022	0.2
11×11	1.047	1.048	0.1
15×15	1.041	1.039	-0.2
20×20	1.053	1.053	0.0

Table 3.5: 9 MeV comparison of measured output data with Pinnacle computed output data. Percent difference = $100\% \times (\text{computed} - \text{measured}) / \text{measured}$.

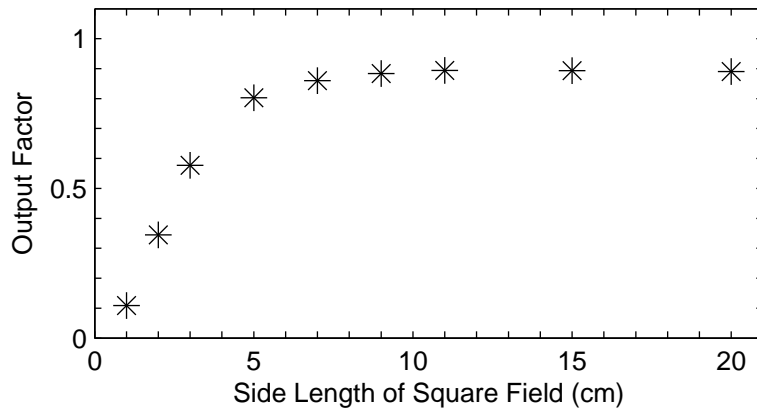
Field Size (cm ²)	Meas. Output (cGy/MU)	Comp. Output (cGy/MU)	% Difference (%)
1×1	0.303	0.322	6.3
2×2	0.627	0.615	-1.9
3×3	0.840	0.830	-1.1
5×5	0.968	0.968	0.0
7×7	0.979	0.979	0.0
9×9	1.001	1.003	0.2
11×11	1.003	1.005	0.2
15×15	0.998	1.000	0.2
20×20	0.998	0.999	0.1

Validation of Treatment Planning System Output Calculations

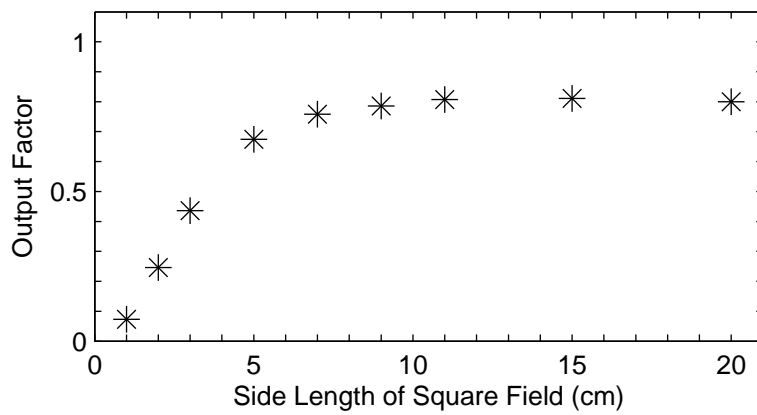
Tables 3.2.1, 3.2.1, 3.2.1, 3.2.1, and 3.2.1 contain the measured output data used for commissioning the dose algorithm and the output data computed in the treatment planning system to validate the correct implementation of the data for calculations on a water phantom.



(a)

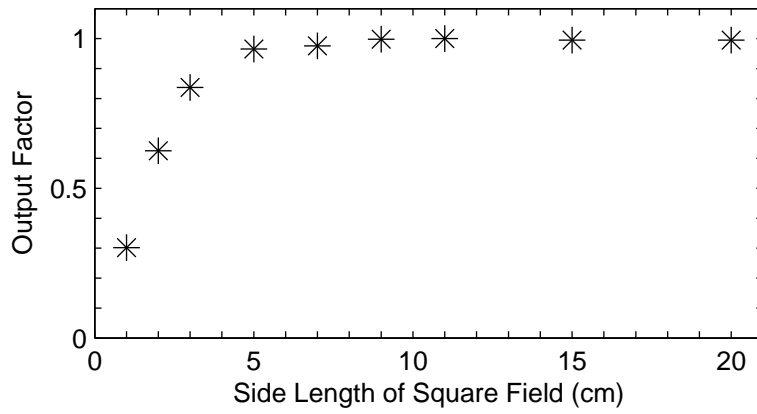


(b)

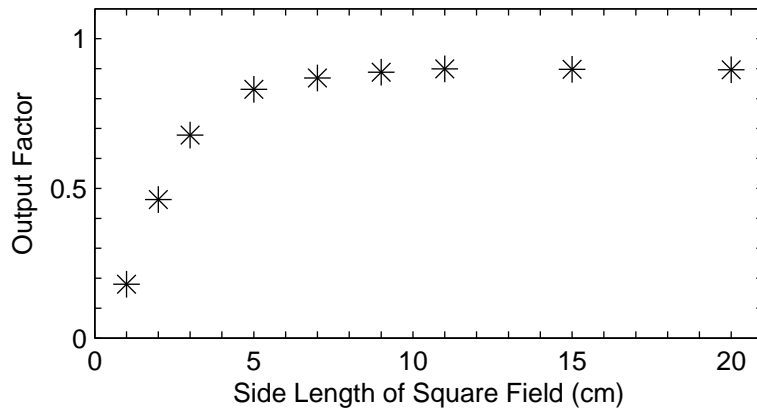


(c)

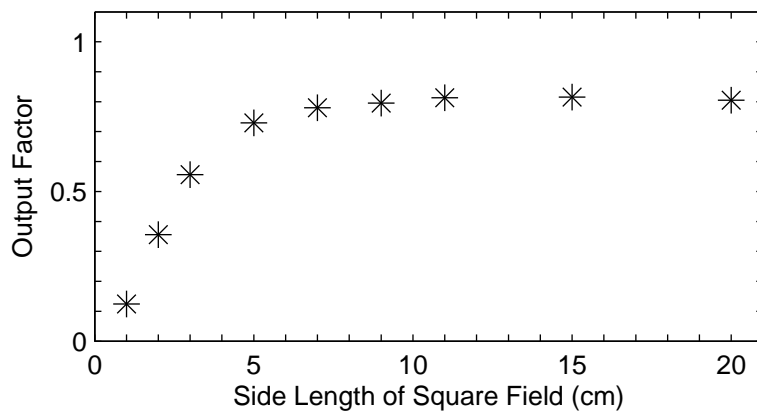
Figure 3.26: 6 MeV output factors vs. field size at 3.26(a) 100 cm SSD, 3.26(b) 105 cm SSD, and 3.26(c) 110 cm SSD.



(a)

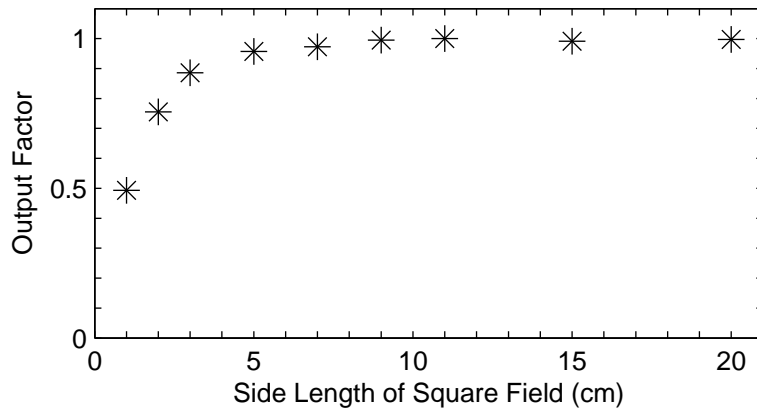


(b)

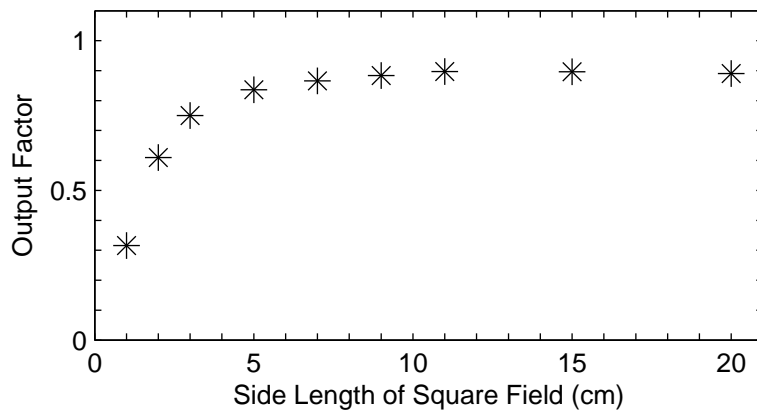


(c)

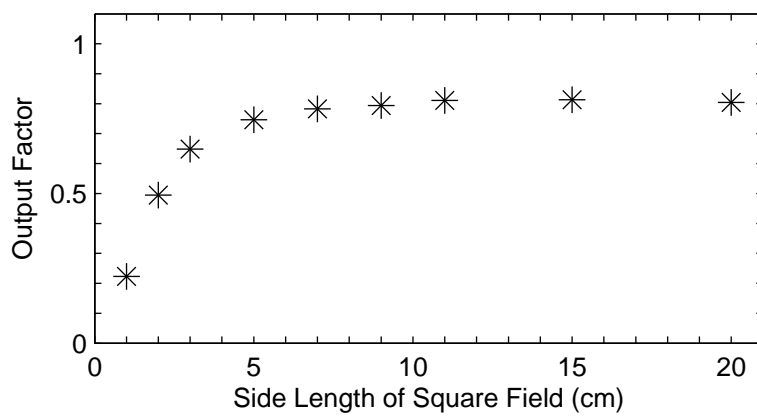
Figure 3.27: 9 MeV output factors vs. field size at 3.27(a) 100 cm SSD, 3.27(b) 105 cm SSD, and 3.27(c) 110 cm SSD.



(a)

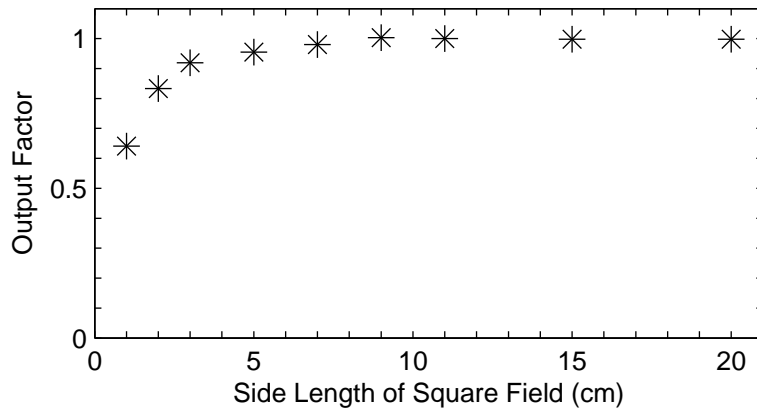


(b)

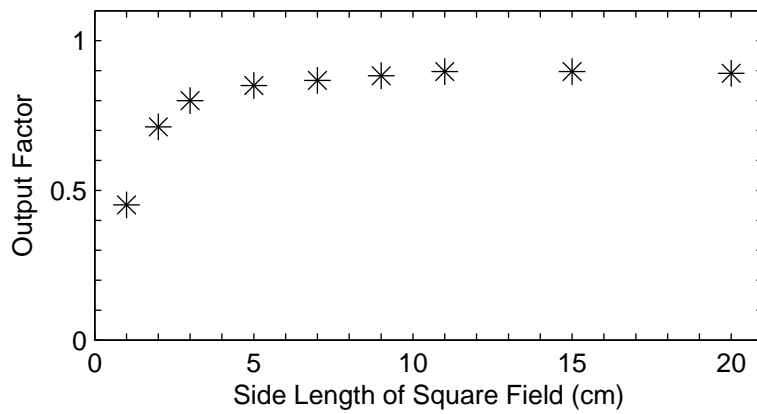


(c)

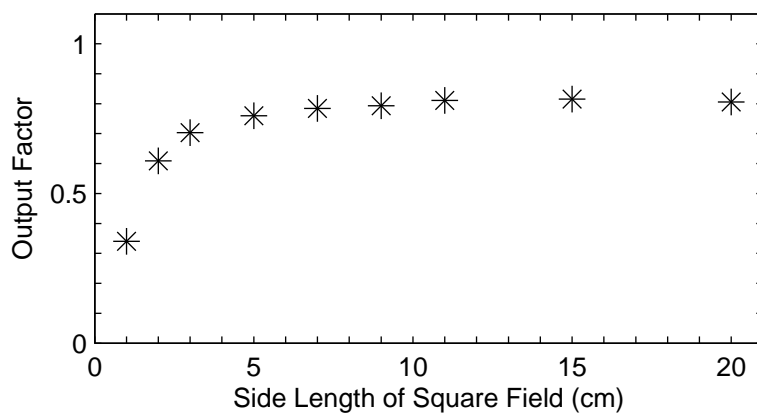
Figure 3.28: 12 MeV output factors vs. field size at 3.28(a) 100 cm SSD, 3.28(b) 105 cm SSD, and 3.28(c) 110 cm SSD.



(a)

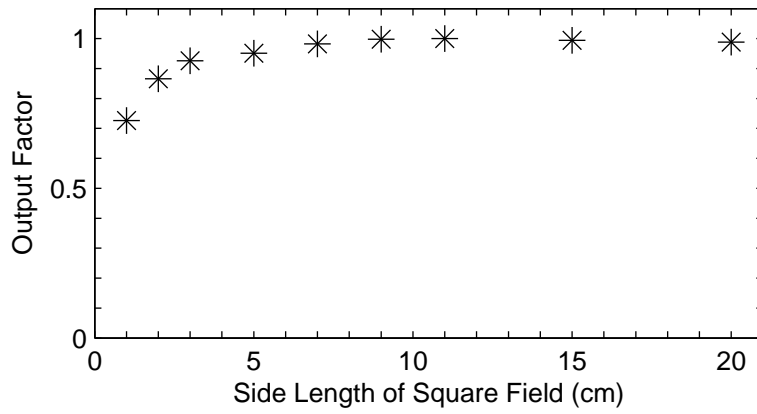


(b)

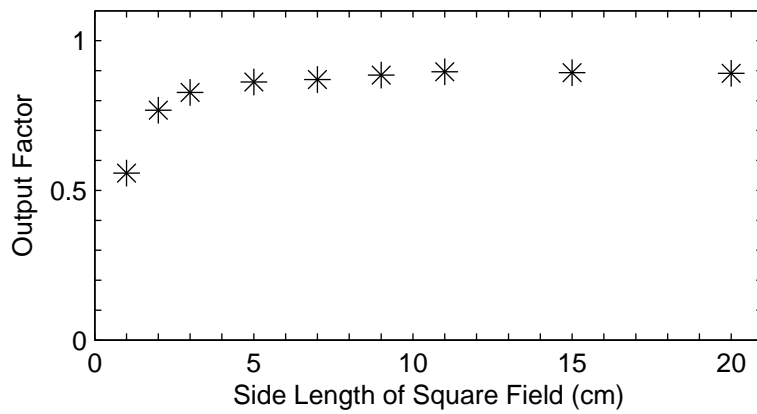


(c)

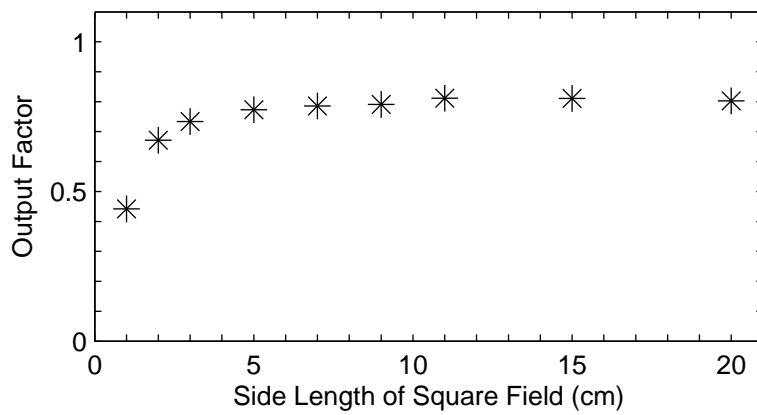
Figure 3.29: 16 MeV output factors vs. field size at 3.29(a) 100 cm SSD, 3.29(b) 105 cm SSD, and 3.29(c) 110 cm SSD.



(a)



(b)



(c)

Figure 3.30: 20 MeV output factors vs. field size at 3.30(a) 100 cm SSD, 3.30(b) 105 cm SSD, and 3.30(c) 110 cm SSD.

Table 3.6: 12 MeV comparison of measured output data with Pinnacle computed output data. Percent difference = $100\% \times (\text{computed} - \text{measured}) / \text{measured}$.

Field Size (cm ²)	Meas. Output (cGy/MU)	Comp. Output (cGy/MU)	% Difference (%)
1×1	0.488	0.490	0.4
2×2	0.747	0.732	-2.1
3×3	0.877	0.872	-0.6
5×5	0.947	0.952	0.5
7×7	0.963	0.965	0.2
9×9	0.985	0.987	0.2
11×11	0.990	0.994	0.4
15×15	0.981	0.982	0.1
20×20	0.987	0.987	0.0

Table 3.7: 16 MeV comparison of measured output data with Pinnacle computed output data. Percent difference = $100\% \times (\text{computed} - \text{measured}) / \text{measured}$.

Field Size (cm ²)	Meas. Output (cGy/MU)	Comp. Output (cGy/MU)	% Difference (%)
1×1	0.631	0.613	-2.8
2×2	0.820	0.809	-1.3
3×3	0.904	0.905	0.1
5×5	0.940	0.941	0.1
7×7	0.964	0.965	0.1
9×9	0.987	0.988	0.1
11×11	0.984	0.984	0.0
15×15	0.982	0.982	0.0
20×20	0.982	0.983	0.1

Table 3.8: 20 MeV comparison of measured output data with Pinnacle computed output data. Percent difference = $100\% \times (\text{computed} - \text{measured}) / \text{measured}$.

Field Size (cm ²)	Meas. Output (cGy/MU)	Comp. Output (cGy/MU)	% Difference (%)
1×1	0.719	0.692	-3.8
2×2	0.858	0.851	-0.8
3×3	0.918	0.918	0.0
5×5	0.942	0.944	0.2
7×7	0.973	0.973	0.0
9×9	0.989	0.989	0.0
11×11	0.991	0.991	0.0
15×15	0.985	0.985	0.0
20×20	0.979	0.979	0.0

Table 3.9: eMLC photon transmission factors. Photon transmission factors determined as the ratio of ionization at measurement depth $R_p + 2\text{cm}$ in plastic water for a field with all eMLC leaves closed to ionization with an open $11 \times 11 \text{ cm}^2$ eMLC field with otherwise identical geometry.

Energy (MeV)	Measurement Depth (cm)	Transmission Factor
6	4.9	0.44
9	6.3	0.49
12	8.2	0.51
16	10.3	0.52
20	12.4	0.52

Photon Transmission through eMLC Leaves

Table 3.9 shows the eMLC photon transmission factors measured for the Pinnacle beam model cutout transmission factor. These values were measured at a depth $R_p + 2\text{cm}$ in plastic water and were used to model the attenuation of the photon dose in blocked regions of the field. Transmission factors increased with electron energy.

Hogstrom et al. (2004) previously measured the x-ray leakage through the eMLC leaves (closed on central axis) for a 15 MeV electron beam (Siemens Primus accelerator) at 1 cm depth in solid-water at 100 cm SSD to be 1.6% of the dose at R_{100} with the leaves fully

open (20×21 cm²). The x-ray contribution to dose for identical measurement setup was determined to be 2.7% for the open beam, corresponding to a transmission factor of 0.59 for the 15 MeV beam, which is slightly higher than the transmission factor of 0.52 measured for the 16 MeV beam in the current study.

3.2.2 Validate Dose Computations with Measured Isodose Curves

Dose distributions computed with the PBA commissioned for the eMLC were validated through measurements of 2D isodose distributions for (7×7 and 15×15) cm² fields at (100 and 110) cm SSD. The isodose planes were normalized to 100% at the central axis maximum dose. Measured and calculated isodose distributions are presented for (6, 9, 12, 16, and 20) MeV.

Tables 3.10, 3.11, 3.12, 3.13, and 3.14 present quantitative comparisons of the measured and computed isodose distributions. The distance to agreement for each isodose contour is given for dose less than 80% of the maximum dose and the percent difference is given for the dose greater than 90% of the maximum dose. Both RMS values and maximum values are presented for each contour comparison. The location of the point of maximum disagreement is given for each contour.

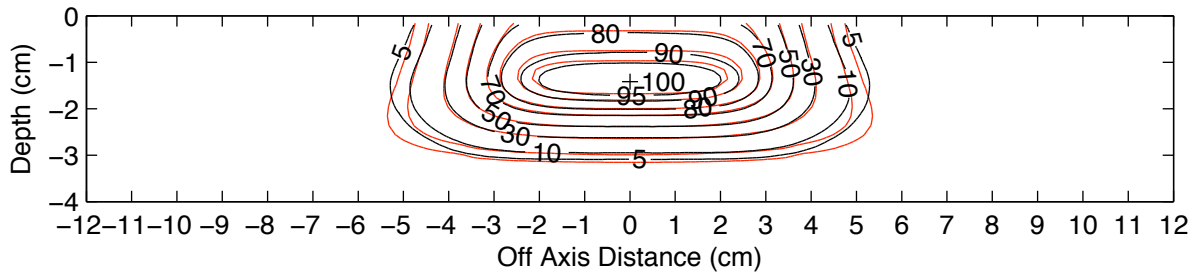
Differences in the dose greater than 90% of the maximum dose were attributed to the assumption of a uniform incident electron fluence (off-axis ratios = 1) throughout the geometric field aperture and were considered to have negligible impact on the investigation of improvements to segmented field ECT abutment dosimetry. Good agreement in central axis percent depth dose indicated that the dose algorithm correctly utilized the commissioning data for the 6, 9, and 12 MeV, 7×7 and 15×15 cm² fields and for the 16 and 20 MeV, 15×15 cm² fields. Good agreement of the measured and computed 50% isodose contours indicated accurate placement of field edge in the treatment planning system.

Disagreement in the computed PDD compared with the measured PDD for the 16 and 20 MeV, 7×7 cm² fields was discovered. Changing the FMCS factor from the 1.2 value used in the present study to 1.0 did not resolve the discrepancy, and the agreement of the large field PDDs for the 15×15 cm² fields suggested that the disagreement was not an error in computed

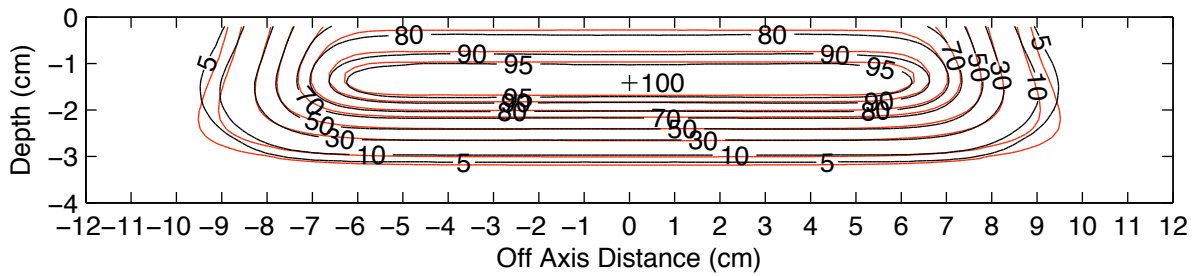
phantom density or stopping power. The effect of increasing and decreasing the field size was investigated. Modification of the 7×7 cm² field aperture in Pinnacle to dimensions slightly greater than (7.2×7.2 cm²) or slightly less than (6.8×6.8 cm²) the nominal field width did not resolve the disagreement. The disagreement was not resolved but was expected to have minimal impact on the study of improvements to the abutment dosimetry for segmented field ECT.

Disagreements in the measured and computed 10% and 5% isodose contours was expected and attributed to differences between the Gaussian approximation to the lateral distribution of electrons from a single pencil beam passing through a slab of material. The Gaussian approximation underestimates the fraction of electrons that undergo large angle scattering; hence, the computed distribution underestimates the lateral extent of the dose distribution falloff in regions shallow to the therapeutic range R_{90} . A second approximation, that the RMS angular distribution of electrons increases continuously with depth, causes the computed distribution to overestimate the lateral falloff distribution at greater depths and extend laterally beyond the range of the measured data. The approximation neglects that the electrons which undergo large angle scattering in the shallow regions do not reach greater depths and the angular distribution of electrons reaching the greater depths is narrower than computed.

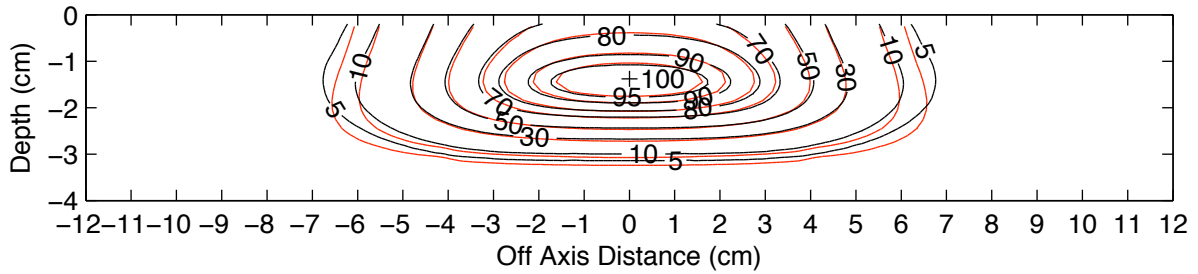
The localized, lateral extension of the 5% isodose contour near the surface for the 20 MeV, 7×7 cm² field led to an investigation of the Pinnacle commissioning data and photon model that has been described in Appendix B and revealed errors in the Pinnacle version 7.4f code. These errors were not determined to be the cause of the lateral extension of the 5% isodose for the 20 MeV field, however, and the shallow low dose was attributed to bremsstrahlung photons produced in the eMLC leaves which may also give rise to electrons emanating from the leaves via Compton interactions of the photons in the brass leaves as suggested by Ma et al. (2000).



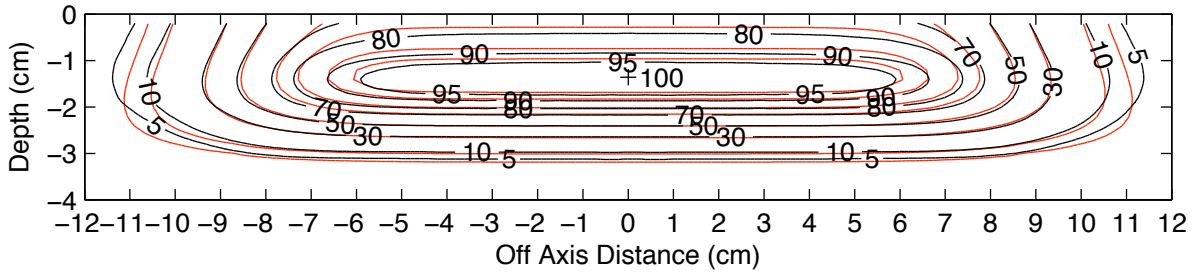
(a)



(b)

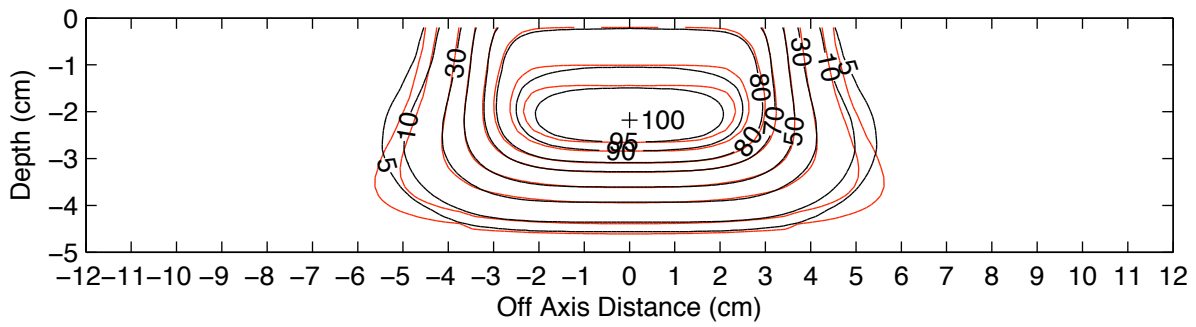


(c)

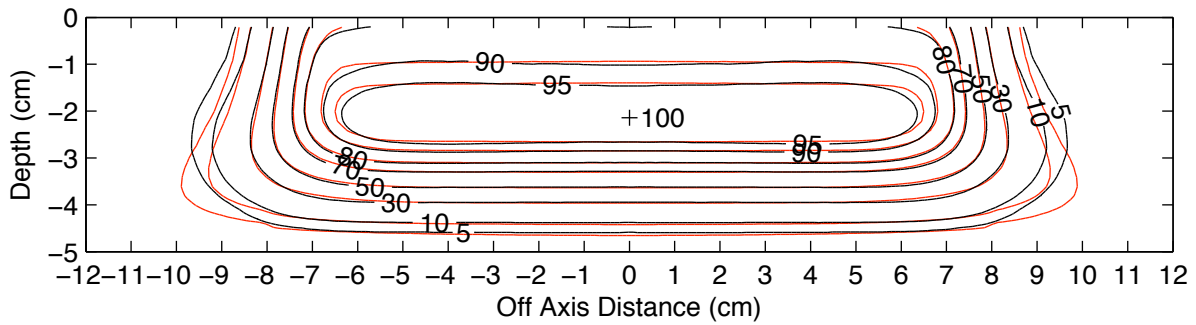


(d)

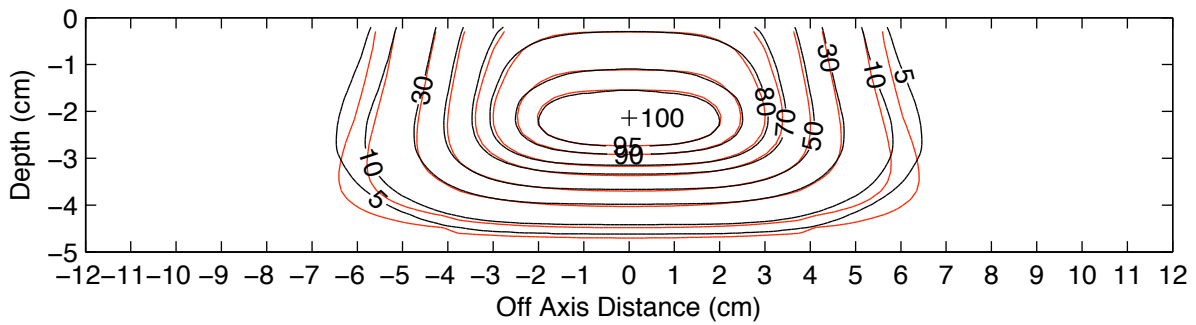
Figure 3.31: Measured (black) vs. Pinnacle computed (red) isodose curves for 6 MeV, 100 (a,b) and 110 (c,d) cm SSD, 7×7 and 15×15 cm^2 field sizes. Depth-cross plane parallel to eMLC leaf motion.



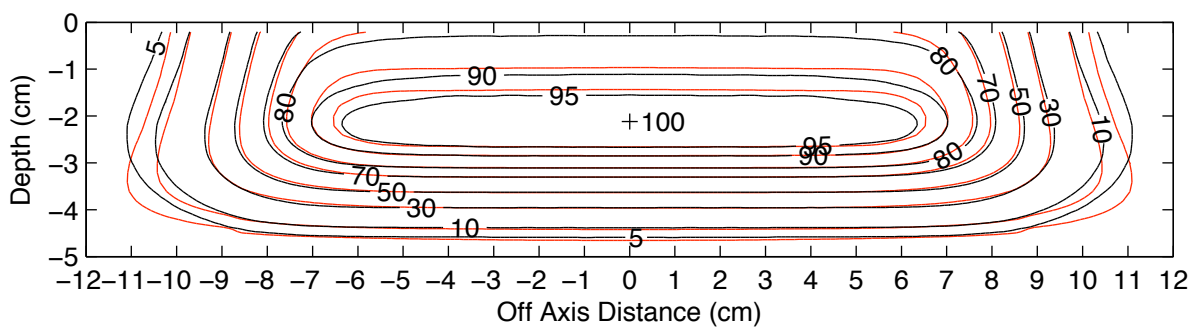
(a)



(b)

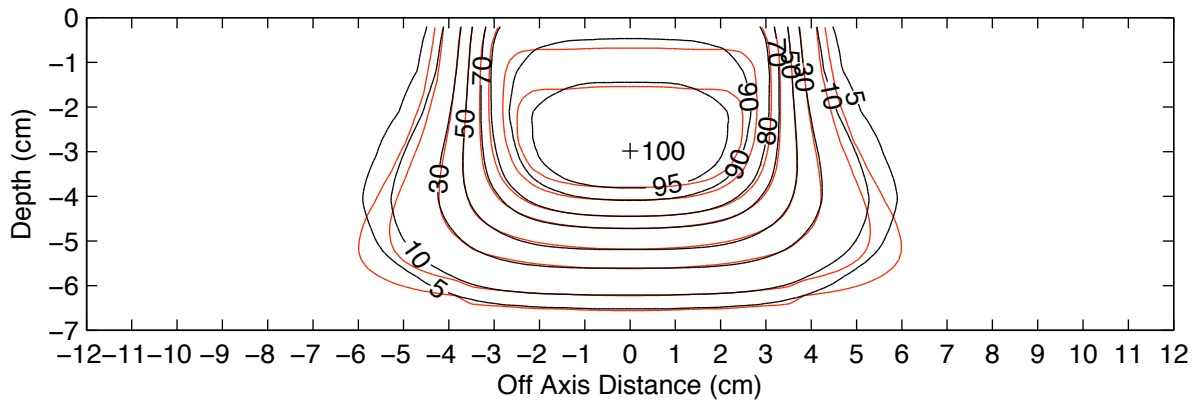


(c)

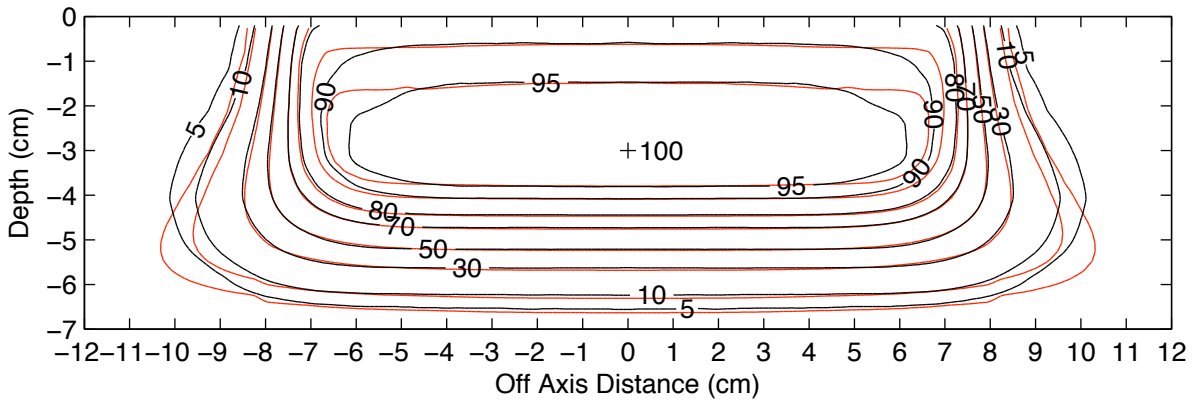


(d)

Figure 3.32: Measured (black) vs. Pinnacle computed (red) isodose curves for 9 MeV, 100 (a,b) and 110 (c,d) cm SSD, 7×7 and 15×15 cm² field sizes. Depth-cross plane parallel to eMLC leaf motion.

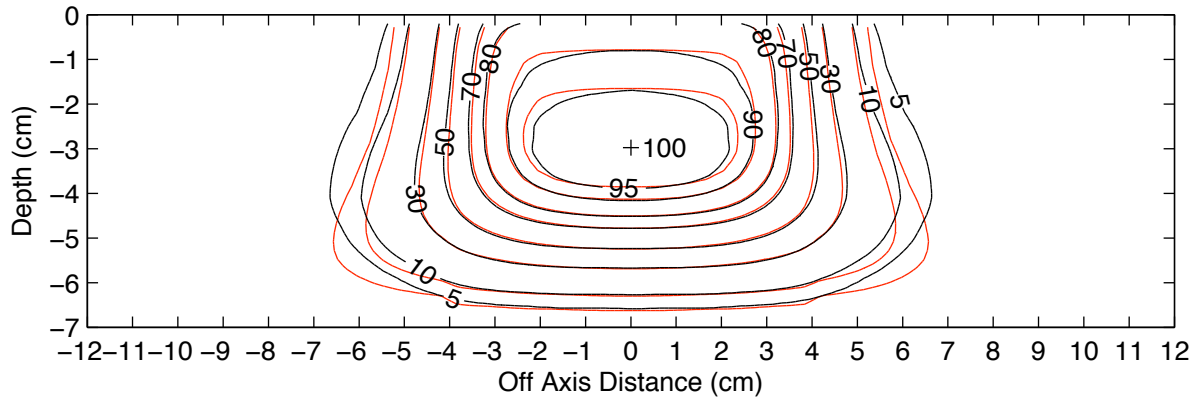


(a)

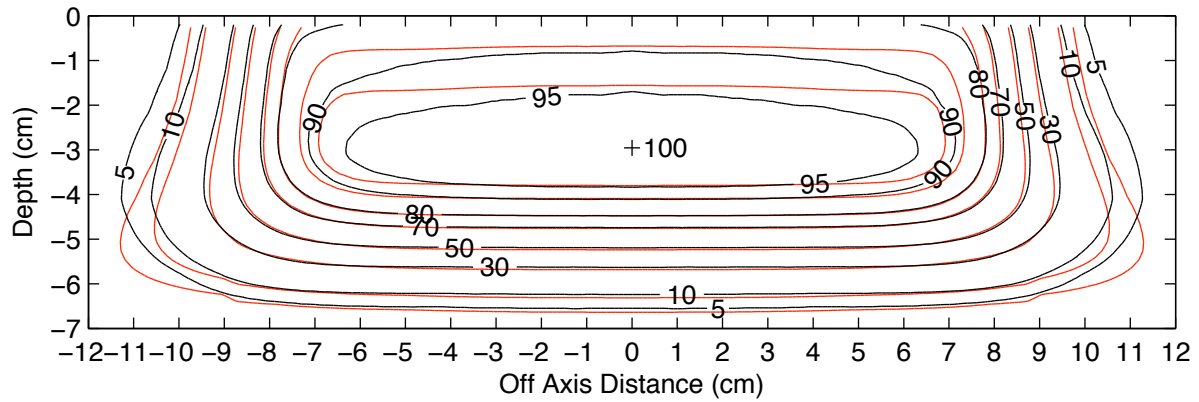


(b)

Figure 3.33: Measured (black) vs. Pinnacle computed (red) isodose curves for 12 MeV at 100 cm SSD, 7×7 and 15×15 cm² field sizes. Depth-cross plane parallel to eMLC leaf motion.

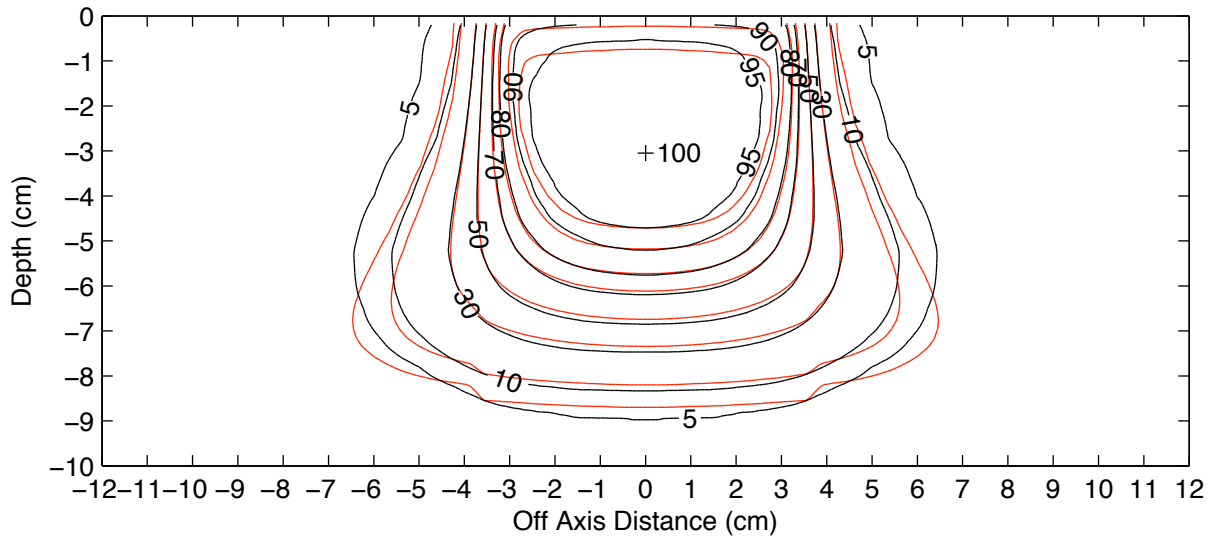


(a)

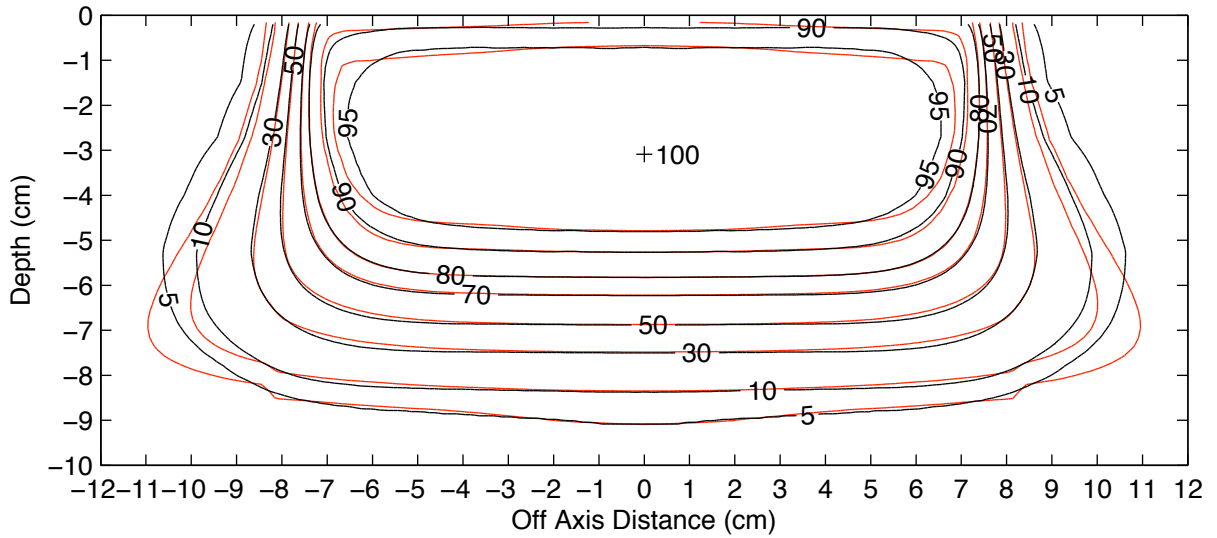


(b)

Figure 3.34: Measured (black) vs. Pinnacle computed (red) isodose curves for 12 MeV at 110 cm SSD, 7×7 and 15×15 cm² field sizes. Depth-cross plane parallel to eMLC leaf motion.

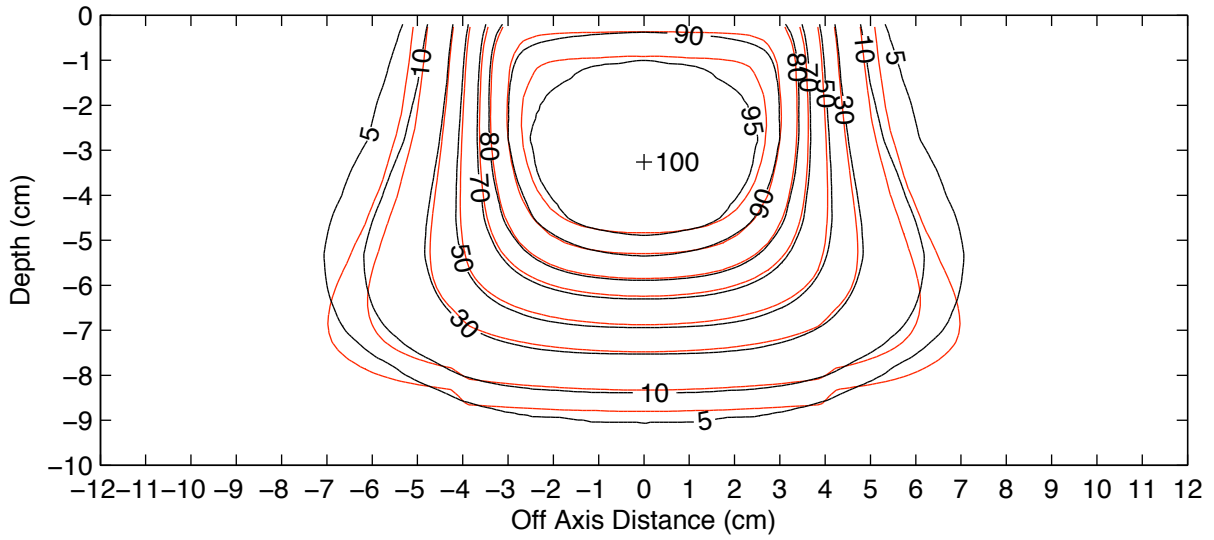


(a)

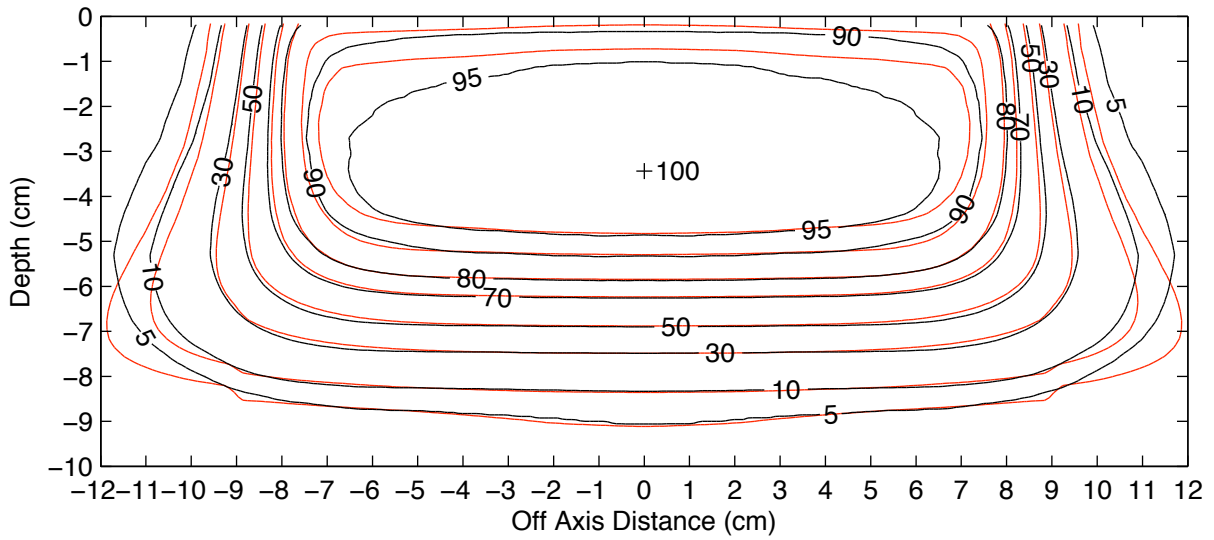


(b)

Figure 3.35: Measured (black) vs. Pinnacle computed (red) isodose curves for 16 MeV at 100 cm SSD, 7×7 and 15×15 cm² field sizes. Depth-cross plane parallel to eMLC leaf motion.



(a)



(b)

Figure 3.36: Measured (black) vs. Pinnacle computed (red) isodose curves for 16 MeV at 110 cm SSD, 7×7 and 15×15 cm² field sizes. Depth-cross plane parallel to eMLC leaf motion.

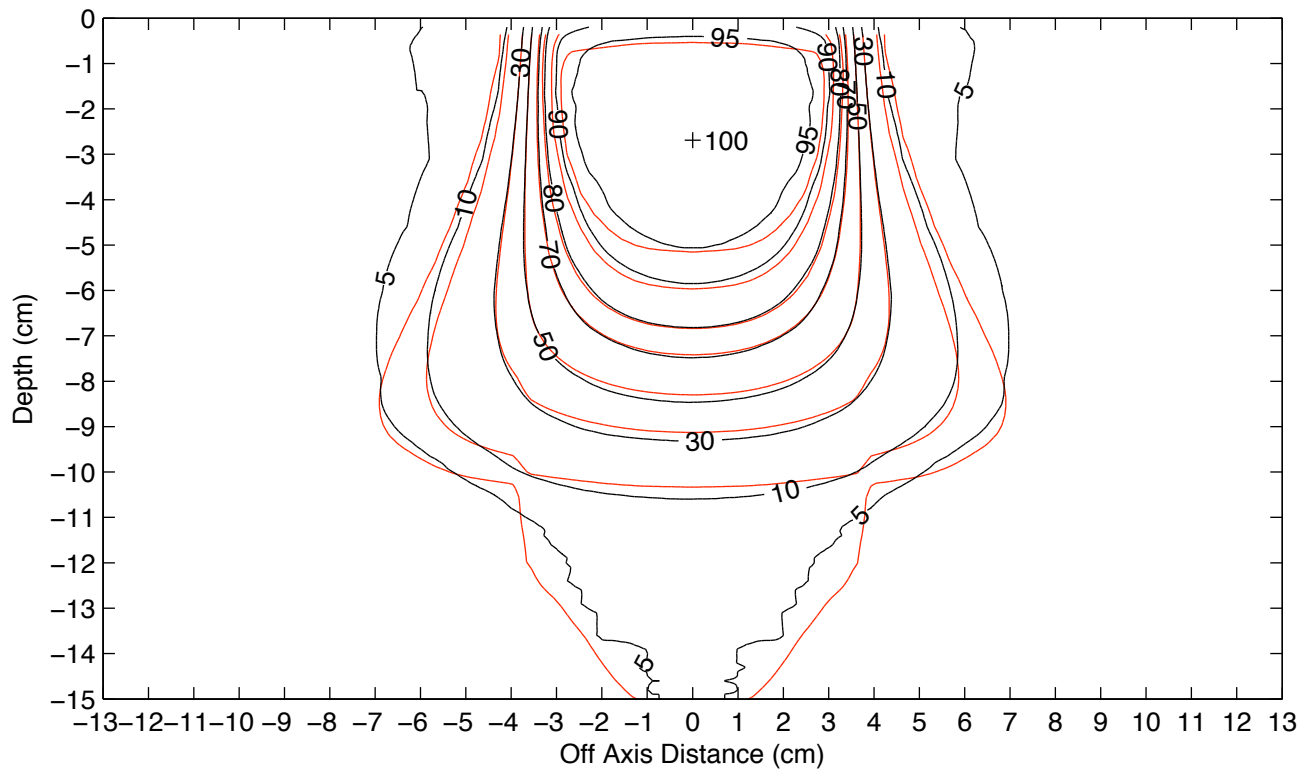


Figure 3.37: Measured (black) vs. Pinnacle computed (red) isodose curves for 20 MeV, 7×7 cm² field at 100 cm SSD. Depth-cross plane parallel to eMLC leaf motion.

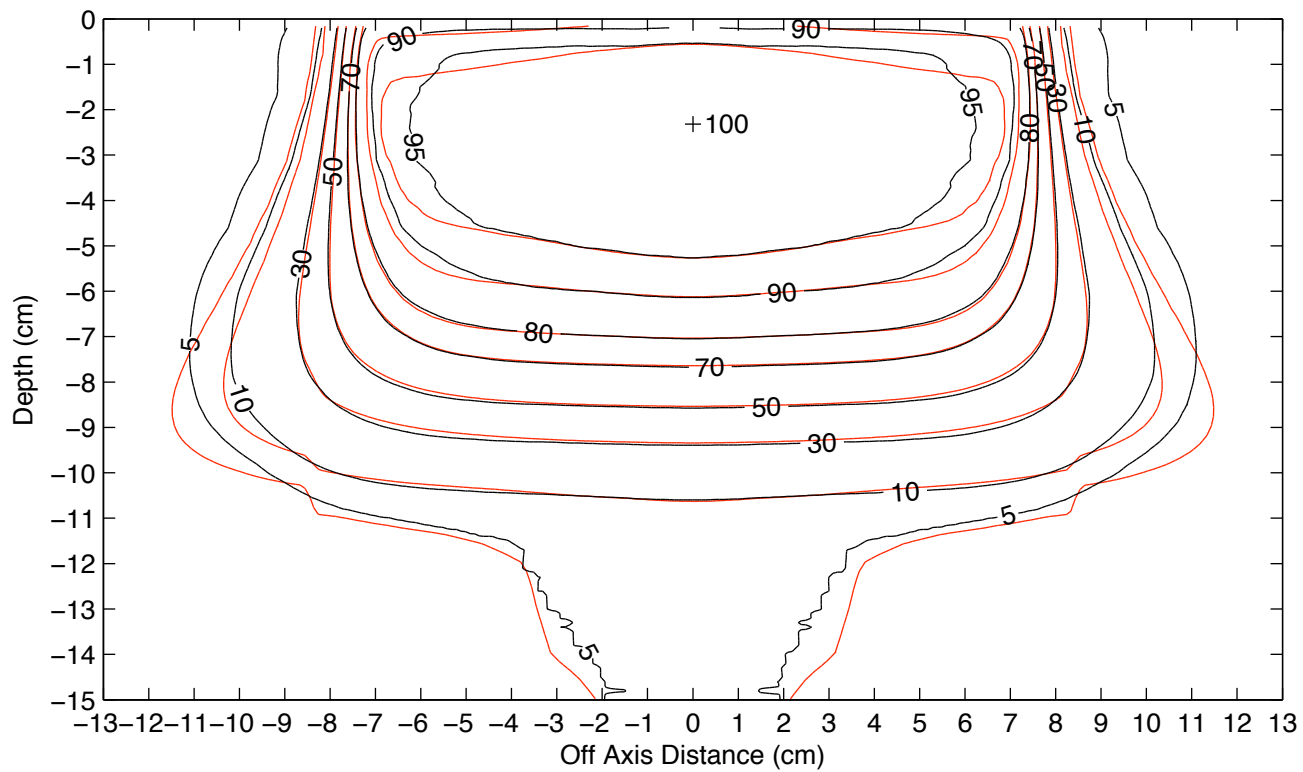


Figure 3.38: Measured (black) vs. Pinnacle computed (red) isodose curves for 20 MeV, 15×15 cm² field at 100 cm SSD. Depth-cross plane parallel to eMLC leaf motion.

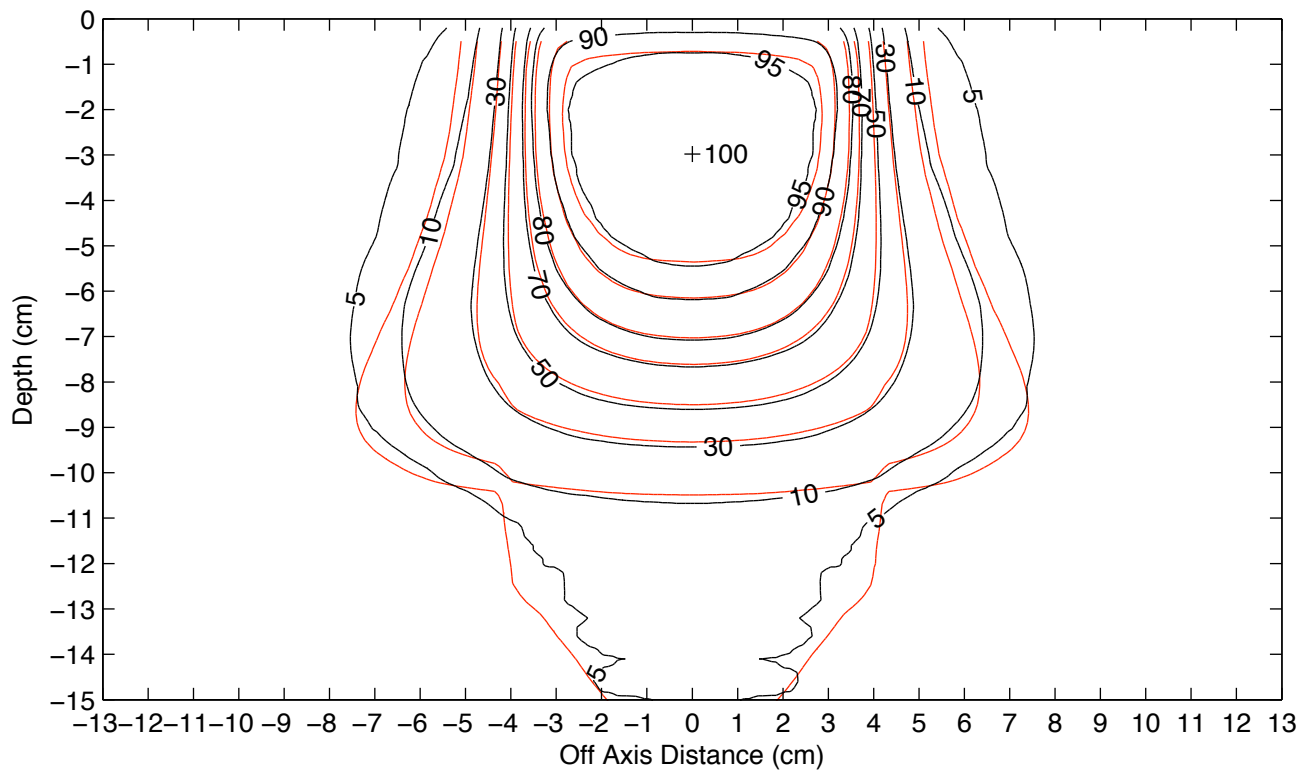


Figure 3.39: Measured (black) vs. Pinnacle computed (red) isodose curves for 20 MeV, 7×7 cm² field at 110 cm SSD. Depth-cross plane parallel to eMLC leaf motion.

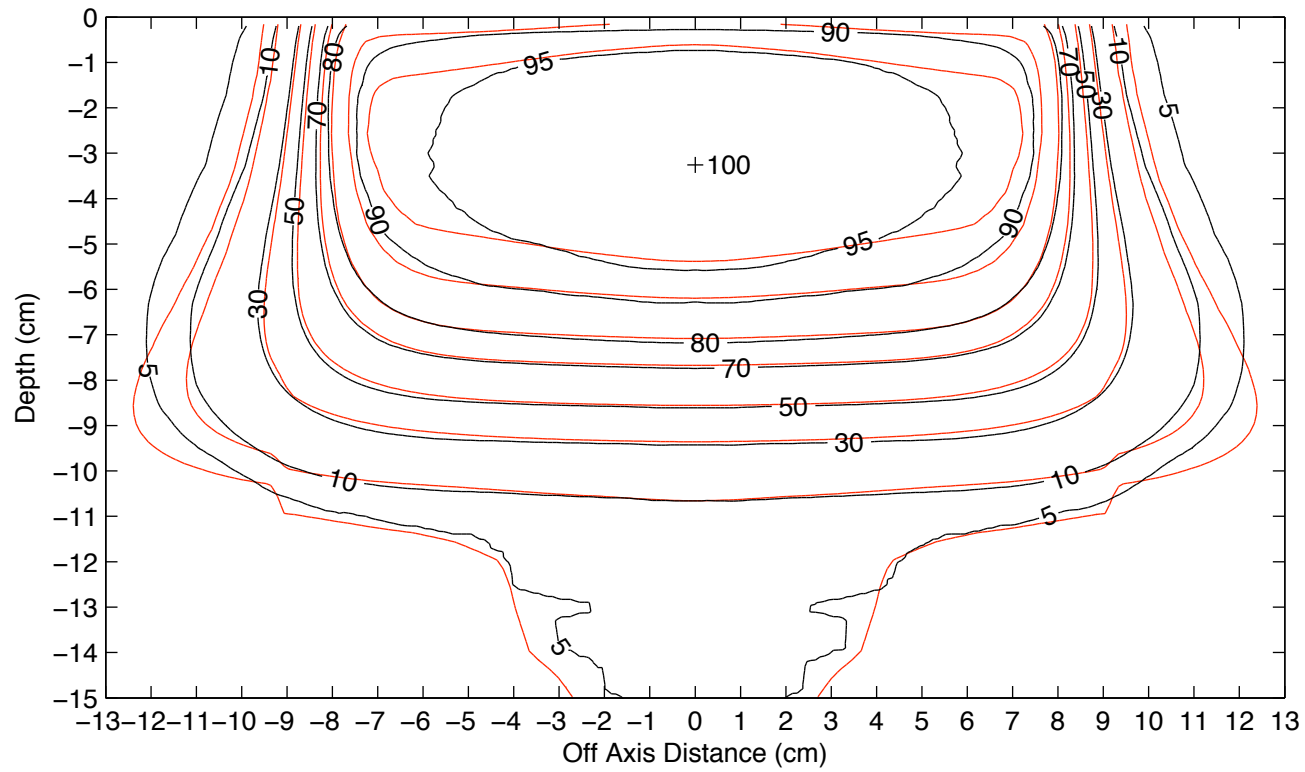


Figure 3.40: Measured (black) vs. Pinnacle computed (red) isodose curves for 20 MeV, $15 \times 15 \text{ cm}^2$ field at 110 cm SSD. Depth-cross plane parallel to eMLC leaf motion.

Table 3.10: 6 MeV comparison of measured and computed dose distributions shown in Figure 3.31. The RMS and maximum distance to agreement (DTA) are given for each isodose (D) contour. The off-axis (OA) and depth (d) coordinates of the max DTA are given. For isodose levels greater than 90%, percent difference is reported rather than DTA as indicated by the % symbol. The 5 and 10 % isodose curve data are separated into regions shallow (a) and deep (b) to distal R_{90} .

SSD (cm)	FS (cm ²)	D (%)	RMS DTA (cm)	Max DTA (cm)	OA (cm)	d (cm)	
100	7×7	>90	0.9%	2.2%	-2.2	-1.1	
		80	0.02	0.08	2.1	-0.5	
		70	0.02	0.04	-3.1	-1.0	
		50	0.02	0.03	-3.5	-0.9	
		30	0.02	0.05	4.0	-1.9	
		10 _a	0.01	0.11	4.8	-1.9	
		10 _b	0.05	0.22	4.6	-2.2	
		5 _a	0.02	0.15	-5.2	-1.2	
		5 _b	0.09	0.35	-4.9	-2.3	
		15×15	>90	1.0%	2.0%	5.8	-0.9
	80		0.02	0.10	-6.2	-0.5	
	70		0.03	0.05	-6.7	-2.0	
	50		0.02	0.05	6.9	-2.3	
	30		0.01	0.04	-8.1	-2.0	
	10 _a		0.01	0.08	9.0	-1.2	
	10 _b		0.04	0.20	8.8	-2.3	
	5 _a		0.02	0.21	9.3	-1.0	
	5 _b		0.07	0.33	-9.1	-2.3	
	110		7×7	>90	0.7%	1.9%	2.2
		80		0.04	0.13	-2.9	-1.4
70		0.04		0.11	3.3	-1.5	
50		0.03		0.08	4.1	-1.5	
30		0.03		0.06	-4.8	-1.4	
10 _a		0.02		0.13	-6.0	-1.3	
10 _b		0.06		0.16	-5.5	-2.3	
5 _a		0.05		0.32	6.7	-1.1	
5 _b		0.09		0.23	5.9	-2.5	
15×15		>90		1.3%	2.9%	4.8	-0.9
		80	0.04	0.18	5.2	-0.5	
		70	0.03	0.12	-7.9	-1.5	
		50	0.02	0.10	-8.6	-1.5	
		30	0.02	0.07	9.4	-1.5	
		10 _a	0.02	0.16	-10.6	-1.1	
		10 _b	0.04	0.18	-10.0	-2.2	
		5 _a	0.04	0.38	-11.3	-1.0	
		5 _b	0.07	0.26	-10.5	-2.3	

Table 3.11: 9 MeV comparison of measured and computed dose distributions shown in Figure 3.32. The RMS and maximum distance to agreement (DTA) are given for each isodose (D) contour. The off-axis (OA) and depth (d) coordinates of the max DTA are given. For isodose levels greater than 90%, percent difference is reported rather than DTA as indicated by the % symbol. The 5 and 10 % isodose curve data are separated into regions shallow (a) and deep (b) to distal R_{90} .

SSD (cm)	FS (cm ²)	D (%)	RMS DTA (cm)	Max DTA (cm)	OA (cm)	d (cm)	
100	7×7	>90	1.0%	2.8%	2.4	-1.9	
		80	0.02	0.06	2.7	-0.7	
		70	0.02	0.04	-3.1	-2.5	
		50	0.01	0.03	3.4	-3.0	
		30	0.02	0.07	-3.9	-3.2	
		10 _a	0.02	0.14	-4.9	-2.1	
		10 _b	0.06	0.30	4.7	-3.4	
		5 _a	0.06	0.30	5.3	-1.9	
		5 _b	0.09	0.49	5.1	-3.5	
		15×15	>90	0.6%	1.9%	-6.4	-1.3
	80	0.02	0.04	6.4	-3.0		
	70	0.02	0.05	-6.9	-3.0		
	50	0.02	0.05	6.4	-3.6		
	30	0.03	0.06	-8.3	-2.1		
	10 _a	0.02	0.17	-9.1	-2.1		
	10 _b	0.05	0.31	-8.9	-3.5		
	5 _a	0.05	0.33	-9.5	-1.9		
	5 _b	0.08	0.51	-9.3	-3.6		
	110	7×7	>90	0.3%	0.7%	-1.6	-1.5
			80	0.03	0.09	2.8	-1.1
70			0.05	0.11	-3.2	-1.0	
50			0.04	0.09	4.1	-2.2	
30			0.03	0.08	4.7	-2.2	
10 _a			0.03	0.16	-5.8	-2.2	
10 _b			0.07	0.24	5.4	-3.5	
5 _a			0.07	0.35	6.4	-2.0	
5 _b			0.10	0.39	-5.9	-3.6	
15×15			>90	0.9%	2.7%	5.6	-1.3
80		0.03	0.20	-6.3	-0.5		
70		0.04	0.12	8.1	-2.1		
50		0.04	0.11	8.7	-2.1		
30		0.03	0.11	9.4	-2.2		
10 _a		0.03	0.19	10.4	-2.1		
10 _b		0.04	0.23	-10.0	-3.5		
5 _a		0.06	0.37	11.0	-1.9		
5 _b		0.08	0.40	-10.6	-3.5		

Table 3.12: 12 MeV comparison of measured and computed dose distributions shown in Figures 3.33 and 3.34. The RMS and maximum distance to agreement (DTA) are given for each isodose (D) contour. The off-axis (OA) and depth (d) coordinates of the max DTA are given. For isodose levels greater than 90%, percent difference is reported rather than DTA as indicated by the % symbol. The 5 and 10 % isodose curve data are separated into regions shallow (a) and deep (b) to distal R_{90} .

SSD (cm)	FS (cm ²)	D (%)	RMS DTA (cm)	Max DTA (cm)	OA (cm)	d (cm)
100	7×7	>90	1.0%	3.4%	2.4	-2.9
		80	0.04	0.08	2.9	-3.0
		70	0.03	0.05	-3.2	-3.4
		50	0.02	0.05	2.1	-5.1
		30	0.03	0.05	4.2	-3.1
		10 _a	0.05	0.23	4.9	-2.9
		10 _b	0.05	0.31	-4.9	-5.1
		5 _a	0.14	0.49	5.4	-2.6
		5 _b	0.09	0.50	5.5	-5.2
	15×15	>90	0.6%	3.7%	6.6	-1.9
		80	0.04	0.08	7.1	-0.7
		70	0.02	0.03	2.2	-4.7
		50	0.02	0.05	7.9	-3.1
		30	0.04	0.09	8.4	-3.1
		10 _a	0.05	0.27	-9.2	-3.0
		10 _b	0.06	0.35	9.2	-5.1
		5 _a	0.11	0.51	-9.7	-2.8
		5 _b	0.10	0.61	-9.7	-5.2
110	7×7	>90	0.7%	1.8%	2.2	-1.5
		80	0.03	0.07	-3.2	-1.2
		70	0.04	0.08	3.5	-1.2
		50	0.05	0.10	4.1	-3.1
		30	0.04	0.12	-4.7	-3.2
		10 _a	0.06	0.30	5.7	-3.1
		10 _b	0.05	0.26	-5.4	-5.2
		5 _a	0.14	0.59	-6.3	-2.7
		5 _b	0.09	0.47	6.0	-5.3
	15×15	>90	1.3%	4.3%	-6.4	-1.9
		80	0.02	0.14	-7.3	-0.5
		70	0.03	0.08	-8.2	-2.5
		50	0.05	0.11	8.8	-3.1
		30	0.06	0.16	9.4	-3.1
		10 _a	0.06	0.33	10.4	-3.1
		10 _b	0.06	0.29	10.1	-5.1
		5 _a	0.12	0.57	-11.0	-2.8
		5 _b	0.10	0.52	10.7	-5.2

Table 3.13: 16 MeV comparison of measured and computed dose distributions shown in Figures 3.35 and 3.36. The RMS and maximum distance to agreement (DTA) are given for each isodose (D) contour. The off-axis (OA) and depth (d) coordinates of the max DTA are given. For isodose levels greater than 90%, percent difference is reported rather than DTA as indicated by the % symbol. The 5 and 10 % isodose curve data are separated into regions shallow (a) and deep (b) to distal R_{90} .

SSD (cm)	FS (cm ²)	D (%)	RMS DTA (cm)	Max DTA (cm)	OA (cm)	d (cm)	
100	7×7	>90	0.9%	2.8%	-2.8	-2.1	
		80	0.03	0.05	2.5	-4.9	
		70	0.04	0.08	-1.4	-6.1	
		50	0.05	0.12	1.4	-6.8	
		30	0.06	0.15	-1.8	-7.4	
		10 _a	0.07	0.27	5.3	-4.4	
		10 _b	0.07	0.26	-5.2	-6.8	
		5 _a	0.23	0.69	-5.7	-3.3	
		5 _b	0.12	0.45	6.4	-5.3	
		15×15	>90	0.5%	2.6%	-6.8	-2.5
	80	0.01	0.04	-7.3	-0.5		
	70	0.03	0.06	5.9	-6.0		
	50	0.04	0.10	6.5	-6.6		
	30	0.05	0.12	-6.2	-7.4		
	10 _a	0.06	0.26	9.3	-3.7		
	10 _b	0.06	0.37	-9.5	-6.8		
	5 _a	0.14	0.59	9.9	-3.3		
	5 _b	0.09	0.71	-10.2	-6.9		
	110	7×7	>90	0.9%	2.4%	-2.4	-2.3
			80	0.04	0.06	-3.3	-0.5
70			0.06	0.09	2.6	-5.8	
50			0.08	0.11	2.3	-6.7	
30			0.07	0.12	-4.8	-5.3	
10 _a			0.08	0.33	-6.0	-4.5	
10 _b			0.06	0.29	6.2	-5.3	
5 _a			0.21	0.74	6.5	-3.6	
5 _b			0.13	0.54	-7.1	-5.3	
15×15			>90	1.2%	3.7%	7.0	-1.3
80		0.03	0.09	7.8	-4.4		
70		0.06	0.12	-8.2	-4.5		
50		0.07	0.13	8.9	-4.3		
30		0.06	0.16	-9.5	-4.1		
10 _a		0.07	0.32	10.6	-4.4		
10 _b		0.05	0.31	-10.5	-6.8		
5 _a		0.15	0.66	-11.2	-3.6		
5 _b		0.10	0.66	11.2	-6.9		

Table 3.14: 20 MeV comparison of measured and computed dose distributions shown in Figures 3.37, 3.38, 3.39, and 3.40. The RMS and maximum distance to agreement (DTA) are given for each isodose (D) contour. The off-axis (OA) and depth (d) coordinates of the max DTA are given. For isodose levels greater than 90%, percent difference is reported rather than DTA as indicated by the % symbol. The 5 and 10 % isodose curve data are separated into regions shallow (a) and deep (b) to distal R_{90} .

SSD (cm)	FS (cm ²)	D (%)	RMS DTA (cm)	Max DTA (cm)	OA (cm)	d (cm)
100	7×7	>90	1.2%	3.6%	3.0	-1.3
		80	0.04	0.07	2.4	-5.7
		70	0.03	0.07	-0.3	-7.5
		50	0.05	0.17	-0.4	-8.5
		30	0.07	0.20	-1.9	-9.2
		10 _a	0.07	0.29	-5.4	-5.2
		10 _b	0.09	0.27	-0.4	-10.6
		5 _a	0.34	1.96	-6.2	-0.6
		5 _b	0.27	0.99	1.0	-13.9
	15×15	>90	0.6%	3.3%	7.0	-2.5
		80	0.02	0.07	5.7	-6.5
		70	0.02	0.04	-6.7	-6.7
		50	0.04	0.09	7.0	-7.9
		30	0.06	0.13	-6.0	-9.2
		10 _a	0.06	0.27	9.8	-5.4
		10 _b	0.06	0.36	-9.9	-8.4
		5 _a	0.17	0.74	9.1	-0.8
		5 _b	0.24	0.98	2.3	-13.3
110	7×7	>90	0.7%	2.0%	-2.4	-2.3
		80	0.05	0.09	-3.4	-0.5
		70	0.07	0.10	2.7	-6.9
		50	0.09	0.13	2.4	-8.3
		30	0.09	0.14	4.4	-8.2
		10 _a	0.07	0.37	6.2	-5.9
		10 _b	0.08	0.37	6.3	-6.1
		5 _a	0.26	1.02	6.4	-2.7
		5 _b	0.27	1.02	-2.8	-12.2
	15×15	>90	0.9%	3.5%	-7.0	-2.5
		80	0.05	0.10	1.1	-7.2
		70	0.08	0.11	7.6	-6.7
		50	0.09	0.15	7.7	-8.0
		30	0.10	0.15	9.7	-6.3
		10 _a	0.06	0.32	-10.8	-5.5
		10 _b	0.06	0.32	-10.7	-8.5
		5 _a	0.17	0.71	-11.3	-4.4
		5 _b	0.28	1.59	-2.3	-12.9

3.3 Aim 3: Investigate eMLC Segmented-field Plans and Edge Feathering

3.3.1 Impact of Number of Discrete Steps on Feathering Solution

The impact of the number of discrete feathering steps on abutment dosimetry was investigated. A worst case scenario abutment of 6 and 20 MeV beams at 1 cm depth in water is shown in Figure 3.41. The abutment dosimetry improves with an increasing number of feathering steps. For the current work, five steps were deemed clinically practical and reduced abutment dose deviations to 1.7% of the composite dose.

3.3.2 Two-step PTV

Beam Geometry

The two-step PTV was treated with a 16 MeV electron beam abutting a 9 MeV beam slightly off central axis. The beam's eye views of the beams are shown in Figure 3.42. To replicate the plan of Richert et al. (2007), the 16 MeV beam was placed with the abutting edge -1 cm off axis (at isocenter) and the outer edges of the beam were extended 1.3 cm beyond the outer edge of the PTV. The 9 MeV beam was placed with the abutting edge -1 cm off axis and the outer edges of the beam were extended 1.3 cm beyond the outer edge of the PTV. The plan was converted to an eMLC aperture, and, therefore, the beam widths in the x direction (perpendicular to leaf motion) were restricted to increments of the finite leaf widths of the eMLC, resulting in the beam edges in the x direction extending 1.6 cm beyond the PTV boundary on both sides. The beam's eye views from the treatment plan created with the discrete Gaussian edge feathering algorithm are shown in Figure 3.43.

Dose Distributions

Dose distributions calculated with the treatment planning system for the two-step PTV are shown for 1-step and 5-step feathering in Figures 3.44 (YZ plane) and 3.45 (XY plane). Off-axis dose profiles (depth = 2 cm) for computed and measured data are presented in Figure 3.46. Measured (XY plane) dose distributions (film depth = 2 cm) are shown in Figure 3.47. PTV dose-volume statistics are given in Table 3.15. All dose distributions have

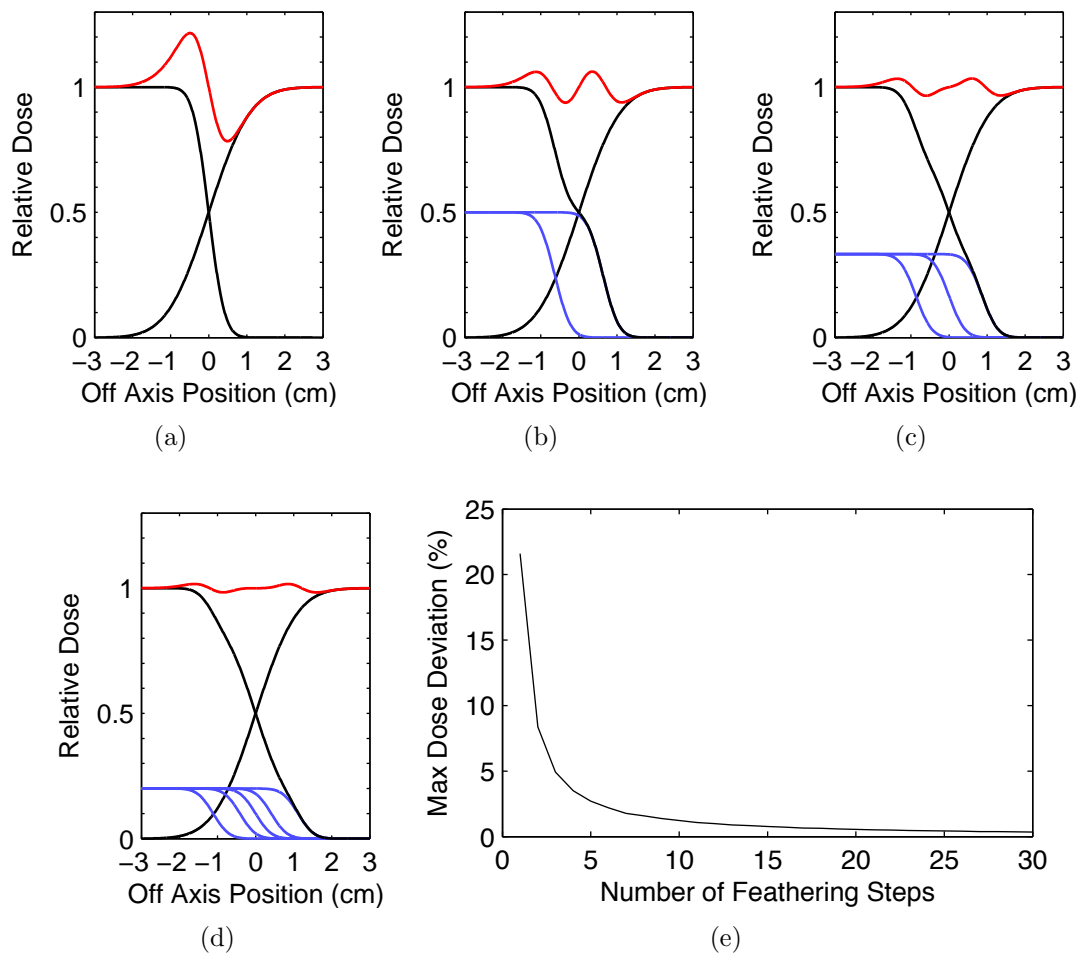


Figure 3.41: Investigation of the optimal number of discrete feathering steps. Results of feathering solutions to match a 20 MeV beam (left) abutting a 6 MeV beam (right). The resulting composite dose profile (1 cm depth in a water phantom) is shown (red) and becomes more homogeneous with an increasing number of feathering steps. The equal-weighted, feathered 20 MeV profiles are indicated in blue. The maximum dose deviations due to abutment dosimetry were 21.6, 6.2, 3.4, and 1.7 % for (a) 1-step (no feathering), (b) 2-step, (c) 3-step, and (d) 5-step, respectively. The data shown for (b, c, and d) were for feathering shifts with the outermost feathering steps optimized to locate deviation minima in the abutment dosimetry. Maximum dose deviation as a function of the number of discrete feathering steps is shown in (e) to illustrate convergence of the discrete solution. The outermost feathering step locations in (e) were not optimized for the specific number of steps.

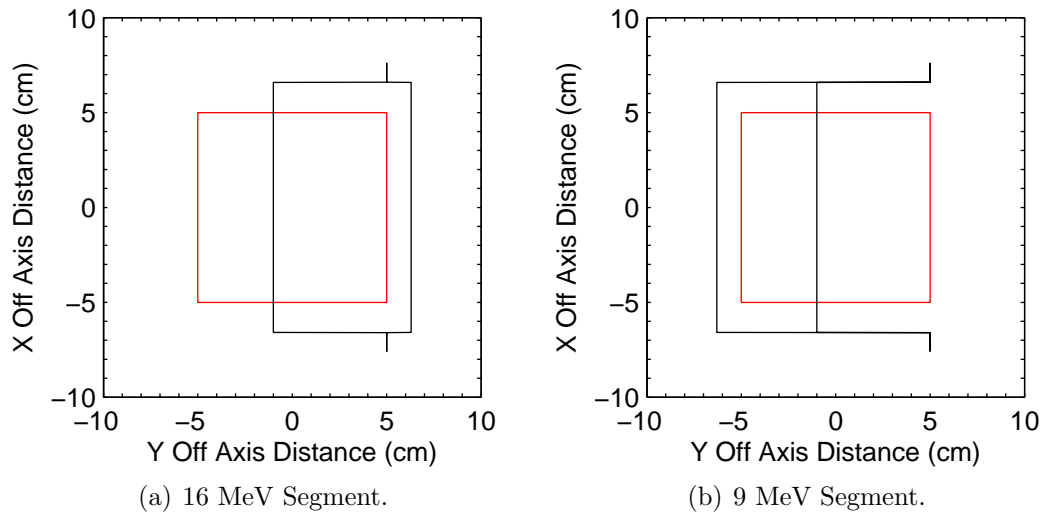


Figure 3.42: Beam's eye view of the two-step PTV segmented field ECT plan. PTV is shown by the red lines and the individual fields are defined by the black lines. The y axis is parallel to eMLC leaf motion.

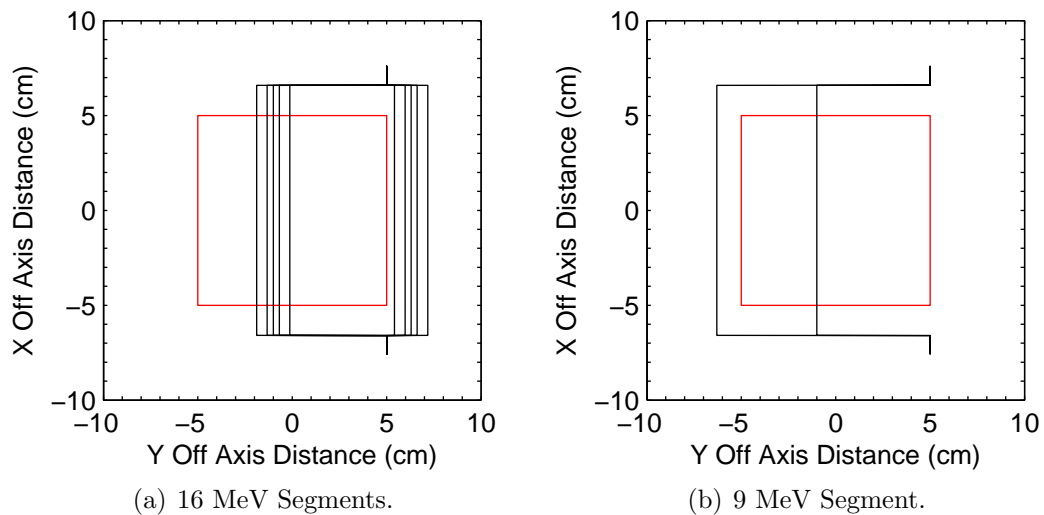


Figure 3.43: Beam's eye view of the two-step PTV segmented field ECT plan with discrete Gaussian edge feathering. PTV is shown by the red lines and the individual fields are defined by the black lines. The y axis is parallel to eMLC leaf motion.

Table 3.15: Computed dose statistics for two-step PTV treatment plans with no feathering and 5 step Gaussian edge feathering.

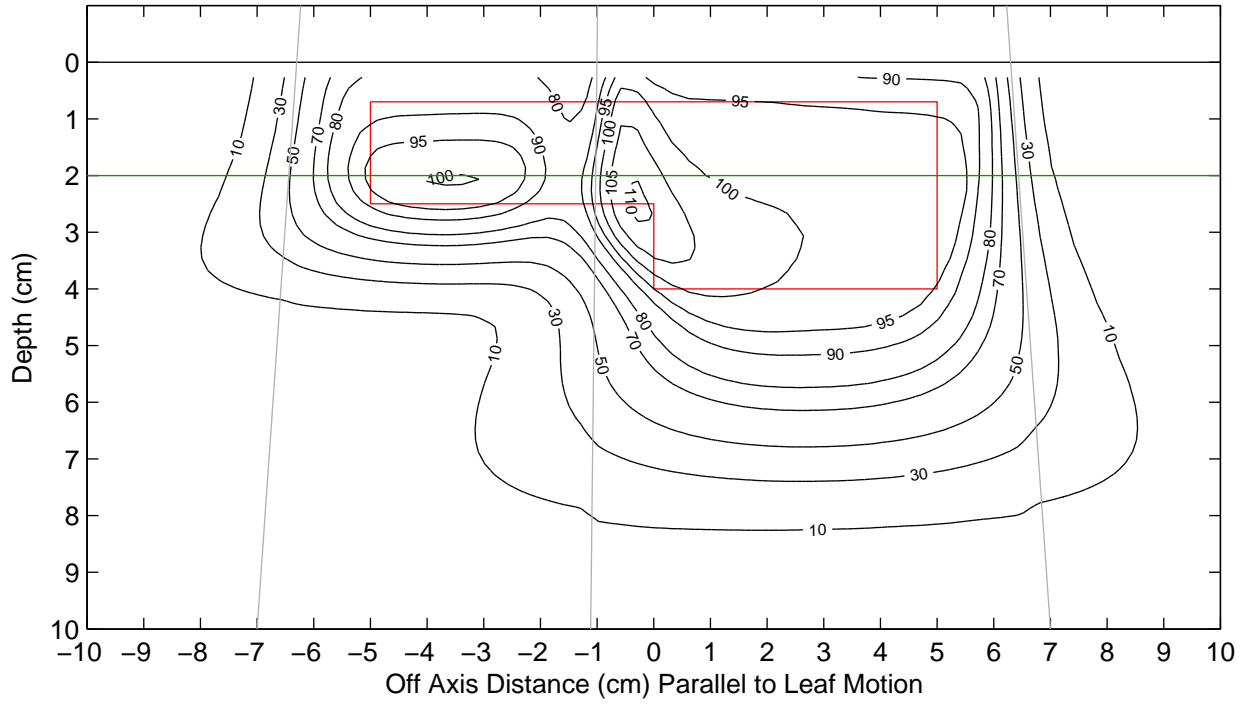
Feathering	D_{mean} (%)	σ_D (%)	D_{min} (%)	D_{max} (%)	$V_{90\%}$ (%)
None	96.8	5.3	74.1	110.8	88.5
5 step	96.9	3.5	84.3	103.6	93.9

been normalized to 100% at a reference point located in the center of the highest energy segment at the treatment planning system reference depth.

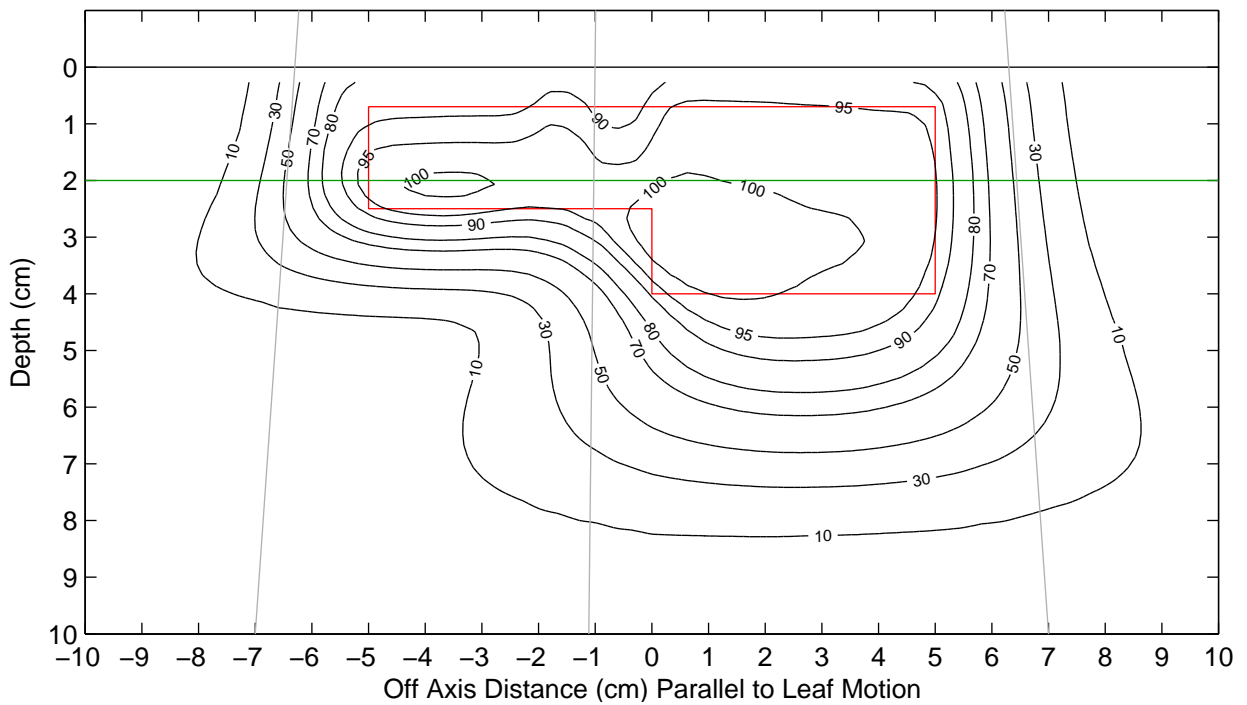
As seen in the parallel plane and perpendicular plane computed dose distributions of Figures 3.44 and 3.45, respectively, the treatment plan with discrete Gaussian edge feathering provides a more homogeneous dose than the plan with no feathering. The standard deviation of dose in the PTV is reduced by 5-step feathering from 5.3% to 3.5%. The percentage of PTV volume receiving at least 90% of the prescription dose, $V_{90\%}$, is increased from 88.5% to 93.9%.

Off-axis profiles shown in Figure 3.46 show both computed and measured data at the depth of penumbra matching in the PTV. In both sets of data, heterogeneity introduced by the abutment of unmatched penumbra is reduced along the y axis parallel to leaf motion. Disagreement between the computed and measured profiles likely results from uncertainty in leaf positioning and imprecise field abutment.

The measured isodose planes normal to the electron beam axis presented in Figure 3.47 show similar improvements to dose homogeneity in the abutment region through discrete Gaussian edge feathering as predicted by the calculated distributions. The therapeutic 90% isodose surface encloses more PTV in the plan with edge feathering, and dose gradients inside the PTV are reduced. A slight irregular appearance of the measured distributions is likely introduced by uncertainty in eMLC leaf position.

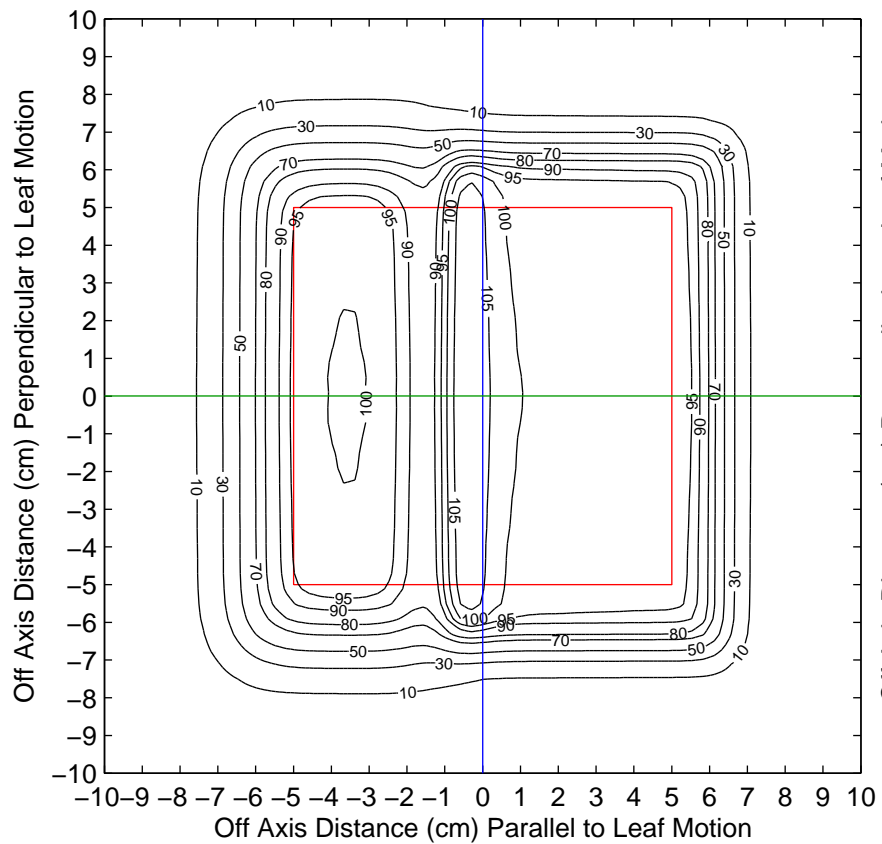


(a)

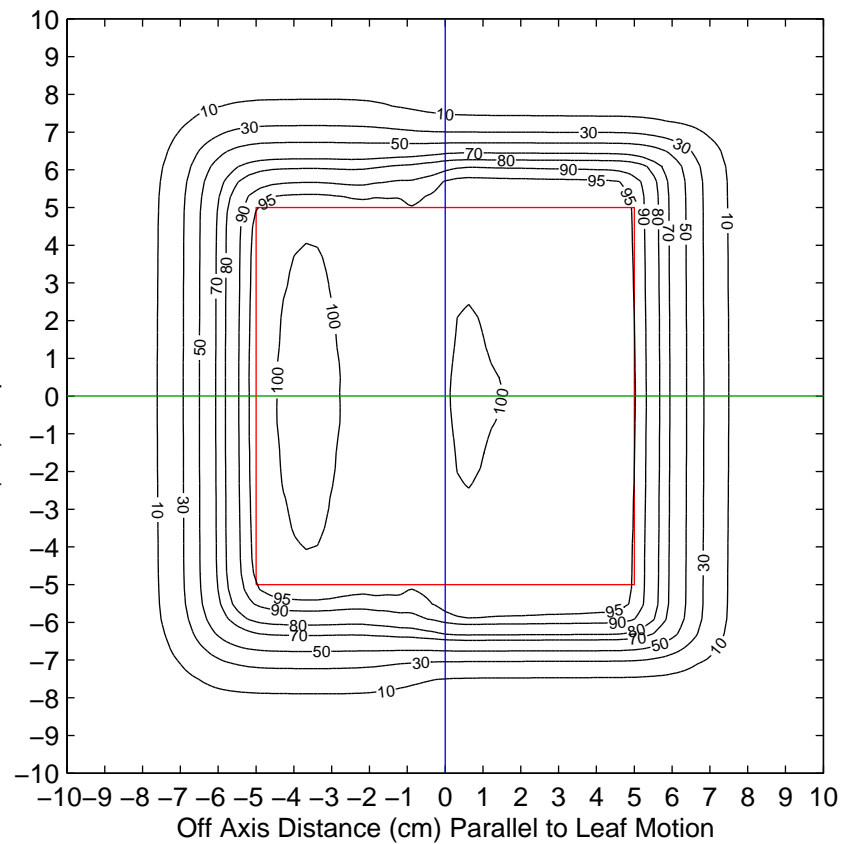


(b)

Figure 3.44: Computed isodose contours in YZ plane for two-step PTV (red) for 1-step (a) and 5-step (b) feathering. Beam edges indicated by diverging lines. Line at 2 cm depth indicates location of dose profiles and film measurement.



(a)



(b)

Figure 3.45: Computed isodose contours in YX plane for two-step PTV (red) for 1-step (a) and 5-step (b) feathering. Green and blue lines indicate location of Y and X dose profiles, respectively.

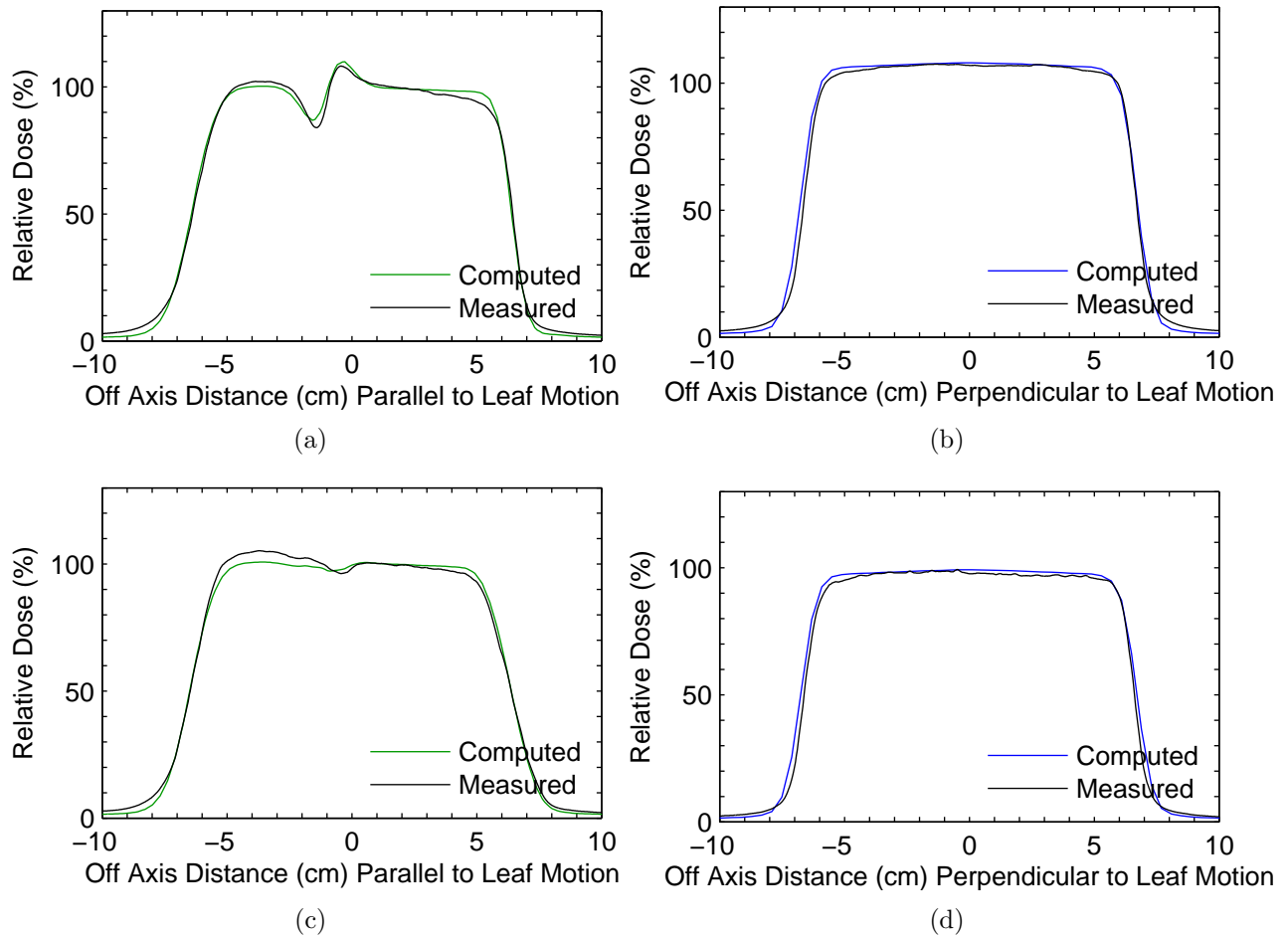


Figure 3.46: Computed vs. measured off-axis dose profiles for two-step PTV with 1-step (a,b) and 5-step (c,d) feathering.

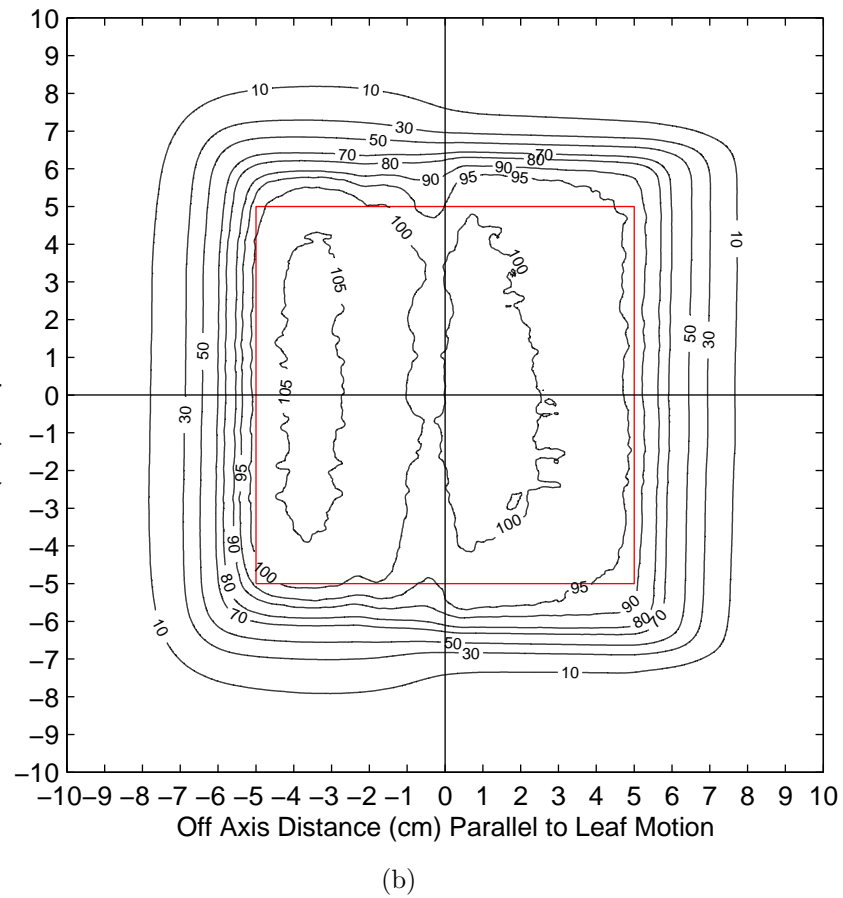
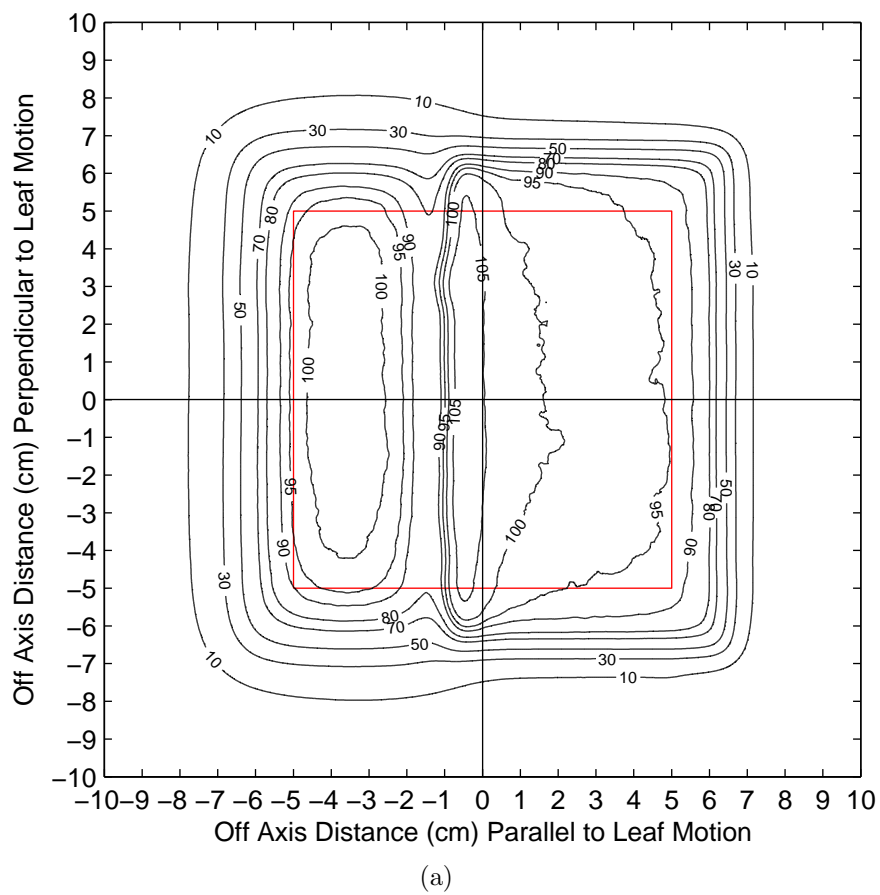


Figure 3.47: Measured isodose contours in YX plane for two-step PTV (red) for 1-step (a) and 5-step (b) feathering.

3.3.3 Wedge PTV

Beam Geometry

The wedge PTV was treated with three abutting beams of 20, 16, and 12 MeV. The beam's eye views of the beams are shown in Figure 3.48. The 20 MeV beam was placed with the abutting edge -1.5 cm off axis and the outer edges of the beam were extended 2.5 cm beyond the outer edge of the PTV. The 16 MeV abutting beam edges were placed at ± 1.5 cm off axis, and the outer edges extended 2.5 cm beyond the PTV boundary. The 12 MeV beam abutted the 16 MeV beam at 1.5 cm off axis and extended 1.5 cm in the y direction beyond the edge of the PTV and extended 2.5 cm in the x direction beyond the PTV edges. The plan was converted to an eMLC aperture, and, therefore, the beam widths in the x direction (perpendicular to leaf motion) were restricted to increments of the finite leaf widths of the eMLC, resulting in the beam edges in the x direction extending 2.6 cm beyond the PTV boundary on both sides. The beam's eye views from the treatment plan created with the discrete Gaussian edge feathering algorithm are shown in Figure 3.49.

Dose Distributions

Dose distributions calculated with the treatment planning system for the wedge PTV are shown in Figures 3.50 and 3.51. Off-axis dose profiles for computed and measured data are presented in Figure 3.52. Measured dose distributions are shown in Figure 3.53. PTV dose-volume statistics are given in Table 3.16. All dose distributions have been normalized to 100% at a reference point located in the center of the highest energy segment at the treatment planning system reference depth.

As seen in the computed dose distributions of Figures 3.50 and 3.51, the treatment plan with discrete Gaussian edge feathering provides a more homogeneous dose than the plan with no feathering. The standard deviation of dose in the PTV is reduced by 5-step feathering from 3.2% to 2.1%. The percentage of PTV volume receiving at least 90% of the prescription dose, $V_{90\%}$, is increased from 97.9% to 99.5%.

Off axis profiles shown in Figure 3.52 show both computed and measured data at the depth of penumbra matching in the PTV. In both sets of data, heterogeneity introduced by

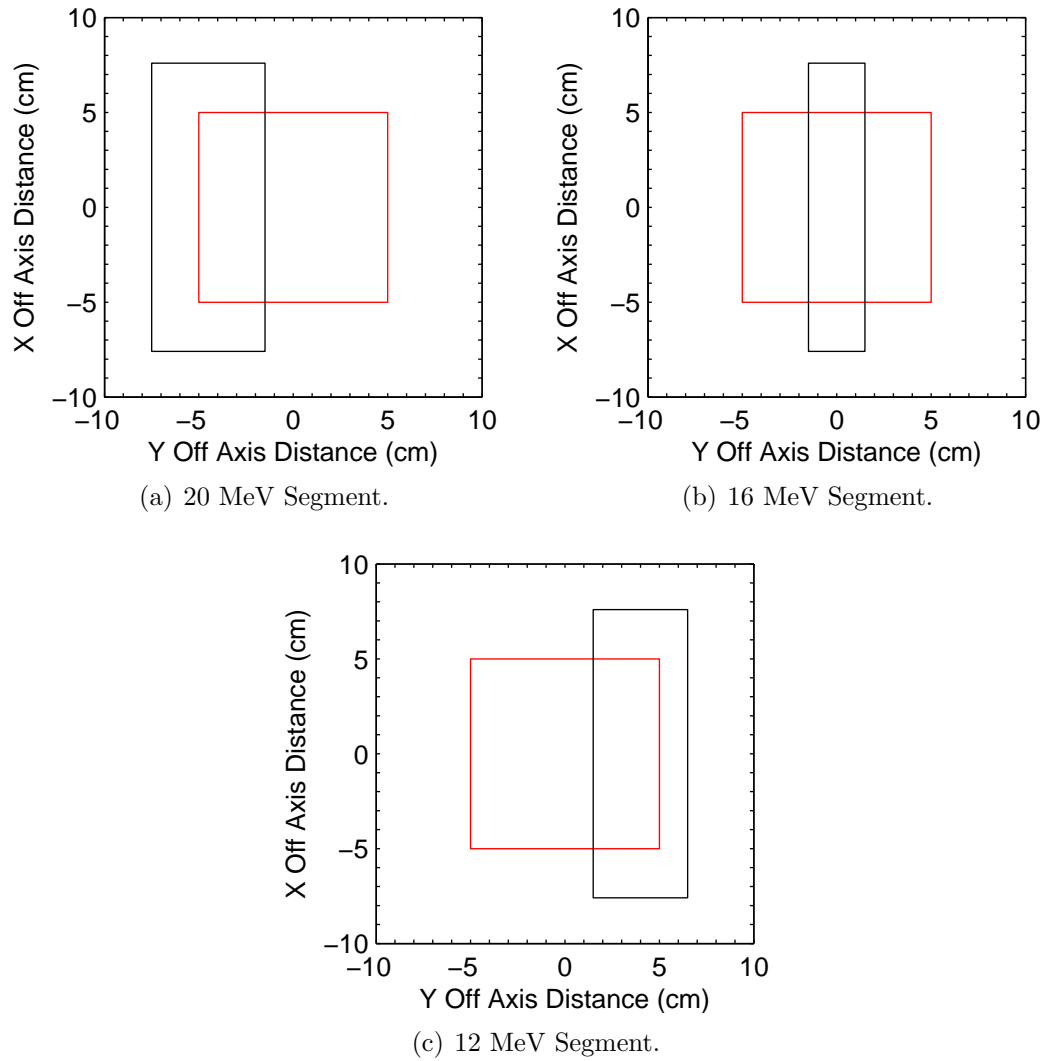


Figure 3.48: Beam's eye view of the wedge PTV segmented field ECT plan. PTV is shown by the red lines and the individual fields are defined by the blue lines. The y axis is parallel to eMLC leaf motion.

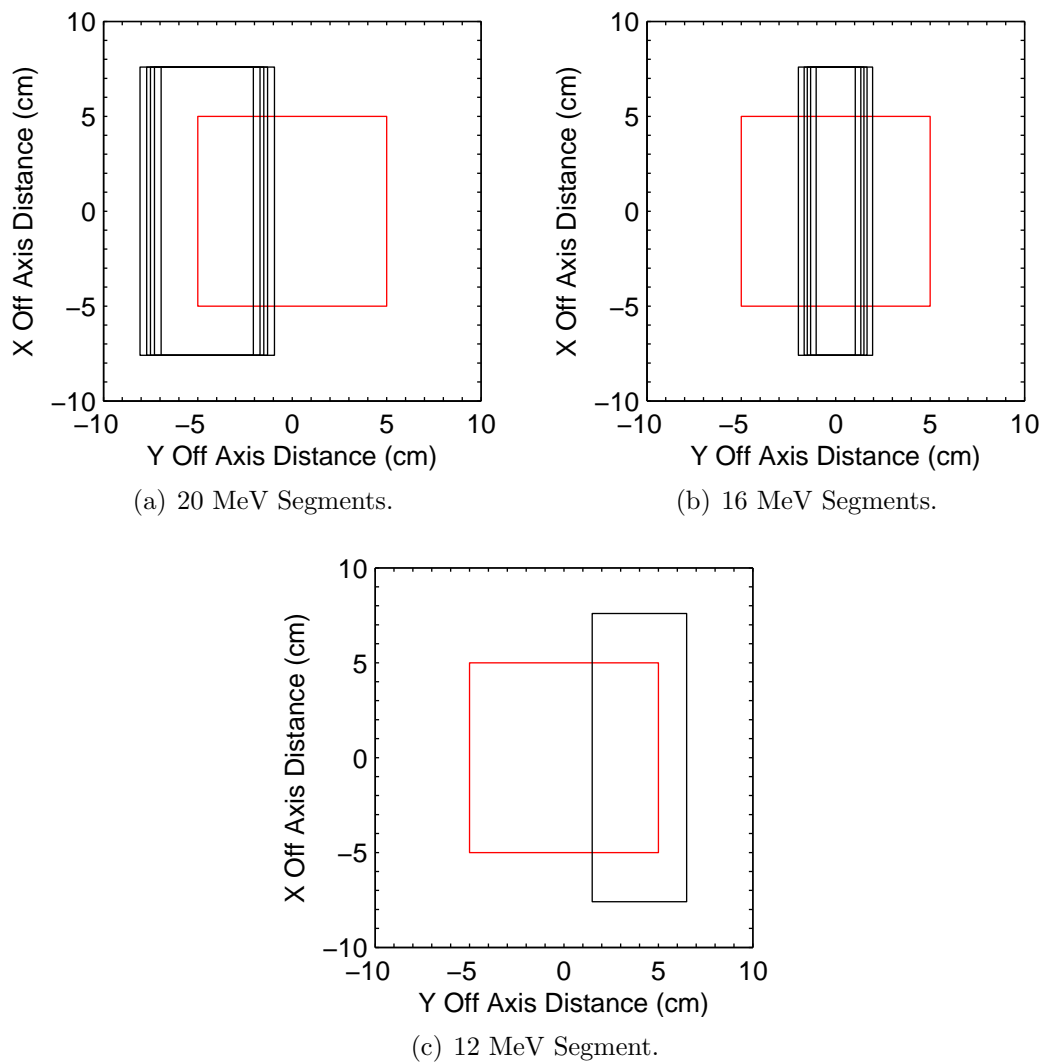


Figure 3.49: Beam's eye view of the wedge PTV segmented field ECT plan with discrete Gaussian edge feathering. PTV is shown by the red lines and the individual fields are defined by the blue lines. The y axis is parallel to eMLC leaf motion.

Table 3.16: Computed dose statistics for wedge PTV treatment plans with no feathering and 5 step Gaussian edge feathering.

Feathering	D_{mean} (%)	σ_D (%)	D_{min} (%)	D_{max} (%)	$V_{90\%}$ (%)
None	96.7	3.2	84.5	103.2	97.9
5 step	96.5	2.1	88.2	101.8	99.5

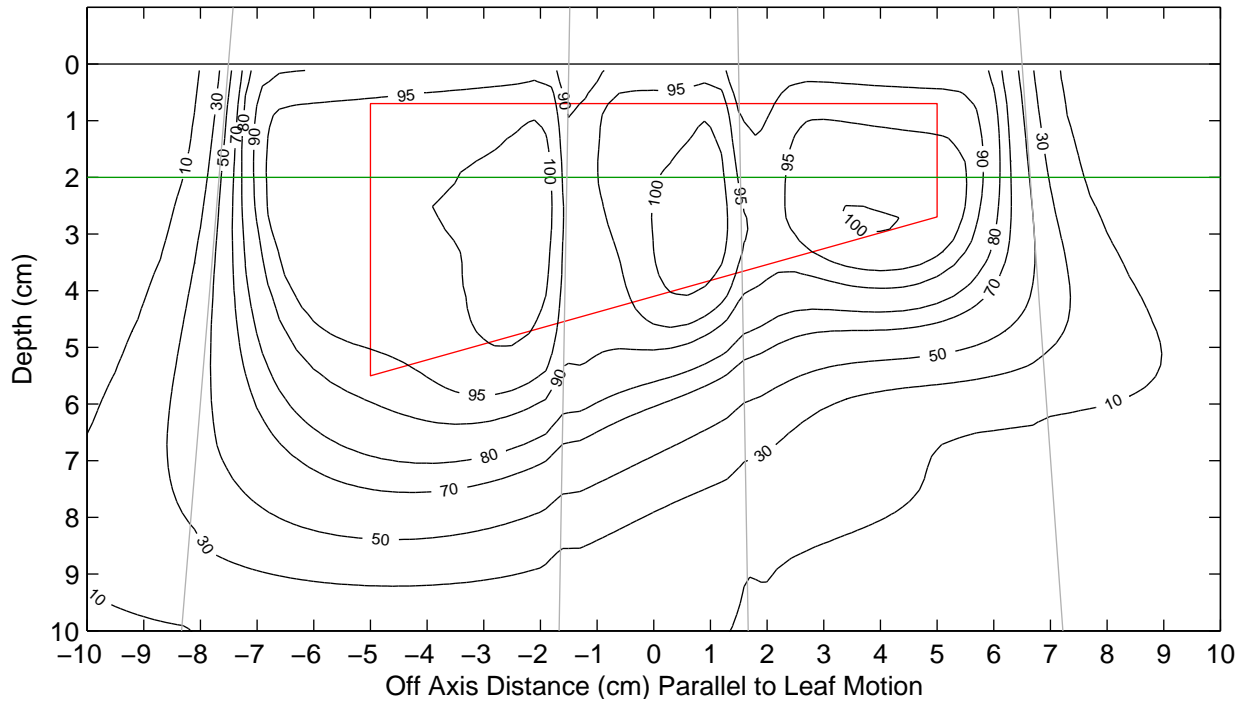
the abutment of unmatched penumbra is reduced along the y axis parallel to leaf motion. Disagreement between the computed and measured profiles likely results from uncertainty in leaf positioning and imprecise field abutment.

The measured isodose planes normal to the electron beam axis presented in Figure 3.53 show similar improvements to dose homogeneity in the abutment region through discrete Gaussian edge feathering as predicted by the calculated distributions. The therapeutic 90% isodose surface encloses more PTV in the plan with edge feathering, and dose gradients inside the PTV are reduced. A slight irregular appearance of the measured distributions is likely introduced by uncertainty in eMLC leaf position.

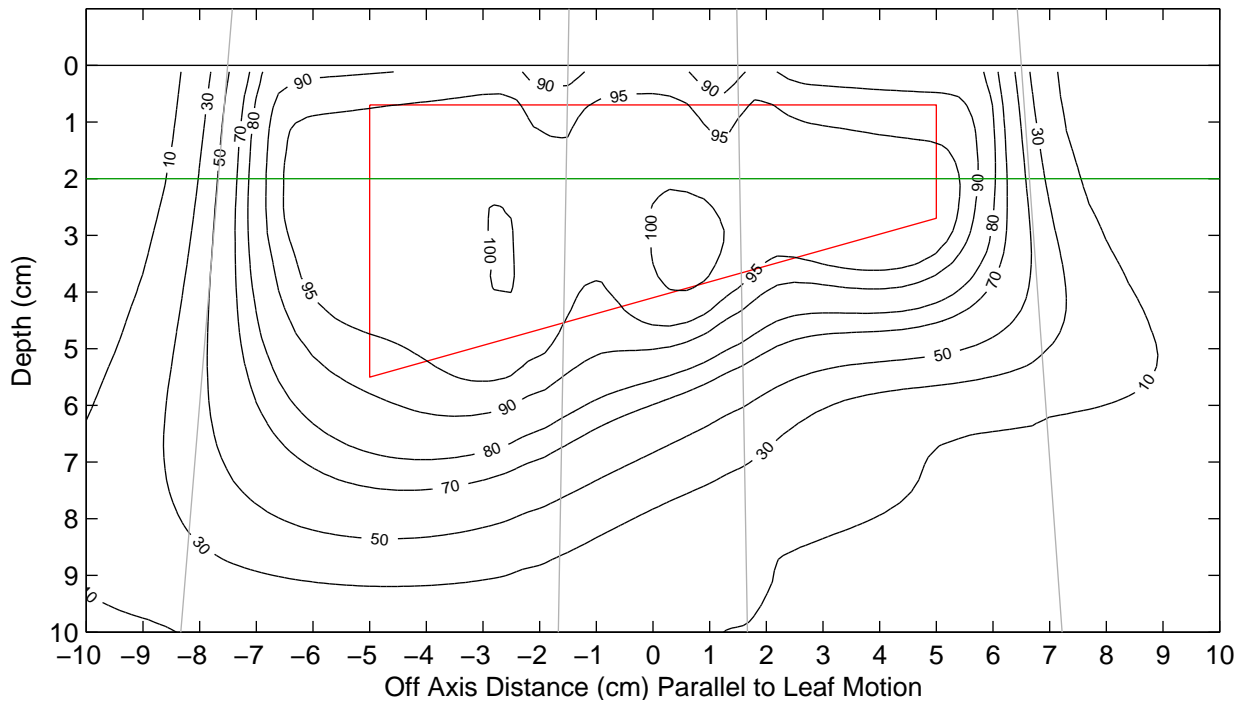
3.3.4 Inverted Well PTV

Beam Geometry

The inverted well PTV was treated with three abutting beams of 20, 12, and 20 MeV. The beam's eye views of the beams are shown in Figure 3.54. The 20 MeV beams were placed with the abutting edges ± 2 cm off axis and the outer edges of the beam were extended 2 cm beyond the outer edge of the PTV. The 12 MeV beam abutted the 20 MeV beams at ± 2 cm off axis and extended 2 beyond the outer PTV edges. The plan was converted to an eMLC aperture, and, therefore, the beam widths in the x direction (perpendicular to leaf motion) were restricted to increments of the finite leaf widths of the eMLC, resulting in the beam edges in the x direction extending 1.6 cm beyond the PTV boundary on both sides. The beam's eye views from the treatment plan created with the discrete Gaussian edge feathering algorithm are shown in Figure 3.55.

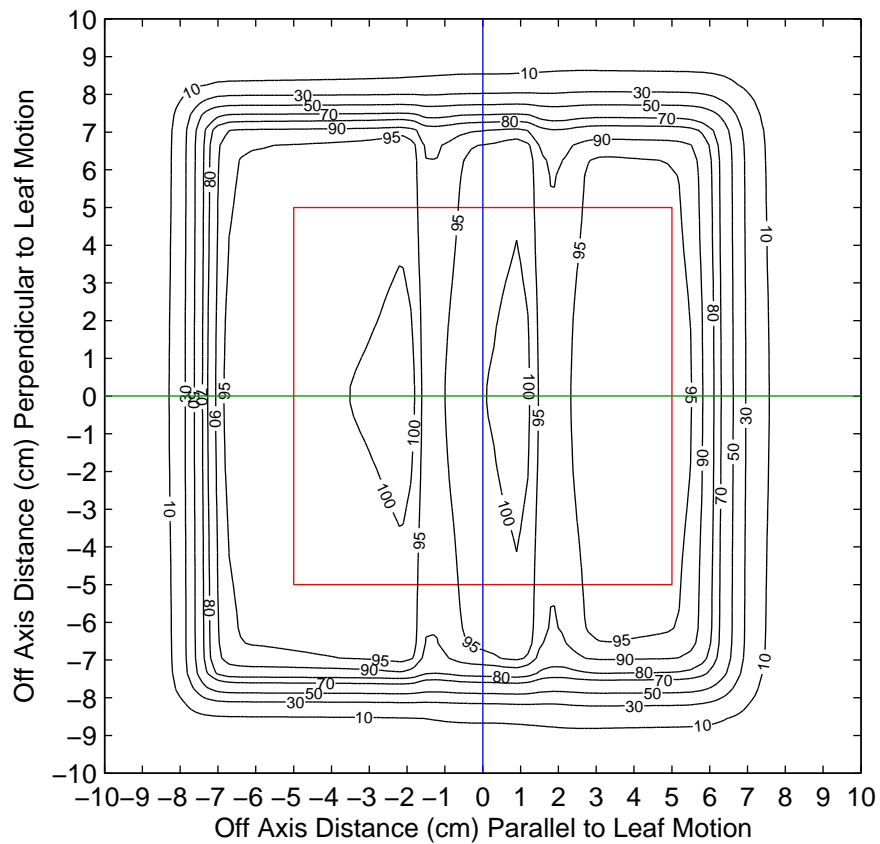


(a)

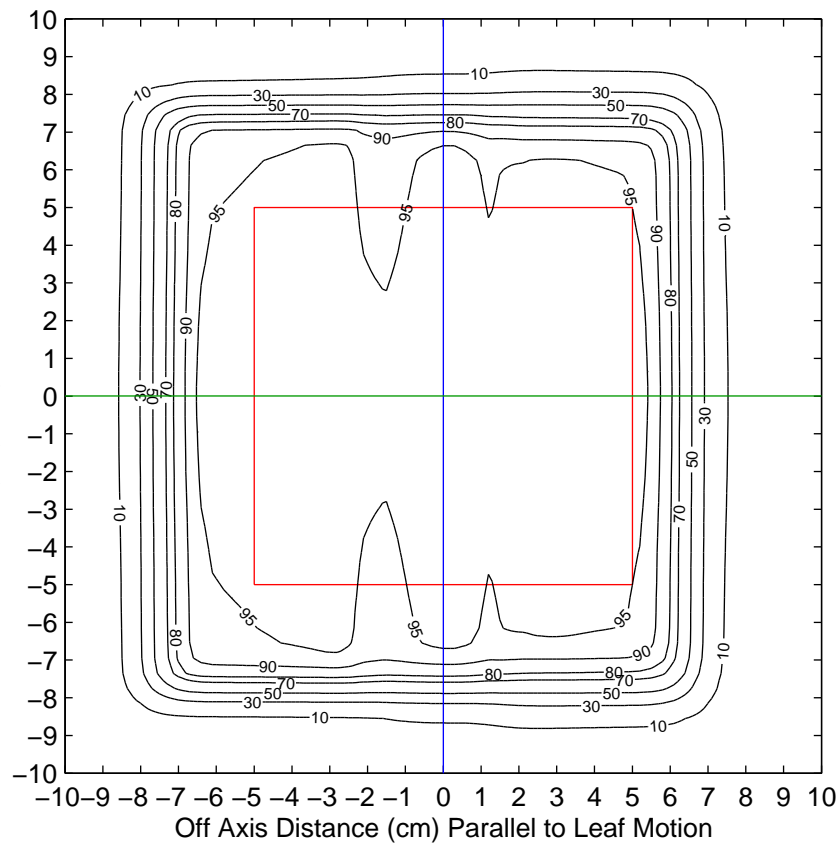


(b)

Figure 3.50: Computed isodose contours in YZ plane for wedge PTV (red) for 1-step (a) and 5-step (b) feathering. Beam edges indicated by diverging lines. Line at 2 cm depth indicates location of dose profiles and film measurement.



(a)



(b)

Figure 3.51: Computed isodose contours in YX plane for wedge PTV (red) for 1-step (a) and 5-step (b) feathering. Green and blue lines indicate location of Y and X dose profiles, respectively.

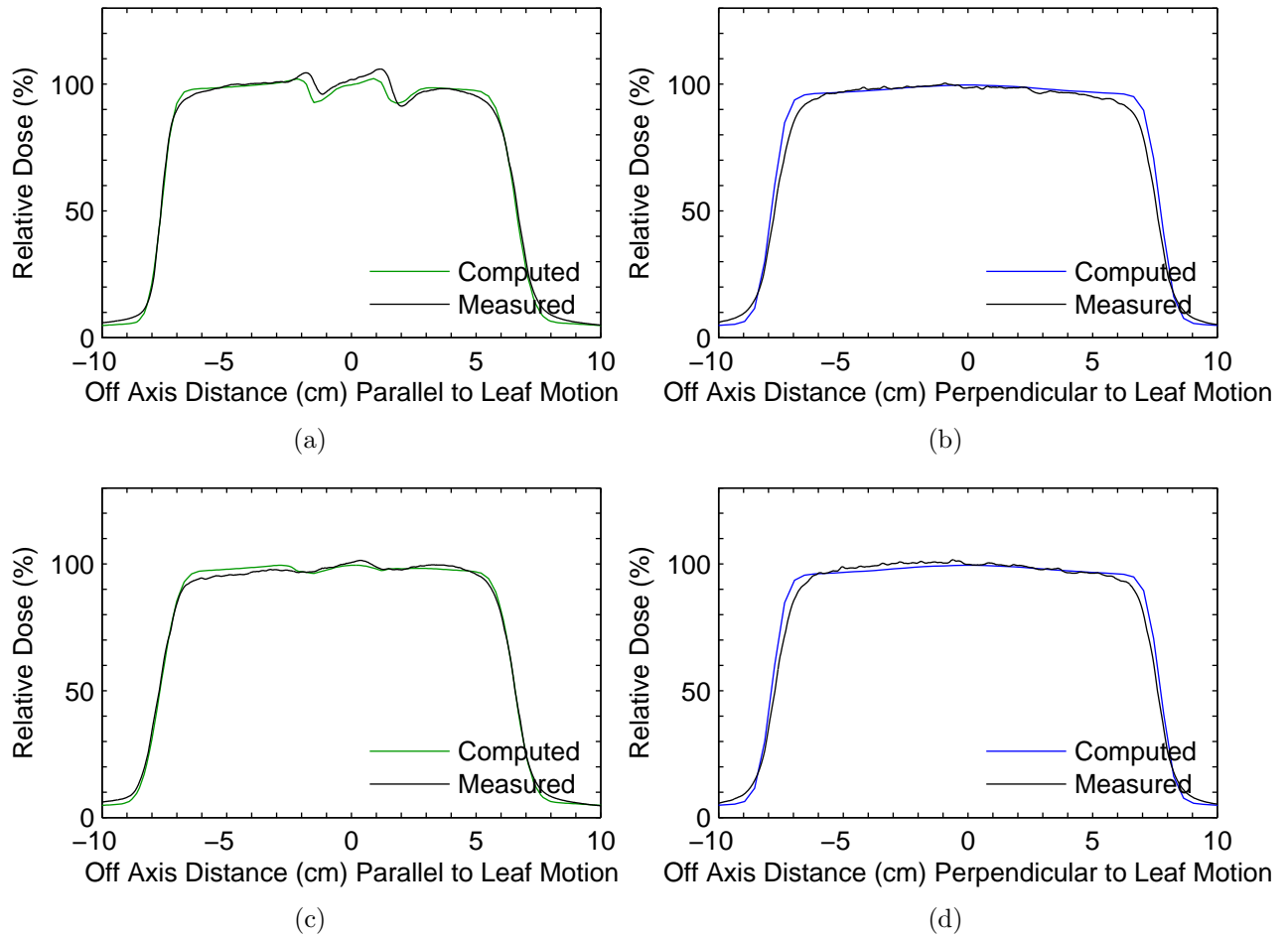
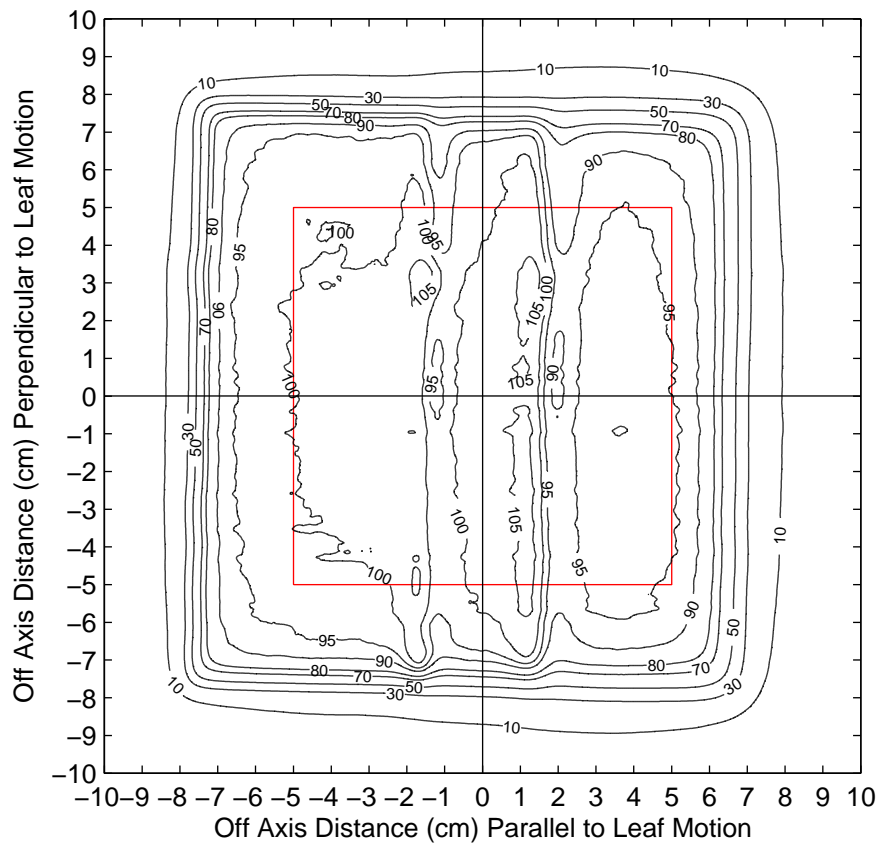
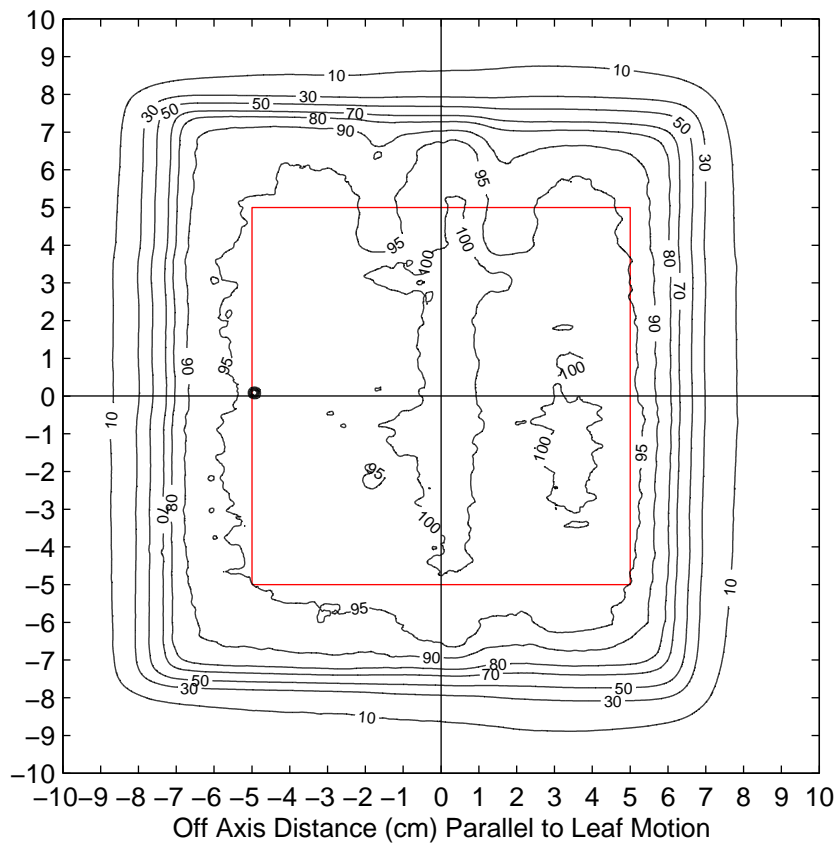


Figure 3.52: Computed vs. measured off-axis dose profiles for wedge PTV with 1-step (a,b) and 5-step (c,d) feathering.



(a)



(b)

Figure 3.53: Measured isodose contours in YX plane for wedge PTV (red) for 1-step (a) and 5-step (b) feathering.

Dose Distributions

Dose distributions calculated with the treatment planning system for the inverted well PTV are shown in Figures 3.56 and 3.57. Off-axis dose profiles for computed and measured data are presented in Figure 3.58. Measured dose distributions are shown in Figure 3.59. PTV dose-volume statistics are given in Table 3.17. All dose distributions have been normalized to 100% at a reference point located in the center of the highest energy segment at the treatment planning system reference depth.

As seen in the computed dose distributions of Figures 3.56 and 3.57, the treatment plan with discrete Gaussian edge feathering provides a more homogeneous dose than the plan with no feathering. The standard deviation of dose in the PTV is reduced by 5-step feathering from 5.1% to 3.1%. The percentage of PTV volume receiving at least 90% of the prescription dose, $V_{90\%}$, is increased from 88.8% to 97.0%.

Off axis profiles shown in Figure 3.58 show both computed and measured data at the depth of penumbra matching in the PTV. In both sets of data, heterogeneity introduced by the abutment of unmatched penumbra is reduced along the y axis parallel to leaf motion. Disagreement between the computed and measured profiles likely results from uncertainty in leaf positioning and imprecise field abutment.

The measured isodose planes normal to the electron beam axis presented in Figure 3.59 show similar improvements to dose homogeneity in the abutment region through discrete Gaussian edge feathering as predicted by the calculated distributions. The therapeutic 90% isodose surface encloses more PTV in the plan with edge feathering, and dose gradients inside the PTV are reduced. A slight irregular appearance of the measured distributions is likely introduced by uncertainty in eMLC leaf position.

3.3.5 Concentric Cylinders PTV

Beam Geometry

The 3D concentric cylinders PTV was treated with three abutting beams of 12, 20, and 12 MeV. The beam's eye views of the beams are shown in Figure 3.60. The 20 MeV beam was placed to form a circle with a diameter of 6 cm on central axis extending 0.5 cm beyond

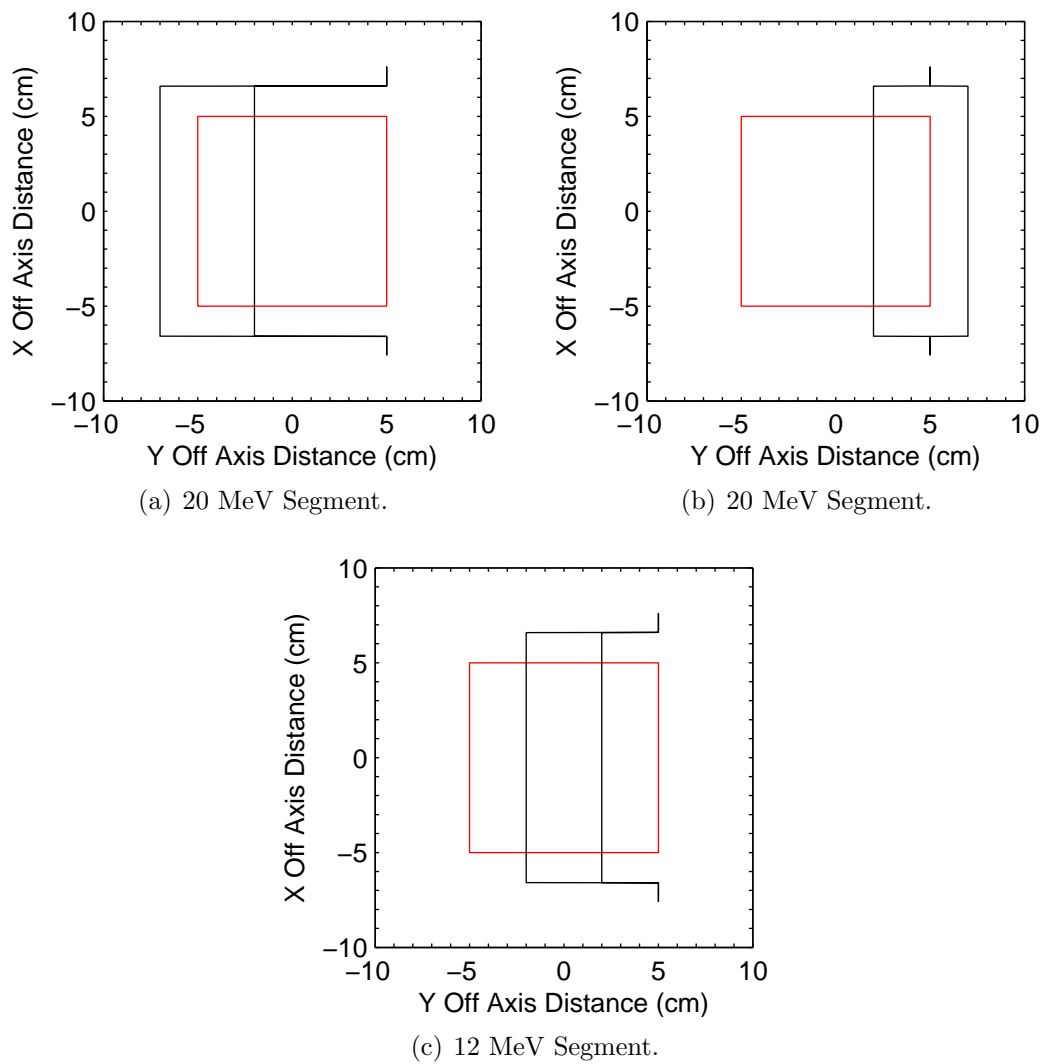


Figure 3.54: Beam's eye view of the inverted well PTV segmented field ECT plan. PTV is shown by the red lines and the individual fields are defined by the black lines. The y axis is parallel to eMLC leaf motion.

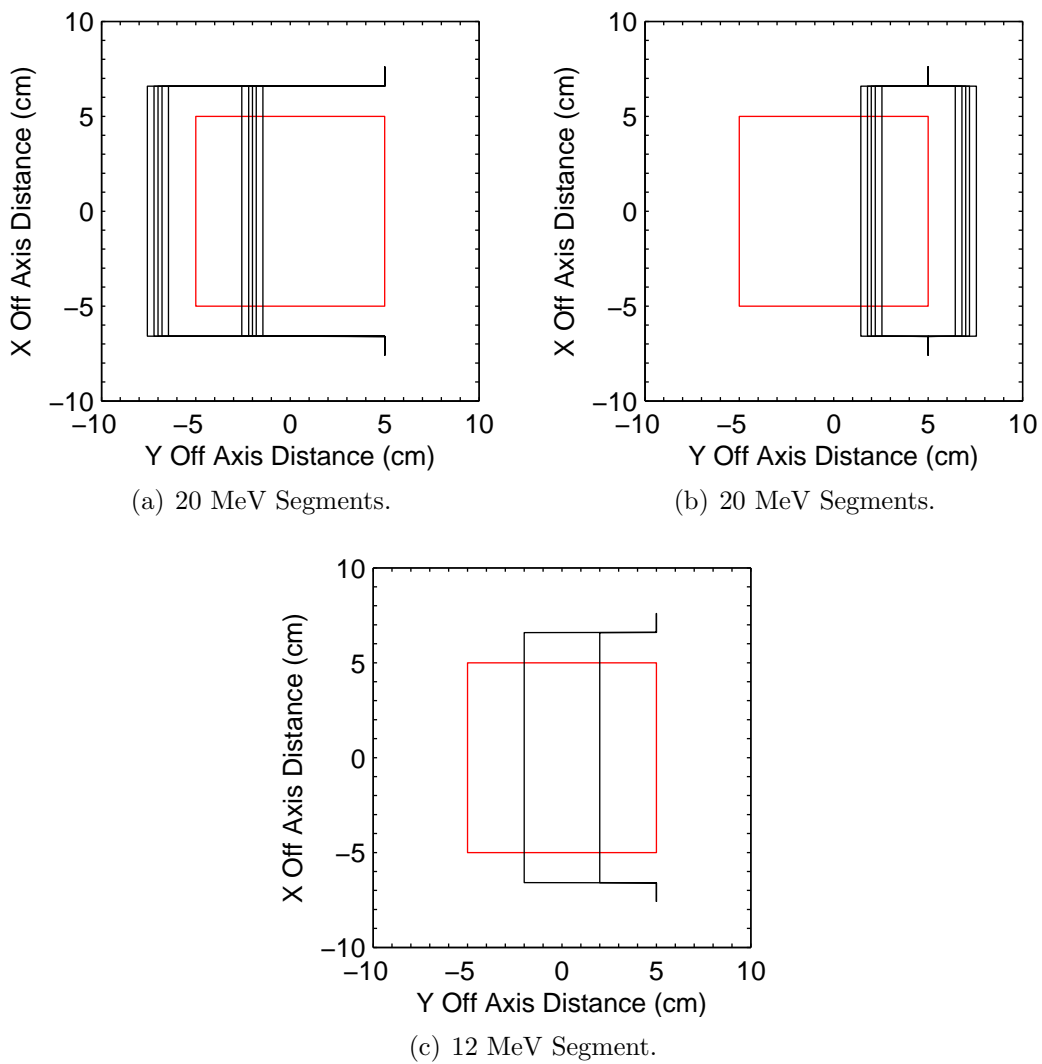
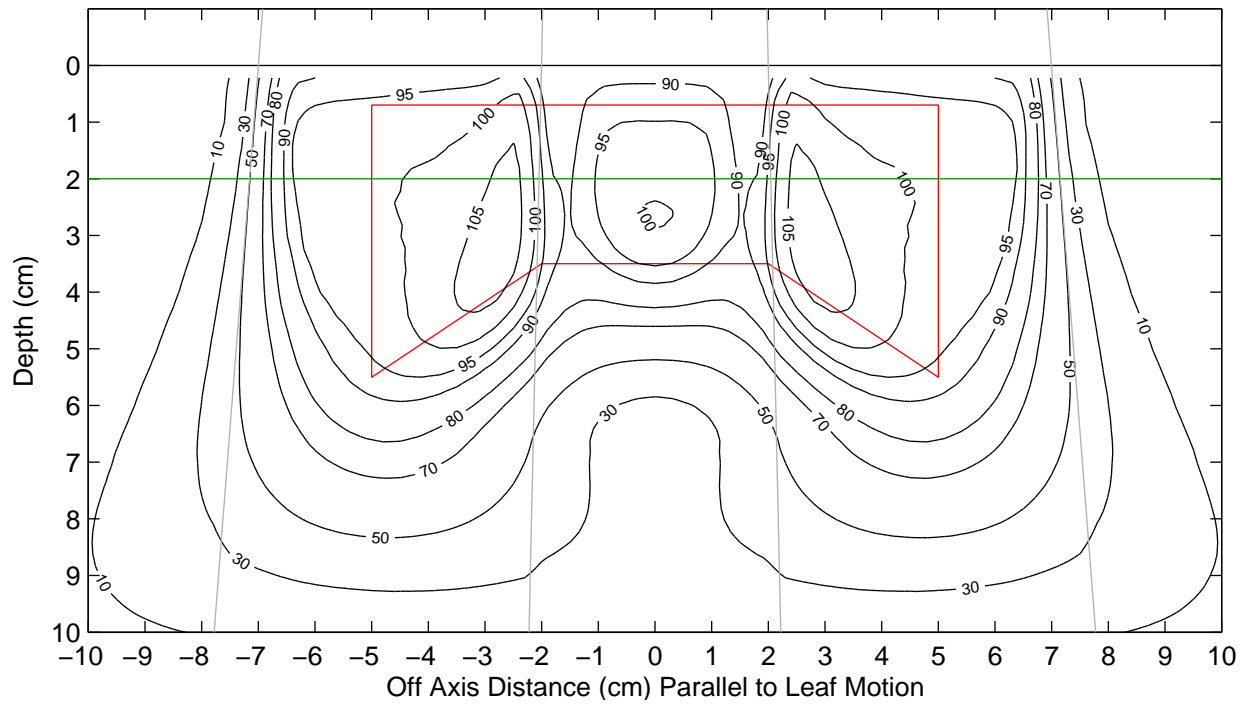
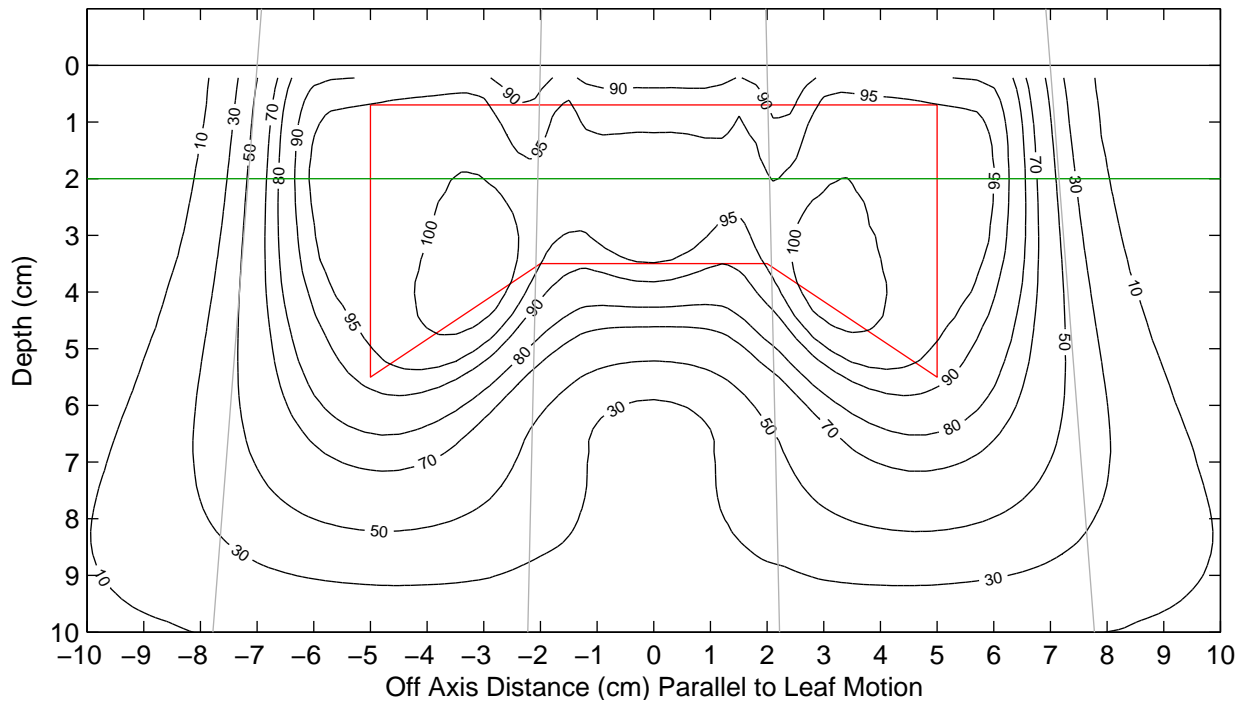


Figure 3.55: Beam's eye view of the inverted well PTV segmented field ECT plan with discrete Gaussian edge feathering. PTV is shown by the red lines and the individual fields are defined by the black lines. The y axis is parallel to eMLC leaf motion.

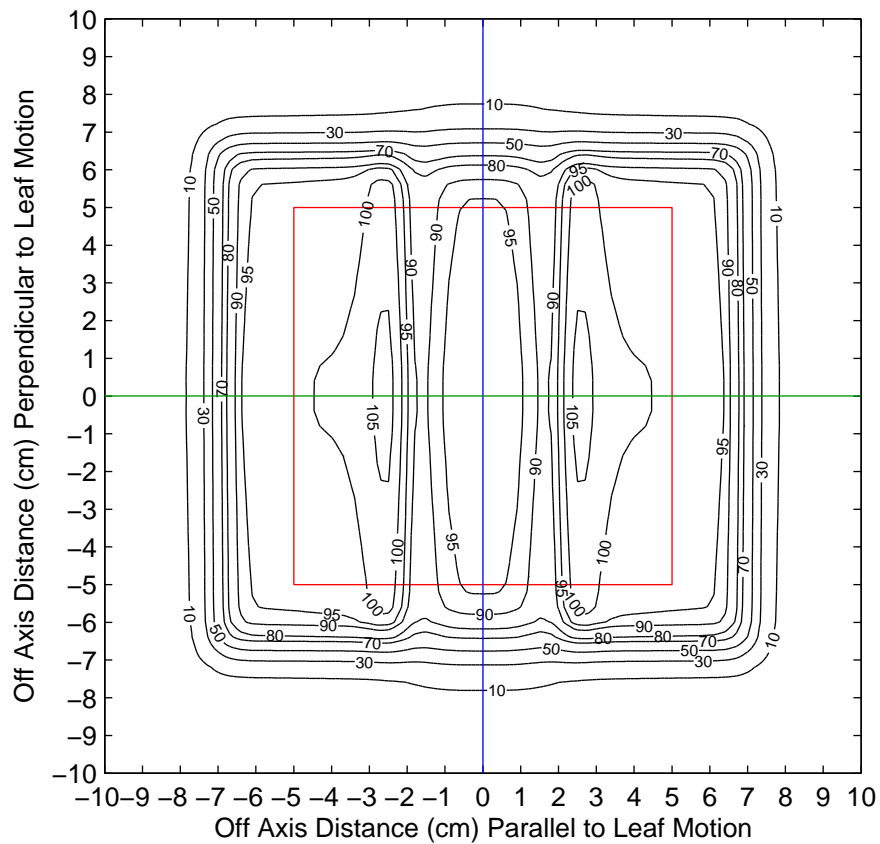


(a)

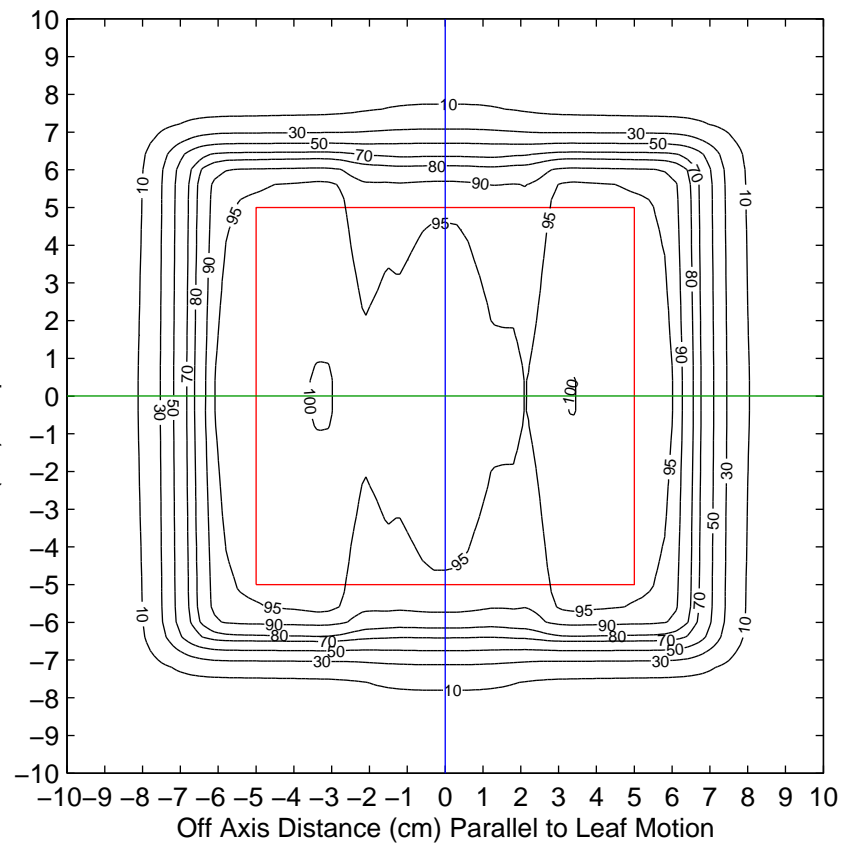


(b)

Figure 3.56: Computed isodose contours in YZ plane for inverted well PTV (red) for 1-step (a) and 5-step (b) feathering. Beam edges indicated by diverging lines. Line at 2 cm depth indicates location of dose profiles and film measurement.



(a)



(b)

Figure 3.57: Computed isodose contours in YX plane for inverted well PTV (red) for 1-step (a) and 5-step (b) feathering. Green and blue lines indicate location of Y and X dose profiles, respectively.

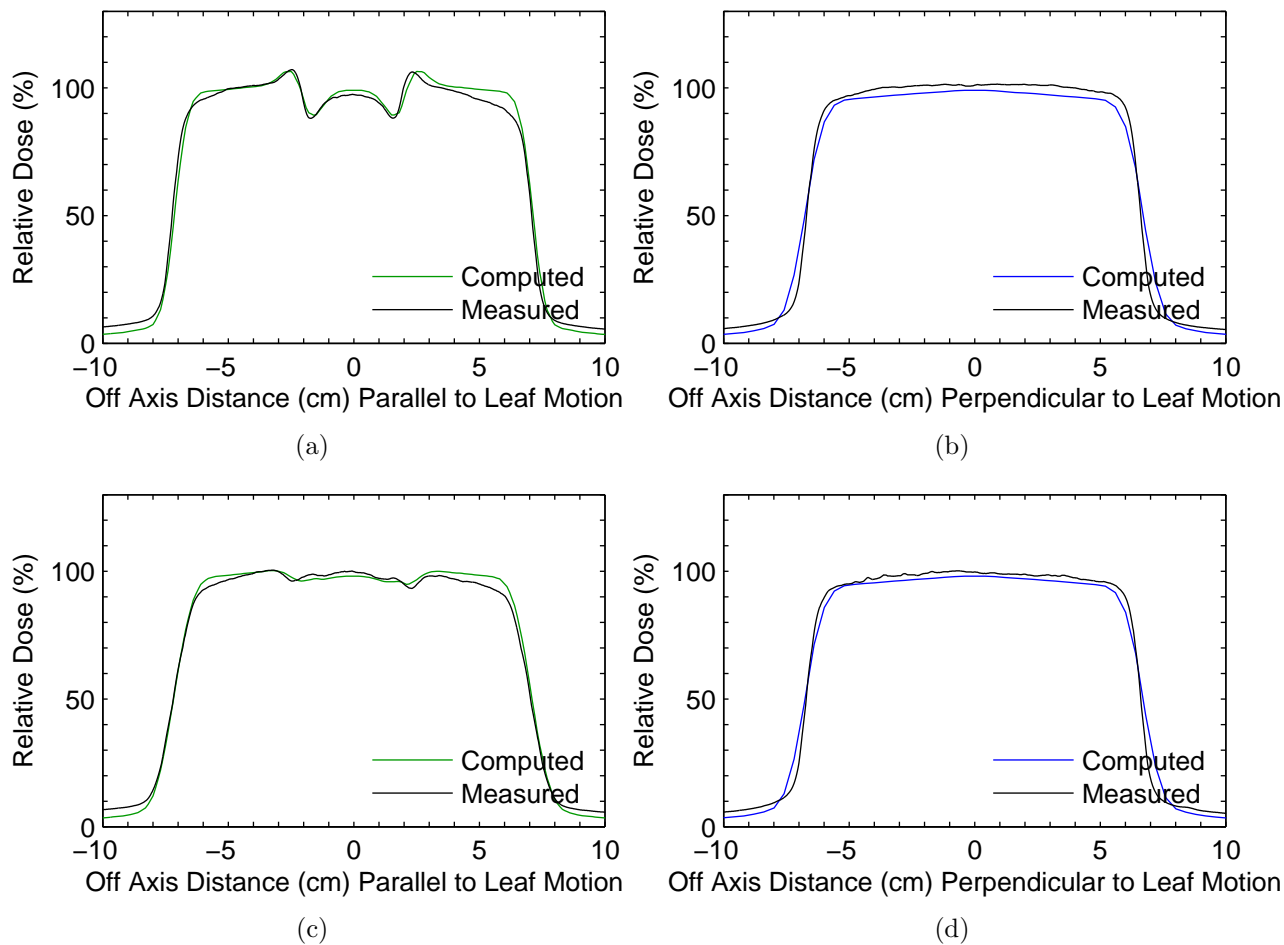
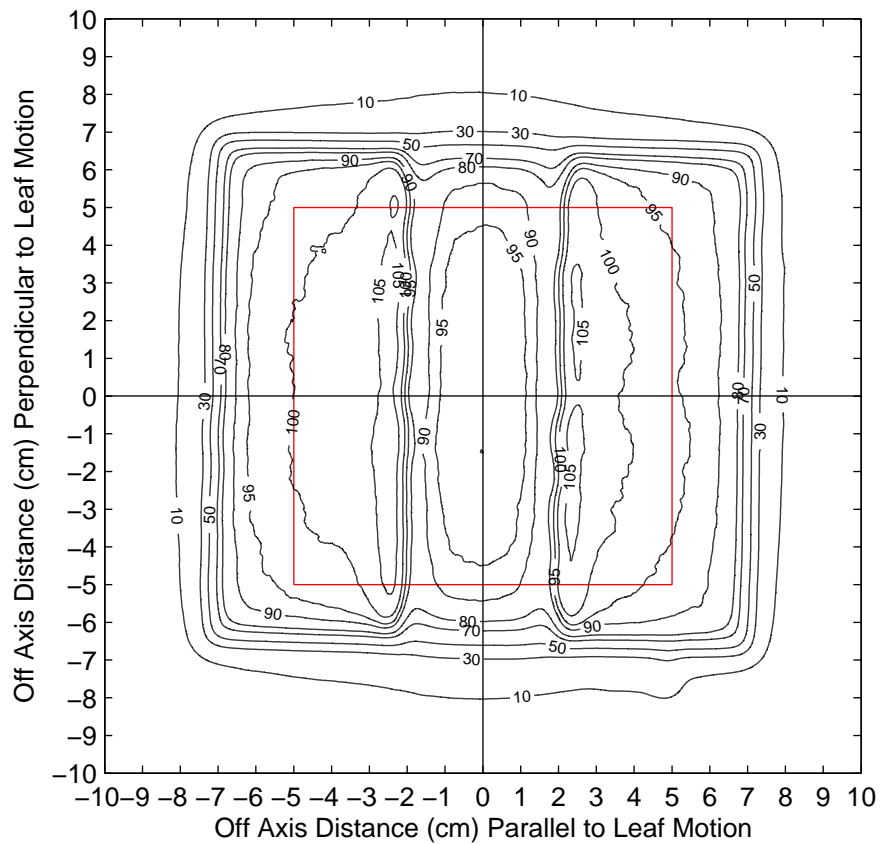


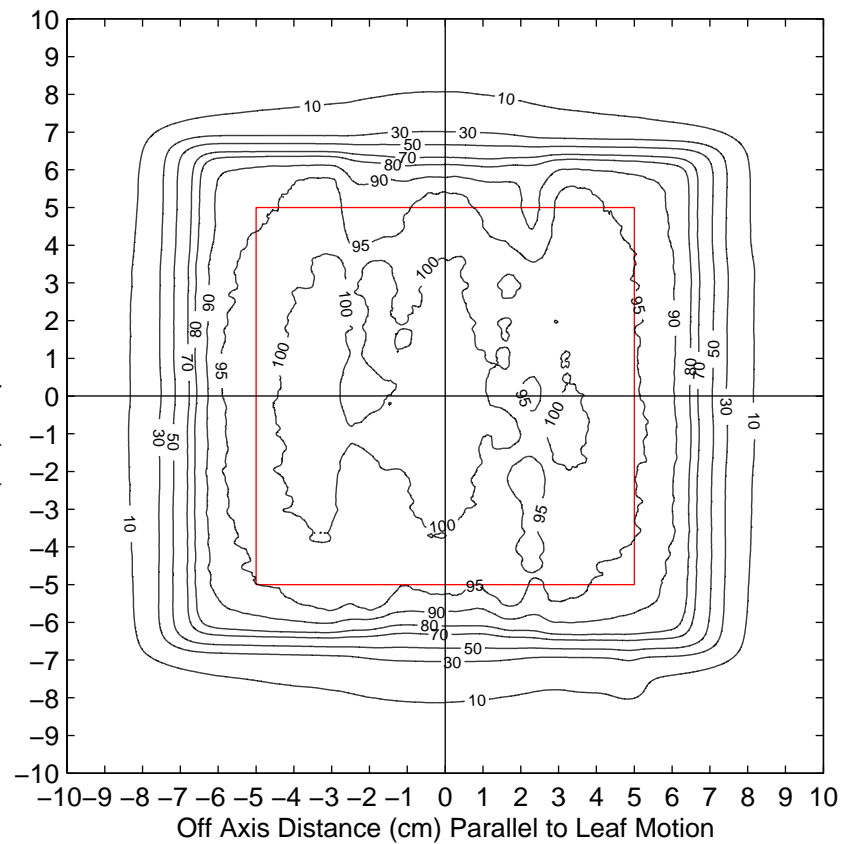
Figure 3.58: Computed vs. measured off-axis dose profiles for inverted well PTV with 1-step (a,b) and 5-step (c,d) feathering.

Table 3.17: Computed dose statistics for inverted well PTV treatment plans with no feathering and 5 step Gaussian edge feathering.

Feathering	D_{mean} (%)	σ_D (%)	D_{min} (%)	D_{max} (%)	$V_{90\%}$ (%)
None	97.2	5.1	80.6	108.3	88.8
5 step	96.1	3.1	83.8	103.8	97.0



(a)



(b)

Figure 3.59: Measured isodose contours in YX plane for inverted well PTV (red) for 1-step (a) and 5-step (b) feathering.

the inner cylinder of the PTV. The 12 MeV beams were positioned to form a ring field with the inner section of the ring abutting the 20 MeV segment and the outer section of the ring extending 1.5 cm beyond the outer edge of the PTV (inner diameter = 6 cm and outer diameter = 15 cm). The plan was converted to an eMLC aperture, and, therefore, the beam widths in the x direction (perpendicular to leaf motion) were restricted to increments of the finite leaf widths of the eMLC, resulting in a cropping of the inner circle x width to 5 cm rather than the desired 6 cm. Likewise, the x width of the outer 12 MeV boundary was 15.2 cm rather than 15 cm. The beam's eye views from the treatment plan created with the 1D discrete Gaussian edge feathering algorithm are shown in Figure 3.61. The beam's eye views from the treatment plan created with the 2D discrete Gaussian edge feathering algorithm are shown in Figure 3.62. The beam's eye views from the treatment plan created with the 2D discrete Gaussian edge feathering algorithm with infinitesimal leaf width are shown in Figure 3.63.

Dose Distributions

Dose distributions calculated with the treatment planning system for the concentric cylinders PTV are shown in Figures 3.64, 3.65(a), 3.66, and 3.67(a). Off-axis dose profiles for computed and measured data are presented in Figure 3.68. Measured dose distributions are shown in Figures 3.70 and 3.71. PTV dose-volume statistics are given in Table 3.18. All dose distributions have been normalized to 100% at a reference point located in the center of the highest energy segment at the treatment planning system reference depth.

As seen in the computed dose distributions of Figures 3.64 and 3.66, the treatment plan with 1D discrete Gaussian edge feathering provides a more homogeneous dose than the plan with no feathering along the y axis parallel to leaf motion. The heterogeneity introduced by the abutment of unmatched penumbras along the x axis perpendicular to leaf motion remains unaffected by the 1D edge feathering. The standard deviation of dose in the PTV is reduced by 1D 5-step feathering from 4.8% to 3.9%. The percentage of PTV volume receiving at least 90% of the prescription dose, $V_{90\%}$, is increased from 97.0% to 98.2%.

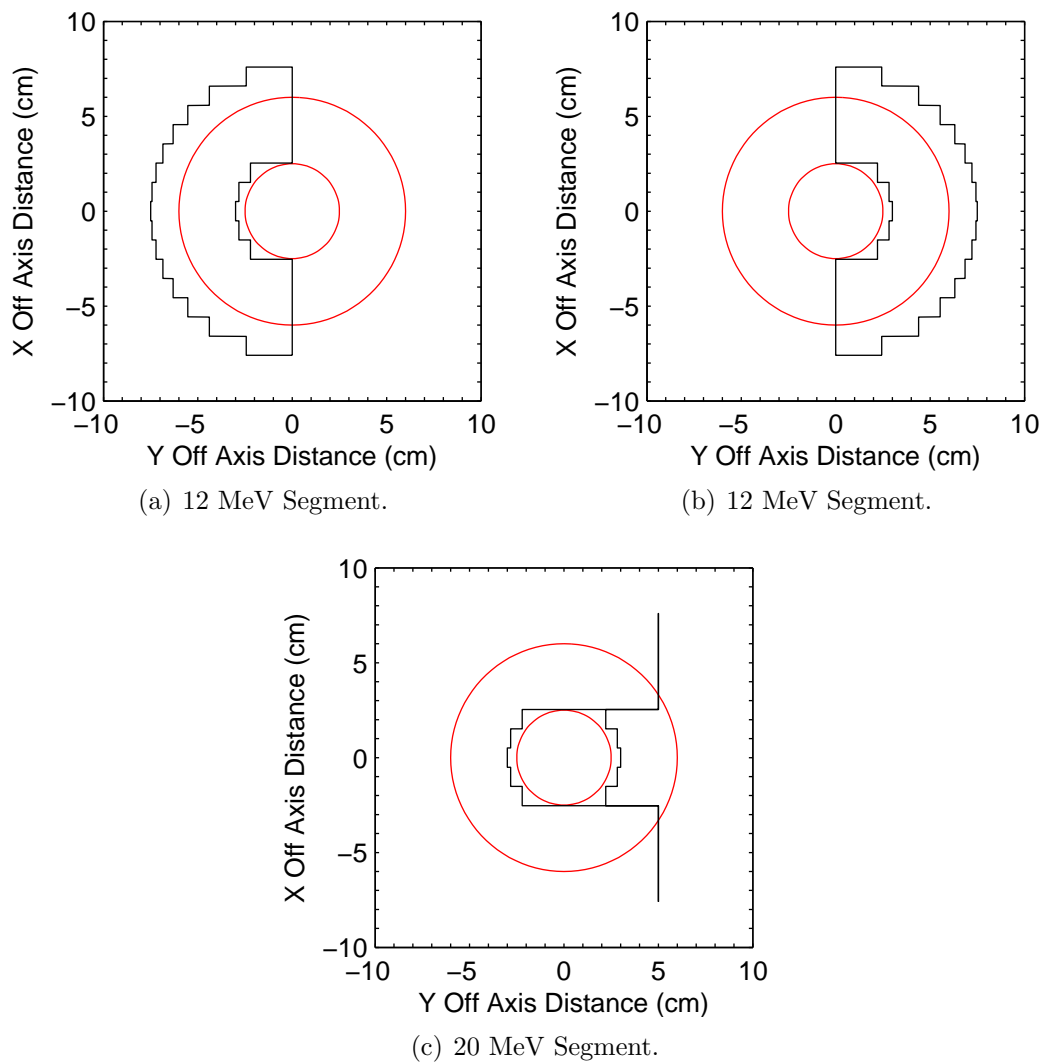


Figure 3.60: Beam's eye view of the concentric cylinders PTV segmented field ECT plan. PTV is shown by the red lines and the individual fields are defined by the black lines. The y axis is parallel to eMLC leaf motion.

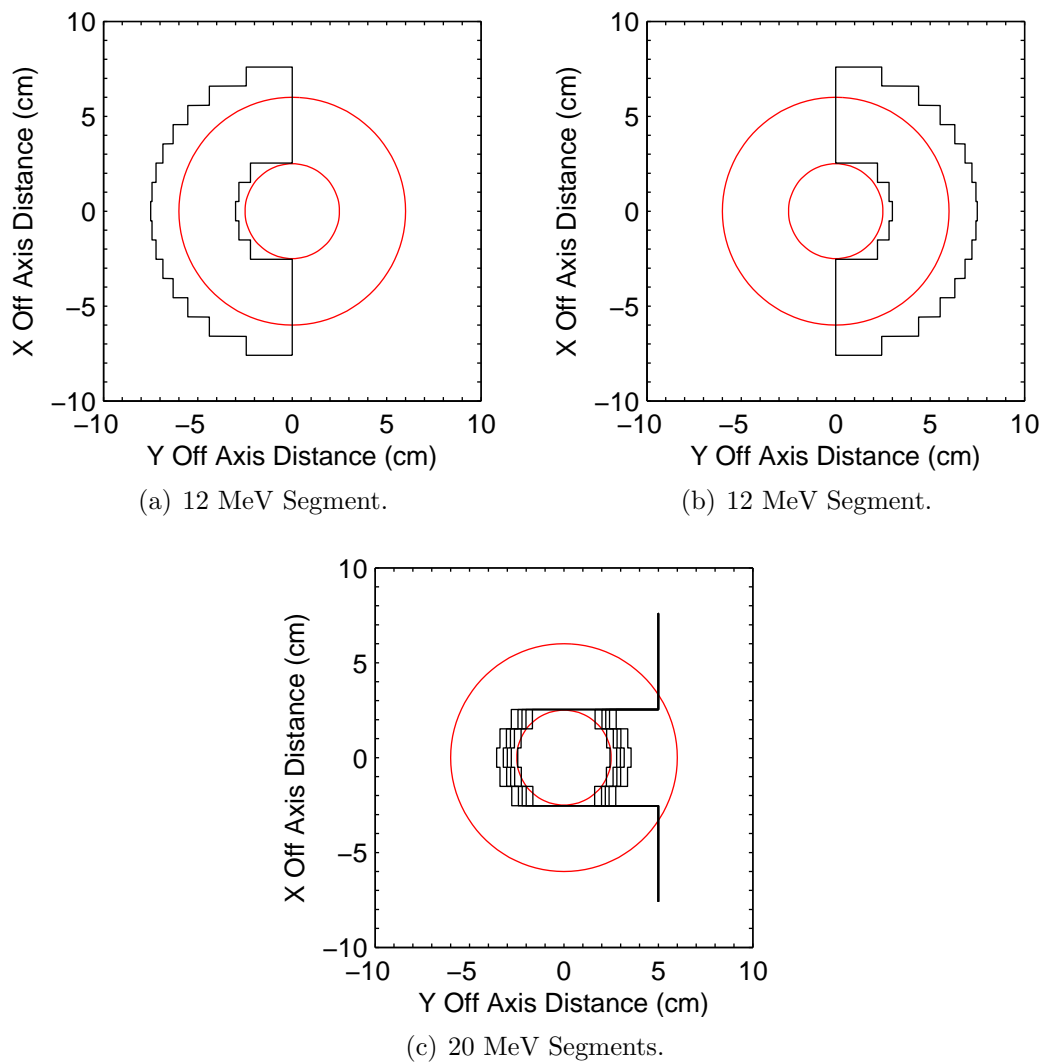


Figure 3.61: Beam's eye view of the concentric cylinders PTV segmented field ECT plan with 1D discrete Gaussian edge feathering. PTV is shown by the red lines and the individual fields are defined by the black lines. The y axis is parallel to eMLC leaf motion.

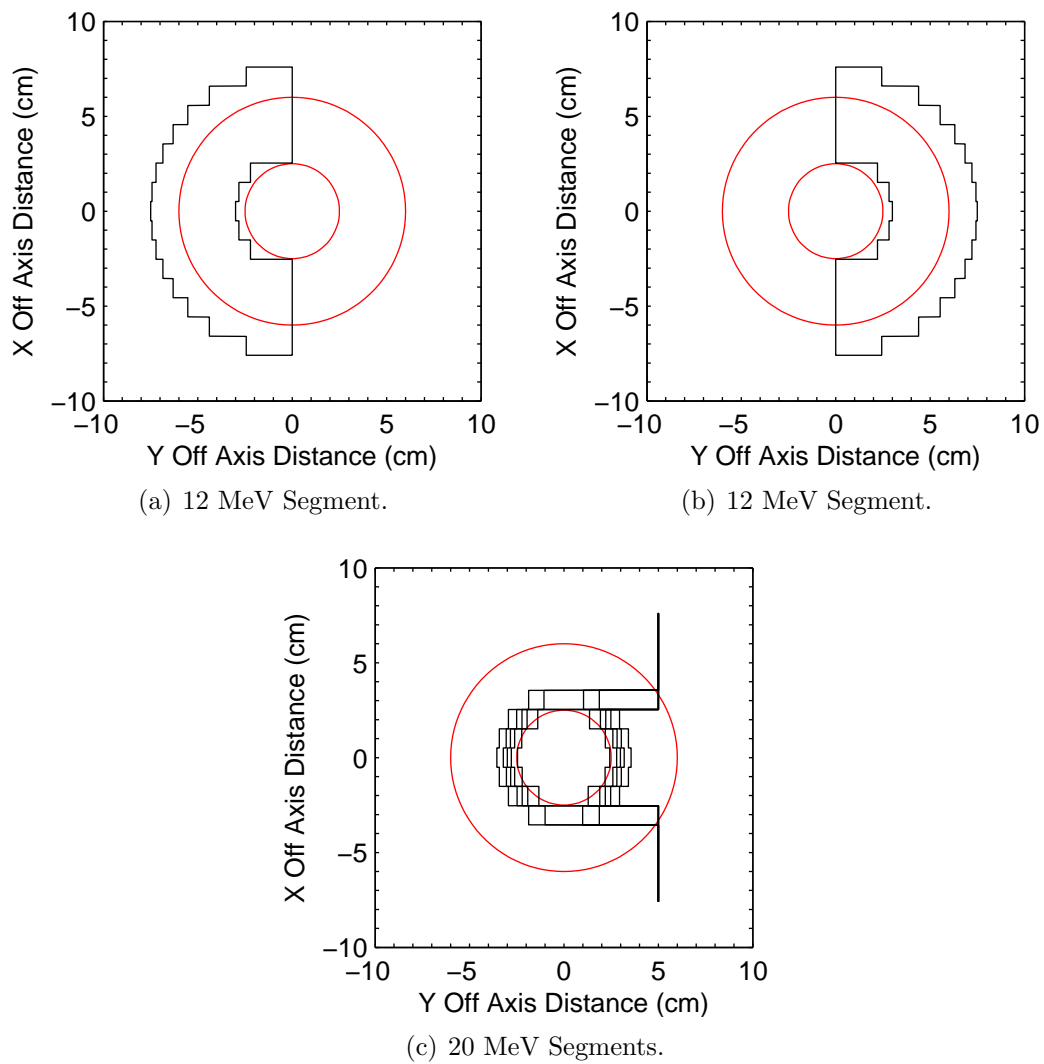


Figure 3.62: Beam's eye view of the concentric cylinders PTV segmented field ECT plan with 2D discrete Gaussian edge feathering. PTV is shown by the red lines and the individual fields are defined by the black lines. The y axis is parallel to eMLC leaf motion.

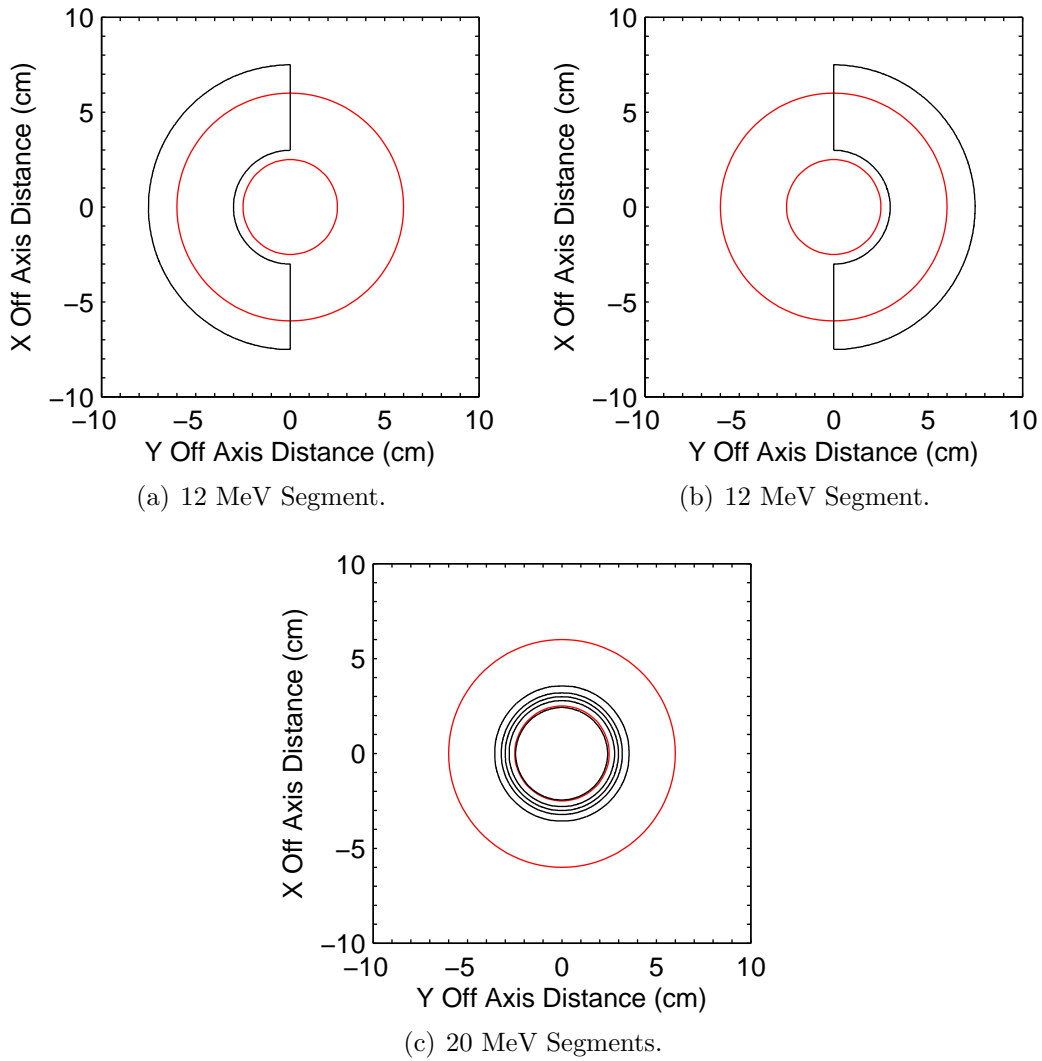
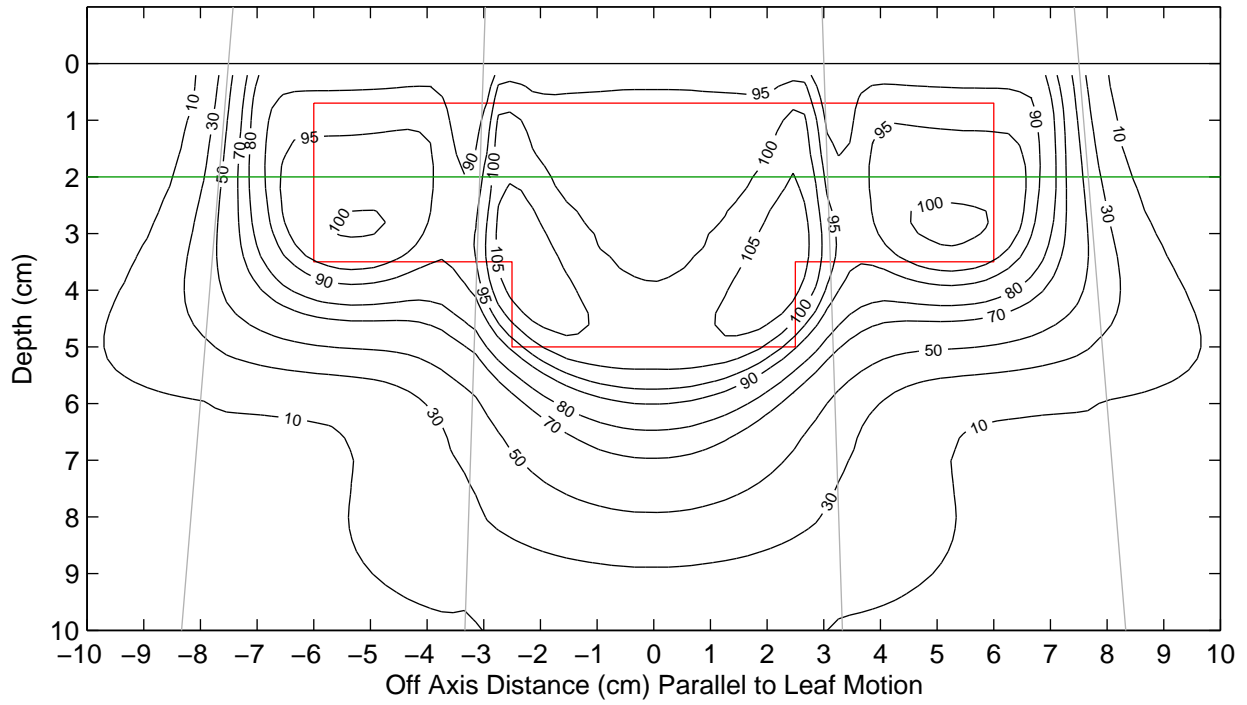


Figure 3.63: Beam's eye view of the concentric cylinders PTV segmented field ECT plan with 2D discrete Gaussian edge feathering and infinitesimal eMLC leaf width. PTV is shown by the red lines and the individual fields are defined by the black lines. The y axis is parallel to eMLC leaf motion.

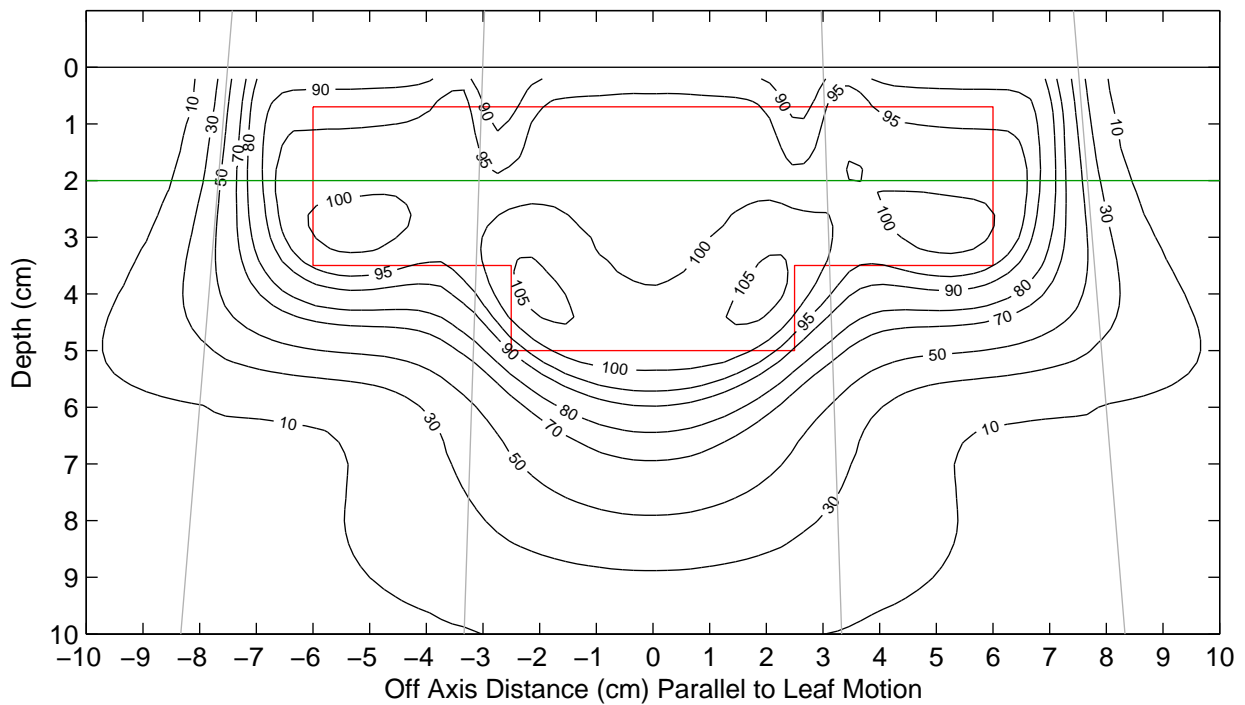
As seen in the computed dose distributions of Figures 3.65(a) and 3.67(a), the treatment plan with 2D discrete Gaussian edge feathering provides a more homogeneous dose than the plan with no feathering along the y axis parallel to leaf motion. However, the heterogeneity along the x axis perpendicular to leaf motion is made worse by the 2D edge feathering due to the finite eMLC leaf width obstructing the correct implementation of the feathering solution. The large increase in dose in the abutment regions perpendicular to leaf motion results from overlap of the abutting segments. The standard deviation of dose in the PTV is increased by 2D 5-step feathering from 4.8% to 5.3%. The percentage of PTV volume receiving at least 90% of the prescription dose, $V_{90\%}$, is increased from 97.0% to 99.3%, and the maximum dose in the PTV is increased from 113.0% to 122.0%.

Off axis profiles shown in Figure 3.68 show both computed and measured data at the depth of penumbra matching in the PTV. In both 1D and 2D feathering, heterogeneity introduced by the abutment of unmatched penumbra is reduced along the y axis parallel to leaf motion. Along the x axis perpendicular to leaf motion, dose heterogeneity is unaffected by the 1D feathering algorithm and is made worse by the 2D feathering algorithm. Disagreement between the computed and measured profiles likely results from uncertainty in leaf positioning and imprecise field abutment.

The measured isodose planes normal to the electron beam axis presented in Figure 3.70 and 3.71 show similar improvements to dose homogeneity in the abutment region parallel to leaf motion through 1D and 2D discrete Gaussian edge feathering as predicted by the calculated distributions. The measurements show the heterogeneity introduced by incorrect implementation of the 2D feathering solution restricted by the finite eMLC leaf width along the x axis perpendicular to leaf motion. The therapeutic 90% isodose surface encloses more PTV in the plan with 1D edge feathering, and dose gradients inside the PTV are reduced. A slight irregular appearance of the measured distributions is likely introduced by uncertainty in eMLC leaf position.

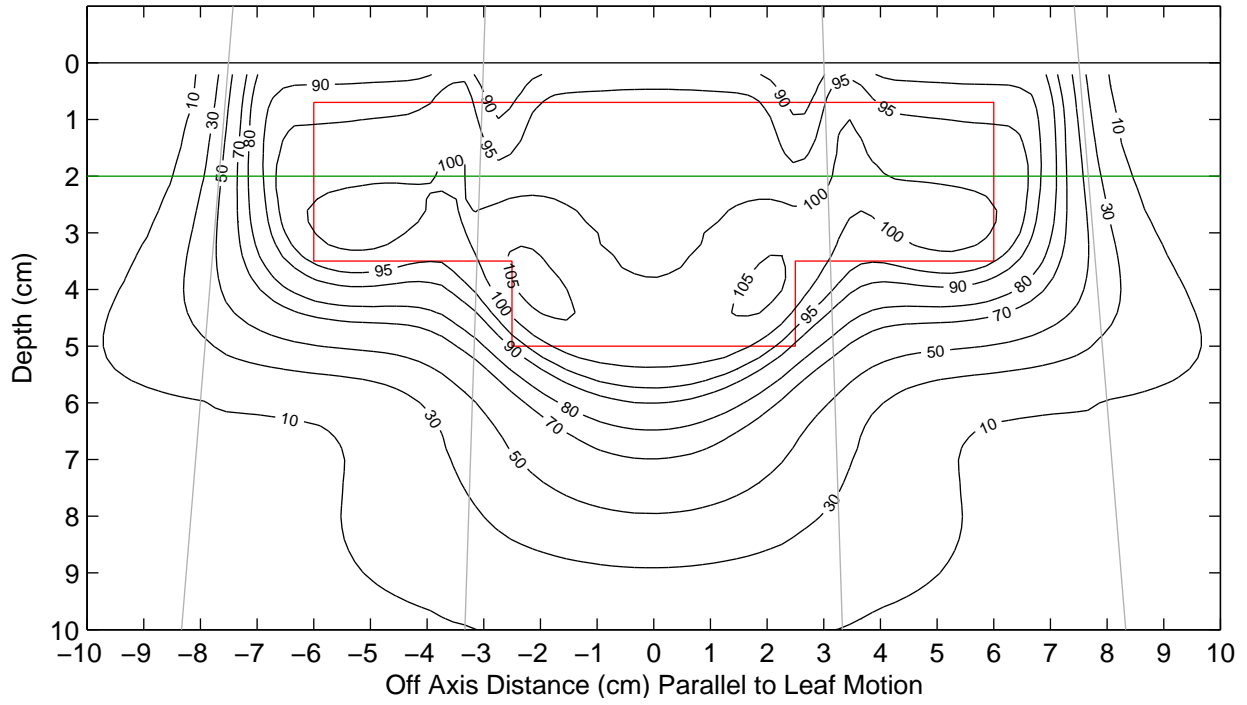


(a)

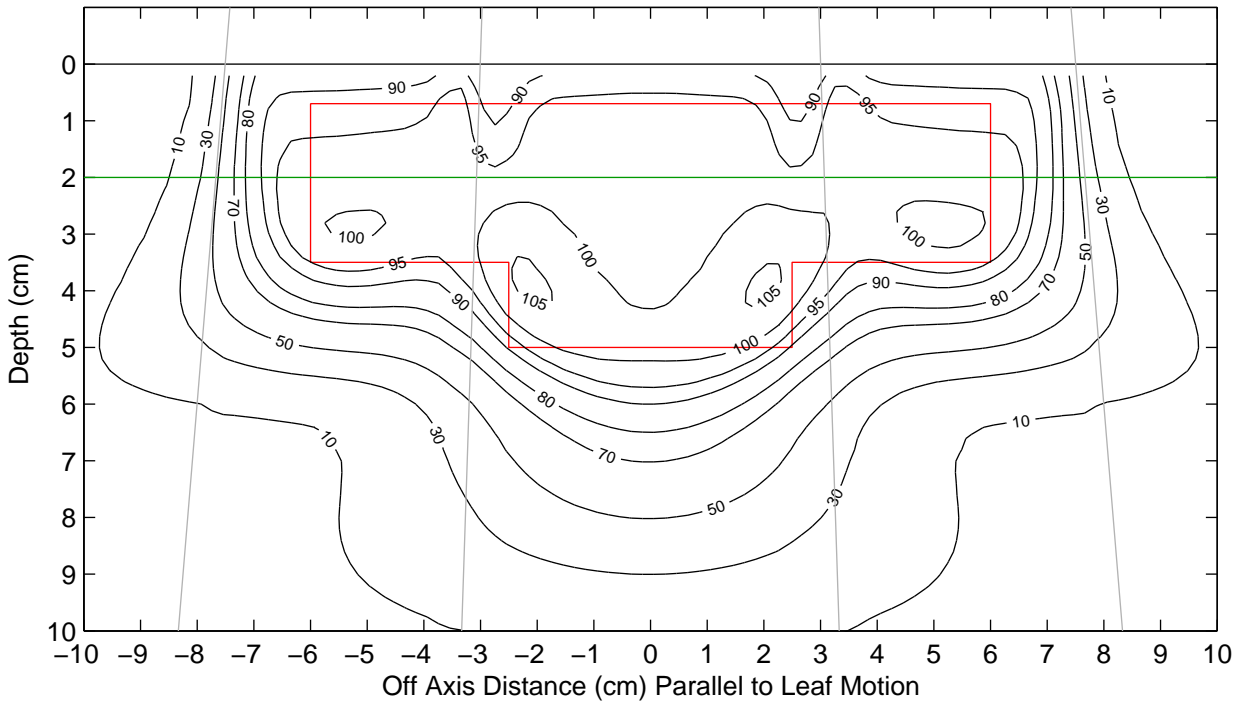


(b)

Figure 3.64: Computed isodose contours in YZ plane for concentric cylinders PTV (red) for 1-step (a) and 1D 5-step (b) feathering. Beam edges indicated by diverging lines. Line at 2 cm depth indicates location of dose profiles and film measurement.

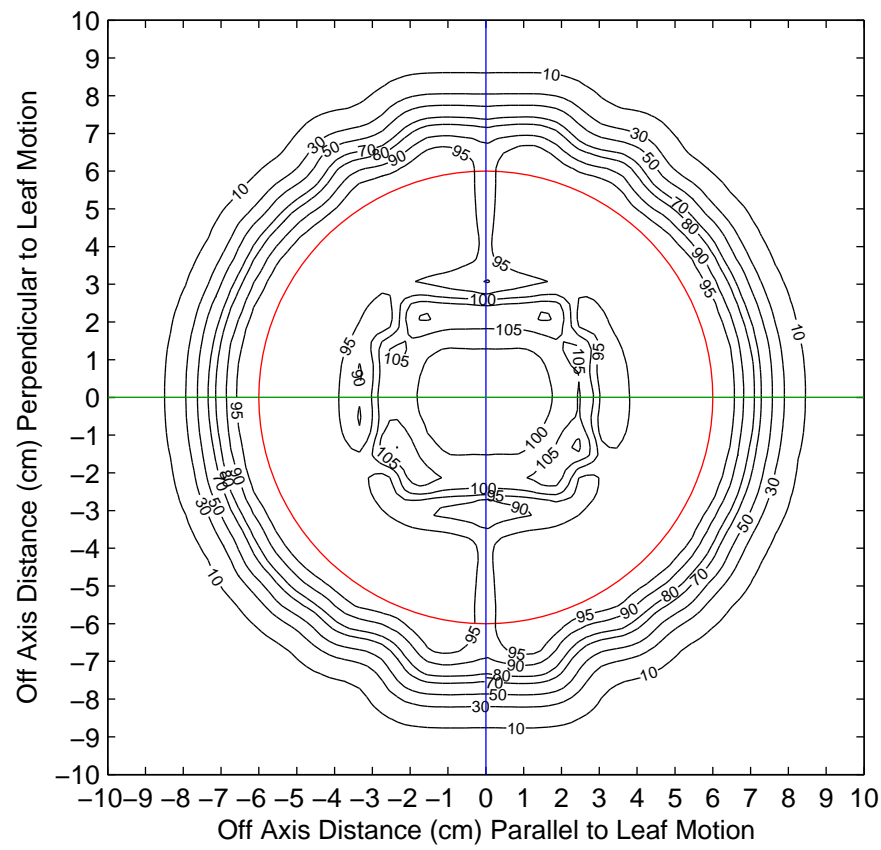


(a)

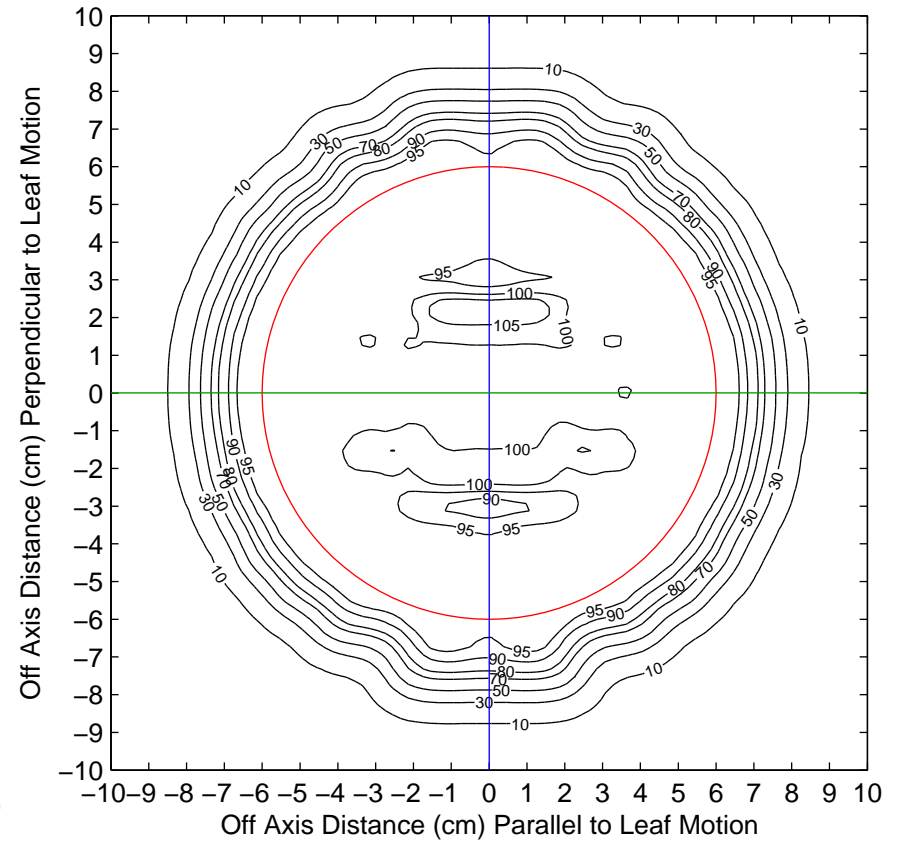


(b)

Figure 3.65: Computed isodose contours in YZ plane for two-step PTV (red) for 2D 5-step (a) and 2D continuous aperture 5-step (b) feathering. Beam edges indicated by diverging lines. Line at 2 cm depth indicates location of dose profiles.

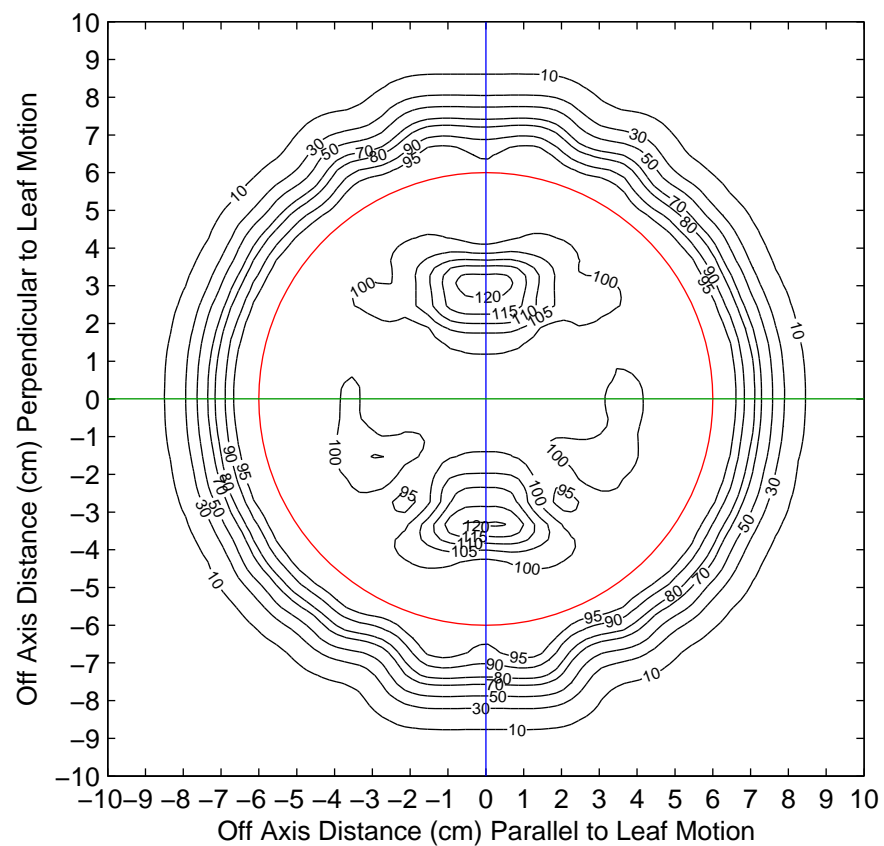


(a)

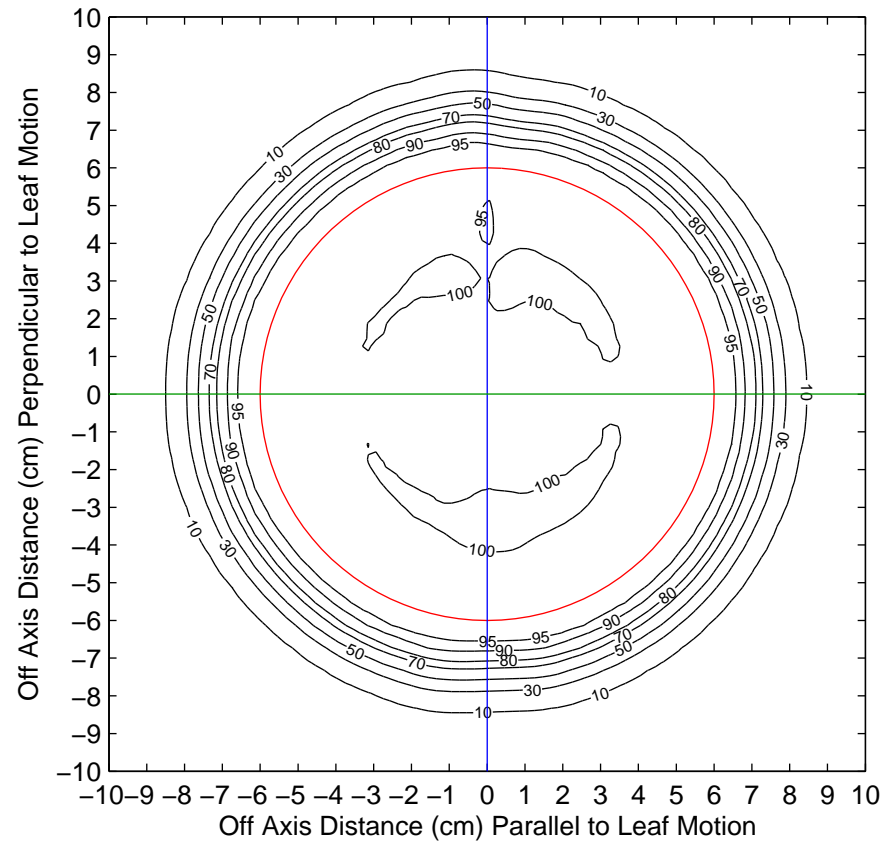


(b)

Figure 3.66: Computed isodose contours in YX plane for concentric cylinders PTV (red) for 1-step (a) and 1D 5-step (b) feathering. Green and blue lines indicate location of Y and X dose profiles, respectively.



(a)



(b)

Figure 3.67: Computed isodose contours in YX plane for two-step PTV (red) for 2D 5-step (a) and 2D continuous aperture 5-step (b) feathering. Green and blue lines indicate location of Y and X dose profiles, respectively.

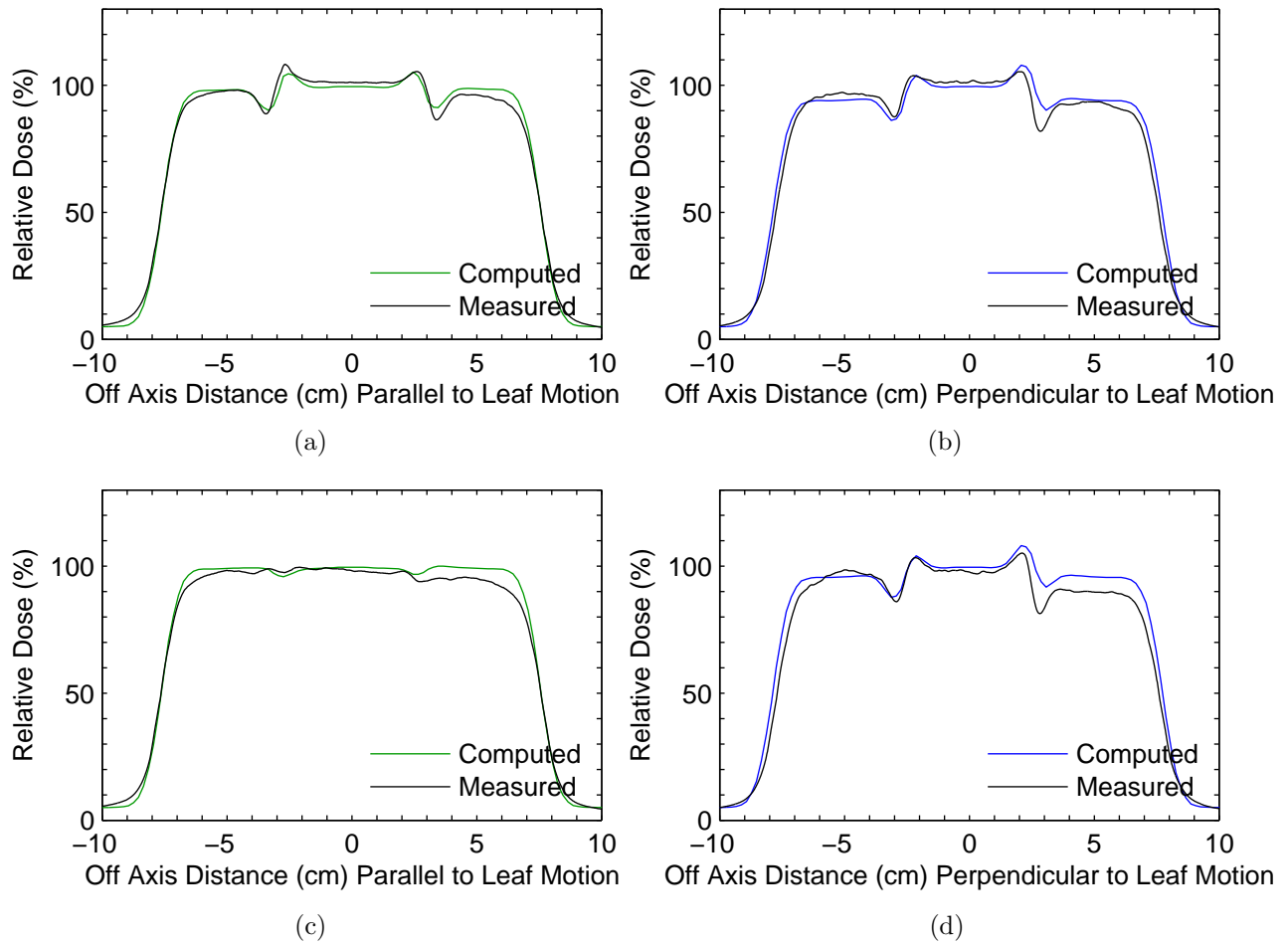


Figure 3.68: Computed vs. measured off-axis dose profiles for concentric cylinders PTV with 1-step (a,b) and 1D 5-step (c,d) feathering.

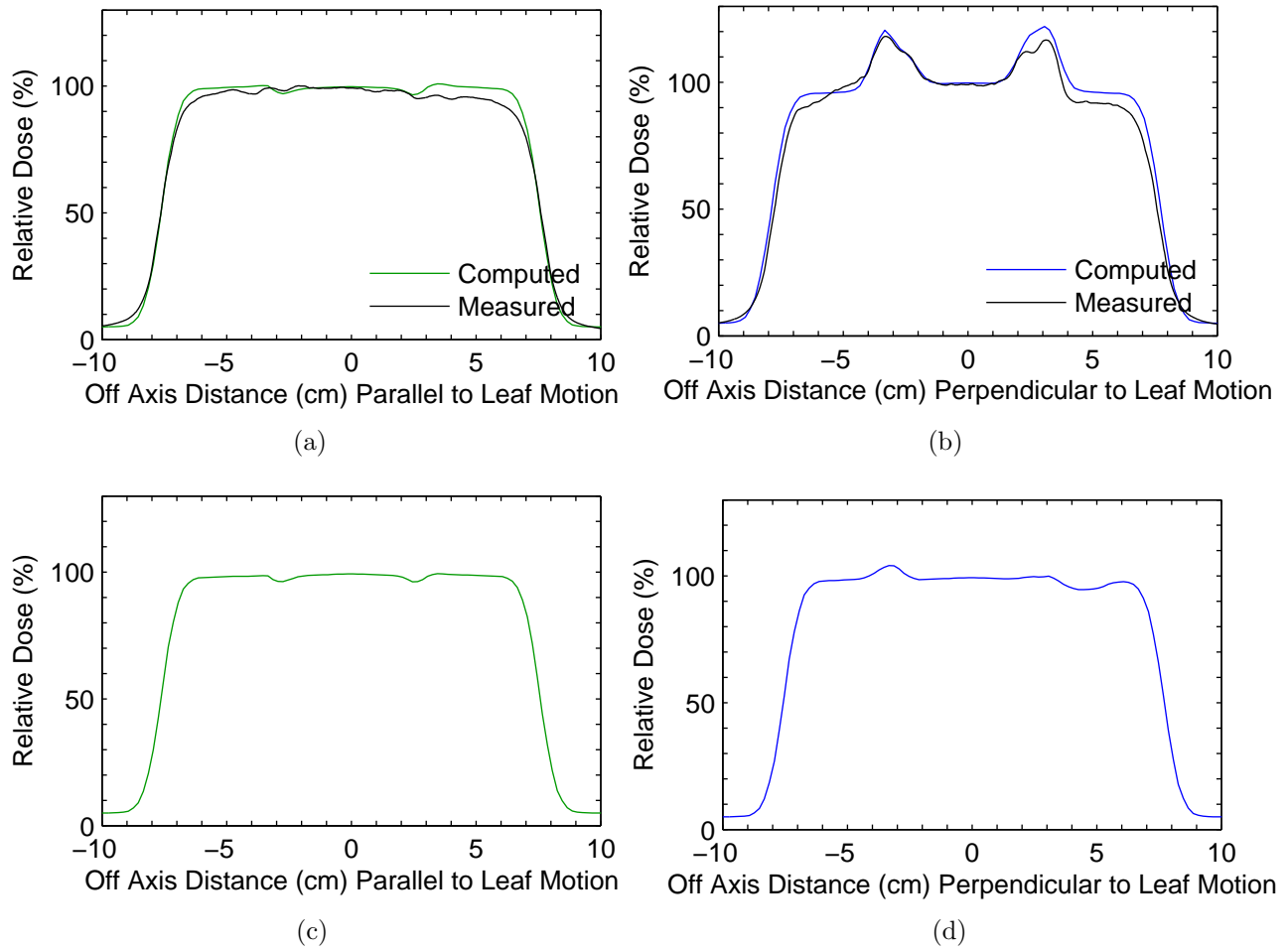
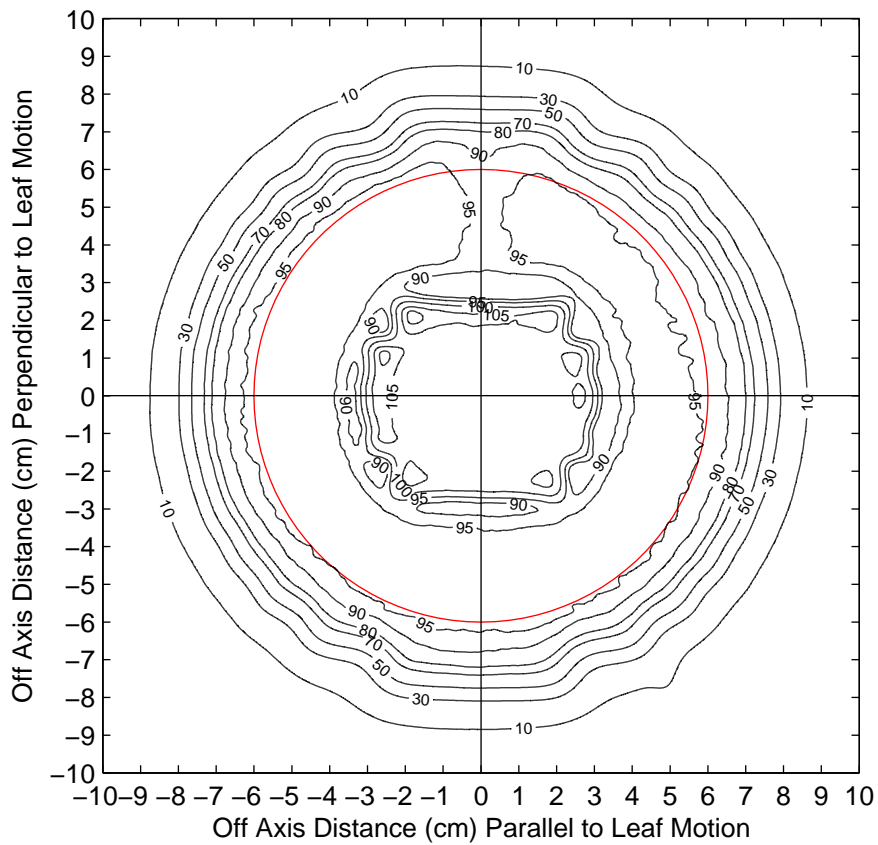
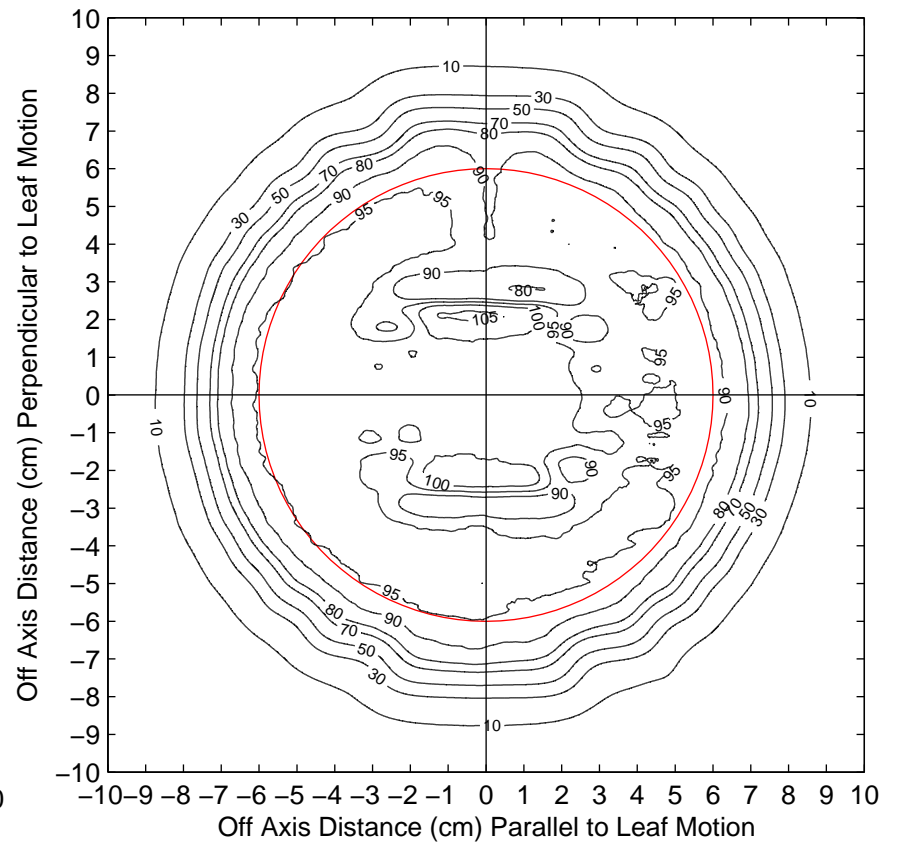


Figure 3.69: Computed vs. measured off-axis dose profiles for concentric cylinders PTV with 2D 5-step (a,b) and 2D continuous aperture 5-step (c,d) feathering.



(a)



(b)

Figure 3.70: Measured isodose contours in YX plane for concentric cylinders PTV (red) for 1-step (a) and 1D 5-step (b) feathering.

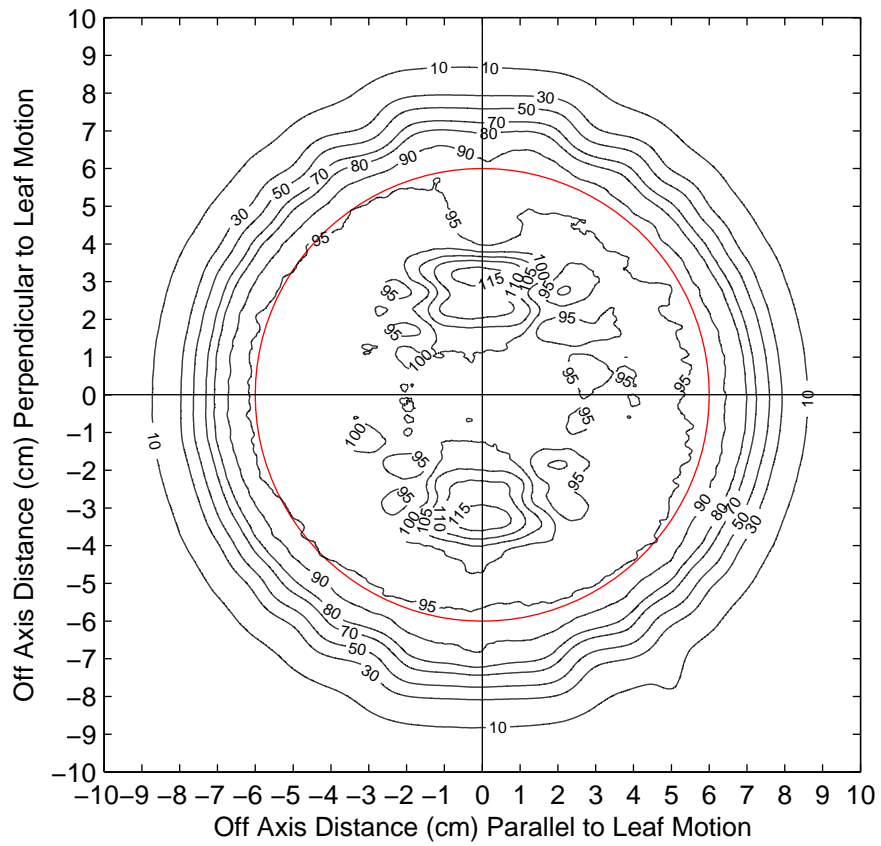


Figure 3.71: Measured isodose contours in YX plane for two-step PTV (red) for 2D 5-step feathering.




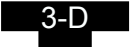
Table 3.18: Computed dose statistics for concentric cylinders PTV treatment plans with no feathering, 1D 5-step Gaussian edge feathering, and 2D 5-step Gaussian edge feathering.

Feathering	D_{mean} (%)	σ_D (%)	D_{min} (%)	D_{max} (%)	$V_{90\%}$ (%)
None	98.1	4.8	80.6	113.0	97.0
1D 5-step	98.5	3.9	80.7	110.8	98.2
2D 5-step	100.4	5.3	84.2	122.0	99.3
2D 5-step CA	98.4	3.2	85.0	107.2	99.5

3.3.6 Summary of PTV Dose Statistics

Table 3.19 summarizes dose-volume statistics for all PTVs evaluated in the current work. In all cases, the standard deviation of dose in the PTV is reduced by 1D 5-step feathering, and the percentage of PTV volume receiving at least 90% of the prescription dose, $V_{90\%}$, is increased.

Table 3.19: Computed dose statistics for test PTV treatment plans with no feathering and 5-step discrete Gaussian edge feathering. Data are expressed as percentages of the prescription dose.

PTV	Feathering	D_{mean} (%)	σ_D (%)	D_{min} (%)	D_{max} (%)	$V_{90\%}$ (%)
 Two-step	None	96.8	5.3	74.1	110.8	88.5
	1D 5-step	96.9	3.5	84.3	103.6	93.9
 Wedge	None	96.7	3.2	84.5	103.2	97.9
	1D 5-step	96.5	2.1	88.2	101.8	99.5
 Inverted Well	None	97.2	5.1	80.6	108.3	88.8
	1D 5-step	96.1	3.1	83.8	103.8	97.0
 Concentric Cylinders	None	98.1	4.8	80.6	113.0	97.0
	1D 5-step	98.5	3.9	80.7	110.8	98.2
	2D 5-step	100.4	5.3	84.2	122.0	99.3
	2D 5-step CA	98.4	3.2	85.0	107.2	99.5

Chapter 4. Conclusions

4.1 Summary of Results

Hypothesis: By feathering the abutting edges of the higher energy electron fields in segmented-field ECT, the standard deviation of the PTV dose distribution will be reduced by 30% relative to segmented-field ECT delivered by an eMLC without edge feathering.

Three specific aims were completed to test the hypothesis, and results for each of the aims are summarized as follow:

Aim 1: eMLC leaf positioning software was designed and tested to form regular and irregular fields with a leaf position uncertainty of less than ± 0.8 mm (2σ). The software utilized an electron virtual point source model for the radiation phase space and positioned eMLC leaves by intersecting the leaf edges tangent to the beam direction with the desired, irregular field aperture at the plane of the accelerator isocenter. Radiographic film measurements confirmed the accuracy of the software and the eMLC electron field delivery to within 0.8 mm at the accelerator isocenter. The establishment of accurate leaf positioning methods allowed for the delivery of irregular segmented field ECT treatments with the accuracy necessary for abutting electron fields with high lateral dose gradients.

Aim 2: The eMLC was commissioned for the 3D Hogstrom electron pencil beam dose algorithm in the Pinnacle treatment planning system. Dose distribution measurements were made with a water scanning system to collect data required for input data into the algorithm and to test the accuracy of computed dose distributions. The accuracy of the dose calculations was consistent with that previously reported for conventional collimating systems, which meet clinically acceptable standards. In high-dose, low-dose-gradient regions (greater than 90% of prescribed dose), all fields were calculated with the greatest difference being less than 5% and the mean difference for each field less than 1.5%. In high-dose-gradient regions (10 to 90% of prescribed dose), all fields agreed at the 50% isodose contour with a maximum distance to agreement of 1.7 mm and a mean distance to agreement less than 0.9

mm. At the 10% isodose contour, all fields agreed with a maximum distance to agreement of 3.7 mm and the mean distance to agreement for each field less than 1.0 mm.

Aim 3: An edge spread function was theoretically determined for the abutment of electron segments of different energies. The analytical solution was discretized into a clinically practical (5-step) discrete Gaussian edge feathering algorithm that was compatible with the Pinnacle treatment planning system. The edge feathering algorithm was tested for hypothetical PTVs in a water phantom. In the 3 PTVs with variation in depth along only one axis, 1D discrete Gaussian edge feathering reduced the standard deviation in PTV dose by at least 30%, in support of the hypothesis. However, for the concentric cylinders PTV with depth variation along two axes, 1D edge feathering improved the dose distribution but did not meet the hypothesis criteria. The 2D application of the feathering solution also failed to support the hypothesis due to the physical constraints (leaf width) of the eMLC. Computations for infinitesimal eMLC leaf widths showed that 2D application of the feathering solution would support the hypothesis and reduce the standard deviation in PTV dose by at least 30% compared to a plan with no feathering.

4.2 Conclusions

Hypothesis: By feathering the abutting edges of the higher energy electron fields in segmented-field ECT, the standard deviation of the PTV dose distribution will be reduced by 30% relative to segmented-field ECT delivered by an eMLC without edge feathering.

- True for 1D feathering for 2D PTVs
- Not true for 1D feathering for 3D PTVs
- Not true for 2D feathering for 3D PTVs due to 1-cm leaf width
- True for 2D feathering for 3D PTVs for infinitesimal leaf width

5-step discretized equal-area Gaussian provides a practical approximation to the Gaussian solution for matching penumbras of electron beams with energies of 6 to 20 MeV.

4.3 Recommendations for Future Study

Eliminate feathering of outer edges of composite field

The current method applies the feathering solution to all segments except those of the lowest energy. In the present study it was unnecessary to apply the feathering solution to the entire boundary of each segment, i.e., it only needs to be applied when the segment boundary is abutting a second, lower-energy segment. An advanced solution should only feather the regions of the segment boundary that are adjacent to segments of different energies.

Optimize depth of penumbra matching for PTV

To improve the impact of the feathering solution, the optimal depth of penumbra matching could be computed for each patient PTV. A numerical solution that computes the overall dose distribution in the PTV as a function of the matching depth may be appropriate.

Include heterogeneous CT data in edge feathering solution

The calculation of the edge feathering solution could be made more robust to include the heterogeneous patient CT data set; however, the Gaussian form of the matching solution would likely be lost and an analytical solution would likely be abandoned in favor of a numerical solution. For a numerical solution, the computation could be further improved by computing the off-axis dose distribution for small fields (the current study uses the matching solution for large fields with side scatter equilibrium to match all field sizes).

Optimize collimator angle for segmented field ECT plan

Considering the results of the current work showing the feathering solution has greatest effect when the abutment of fields is perpendicular to leaf motion, an algorithm may be developed to optimize the collimator angle for a general segmented field ECT plan where the optimization would be weighted by the length of abutment regions collapsed to the axis perpendicular to leaf motion and weighted by the difference in energy between the various segments. However, collimator angles could be restricted due to patient collision, depending on the design and SCD of the eMLC.

Future eMLC design

For a future eMLC prototype, leaf position accuracy and precision should be less than 0.3 mm, though less than 0.1 mm would be preferable. Feedback of leaf positions through potentiometers or optical systems would improve positional accuracy, as would a calibration routine that does not involve forcefully driving the leaves against the calibration bar. A denser metal (e.g., tungsten) would allow thinner leaves, which would minimize the effect of finite leaf width on field width limitation and perhaps allow for 2-D feathering with a 2-step feathering implementation in the direction perpendicular to leaf motion. Direct acquisition of linac beam monitor could allow for a flux-coupled application of the continuous feathering solution if an improved leaf motor control system was available. For clinical implementation, the leaves should be focused correctly to the accelerator virtual electron source, although this was not a major problem in the present work as the focal point was only 5 cm away from the virtual electron source.

References

- ADAC. 2001. *Pinnacle³ Beam Data Collection Guide Version 6.0*.
- Almond, P. R., P. J. Biggs, B. M. Coursey, W. F. Hanson, M. S. Huq, R. Nath, and D. W. O. Rogers. 1999. "AAPM's TG-51 protocol for clinical reference dosimetry of high-energy photon and electron beams." *Medical Physics* 26 (9): 1847–1870.
- Eyges, L. 1948. "Multiple scattering with energy loss." *Physical Review* 74:1534–5.
- Hogstrom, K. R. 2003. "Electron beam therapy: dosimetry, planning, and techniques." Edited by C. Perez, I. Brady, E. Halperin, and R. Schmidt-Ulrich, *Principles and Practice of Radiation Oncology*. Lippinkott, Williams, and Wilkins, 252–282.
- Hogstrom, K. R., and P. R. Almond. 2006. "Review of electron beam therapy physics." *Physics in Medicine and Biology* 51:R455–R489.
- Hogstrom, K. R., J. A. Antolak, R. J. Kudchadker, C. Ma, and D. D. Leavitt. 2003. "Modulated Electron Therapy." *Intensity Modulated Radiation Therapy, The State of the Art: Proc. 2003 AAPM Summer School*, pp. 749–86.
- Hogstrom, K. R., R. A. Boyd, J. A. Antolak, M. M. Svatos, B. A. Faddegon, and J. G. Rosenman. 2004. "Dosimetry of a prototype retractable eMLC for fixed-beam electron therapy." *Medical Physics* 31 (3): 443–462.
- Hogstrom, K. R., M. D. Mills, and P. R. Almond. 1981. "Electron beam dose calculations." *Physics in Medicine and Biology* 26 (3): 445–459.
- Hogstrom, K. R., M. D. Mills, J. A. Meyer, J. R. Palta, D. E. Mellenberg, R. T. Meoz, and R. S. Fields. 1984. "Dosimetric evaluation of a pencil-beam algorithm for electrons employing a two-dimensional heterogeneity correction." *International Journal of Radiation Oncology, Biology, Physics* 10 (4): 561–569.
- ICRU. 1984. "Radiation Dosimetry: Electron Beams with Energies Between 1 and 50 MeV (ICRU Report No. 35)." Technical Report, International Commission on Radiation Units and Measurements.
- IDL. 2005. IDL 6.2 Reference Guide.
- Jamshidi, A., F. T. Kuchnir, and C. S. Reft. 1986. "Determination of the source position for the electron beams from a high-energy linear accelerator." *Medical Physics* 13 (6): 942–948.
- Khan, F. M., K. P. Doppke, K. R. Hogstrom, G. J. Kutcher, R. Nath, S. C. Prasad, J. A. Purdy, M. Rozenfeld, and B. L. Werner. 1991. "Clinical electron-beam dosimetry: Report of AAPM Radiation Therapy Committee Task Group No. 25." *Medical Physics* 1:73–109.
- Low, D. A., G. Starkschall, S. W. Bujnowski, L. L. Wang, and K. R. Hogstrom. 1992. "Electron bolus design for radiotherapy treatment planning: Bolus design algorithms." *Medical Physics* 19:115–124.
- Ma, C., T. Pawlicki, S. B. Jiang, J. S. Li, J. Deng, B. Yi, E. Mok, and A. L. Boyer. 2000. "Energy- and intensity-modulated electron beams for radiotherapy." *Physics in Medicine and Biology* 45:2293–2311.

- Meyer, J. A., J. R. Palta, and K. R. Hogstrom. 1984. "Demonstration of relatively new electron dosimetry measurement techniques on the Mevatron 80." *Medical Physics* 11:670–677.
- Million, R. R., J. T. Parsons, F. J. Bova, and K. J. Kalbaugh. 1991. "Electron Beam: The Management of Head and Neck Cancer." Edited by J. M. Vaeth and J. L. Meyer, *The Role of High Energy Electrons in the Treatment of Cancer: 25th Annual San Francisco Cancer Symposium, San Francisco, California*, Frontiers of Radiation Therapy and Oncology. 107–127.
- NIST. 2009. ESTAR Compounds and Mixtures Compositional Data. <http://physics.nist.gov/cgi-bin/Star/compos.pl>.
- Perrin, D. J. 2008. "Segmented field electron conformal therapy planning algorithm." Master's thesis, Louisiana State University. <http://etd.lsu.edu/docs/available/etd-11072008-213756/>.
- Ravindran, B. P., I. R. R. Singh, S. Brindha, and S. Sathyan. 2002. "Manual multi-leaf collimator for electron beam shaping - a feasibility study." *Physics in Medicine and Biology* 47:4389–4396.
- Richert, J. D. 2006. "Improved abutment dosimetry in segmented field electron conformal therapy." Master's thesis, Louisiana State University. <http://etd.lsu.edu/docs/available/etd-07132006-154808/>.
- Richert, J. D., K. R. Hogstrom, R. S. Fields, K. L. Matthews, and R. A. Boyd. 2007. "Improvement of field matching in segmented-field electron conformal therapy using a variable-SCD applicator." *Physics in Medicine and Biology* 52:2459–2481.
- Robinson, D. 2006. *Electron Multi-leaf Collimator Internal Report*.
- Schroder-Babo, P. 1983. "Determination of the virtual electron source of a betatron." *Acta Radiologica Supplementum* 364:7–10.
- Shiu, A. S., S. S. Tung, C. E. Nyerick, T. G. Ochransky, V. A. Otte, A. L. Boyer, and K. R. Hogstrom. 1994. "Comprehensive analysis of electron beam central axis dose for a radiotherapy linear accelerator." *Medical Physics* 21 (4): 559–66.
- Starkschall, G., A. S. Shiu, S. W. Bujnowski, L. L. Wang, D. A. Low, and K. R. Hogstrom. 1991. "Effect of dimensionality of heterogeneity corrections on the implementation of a three-dimensional electron pencil-beam algorithm." *Physics in Medicine and Biology* 36 (2): 207–27.
- Tapley, N. D. 1976. *Clinical Applications of the Electron Beam*. New York: John Wiley & Sons.
- Zackrisson, B., and M. Karlsson. 1996. "Matching of electron beams for conformal therapy of target volumes at moderate depths." *Radiotherapy and Oncology* 39:261–270.
- Zuppinger, A., and G. Poretta, eds. 1965. *Symposium on High Energy Electrons (Montreux)*. Berlin: Springer.

Appendix A: Film Dose Measurements

Calibration films were irradiated with each measurement set to allow absolute dosimetry with film. The purpose of film calibration was to remove inter-batch variation in the silver bromide distribution and day-to-day variation in processor conditions from the sources of uncertainty in film dose measurements. In the current study, three sets of calibration films were irradiated for the eMLC film measurement sets. The purpose of the three sets of calibration films was to estimate the uncertainty in film dose measurement introduced by intra-batch variation in silver bromide distribution and film-to-film variation in processing and scanning conditions.

In order to achieve an accurate calibration procedure, the absolute doses at the film calibration points were determined. An ionization chamber (IC) was set up in an identical geometry to the film calibration geometry. As detailed later this included dose from the primary field and leakage and scatter dose from adjacent fields to be included in dose measured at the film calibration points.

Dose measurement with an IC followed the guidelines of the American Association of Physicists in Medicine (AAPM) Report TG-51 (Almond et al. 1999). The guidelines required that absolute measurements of dose be carried out at a depth d_{ref} in a water phantom. To establish this depth, an equilibrium field size (20×20 cm²) central axis percent depth dose was measured for a 9 MeV electron beam on the Varian Clinac 21EX (serial number 1412) in a water phantom with a parallel-plate IC. A Standard Imaging 1D Water Scanning System REF70800 and REF91800 (serial number T062561) was set up on the wooden service top to the patient couch. The PTW TN34001 (serial number 1001) Roos parallel-plate chamber had an active volume diameter of 1.5 cm, an active volume thickness of 0.2 cm, and an entrance window thickness of 0.1 cm, as specified by the manufacturer. It was positioned at the water surface and shifted 1.0 mm up with a motorized drive to position the effective point of measurement at the water surface (100 cm SSD). The uncertainty in the initial visual positioning at the water surface was estimated to be ± 0.3 mm. 200 MU were delivered

at 400 MU/min to the chamber at depths ranging from 2.0 mm to 100.0 mm at 1 mm intervals shallower than 50 mm and 5 mm intervals deeper than 50 mm. The IC charge was collected with a Keithley 614 Electrometer (serial number 312275). As described in TG-51, temperature, pressure, ion recombination, polarity, electrometer corrections, and electron stopping-power ratios were applied to the charge reading on the electrometer to determine the depth dose. The reference depth, d_{ref} was calculated by the relation

$$d_{ref} = 0.6 R_{50}(\text{cm}) - 0.1(\text{cm}) \quad (\text{A.1})$$

to be 1.99 cm. This measurement validated the use of a $(30 \times 30 \times 2)$ cm³ slab of Plastic Water as the buildup material for calibration films.

The plane parallel IC was used to measure the electron dose output in the center of each calibration field. A $30 \times 30 \times 2$ cm³ slab of Plastic Water, specifically designed to house the PTW TN34001 IC, was used for measurements in the film calibration geometry. A slab of 2 cm Plastic Water was used for buildup and 5 cm was used for backscatter.

Each calibration set consisted of 5 films. One film was a background film and was not irradiated but was otherwise handled the same as the other calibration films. Three films were irradiated with $4, 10 \times 10$ cm² electron fields with increasing dose to the calibration points. Figure A.1 shows the calibration-film field geometry. One film was irradiated with $2, 10 \times 10$ cm² electron fields in only the top positions shown in Figure A.1. The Varian Clinac 21EX accelerator delivered a 9 MeV electron beam with a 10×10 cm² electron applicator with the 10×10 cm² standard insert to a Kodak X-Omat V film placed beneath Plastic Water 2 cm thick and above 5 cm of Plastic Water as shown in Figure A.2. The SSD to the top of the plastic was 100 cm. For each calibration film, two small pinholes were pricked in the film jacket to release trapped air in the jacket that could have caused problems with charged particle equilibrium at the plane of measurement. The holes were made at the edge of the film jacket to the side of the film in the blue striped area. Pinholes were made immediately prior to irradiation, and the films were promptly returned to a light tight box

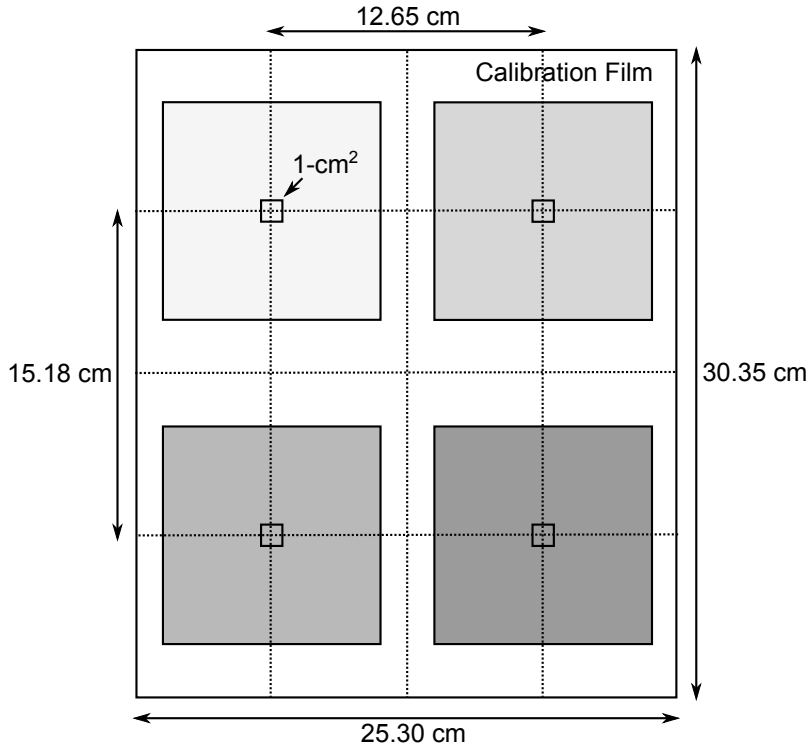


Figure A.1: Beam’s eye view of a calibration film. The four electron fields were centered in the film quadrants. The different greyscale values represent the increasing dose delivered to the film. The standard sequence was from lowest dose to highest dose: top left, top right, bottom left, and bottom right. Data in the central 1 cm² areas were used for the dose calibration points.

after irradiation. The background film was not irradiated (0 cGy). The fields on the first film were given 1, 7, 13, and 19 monitor units corresponding to calibration doses of 1.1, 7.2, 13.2, and 19.3 cGy. The second film was given 25, 31, 37, and 43 monitor units corresponding to calibration doses of 25.6, 31.6, 37.7, and 43.7 cGy. The third film was given 49, 55, 61, and 67 monitor units corresponding to calibration doses of 50, 56, 62, and 68 cGy. The fourth film was given 73 and 79 monitor units corresponding to calibration doses of 74 and 80 cGy. The films were processed and scanned at the same time as were the eMLC measurement films. The RIT 113 version 5.0 software calibration tool allowed extraction of the scanner A/D mean value in a 1×1 cm² area that was visually placed in the center of the radiation field in the digitized film image.

After acquiring the scanner A/D value that corresponded to delivered calibration doses, the calibration curve was created and used to calibrate the measurement films. Conversion of

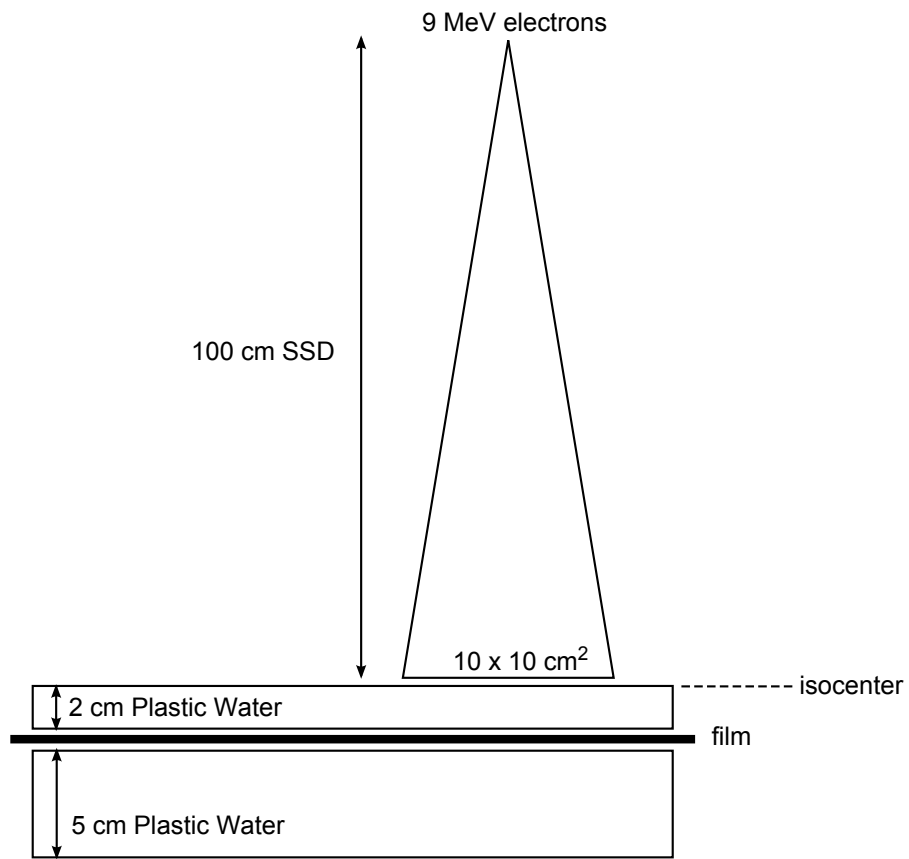


Figure A.2: Film calibration setup geometry for one of 4 fields used to irradiate film (cf. Figure A.1).

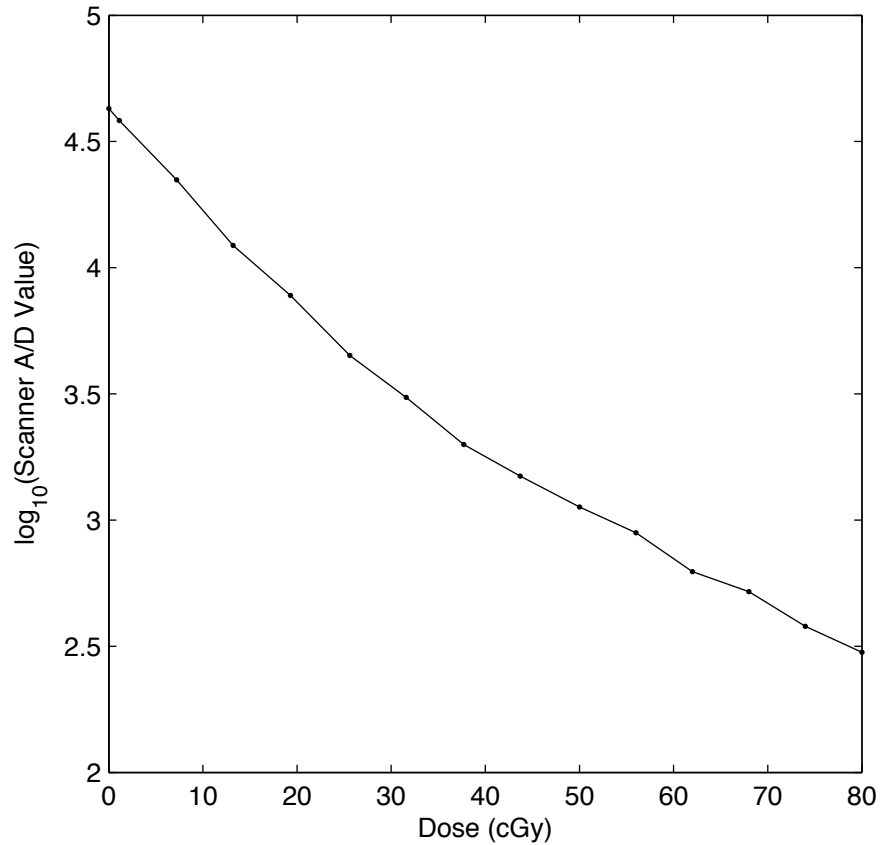


Figure A.3: Film dose calibration curve. The logarithms (base 10) of the scanner A/D values were plotted against the calibration doses and linearly interpolated to form a calibration curve, which was used to determine the dose for a given pixel value.

the scanned A/D values to dose was performed in Matlab software developed for this work. This required the raw film data be exported from the RIT software in a Matlab compatible format. Calibration films were scanned at the same scanner resolution as the measurement films (178 μm). The Vidar pixel calibration was performed before each batch of films to be scanned and never performed in the middle of a scanning batch.

The dose measurement program developed in Matlab converted scanner A/D values to dose by linearly interpolating the calibration points shown in Figure A.3 and Table A.1 using the logarithm (base 10) of the scanner A/D values and the calibration doses. The line equation was solved for each interval between a low dose, d_l , and high dose, d_h with

Table A.1: Film calibration curve data used in the Matlab program.

Film	Dose (cGy)	Scanner A/D Value
Background	0	42752
Film 1	1.11	38293
	7.2	22295
	13.2	12262
	19.3	7762
Film 2	25.6	4487
	31.6	3060
	37.7	1994
	43.7	1492
Film 3	50	1127
	56	890
	62	624
	68	521
Film 4	74	380
	80	299

corresponding pixel A/D values p_l and p_h , respectively, and inverted to give dose as a function of pixel A/D value.

$$D = D_l + (\log_{10}(p) - \log_{10}(p_l)) \frac{D_h - D_l}{\log_{10}(p_h) - \log_{10}(p_l)}. \quad (\text{A.2})$$

Appendix B: Pinnacle Photon Model

Discrepancies in the dose distributions computed with the Pinnacle dose algorithm compared with the measured dose distributions described in Section 3.2.2, particularly the differences in the 5% isodose contours near the water surface, led to an investigation of the Pinnacle treatment planning system electron beam models. In the physics mode of Pinnacle, the electron beam models were inspected and two errors were found in the handling of the bremsstrahlung photon dose component.

Measured off-axis photon dose profiles at depth $R_p + 2$ cm were compared with the Pinnacle computed profiles displayed in the physics mode electron beam model. Figures B.1 and B.2 shows the measured commissioning profile compared with the Pinnacle computed profile for field sizes of 20×20 and 7×7 cm². Three differences are noted, though only two were considered errors.

First, the off-axis photon dose profile is forced to zero at field-size dependent distances off-axis, approximately 4 cm beyond the geometric field edge. This difference was expected (and not considered an error), and likely was implemented to decrease computation time by reducing the amount of data used in a single dose computation. However, for future dose calculations for segmented field ECT, this omission of data should be reconsidered, as the location of the dose cutoff point could be in the center of an abutting field and appear (incorrectly) in the composite dose distribution as a dose heterogeneity in the PTV.

Second, the computed dose profile outside of the geometric field edge is too low. This is attributed to the cutout transmission factor being applied to the measured profile beyond the field edge of the nominal field size to create the computed, model-profile which is used in each dose calculation. The cutout transmission factor should not be applied to the measured profile beyond the field edge because the measured profile was measured with the collimator (cutout) in place. The cutout transmission factor should only be applied inside the geometric field edge to represent the attenuation of photons by eMLC leaves (or cerrobend inserts) which extend into the field for irregular fields. The effect of applying the cutout transmission

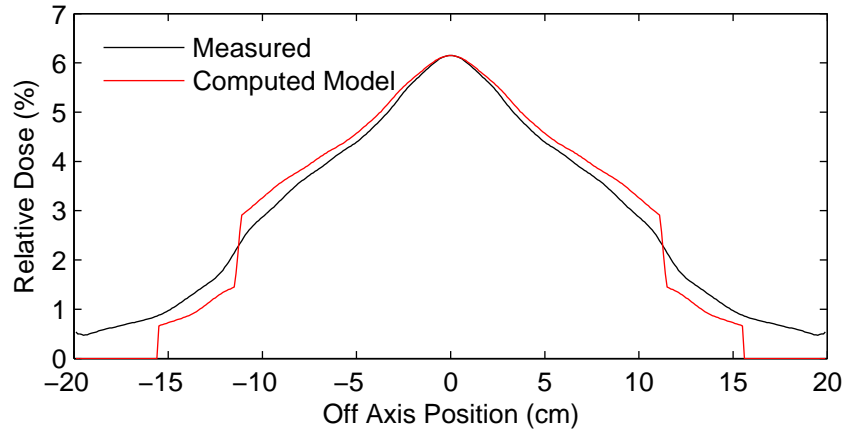


Figure B.1: Photon model off-axis dose profiles for 20 MeV, $20 \times 20 \text{ cm}^2$ field data. Measured profile (black) was used by Pinnacle to create the computed model profile (red).

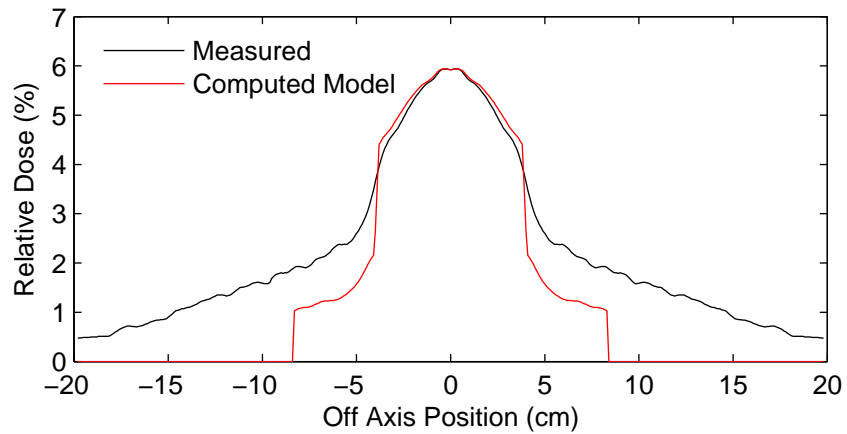


Figure B.2: Photon model off-axis dose profiles for 20 MeV, $7 \times 7 \text{ cm}^2$ field data. Measured profile (black) was used by Pinnacle to create the computed model profile (red).

factor outside of the geometric field edge of the measured data is equivalent to applying the transmission factor twice, giving rise to a beam-model profile with too little dose outside the geometric field edge.

Third, the measured photon dose profile does not agree with the computed model profile inside of the geometric field edge. The difference appears linear and increases with distance from central axis. This is attributed to improper implementation of the beam divergence. The photon model profile is used throughout the depth range of calculation by scaling the lateral distribution of the profile according to the appropriate divergence from the electron source. The computed model profile indicates that the treatment planning system has used the measured input as if that were the lateral distribution at the water surface ($SSD = 100$ cm) and applied the divergence appropriate for the photon profile depth ($R_p + 2$ cm). The implementation is incorrect because the measured profile was taken at the photon profile depth. The lateral distribution of photons at the water surface should be modeled by converging the profile lateral distribution by a factor of $SSD/(SSD + R_p + 2$ cm).

Considering these two errors in the photon model implementation, an improved methodology was investigated. First, rather than use the photon profile measurements for each commissioned field size as input, only use the photon profile for the largest field size for each field. This does not resolve the problem that the cutout transmission factor has been applied effectively twice beyond the largest field size geometric field edge, but does reduce the impact of this error for the smaller fields. Second, the divergence error can be mathematically corrected by scaling the off-axis coordinates of the measured input profile by a factor of $SSD/(SSD + R_p + 2$ cm). This correction causes the error in Pinnacle to transform the scaled input data into the correct model profile at the photon measurement depth.

Although these investigations suggest errors in the Pinnacle version 7.4f code, the significance of these errors (and the impact of the proposed solutions) is on the order of a 1% impact on the dose distribution. The impact of the discussed improvements on the overall dose distribution is shown in the comparisons of Figures B.5, B.6, B.7, and B.8 for the 7×7 and 15×15 cm² fields discussed in Section 3.2.2.

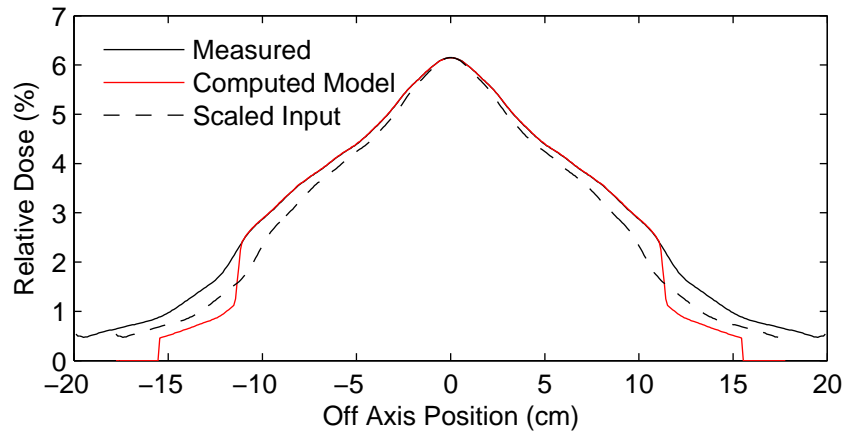


Figure B.3: Modified photon model off-axis dose profiles for 20 MeV, $20 \times 20 \text{ cm}^2$ field data. Measured profile shown in black. Scaled input profile (black, dashed), created by converging the measured profile, used by Pinnacle to create the computed model profile (red).

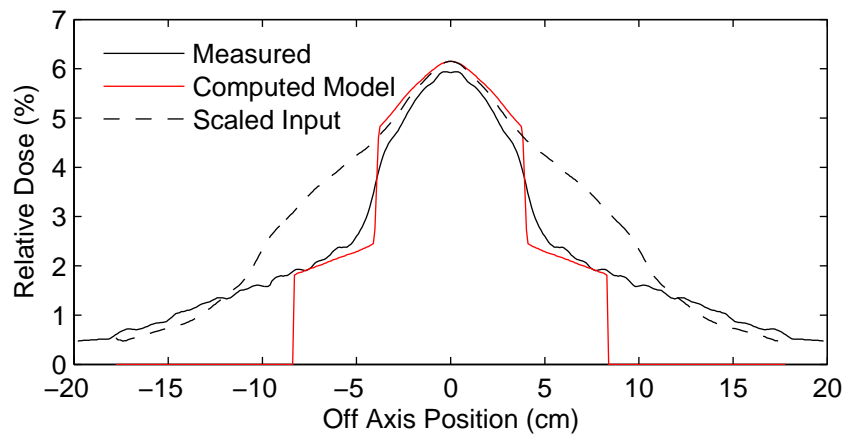


Figure B.4: Modified photon model off-axis dose profiles for 20 MeV, $7 \times 7 \text{ cm}^2$ field data. Measured profile shown in black. Scaled input profile (black, dashed), created by converging the $20 \times 20 \text{ cm}^2$ measured profile, used by Pinnacle to create the computed model profile (red).

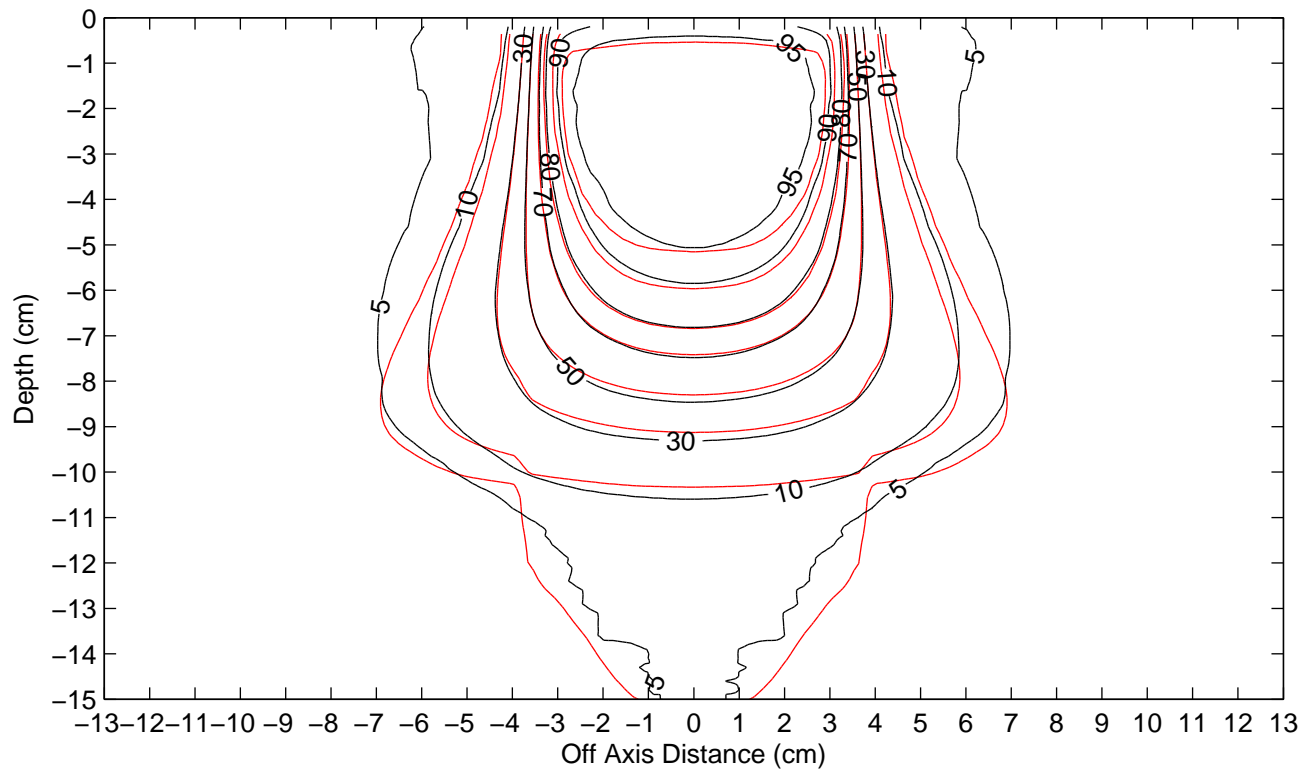


Figure B.5: Computed vs. measured isodose contours for 20 MeV, $7 \times 7 \text{ cm}^2$ field size. Standard Pinnacle photon model.

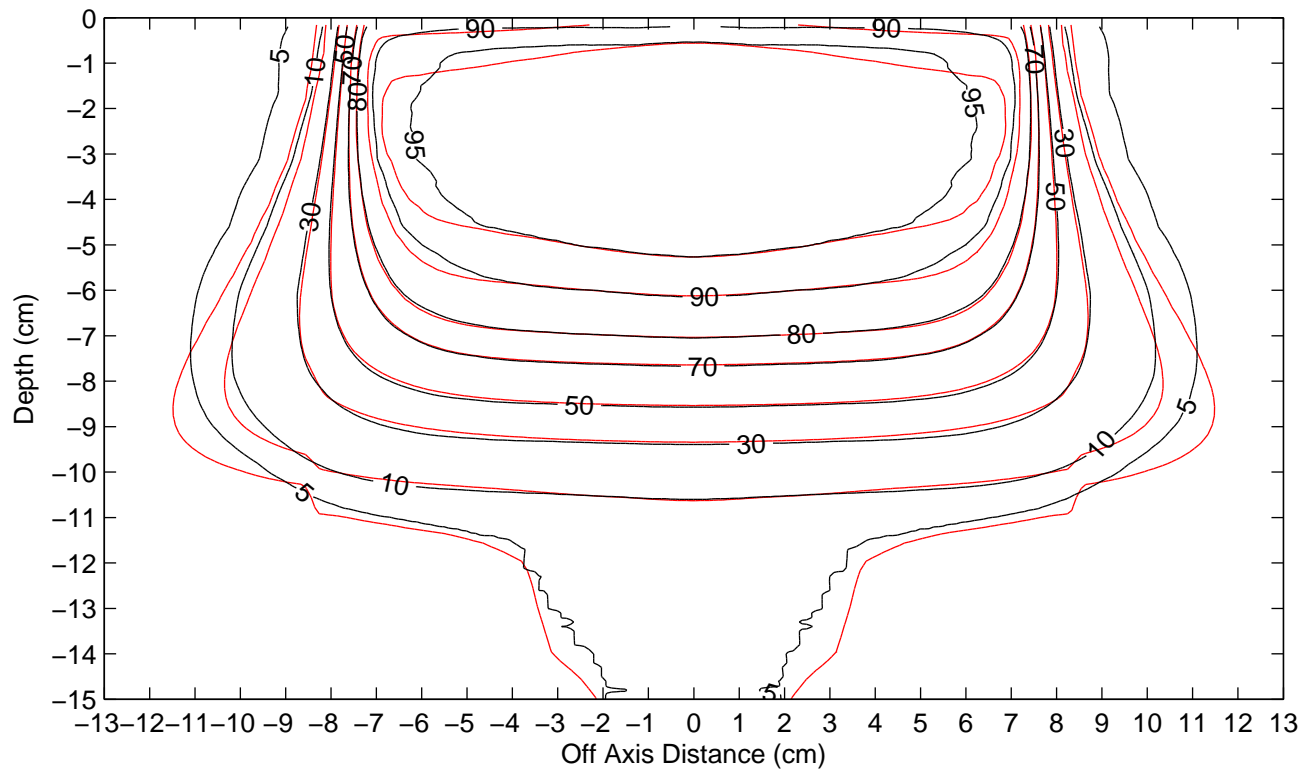


Figure B.6: Computed vs. measured isodose contours for 20 MeV, $15 \times 15 \text{ cm}^2$ field size. Standard Pinnacle photon model.

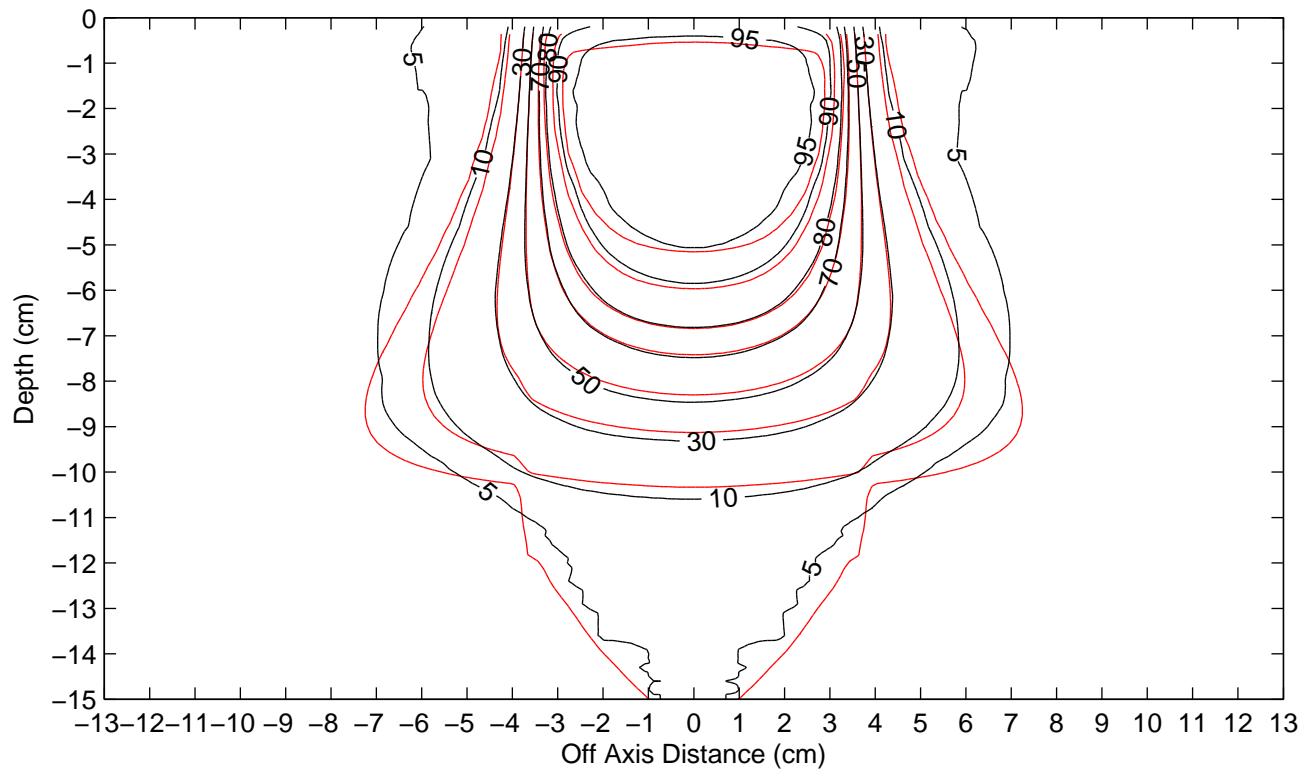


Figure B.7: Computed vs. measured isodose contours for 20 MeV, $7 \times 7 \text{ cm}^2$ field size. Modified Pinnacle photon model. The input photon off-axis dose profile was the $20 \times 20 \text{ cm}^2$ photon profile scaled to correct the divergence error.

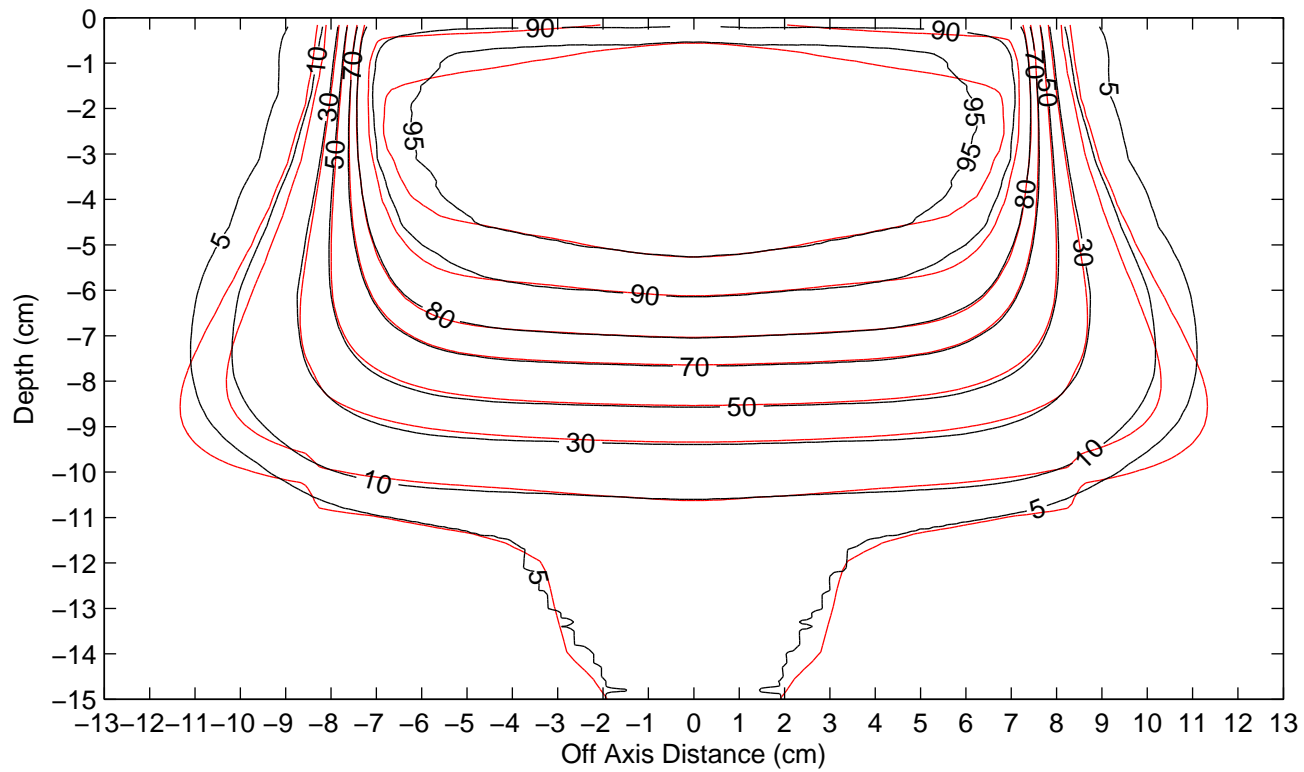


Figure B.8: Computed vs. measured isodose contours for 20 MeV, $15 \times 15 \text{ cm}^2$ field size. Modified Pinnacle photon model. The input photon off-axis dose profile was the $20 \times 20 \text{ cm}^2$ photon profile scaled to correct the divergence error.

The discrepancies in the shallow 5% isodose contours for the measured and computed distributions were not attributed to errors in the photon model and were not resolved by modifications to the photon model. The errors in the photon model were determined to have an lesser impact on the results of the current study than other limitations of the dose algorithm. Therefore, dose computations for the current study were performed with the standard, unmodified photon model.

Vita

John Eley was born in Jackson, Mississippi in 1983. He grew up with his parents and two sisters until his graduation from St. Andrew's Episcopal School in 2001. Later that year, he moved to Charleston, South Carolina to attend the College of Charleston and pursue a Bachelor of Science in physics that he earned in 2005. In 2006, he moved to Baton Rouge, Louisiana to begin a Master of Science in medical physics and health physics at Louisiana State University. John currently lives in Houston, Texas and is working on his doctorate in medical physics at The University of Texas M. D. Anderson Cancer Center. He hopes to begin his career with a combination of research and clinical work and, ultimately, become a professor of medical physics.